

# **Optical Spectroscopy Instrumentation for the Characterisation of Wide Band Gap Materials**

**Rachel Elizabeth Cross**

Department of Physics

Aberystwyth University

This thesis is submitted for the degree of

*Doctor of Philosophy*

2015



I would like to dedicate this thesis to my loving and long-suffering husband Gareth.





## **Declaration**

This work has not previously been accepted in substance for any degree and is not being concurrently submitted in candidature for any degree

Signed

Date

## **STATEMENT 1**

This thesis is the result of my own investigations, except where otherwise stated. Where correction services have been used, the extent and nature of the correction is clearly marked in the footnote(s)

Other sources are acknowledged in the text giving specific references.

A bibliography is appended

Signed

Date

## **STATEMENT 2**

I hereby give consent for my thesis, if accepted, to be available for photocopying and for inter-library loan, and for the title and summary to be made available to outside organisations.

Signed

Date



## Summary

This thesis presents work undertaken in the design, build, characterisation and first results of a new instrument for the optical characterisation of wide band gap materials by their luminescence.

Optical spectroscopy is a promising method for investigating material properties due to its non-destructive nature and high sensitivity. The ability to relate to a material's optical properties to its structure and composition is highly desirable in Materials Physics applications. Spatial information is lost when measuring heterogeneous samples due to the convolution of spectral information from different regions within the sample. Though the combination of imaging and spectroscopy spatially resolved data can be a. In this work the spectro-radiometrically calibrated instrument HeLIOS (Hyperspectral Imaging for Optical Spectroscopy) is introduced. This instrument has allowed the collection of spatially resolved radiometrically calibrated photoluminescence investigations on a number of wide band gap materials.



## Acknowledgements

I would like to acknowledge and thank the people who have helped me through my studies; those who have celebrated the highs and suffered the lows with me. Firstly I would like to thank my supervisor, Prof Andy Evans, for the opportunity to do this PhD, his patience through lengthy discussions and his support. I would also like to thank my second supervisor, Dr David Langstaff, for all his help with LabVIEW and his support and encouragement. I am grateful to both supervisors for allowing me to take the difficult but rewarding decision to change focus mid-way through my studies and concentrate on instrumentation development. I would like to also thank the late Prof Dave Barns for introducing me to a new avenue of research, and inviting me into his team. I shall always regret he passed away before we realised our collaboration, but will endeavour to continue on the path he helped set me on in my research.

Special thanks must go to Dr Matt Gunn for day-to-day support, technical assistance and general motivation throughout this work. Thank go to my fellow PhD. students Dr Simon Cooil, Mr Steven Turner and Mr Morgan Jones for their camaraderie. Much of this work would not have been possible without the skills of the technicians in our Mechanical Workshop and Electronics Workshop. I am grateful to have worked with such skilled and knowledgeable people including Mr John Parry, Dr Matt Gunn, Mr Leslie Dean and Mr David Lewis.

This project was possible through generous funding from the European Union and Welsh assembly as a KESS Scholarship with industrial sponsorship from Scanwel Ltd. I would like to thank Mr Ian Owen and Dr Rupert Smith for their support and advice throughout this work.

In addition to my colleagues I would like to thank my family and friends for their support, encouragement and patience throughout this period. Without them I could not have completed this work.

Finally thanks must go to my husband, Gareth, for facilitating our move back to Wales to enable me to study for this PhD and for his constant love and reassurance.



*I often say that when you can measure what you are speaking about, and express it in numbers, you know something about it; but when you cannot measure it, when you cannot express it in numbers, your knowledge is of a meagre and unsatisfactory kind; it may be the beginning of knowledge, but you have scarcely, in your thoughts, advanced to the stage of science, whatever the matter may be.*

*Lord Kelvin*





## Publications

### Papers

Noebels, Matthias, **Cross, Rachel E.**, Evans, D. A., Finlayson, Chris E. *Characterization of spray-coating methods for conjugated polymer blend thin films*, Journal of Materials Science **49** 12 pp 4279-4287 (2014)

Harris J.K., Cousins C.R., Gunn M., Grindrod P.M., Barnes D., Crawford I.A., **Cross R.E.**, Coates A.J. *Remote detection of past habitability at Mars-analogue hydrothermal alteration terrains using an ExoMars Panoramic Camera Emulator*, Icarus **252** pp 284-300 (2015)

Finlayson, C., **Cross R. E.**, Evans D. A., Cooil S. P., Schulte, K., Friend R., Kouwer, P., Alan, R. *Temperature dependent mobility in thin-film transistors based on supramolecular perylene arrays*, Journal of Physics D (submitted)

**Cross, R. E.**, Gunn, M., Langstaff, D.P., Evans, D.A. *A new instrument for luminescence imaging – HeLIOS (Hyperspectral Luminescence Imaging for Optical Spectroscopy)*, Review of Scientific Instruments (in-preparation)

**Cross, R. E.**, Jones G. O., Gunn, M., Veary-Roberts A. R, McGlynn A. G. , Roberts, O. R., Evans, D.A., Twitchen, D., Martineau, P, Lawson, S., Fisher, D *Correlated local bonding and light emission in brown diamonds: a combined luminescence, Raman and x-ray absorption approach*, Diamond and Related Material (in-preparation)



## **Conference Proceedings** (presenting author)

A. G. McGlynn, **R. E. Cross**, D.A. Evans *Light emission from ultrathin organic films grown by in-vacuo electrospray deposition*, Condensed Matter Materials Physics Conference, Warwick University (2010)

**R. E. Cross**, A. G. McGlynn, D. P. Langstaff, D. A. Evans *Light emission and molecular orientation in thin films of solution-processed semiconducting polymers*, MRS Spring Meeting, San Francisco (2013)

**Cross, R. E.**, Gunn, M., Cooil, S. P., Owen, G. J., Turner, S. P., Langstaff, D. P., Evans, D.A. *Hyperspectral optical imaging for light emission and scattering in diamond*, Proceedings of The 64th Diamond Conference, Warwick University (2013)

**Cross, R. E.**, Gunn, M., Jones, G. O., Langstaff, D.P., Evans, D.A. *Hyperspectral optical imaging for material characterisation*, Proceedings of the UK Luminescence and ESR Meeting, University of St. Andrews (2013)

**Cross, R. E.**, Gunn, M., Langstaff, D.P., Evans, D.A. *Radiometrically calibrated hyperspectral optical imaging for light emission and scattering in diamond*, Proceedings of The 65th Diamond Conference, Warwick University (2014)

**Cross, R. E.**, Gunn, M., Langstaff, D.P., Barnes, D. P., Evans, D.A. *Radiometrically calibrated hyperspectral photoluminescence imaging*, The European Astrobiology Network Association, Edinburgh University (2014)

Barnes, D., Josset, J-L., Coates, A., Cousins, C., Cockell, C., Gunn, M. **Cross, R.**, Langstaff, D., Griffiths, A., Josset, M., Souchon, A., Verhaeghe, A., Grindrod, P., Dartnell, L., Team, HyperCLUPI *Developing a Hyperspectral CLose UP Imager With UV Excitation (HyperCLUPI) for Mars Exploration*, European Planetary Science Congress 2014 Vol. 9 EPSC2014-729 (2014)



# Contents

|   |      |
|---|------|
| Contents.....   | xvii |
| Chapter 1    Introduction .....                       | 1    |
| 1.1    Introduction.....                              | 1    |
| 1.2    Layout of thesis and contributions.....        | 3    |
| 1.2.1    Chapter 2.....                               | 3    |
| 1.2.2    Chapter 3.....                               | 4    |
| 1.2.3    Chapter 4.....                               | 4    |
| 1.2.4    Chapter 5.....                               | 4    |
| 1.2.5    Chapter 6.....                               | 5    |
| 1.2.6    Chapter 7.....                               | 6    |
| Chapter 2    Techniques .....                         | 7    |
| 2.1    Introduction.....                              | 7    |
| 2.2    Interaction of radiation with matter .....     | 7    |
| 2.2.1    Luminescence .....                           | 9    |
| 2.2.2    Raman Spectroscopy.....                      | 21   |
| 2.2.3    Optical Microscopy .....                     | 32   |
| 2.3    Material preparation and characterisation..... | 34   |
| 2.3.1    ApREES .....                                 | 34   |
| 2.3.2    Deposition Techniques .....                  | 40   |
| 2.3.3    Excitation sources .....                     | 40   |
| 2.3.4    Atomic Force Microscopy .....                | 49   |

|           |  |     |
|-----------|--|-----|
| 2.4       | Chapter summary.....                                     | 51  |
| Chapter 3 | Spectral Imaging.....                                    | 53  |
| 3.1       | Introduction.....  | 53  |
| 3.1.1     | Spectroscopy.....  | 53  |
| 3.1.2     | Imaging.....   | 55  |
| 3.1.3     | Spectral and Hyperspectral Imaging.....                  | 57  |
| 3.2       | Instrumentation and Components.....                      | 71  |
| 3.2.1     | Spectral dispersion.....                                 | 72  |
| 3.2.2     | Objectives and lenses .....                              | 80  |
| 3.2.3     | Detection.....   | 84  |
| 3.3       | Chapter summary.....                                     | 93  |
| Chapter 4 | Helios.....  | 94  |
| 4.1       | Introduction.....  | 94  |
| 4.2       | System Development .....                                 | 95  |
| 4.3       | Characterisation and calibration.....                    | 105 |
| 4.3.1     | Instrumentation .....                                    | 107 |
| 4.3.2     | Nomenclature of Characterisation and Calibration.....    | 114 |
| 4.3.3     | Noise .....  | 119 |
| 4.3.4     | Photon Transfer (DN to $\lambda$ ).....                  | 142 |
| 4.3.5     | Photometric response and calibration uncertainties ..... | 150 |
| 4.4       | Experimental data acquisition.....                       | 161 |
| 4.5       | Chapter Summary.....                                     | 168 |
| Chapter 5 | Experimental Results .....                               | 169 |
| 5.1       | Introduction.....  | 169 |

|            |  |     |
|------------|--|-----|
| 5.2        | Diamond samples .....  | 172 |
| 5.2.1      | Natural diamonds .....   | 184 |
| 5.2.2      | Synthetic diamonds .....   | 207 |
| 5.2.3      | Non-diamond mineral samples.....   | 264 |
| 5.3        | Summary .....  | 279 |
| Chapter 6  | Discussion and Conclusions .....   | 280 |
| 6.1        | Introduction.....  | 280 |
| 6.2        | ApREES in-situ monitoring .....  | 280 |
| 6.3        | HeLIOS .....   | 283 |
| 6.4        | Birefringence in diamond .....   | 284 |
| 6.5        | Photoluminescence features in diamond .....  | 288 |
| 6.5.1      | High-resolution and spatially resolved PL of diamond .....   | 290 |
| 6.6        | Raman spectroscopy of diamond.....   | 295 |
| 6.7        | Colouration in diamonds.....   | 304 |
| 6.7.1      | Absorption due to lattice dislocations.....  | 305 |
| 6.7.2      | Absorption due to $sp^2$ carbon in the form of graphitic inclusions or amorphous carbon at micro domains ..... | 306 |
| 6.8        | High-resolution and spatially resolved PL of additional samples .....  | 307 |
| 6.9        | Summary .....  | 309 |
| Chapter 7  | Further Work.....  | 311 |
| References | .....  | 315 |





# Chapter 1 Introduction

## 1.1 Introduction

Wide-band gap materials are of relevance in diverse fields such as Materials Physics, Earth Sciences, Optoelectronics, and Quantum Technology. The primary objective of this work is to investigate the interaction of light with such materials to understand phenomena such as defect type and distribution, residual stress and compositional variation. Materials studied include natural and synthetic diamond, synthetic oxides, and natural minerals.

The development of suitable optical characterisation techniques is central to the understanding of complex natural materials and the production of high quality synthetics. Such techniques require the control of incident radiation sources, precision optics for the collection of the subsequently scattered or emitted light, and efficient detection.

Diamond has been chosen as the primary material for study due to its wide range of applications, where deviation from its simple elemental and crystallographic structure and near UV band gap (5.5 eV) is fundamental to understanding its macroscopic properties. Defects in diamond affect the optical and electronic properties, and are readily probed by optical absorption and emission using UV-VIS excitation. Photoluminescence spectroscopy is a widely used as a sensitive probe of defects within the diamond band gap which affect properties such as colouration, electrical conductivity and quantum spin states. It is also widely used in the study of optoelectronic materials and Earth and planetary minerals, examples of which have been included in this work (ZnO and CaCO<sub>3</sub>).

## 1.1 Introduction

---

Larger scale imperfections due to local variations in chemical bonding and stress can be probed using inelastic light scattering, in particular Raman spectroscopy, which for example makes use of diamond's well-defined first order Raman phonon frequency. Understanding the inherent stress in materials, such as diamond, is important for tribological phenomena such as wear, erosion, and abrasion.

For complex materials, with variation in composition and structure over different length scales, conventional single point spectroscopy can be restrictive and there is a need to expand the capability of the techniques. In many cases it is also desirable to apply such techniques during material processing. In this work, spatially resolved photoluminescence and Raman spectroscopies have been applied in controlled environments. This has included the development, build and calibration of instruments for materials characterisation by imaging luminescence emission and in-vacuo monitoring by Raman spectroscopy. This work has been multidisciplinary, involving collaboration with colleagues in Earth Sciences, Computer Science, Chemistry and Astrobiology.

Optical characterisation has been integrated in a new multi-technique, ultra-high vacuum (UHV) system, developed for **Real-time Electron Spectroscopy (REES)** <sup>1-8</sup>, named ApREES; a play on words for the Welsh word "*ap*" meaning "*son of*".

A dedicated variable temperature hyperspectral imager, HeLIOS (**Hyperspectral Luminescence Imaging for Optical Spectroscopy**), has been developed to extend the application of PL from single point spectroscopy to spatially resolved for the study of complex wide band gap materials. HeLIOS acquires images of samples to allow spatial and spectral investigations for non-destructive material characterisation. The instrument has been subject to a calibration protocol to enable accurate representative data in absolute units of irradiance, rather than the conventional digital counts or relative values. This enables direct comparison and use in the calibration of other systems in the future; such as the proposed

Mars exploration instrument HyperCLUPI <sup>9</sup> and other space hardware currently under development <sup>10–12</sup>.

Photoluminescence imaging allows quantification of spatial variations from mm to  $\mu\text{m}$ . The unique feature of sample mounting directly on a cryostat allows samples to be imaged at a wide range of temperatures, exploiting the enhanced luminescence emission seen at low temperatures. The cryostat is mounted in such a way to provide three axis directional movement to allow sample manipulation.

There is a continued drive to develop these instruments further, incorporating the imaging and in-situ processing instrumentation together.

## **1.2 Layout of thesis and contributions**

All figures, tables, diagrams, images and data are the work of the author unless stated.

### **1.2.1 Chapter 2**

Chapter 2 introduced the theory of the interaction of radiation with matter, providing an introduction to luminescence and Raman scattering. The commissioning of the ApREES system is reviewed, with motivation behind its design and development. In this chapter key equipment used throughout this thesis are presented and discussed.

The novel contributions to this chapter are the design and assembly of the ApREES instrument. The sample stage and heater are the author's design, and were fabricated by the Aberystwyth Mechanical Workshop to the author's specifications.

### 1.2.2 Chapter 3

Chapter 3 provides a literature review of spectroscopy instrumentation and introduces the concept of hyperspectral imaging. A component level discussion of HeLIOS is discussed in the context of hyperspectral imaging and instrumentation. Here the technology of the detector, filters, and excitation sources is discussed.

### 1.2.3 Chapter 4

Chapter 4 contains the construction and calibration of HeLIOS. In this chapter the development of HeLIOS, from the components discussed in Chapter 3, is discussed and the configurations utilised in this work. The characterisation and calibration of HeLIOS is then discussed, introducing the relevant terminology and theory for noise calculations, photon transfer methods, and radiometric calibration. Data processing protocols have been developed to collect calibration data and apply a radiometric calibration to experimental hyperspectral data.

This chapter describes the novel work in the assembly and calibration of HeLIOS. All measurements and analysis presented here were undertaken by the author. In this chapter a new radiometrically calibrated hyperspectral instrument is presented with calculations of the uncertainties in the measurement using covariance error analysis enabling spatially resolved data in absolute units of irradiance,  $\mu\text{Wcm}^{-2}\text{eV}^{-1}$ .

### 1.2.4 Chapter 5

Chapter 5 presents the data obtained using optical characterisation techniques arranged by sample, with a brief introduction to each, along with cross-polarisation images show birefringence. Diamond has been chosen as an interesting wide band-gap material for the

primary study. Here natural, synthetic single crystal carbon vapour deposition (CVD), and Polycrystalline CVD (PcCVD) samples are examined using high-resolution PL, spatially resolved PL, Raman spectroscopy, and cross-polarisation microscopy. In addition to the diamond samples, three alternative wide band gap materials have been studied using high-resolution and spatially resolved PL spectroscopy. These samples, (ZnO, CaCO<sub>3</sub>, and snail opercula), have been selected to relate to additional uses of HeLIOS for Earth Science and Mars exploration collaborations. They provide a uniform material (ZnO) and spatially interesting materials (CaCO<sub>3</sub> and opercula) for the first testing of HeLIOS.

The results of processing the acquired hyperspectral data using the developed radiometric protocol are present, providing for the first time, spatially resolved hyperspectral luminescence data in absolute units of irradiance.

Complimentary to the spatially resolved data, Raman spectroscopy mapping results are presented for the diamond samples along with analysis of the first order Raman line observed. An assessment of the inherent stress in the samples, through relation with the first order peak position, is also given.

### **1.2.5 Chapter 6**

Chapter 6 provides a review of the data acquired and processed in Chapter 5. A discussion of the instrument development and characterisation is also given. In this chapter the spectral information obtained of the diamond samples are compared and evidence pointing to the correlation between key spectral features, stress and the brown colouration in diamonds is presented.

The use of the ApREES system for in-situ temperature measurements of diamond using Raman spectroscopy is presented.

### **1.2.6 Chapter 7**

A concluding discussion is provided in Chapter 7 along with planned further work and developments. Future instrumentation directions and applications, including those projects the author is currently funded on and those that have been submitted for funding, are briefly discussed.

## **Chapter 2     Techniques**

### **2.1    Introduction**

The work presented in this thesis primarily focuses on optical techniques; Raman, photoluminescence and cross-polarisation microscopy. This chapter serves as an introduction to the theory behind the techniques used in this work and a review of the complimentary work done in parallel to the development of the imaging luminescence instrument HeLIOS (Hyperspectral Luminescence Imaging for Optical Spectroscopy) presented in Chapter 4.

Throughout the course of this work additional instrumentation was developed in parallel for materials characterisation and fed into the development of HeLIOS. The UHV (Ultra High vacuum) and HV (High Vacuum) environments and the challenges they pose are discussed, leading to the development and build of the ApREES instrument. In this chapter key equipment used throughout the work conducted during this thesis are presented and discussed. These include the Raman spectrometer system, complete with Super-Head optics, cross-polarising microscope, methods of sample processing and characterisation.

### **2.2    Interaction of radiation with matter**

The core of this work concerns the interaction of radiation with a sample of interest and the design of instrumentation for its detection. When electromagnetic radiation, for example light, impinges on a material it can propagate in a number of ways: reflection, scattering and absorption. The following sections introduce the theory and techniques used to measure materials through their interaction with light.

## 2.2 Interaction of radiation with matter

---

The optical properties of a material determine how it interacts with the incident light; by studying these interactions much can be learned about the material. When this incident energy is absorbed this can lead to luminescence; which is the primary characterisation technique used in this work. The scattered light can provide information on the size of particles and the refractive index of the material. Most of the incident light is elastically scattered; i.e. the photon energy is conserved. A small fraction is inelastically scattered causing a wavelength shift; this is Raman scattering and will be discussed later in this chapter as an important complementary technique used in this thesis. Light that is absorbed in the visible range corresponds to the electronic states of the absorbing molecule, whereas absorption in the near infrared (NIR) and infrared (IR) corresponds to vibrational modes. After absorption, in order to conserve energy, the excited material returns to its ground state, releasing energy in the form of radiation. This can be achieved in a number of ways including thermal, luminescence or through energy transfer to another molecule.

Figure 2-1 shows the possible methods of interaction of light with a material. The work presented in this thesis is concerned only with that light which is Raman shifted and that which results in luminescence. Reflectance measurements are possible using the developed instrumentation, but are not presented as part of this thesis.

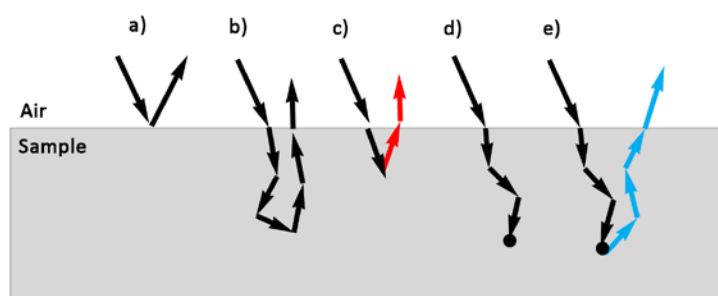




Figure 2-1 Methods of the interaction of light with a material; a) specular reflection, b) elastic scattering followed by diffuse reflection, c) inelastic scattering followed by emission of Raman shifted light (red lines), d) absorption, and e) absorption followed by photoluminescence emission (blue lines). Reproduced from Edelman *et al* <sup>13</sup>.

## 2.2.1 Luminescence

### 2.2.1.1 Introduction

The term luminescence is derived from the Latin root of *lumen*, which means light. A thorough historical review by Valeur <sup>14</sup> examines the history of luminescence through key observations and discoveries. These began as early as 1845 with Sir John Frederick William Herschel's observation and documentation of a blue glow from quinine under illumination. George Gabriel Stokes introduced the term *fluorescence* in 1852 <sup>15</sup>, deriving the term from the mineral fluorspar. Stokes took Herschel's observations further by using filters to select UV light to excite a quinine solution. The German physicist, Eilhard Wiedemann first reported the term 'luminescence' in 1888 as *luminescenz*, using it to describe "*all those phenomena of light which are not solely conditioned by the rise in temperature*". In 1953 Alexander Jablonski used an energy level diagram to describe the process of fluorescence, the diagram is still in use today (Figure 2-2).

The Jablonski diagram, Figure 2-2, illustrates the possible processes that can take place on absorption of a photon. A photon can be absorbed and undergo internal conversion, leading to fluorescence, or undergo intersystem crossing leading to phosphorescence or delayed fluorescence via triplet-to-triplet transitions. As the absorption is very fast, compared to the other processes, the Franck-Condon principle is valid.

## 2.2 Interaction of radiation with matter

---

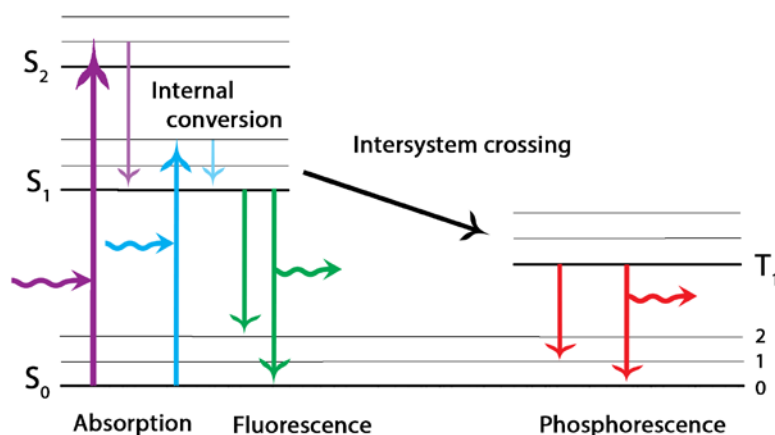


Figure 2-2 Simplified Jablonski energy diagram. Each of the columns represents a specific spin multiplicity.

Bold horizontal lines represent the limits of electronic states, with a portion of the possible vibronic eigenstates represented by the narrower horizontals. Pictured are the processes of absorption, relaxation by internal conversion, followed by emission by fluorescence or alternatively intersystem crossing leading to delayed emission (phosphorescence).

Early research confused the concepts of thermal and non-thermal radiators. A thermal radiator emits a radiation spectrum that equals black body radiation at a corresponding temperature (Planck radiation), examples of which are cosmic background radiation, and household halogen and incandescent lamps. In contrast to this luminescence is a non-thermal radiator, a method that emits a radiation spectrum originating from electronic transitions between discrete electronic energy levels. LEDs and lasers are examples of non-thermal radiators. The process of absorption and emission can be visualised using the Jablonski diagram (Figure 2-2) and the Franck-Condon diagram (Figure 2-3).

The Franck-Condon principle shows that the electronic excitation will be vertical in his diagram as the nuclei respond to the change of electronic structure on a much longer

timescale than the electronic transition itself. These electronic transitions are very much faster compared with the nuclear motions. When applied to luminescence, the vertical upwards arrows represent absorption and the downward arrows represent emission. Due to this fluorescence emission is always red shifted relative to absorption.

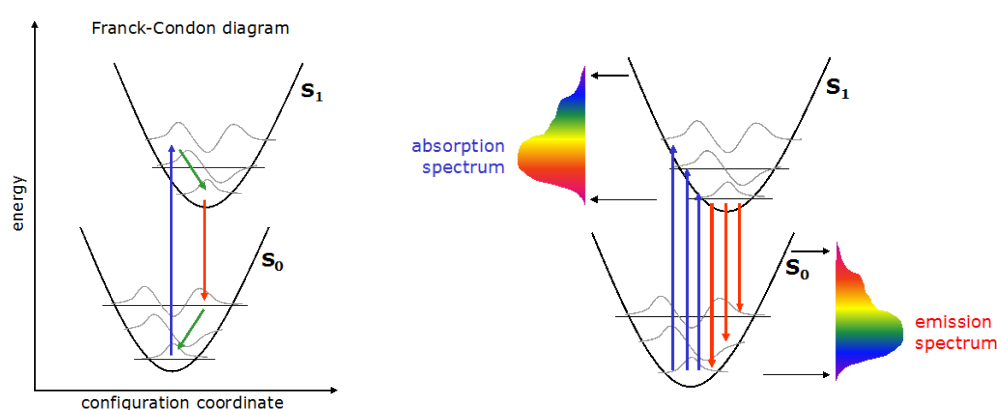


Figure 2-3 Configurational coordinate diagrams offer a complementary depiction the origins of absorption and emission spectra. The two parabolas represent the potential energy of the initial and final electronic states involved in the transaction. A path from minimum to minimum of the parabolas represents the zero-phonon line of an optical transition, however a vertical transition (as shown) are more likely.

The configurational coordinate diagram can be used to explain the optical properties of a material's luminescent centres including the effects related to lattice vibrations. The model uses a number of potential curves to represent the total energy of a molecule in its ground and excited state. This model is useful to illustrate principles such as Stokes' Law as the energy of absorption is higher than that of emission, with the Stokes' shift represented by the difference between the two levels. The diagram can also illustrate the widths of absorption or emission bands and their temperature dependence and a qualitative representation of the

## 2.2 Interaction of radiation with matter

---

effects of thermal quenching. The total energy is represented by the curve centred on its equilibrium configuration. Ground and excited states have different equilibrium configurations giving two different total energy curves with different minima. The higher curve is the excited state.

The light emission, luminescence, can be subdivided into three main categories: fast fluorescence, slow phosphorescence and afterglow.

Fast fluorescence is defined as spin allowed transitions. Fluorescence is a photoluminescent emission arising from the singlet electronic state. The human eye can only observe fluorescence when the excitation is incident on the radiating material. Fluorescence occurs when radiation is emitted from the first singlet state,  $S_1$ .

Slow phosphorescence comprises of spin forbidden transitions. Phosphorescence occurs when radiation is emitted from the triplet state,  $T_1$ , following intersystem crossing from the singlet state. These emissions last far longer than fluorescence and the excited material can be seen to emit after the source of excitation has been removed.

Afterglow is an additional subset of luminescence due to emission following the trapping of an electron elsewhere, it is also referred to as delayed fluorescence in literature. Compared to fluorescence and phosphorescence, afterglow is a rare phenomenon that occurs when the emission crosses over from the singlet to the triplet state, but returns to the singlet state prior to leaving the material. Afterglow is caused by the storage of electrons/holes in vacancies and impurities in the host lattice. These can cause deep traps, which can only be emptied by activation with a higher intensity and corresponding excitation such as a laser. Shallow traps, causing afterglow, can be emptied at room temperature. Red or infrared can be used as a trigger for the release of previously stored energy.

The term luminescence covers many different forms of light emission due to a stimulus. Different forms of luminescence are listed in the table below along with examples.

| Name                       | Method  | Example                       |
|----------------------------|---|-------------------------------|
| <b>Electroluminescence</b> | Electric field - Passage of an electric current through an ionized gas  | A gas discharge lamp          |
| <b>Radioluminescence</b>   | Charged particles - Radioactive decay, ionizing radiation   | XEOL, used for dosimetry      |
| <b>Triboluminescence</b>   | Friction or pressure – due to the effect of stressed, crushed or broken crystals                                  |                               |
| <b>Sonoluminescence</b>    | Acoustic energy – due to liquids exposed to intense sound waves.  |                               |
| <b>Chemiluminescence</b>   | Inorganic chemical reactions – energy derived from the breaking of chemical bonds                                 |                               |
| <b>Bioluminescence</b>     | Organic chemical reactions – a subdivision of chemiluminescence where the reaction takes place in a living system | Glow worms, fireflies         |
| <b>Cathodoluminescence</b> | Electron beam -   |                               |
| <b>Thermoluminescence</b>  | Heating (below the point of incandescence) – re-emission of absorbed light when heated                            | Used for dating and dosimetry |
| <b>Photoluminescence</b>   | Light – due to the absorption of light energy.  |                               |

Table 2-1 Examples of different forms of luminescence

## 2.2 Interaction of radiation with matter

---

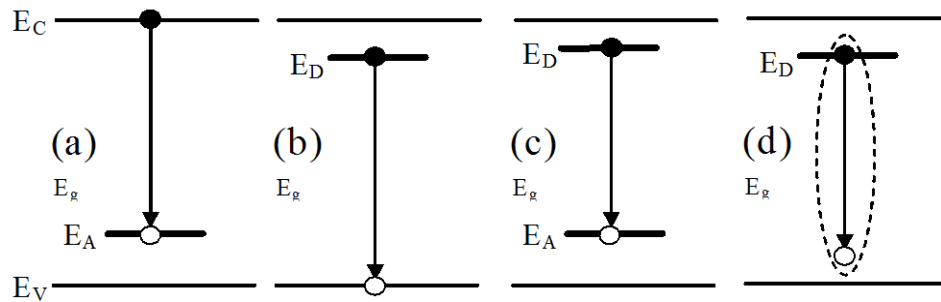


Figure 2-4 Illustration of radiative recombination involving impurity levels in an inorganic material; a) conduction-band-acceptor-state transitions, b) donor-state-valence-band transitions, donor-acceptor recombination, and d) bound-exciton recombination. Reproduced from <sup>16</sup>.

The process of luminescence is of importance to many fields including; physics, chemistry, biology, materials science, earth science and medicine. It is in use every day all around us in the form of fluorescent tubes, phosphorescent paints and labels, safety signs and counterfeit detection.

Luminescence as a broader definition can be thought of as the spontaneous emission of light by excited atoms in a solid-state material. But why use luminescence to study wide band gap materials? Luminescence spectroscopy techniques have been in use for many years to assess the quality of wide band gap materials as the emissions can provide information revealing the presence of defects and intrinsic emission process such as the decay of excitons <sup>17</sup>.

There are many advantages in using luminescence spectroscopy compared to other characterisation techniques. Luminescence has a high sensitivity and where materials are naturally, or engineered to be, highly luminescent at very low concentrations (parts per billion) <sup>18</sup>. Luminescence can have a substantially greater sensitivity compared to absorption spectroscopy, as absorption spectroscopy fundamentally involves an indirect measurement, measuring a comparison of the incident and transmitted light, whereas luminescence is

direct. As luminescence directly measures the emitted light, this signal can be amplified, for example using an electron multiplying CCD, as HeLIOS does, greatly increasing the sensitivity of a detection system down to single photon detection. Photon counting is not a trivial activity, the challenges of true photon counting instrumentation are well documented in literature <sup>19</sup>. A great deal of selectivity is possible with luminescence; a particular feature, such as a defect can be monitored via its luminescent response to changing stimuli. Perhaps most importantly for its use in high throughput operations, the sample preparation required is minimal. When compared to other optical techniques, such as optical absorption and reflection, luminescence spectroscopy has far less stringent requirements on sample size, shape and geometry. Extending that comparison to electron based techniques such as XPS (x-ray photoelectron spectroscopy), where sample cleanliness and a UHV environment is essential, luminescence can offer a fast and flexible method of material characterisation.

A luminescent material is one that can convert incident energy into visible electromagnetic radiation in excess of thermal radiation, it requires localisation of absorbed energy by discrete states. These materials consist of a host lattice and a luminescent centre, referred to as an activator in some literature. Luminescence spectroscopy measures the energy levels of these luminescence centres. The HeLIOS instrument, presented in Chapter 4, has been used to investigate a number of wide band gap materials including diamonds, ZnO, and CaCO<sub>3</sub> via their luminescence, presented in Chapter 5.

### **2.2.1.2 Photoluminescence**

When a material is excited optically and creates electron-hole pairs they can recombine in two ways: non-radiatively, generating photons and heat; or radiatively, emitting light as photoluminescence. Photoluminescence, a subset of luminescence, is the spontaneous

emission of light from a material under optical excitation. By choosing carefully the excitation energy and intensity different properties and constituents can be investigated. Photoluminescence is non-destructive, with little sample preparation and sample environment control. This makes it very attractive for device characterisation compared to electron-based techniques, which require high levels of vacuum and careful sample preparation for cleanliness. Photoluminescence can provide electronic characterisation, and the emission spectrum can identify surface, interface, and impurity levels. The intensity of the signal provides information on the quality of a surface or interface. Optical transitions provide direct access to the energy level structure of a system<sup>20</sup>. Examining the energy of the photons that are absorbed or emitted by a material gives information on its electronic states. Photoluminescence is useful in identifying low-lying states, as photoexcited carriers quickly thermalize through bands and closely spaced states to within  $kT$  of the lowest available levels. This is particularly useful for interfaces, where defect and impurity states are most abundant. These attributes make it an attractive technique for the study of wide band gap materials.

In this work photoluminescence emission spectroscopy has been used as the primary tool to design the instrumentation around for the investigation of wide-band gap materials, as demonstrated it is a powerful characterisation technique for the study of surfaces and interfaces. The resultant luminescence intensity has been measured over the UV-NIR emission wavelengths under a fixed excitation wavelength. This should not be confused with luminescence excitation spectroscopy where a particular feature of interest is monitored whilst changing the excitation wavelength. Excitation spectroscopy is a technique currently being explored with HeLIOS using the Aberystwyth Tuneable Light Source (ATLS) (Chapter 7). Here steady-state continuous wave luminescence spectroscopy has been employed where an excitation source illuminates the sample at a constant intensity over the time the measurements are performed. The emission spectrum is represented as a distribution of photons as a function of energy. Due to the timescale of the fluorescence, once exposed to



the incident light the steady state is achieved almost instantly. A steady state observation can be thought of as an average of the time resolved information over the intensity of decay of the sample. This work has looked at intrinsic samples; i.e. the fluorescence occurs naturally and is not due to an introduced component. Time resolved work was not undertaken in the course of developing the instrumentation, however the expansion to time resolved studies is possible due to the selection of components and is planned for future work (Chapter 7).

#### **2.2.1.2.1 Features of photoluminescence spectra**

PL spectra can comprise of sharp features and broad bands, both of which are temperature dependant. PL features are commonly also found in other optical techniques such as Raman spectroscopy, where a material may have an inherently strong PL background on which the Raman spectra sits.

With reference to the configuration coordinate Franck-Condon diagram, Figure 2-3, it can be seen that vertical arrows represent optical transitions. The absorption transition starts in the lowest vibrational level of the ground state, whereas emission starts at the lowest vibrational level of the excited state following non-radiative relaxation. These processes give rise to vibronic bands, visually recorded as spectra. Transitions from the lowest vibrational ground state to the lowest level of the excited state are referred to as zero-phonon lines (ZPL). In absorption spectra the bands of vibronic transitions will be to higher energies than the ZPL, with the opposite true of emission.

#### **2.2.1.2.2 Temperature dependence of photoluminescence**

Photoluminescence exhibits strong temperature dependence, with spectral features tending to become sharper and more intense on cooling causing additional features to be resolved. This effect should not be confused with thermoluminescence – where heat is used to stimulate the light emission. The effects can be seen where samples are cooled, an example

## 2.2 Interaction of radiation with matter

---

of which is shown in Figure 2-5 where there is a clear difference between the data acquired at 144 K and that at 50 K.

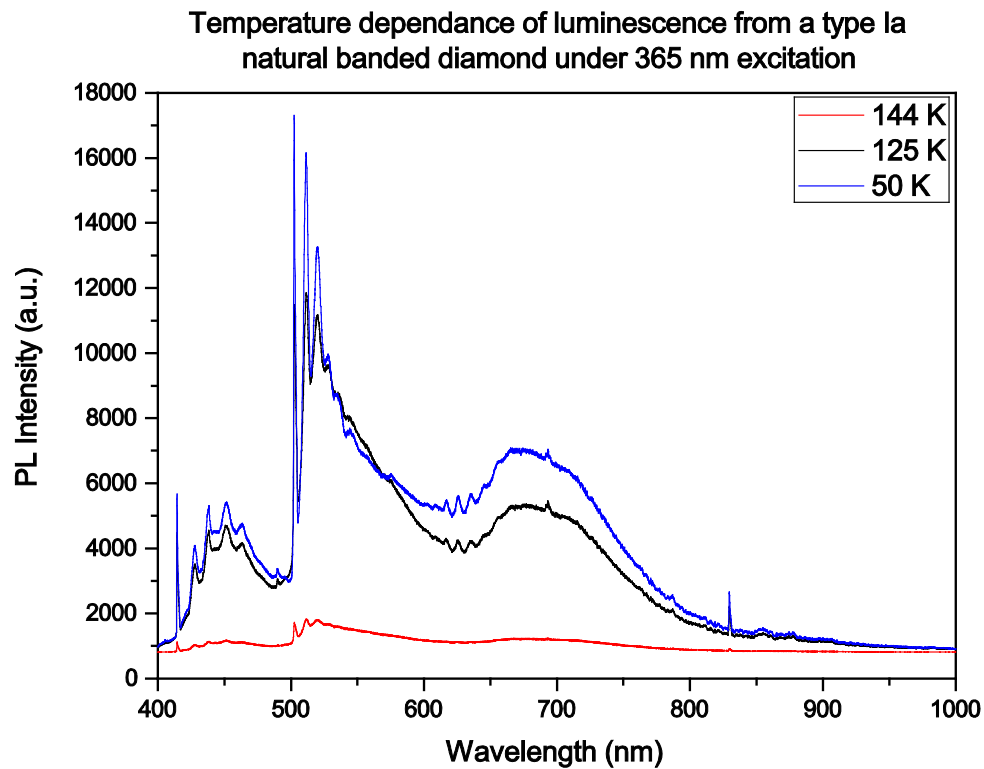


Figure 2-5 Photoluminescence emission of a natural diamond under 365 nm LED excitation displays a clear temperature dependence. With decreasing sample temperatures the PL emission increases and spectral features become more pronounced. For this reason PL measurements of diamonds are conducted at liquid nitrogen temperatures or lower.

This temperature dependence is due to the effect of non-radiative emissions. Luminescence becomes stronger and features become more pronounced as the sample temperature is reduced as the effects of quenching are reduced. This effect is due to the increased

probability of the decay/recombination of excited electrons being dominated by non-radiative processes. An increase in temperature generally results in a decrease in the fluorescence quantum yield and lifetime, as the non-radiative processes related to thermal agitation (collisions with solvent molecules, intra-molecular vibrations and rotations etc.) are more efficient at high temperatures. Luminescence quenching increases with increasing phonon frequencies, it is due to this that the majority of organic compounds only show luminescence at low temperatures.

There is an increase of the exciton-phonon interaction at room temperature, which leads to broadening of PL bands and the overlapping of bands that are close in energies. As observed in Figure 2-5, the fine spectral detail is washed out amongst the broad background when not sufficiently cooled; these data were acquired with identical parameters. Key features to ascribe to individual defects and impurities such as zero phonon lines (ZPL) of donor acceptor pairs (DAP) are visible more clearly at low temperatures. By performing measurements at low temperatures, bands become sharper and features are more distinguishable. At room temperature charge carriers have sufficient energy to move to non-radiative recombination centres, hence reducing the intensity of the PL emission. At low temperature these carriers are effectively 'frozen'. The higher the quantum yield, the easier to observe, and so measurements are often acquired under low temperature conditions where possible. For this reason cryostat stages were incorporated into the design of HeLIOS and ApREES.

The configurational coordinate diagram can again be used, illustrating the thermal dependence of photoluminescence transitions (Figure 2-6). At low temperature the ground state system is in its lowest vibrational energy mode, higher excited modes are separated by phonon energy,  $w$ . In this model the excited state of the defect can be thought to be intrinsic to either the defect itself or the conduction band. At elevated temperatures thermal quenching of the emitted luminescence occurs due to increased probability of non-radiative transitions from the excited state to the ground state at the point where the interaction of

## 2.2 Interaction of radiation with matter

---

these levels is greatest. On the opposite end, at very low temperatures, the emission spectrum from a direct gap semiconductor begins to depart from the form predicted by Boltzmann statistics <sup>21</sup>. This occurs even for very low carrier concentrations due to the formation of excitons and the potential for radiative recombination involving impurities.

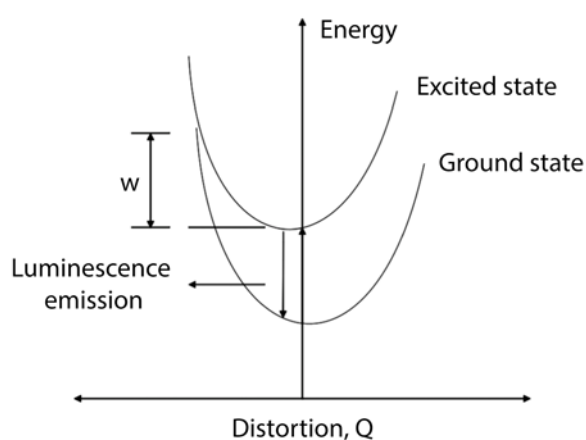


Figure 2-6 Configurational coordinate diagram for a simple two-level system. At high temperatures the Stokes shifted luminescence is quenched with an activation energy,  $W$ , due to the increased probability of non-radiative decay. Reproduced from Poolton *et al* <sup>22</sup>.

### 2.2.1.3 X-ray Excited Optically Detected Luminescence

The HeLIOS instrument has been designed with a view to integration to a synchrotron end station in the future, therefore provision for an X-ray source has been made extend the use from PL to XEOL (x-ray excited optical luminescence). XEOL is a material characterisation technique performed using laboratory soft X-rays, such as HeLIOS' Cu  $K_{\alpha}$  (8.04 eV), ApREES' Mg  $K_{\alpha}$  (1263.6 eV) and Al  $K_{\alpha}$  (1486.6 eV), and also soft X-ray synchrotron light. It involves the

absorption of the X-ray photon produced a large number of energetic electrons that in turn lead to the creation of excited electron-hole pairs in the conduction and valence bands of the solid. Such e-h pairs will rapidly recombine and may condense into excitons<sup>23</sup>. In either method of relaxation of the excited particle light is emitted as visible luminescence. There are many applications in literature to the use of XEOL<sup>23–35</sup>.

## **2.2.2 Raman Spectroscopy**

### **2.2.2.1 Introduction**

As discussed earlier, when monochromatic radiation is incident on a material the radiation, in this case light, can interact with the material in a number of forms. Raman spectroscopy makes use of one of the processes of light scattering. Developed in 1928 by Professor C. V. Raman, Raman spectroscopy is a light scattering technique exploiting the interaction of light with a material to produce scattered radiation that can then be measured and analysed, for which he received the Nobel Prize in 1930.

When an incident photon strikes a material and changes direction it can be said it has been radiatively scattered. Photons of the exciting radiation interact with the molecules of the sample being irradiated and the energies of the scattered photons are either increased or decreased relative to the exciting photons by quantised increments, which correspond to the energy differences in the vibrational and rotational energy levels of the molecules. There are a number of possible types of radiative scattering of which Raman scattering is one, others being Tyndall and Rayleigh. Rayleigh and Raman scattering occur when the particle dimensions are small compared to the incident radiation wavelength. The mechanism for Rayleigh and Raman are very similar, however where in Rayleigh scattering the frequency of

## 2.2 Interaction of radiation with matter

---

the scattered radiation is identical to incident radiation, in Raman scattering the scattered frequency is higher, or lower. The light is inelastically scattered. Inelastic scattering is affected by a number of excitations in a material, such as phonons, magnons or plasmons. It differs from another form of scattering, Brillouin, by the phonons involved. Raman scattering is concerned with the inelastic light scattering from optical phonons whereas Brillouin scattering is concerned with acoustic phonons. It is this shift in the wavelength of the inelastically scattered radiation, which provides the chemical and structural information of the sample under investigation.

The inelastic scattering from optical phonons can be subdivided into two types: Stokes and Anti-Stokes scattering. Stokes scattering corresponds to the emission of a phonon, Anti-Stokes scattering corresponds to the absorption of a phonon. In Stokes scattering the incident light is shifted down to a lower energy where in Anti-Stokes scattering it is shifted up to a higher energy, as illustrated in Figure 2-7.

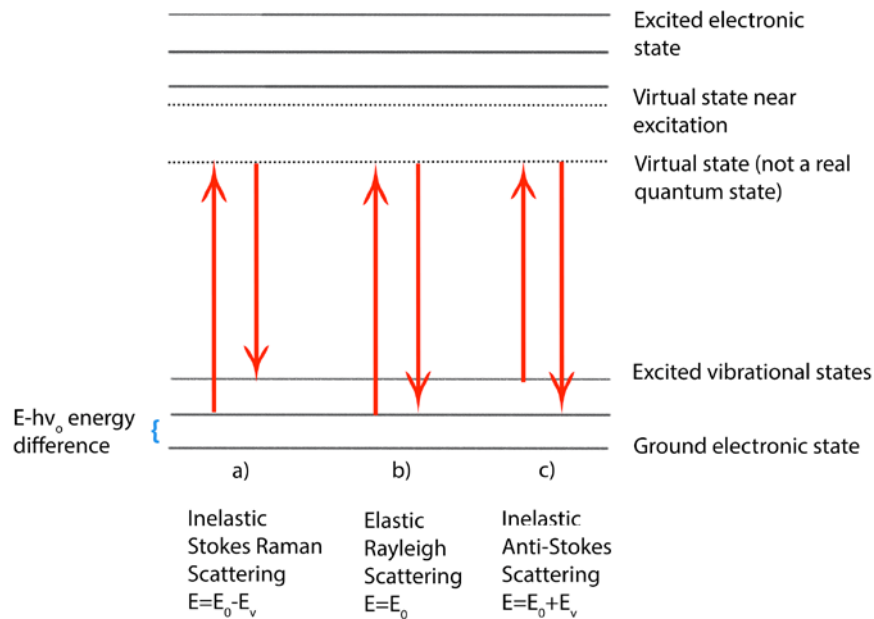


Figure 2-7 Simplified energy level diagram showing the states involved in light scattering.

In Raman spectroscopy the process of inelastic scattering of light is analysed, where energy is transferred between an incident photon of energy  $\hbar\omega_i$  and a sample of interest, resulting in a scattered photon of different energy  $\hbar\omega_s$ . The energy transferred in this action corresponds to the Eigen-energy  $\hbar\Omega_j$  of an excitation  $j$ . This is illustrated in Figure 2-8. The excitation  $j$  can be a number of types; phonon, polariton, plasmon, coupled plasmon-phonon mode or a single electron or hole excitation<sup>36</sup>. The Eigen-frequencies of these excitations can be found by inspecting the peak frequencies,  $\omega_s$ , of the scattered light. As the incident light is carefully controlled to a narrow bandwidth of known value through the use of lasers and filters the conservation of energy in the process can be expressed thus:

$$\hbar\omega_s = \hbar\omega_i \pm \hbar\Omega_s \quad \text{Equation 2-1}$$

## 2.2 Interaction of radiation with matter

---

The negative term represents the Stokes' scattering, where an excitation is generated (phonon emission) and the positive term represents the anti-Stokes' scattering process, implying the annihilation of an excitation (phonon absorption).

By considering Equation 2-1 in terms of quasi-momentum conservation law, the correlation between wavevectors can also be described:

$$\mathbf{k}_s = \mathbf{k}_i \pm \mathbf{q}_j \quad \text{Equation 2-2}$$

This relationship is useful when considering a thin film deposited on a substrate, a multilayer material, or a material grown in a layer-by-layer process as it can be expanded to include a material's interior wavevectors by considering the refractive index. Considering the Stokes' scattering typically of Raman spectroscopy;

$$\mathbf{q}_j = \frac{1}{c_0} (n(\omega_i)\omega_i + n(\omega_s)\omega_s) \quad \text{Equation 2-3}$$

Where  $c_0$  is the velocity of light in vacuum. From this a quasi-momentum transfer value is found, proportional to the incident laser frequency. By inspecting the  $q$  values it can be determined if the interaction is near the Brillouin zone. Small  $q$  values indicate scattering from phonons where the energy transfer  $\hbar\Omega_j$  is independent of  $\omega_i$ . Plasmon-LO-phonon interactions are characterised by a dependency and larger  $q$  values, these interactions can be investigated by changing the incident frequency.

When considering Raman spectra, a well-defined momentum in a sample of interest requires an ideal homogeneity of the lattice. In reality impurities and dislocations give rise to momentum non-conservation. This deviation from an ideal structure is shown in the spectral data as corresponding broadening of the observed spectral features. In disordered samples, such as amorphous materials, the Raman phonon spectra can be thought of as an



approximation of the density of the phonon states by averaging over the Brillouin zone. By this approximation the lineshape of Raman spectra can be used to characterise the disorder in a material.

Through careful selection of geometry of the sample and light collection, the orientation of a material can also be determined from the Raman scattering. Figure 2-8 depicts conventional Raman backscattering geometry. The main instrumentation includes a narrow wavelength excitation source, light collection optics, monochromator and detector. The inset shows an illustration of scattered light intensity vs frequency shift  $\Delta\omega$  corresponding to a Stokes process (energy loss) from the incident light  $\omega_i$  and scattered component  $\omega_s$  generating Eigen-frequencies of elementary excitations ( $j=1,2$ ).

Phonons with an even symmetry are Raman active, and those with odd symmetry are IR active as only those phonons of even symmetry lead to coupling of electronic states of equal symmetry, which allows coupling to the ground state. By observing if a sample is Raman or IR active, and in what geometry, information can be found on the orientation. In a, illustrated in Figure 2-8, at a (100) surface only LO (longitudinal optical) phonons are allowed. In (110) only TO (transverse optical) phonons are allowed and in (111) surfaces TO and LO phonons may be visible.

## 2.2 Interaction of radiation with matter

---

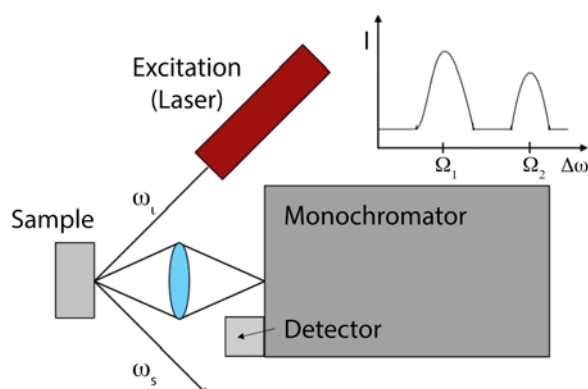


Figure 2-8 Raman backscattering experimental geometry. Reproduced from Bauer and Richter <sup>36</sup>.

Raman data is very information rich making the technique an important analytical and research tool. Applications are varied and wide ranging including; analysis of semiconducting layers, assessing the quality of CVD diamond films and bulk material, pharmaceuticals process monitoring <sup>37</sup>, assessing and monitoring the stress in materials, astrobiology, space applications (Raman spectroscopy is part of the Pasteur payload for ExoMars, <sup>38,39</sup>), mineral and gem identification <sup>40</sup>, biomedical <sup>41</sup>, archaeology and art conservation <sup>42</sup>. Raman spectroscopy has previously been used to study photochemical and photophysical properties of phthalocyanines <sup>43</sup>.

Raman spectroscopy requires specialised instrumentation to overcome the technique's difficulties. The Raman signal is relatively weak, Rayleigh scattering being typically four or five orders of magnitude greater than that emitted during Raman scattering <sup>44</sup>; hence an intense monochromatic light source is required with the advent of laser technology enabling Raman spectroscopy to flourish. Laser selection is important where samples display fluorescence, as this signal is far stronger and can swamp the weak Raman signal. Shorter wavelength excitations, such as blue and green lasers, may promote fluorescence in organic or biological samples however this can be overcome by switching to a longer wavelength into the red or

NIR. With this in mind a trade-off is needed between the fluorescence background and the integration time for measurements as the longer the wavelength the lower the scattering efficiency, leading to longer measurement times and the need for higher power lasers. Specialist notch filters with high rejection and optical blocking are required to prevent the stronger elastically scatter light swamping the Raman signal. Modern systems such as the instrument used in this work employ a monochromator and cooled CCD detector.

Raman is valuable as it provides readily distinguishable signatures for the different allotropes of carbon <sup>45</sup> and so has been chosen as a complimentary spectroscopic technique in this work. The technique has been used to characterise both natural and synthetic diamond samples (Chapter 5). Raman mapping can produce spatially resolved maps of the different forms of carbon within a sample. The strengths and weaknesses of Raman spectroscopy for the study of diamond are comprehensively discussed by Praver <sup>45</sup>. It is a popular tool for the study of diamond as it is non-destructive, requires minimal sample preparation, can be performed in-situ or at the laboratory bench via confocal microscopy allowing small samples to be examined. There is a large catalogue of data to compare with, one of the most comprehensive being that compiled by Zaitsev <sup>46</sup>.

In addition to micro-Raman studies, a method of acquiring in-situ Raman spectroscopy has been develop to study samples in an UHV environment utilising a Super-Head camera system and fibre coupling through a specially designed recessed window into the vacuum chamber and a custom lens assembly for maximum light collection. The Super-Head has been modified to include kinematic mounts to enable fast filter changeover to correspond to changes in the excitation being used. It is mounted onto standard Thorlabs dovetail optical rail for flexibility in mounting to a range of vacuum viewports. Figure 2-9 shows its arrangement on the bench top for collecting Raman and PL data using microscope objectives when coupled to a Horiba iHR320 spectrometer and when mounted onto the ApREES vacuum system for in situ Raman and PL studies.

## 2.2 Interaction of radiation with matter

---

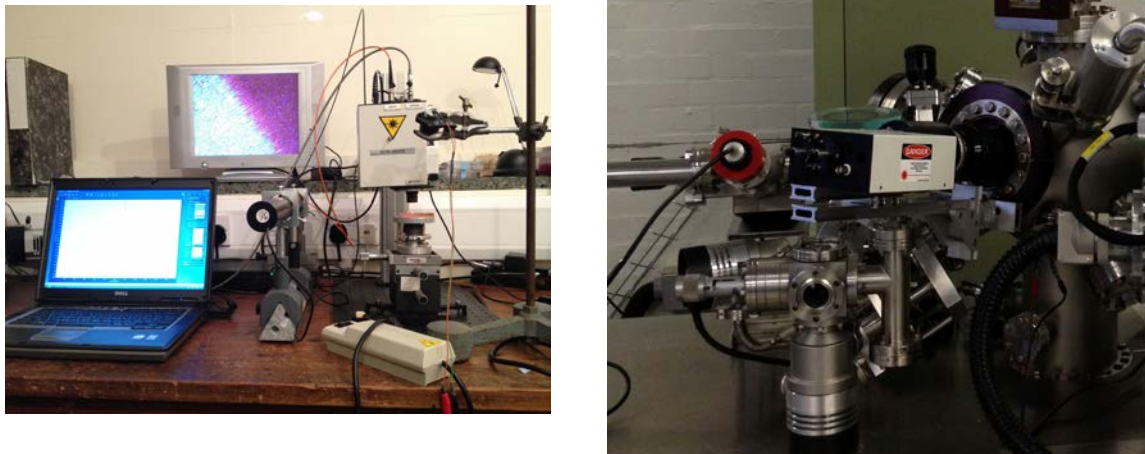


Figure 2-9 Applications of the Super-Head light collection accessory; (left) bench top micro-Raman, (right) in-situ Raman at the ApREES.

The Super-Head is used to acquire standoff Raman data in a number of environments. By coupling to a UHV system such as the ApREES, samples can be monitored by Raman spectroscopy during heating, cooling and other treatments, Figure 2-10 shows monitoring of the first order diamond Raman peak with temperature increasing. A discussion of the success of this method using the ApREES is presented in Chapter 6.

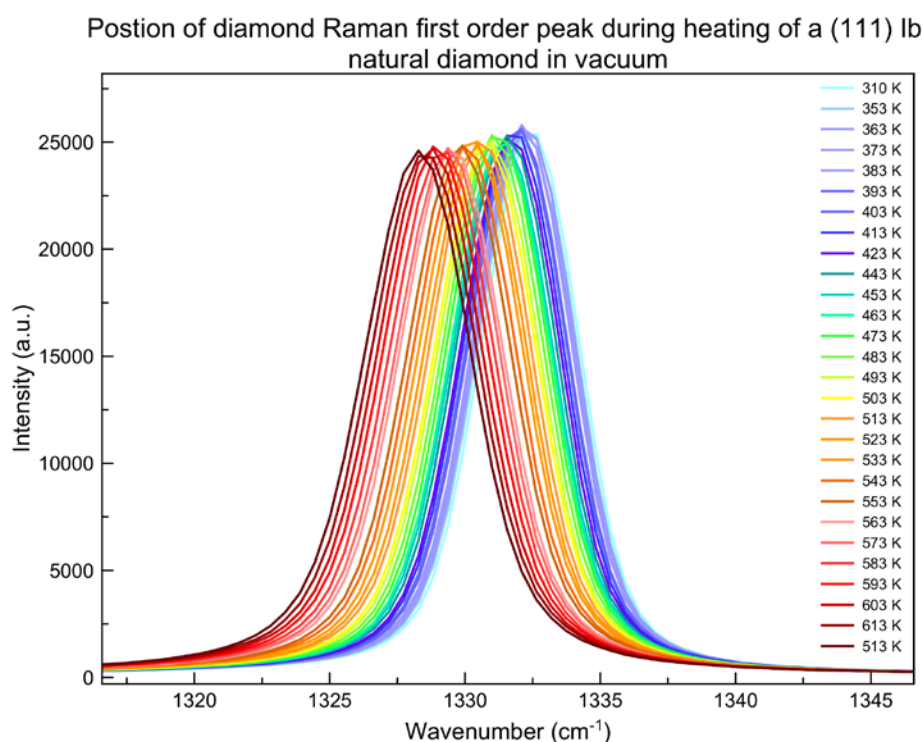


Figure 2-10 Monitoring of the first order Raman peak during the heating of a (111) type Ib natural diamond in the ApREES using the Super-Head for stand-off measurements. The peak can be observed to move to shorter wavenumbers with heating.

Raman spectroscopy can provide the user with a large amount of information in relatively short timescales with little material preparation and is primarily used for qualitative analysis. From a single spectrum it is possible to identify the material, molecular structure and phase from the position of the peaks. The intensity of the peaks provides information on the material's concentration and the width of the peak provides information on the crystallinity and phase. It is a widely used industrial and research analytical tool. Raman spectroscopy has become a very powerful tool to analyse carbon nanomaterial including nanodiamonds. It can provide information on structure, composition, homogeneity, bonding surfaces and surface

## 2.2 Interaction of radiation with matter

---

functionalities. A spectrum can be thought of as a fingerprint that can be associated to a particular material and its allotropes. As illustrated in Figure 2-12 it can also be used to monitor temperature and stress in materials.

The technique is attractive as it is non-destructive, requiring very little sample preparation and when combined with a confocal microscope and motorised sample stage can produce maps of micron sized areas. Impurities on the surface such as dust particles can cause the Raman spectra to contain Tyndall scattering caused by the interaction between photons and dust particles rather than atoms or molecules.

Raman can provide sufficient sensitivity to investigate and monitor monolayers of material whilst having the advantages of minimal sample preparation, non-contact and non-destructive. By selecting an appropriate power density of the laser (spot size and power) it is possible to examine delicate materials and those that are susceptible to heating. This fine-tuning is most important when Raman spectroscopy is being used to monitor strain or temperature of a material as to not affect the result.

### 2.2.2.1.1 Experimental details

Raman measurements in standard micro-spectroscopy and mapping configurations were performed using a Jobin Yvon Horiba LabRam HR Raman Spectrometer. Two lasers were available for sample excitation, depending on sample fluorescence observed, a Class 3B HeNe (632.8nm) and a Class 3B Argon-ion blue laser (488nm). Within the standard configuration there are several instrumental parameters that can be adjusted in addition to the excitation source. The laser power measured at the sample was less than 5  $\mu$ W, well below the threshold for local sample changes. The first order phonon of diamond, for example, is sensitive to temperature and can in fact be used as a temperature probe<sup>47,48</sup>. There is also literature citing the use of Raman spectroscopy as a temperature probe in life-sciences and materials

processing<sup>49–51</sup>. There is a choice of two gratings available for dispersion of the scattered light with different groove density, 1800 and 2400 mm<sup>-1</sup>. The work presented here was performed using the 1800 grating, as the 2400 gives greater resolution but at the cost of intensity requiring far longer acquisitions times inconvenient for in-situ measurements and mapping. The microscope stage can take a variety of objectives owing to its standard 20.32 mm diameter nosepiece mounting thread. Objective selection is an important consideration, not just for magnification of features, but to optimise the area to be sampled/excited and the collecting angle. Several microscope objectives are available for sample imaging and micro-Raman, the three used in this work are; MPlan 10x/0.25 NA, LMPlan 50x/0.5 NA and MPlan 100x/0.9 NA. The power of the excitation source can be controlled via neutral density filters, this is particularly important when dealing with delicate materials such as polymers which can easily be damaged by the intense laser light. The size of the spectrometer's slit and confocal hole can also be adjusted to set the spatial and spectral resolution of the instrument. The spectrometer is fitted with a computer controlled motorized x-y stage to allow precision spatial investigation of a sample and programmable mapping spectroscopy. The Raman data presented here were acquired at room temperature, as there is little gain in the sharpening of features at low temperatures, for example Grimsditch *et al*<sup>52</sup> showed a change in line width of 1.65 cm<sup>-1</sup> at 300K and 1.48 cm<sup>-1</sup> at 79K and at 15K. Raman mapping was performed by acquiring a spectrum at each sample point as defined in the control software, producing hyperspectral datasets consisting of many individual Raman spectra.

#### **2.2.2.1.2 Raman for strain measurements**

Lattice mismatch is known to cause biaxial stress<sup>36</sup> which can induce lattice deformation affecting the lattice dynamics, which in turn can then be analysed by evaluating the phonon frequencies in the Raman spectrum.

## 2.2 Interaction of radiation with matter

---

The relationship between the phonon frequencies and the strain tensor,  $\epsilon$ , is described quantitatively by the phonon deformation potential tensor. In cubic materials, such as diamond, this tensor has three independent non-vanishing components,  $p$ ,  $q$ , and  $r$ . These are not to be confused with the electronic deformation potentials.

Although strain determination by Raman is not as accurate as X-ray diffraction, however it does provide a lateral resolution in the micron range via techniques such as micro-Raman mapping. Raman also has the advantages of being non-destructive and can be performed on thin films.

### 2.2.3 Optical Microscopy

Polarised light microscopy allows a material's optically anisotropic characteristics to be investigated. Images are acquired by placing a polariser in the light path before the sample and an analyser (second polariser) in the optical path between the material and the eyepiece or camera mount. A birefringence pattern arises where contrast is generated from the interaction of plane-polarised light with the sample producing two individual wave components, each polarised in mutually perpendicular planes. Their velocities differ and vary with the propagation direction in the sample. Once the light has passed through the sample the light is now out of phase and recombines as constructive and destructive interference on passing through the analyser. The image contrast in a material can be adjusted by rotating the polariser, thus changing the direction of polarisation. The images where acquired at maximum extinction; i.e. the polariser and analyser are crossed at a  $90^\circ$  angle giving a dark background and maximum sample birefringence.

The intensities and patterns produced can also provide information on the cause of the colouration and strain. Birefringence is effectively the photo-elastic effect and is visualised



due to a change in the refractive index of the material caused by strain. Diamond for example is a cubic crystal and in principle should not exhibit birefringence due to its isotropic nature, however natural diamond usually exhibits a degree of birefringence due to inherent dislocations in the crystal lattice formed during its formation and migration to the surface.

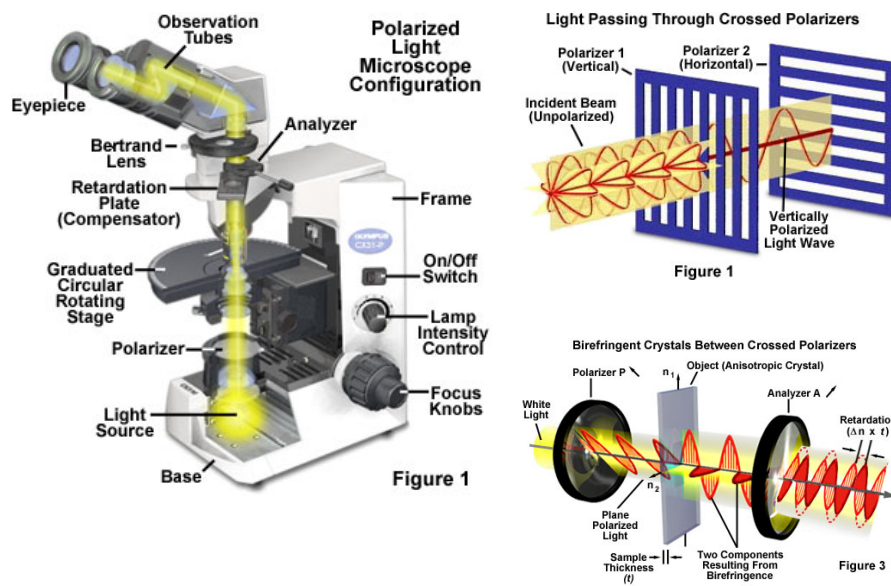


Figure 2-11 Example cross-polarising microscopy experimental set up representative of that used in this work, reproduced from Nikon.

Birefringence can be used to visualise and identify local strain fields in materials<sup>53</sup>. Where a dislocation or extended defect is present in a crystal, this causes a local strain field that can induce birefringence in the light passing between the crystal and cross-polarisers. Where a strain field is applied to a crystal there is a corresponding change in the refractive index due to a change in the dielectric constant. For these reasons birefringence is used as a test of crystal perfection.

## 2.3 Material preparation and characterisation

---

Optical microscopy has been used to examine birefringence in diamond samples using a Meiji MX9430 Polarising microscope with Triocular head, strain free 4X, 10X, and 40X objectives, 10X eyepieces, rotation stage with XY mechanical translation, transmitted and reflected Koehler 30 W illumination. A commercial digital SLR camera and photo eyepiece was used to acquire the images presented in this work.

Cross-polarised images are included in Chapter 5 as an introduction to the samples and the results for each specimen are present alongside the results of the other optical techniques applied. A discussion of the images is presented in Chapter 6.

## 2.3 Material preparation and characterisation

### 2.3.1 ApREES

The ApREES has been designed as a prototype to uniquely combine in-situ characterisation of materials during processing. This is achieved through the combination of X-ray electron and optical spectroscopies (PL, XEOL, CL, and Raman) in a controlled UHV (Ultra High Vacuum) environment. Through this combination, bulk and surface properties can be investigated.

The system consists of a Mu-metal analysis chamber and a fast load-lock entry chamber, isolated from each other by a hand operated UHV valve. The load-lock is pumped by a rotary backed turbo-molecular pump and held by an ion pump during sample transfer. A magnetic arm is used for sample transfer between the load lock and analysis chamber. The main analysis chamber is pumped initially by a rotary backed turbo pump, followed by an ion pump and titanium sublimation pump to achieve a base pressure of better than  $1 \times 10^{-9}$  mbar. The chamber is equipped with a twin anode x-ray gun and a number of metal and organic

semiconductor K-cells. Due to the close proximity of the deposition cells to each other a dual shutter has been designed and installed to prevent cross contamination during deposition. A mass spectrometer is located in the chamber to monitor for leaks and vacuum quality. An Ar<sup>+</sup> sputtering gun has been mounted for sample cleaning along with a single point gold probe for surface conductivity measurements. An electrospray deposition of thermally liable molecules from solution is performed in the fast entry load lock. This system is mountable on any CF70 flange. An electron gun is currently being commissioned to allow CL measurements. The chamber is equipped with a number of view ports for optical detection including a recessed window for in situ Raman, PL and XEOL studies using the Super-Head and a custom built lens assembly and UV UHV fibre to maximise light collection. A number of these components can be seen in Figure 2-13 and Figure 2-13.

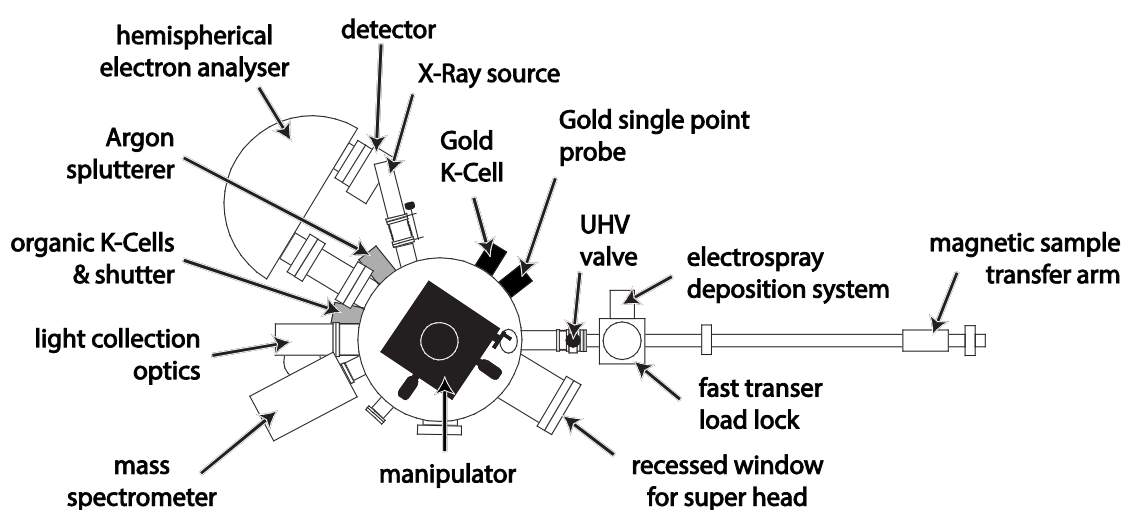


Figure 2-12 ApREES system diagram showing key components.

## 2.3 Material preparation and characterisation

---

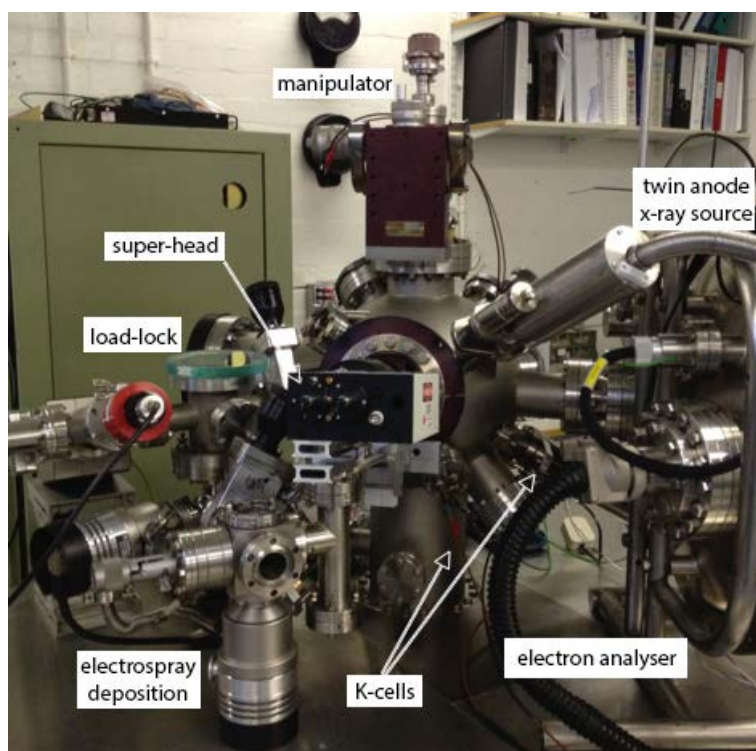


Figure 2-13 ApREES system showing Raman Super-Head mounted on dovetail rail for focusing. Also seen is the hemispherical analyser (not covered in this work), twin x-ray source, manipulator, fast throughput load lock, deposition cells and electrospray deposition system (not covered in this work).

UHV is very important for surface sensitive characterisation and its achievement is not trivial. Pumping stages of roughing, turbo, ion and TSP (titanium sublimation pump) are required. The system must be leak free, checked by probing for He applied around potential leak sites (such as ports and electrical feeds) using a mass spectrometer mounted in the chamber. This process would take a considerable amount of time to achieve UHV due to absorbed substances outgassing over time from the chamber's internal surfaces. This is expedited to reasonable times by a procedure called baking where the entire system is heated to approximately 120°C to drive off absorbed materials which have low vapour pressures at

these temperatures. These contaminants are then pumped away via the various stages of pumping to reduce the base pressure of the system.

UHV is needed for processes involving the detection or emission of electron. In the case of the ApREES, this is needed when operating with a hemispherical electron analyser in XPS mode or when the electron gun is in use during CL spectroscopy in this system. The twin anode X-ray source requires a vacuum better than  $10^{-7}$  mbar for operation to protect the filament from oxidation. When investigating surfaces looking at surfaces the UHV setting provides a clean environment to work in.

### **2.3.1.1 Manipulator and Sample Stage**

The sample stage is mounted on a customised UHV manipulator, providing electrical feedthroughs for sample heating, drain current, sample biasing and thermocouple connection.

#### **2.3.1.1.1 Heating**

Heating is used to clean substrate materials and to conduct temperature dependent experiments. A new type of heating stage has been designed around a small tungsten filament element that is capable of reaching over 800 °C. The ApREES sample heater was designed by the author and fabricated by the Mechanical Workshop as part of this research.

The heater had to accommodate existing sample holders from the REES system for flexible use, the materials used needed to be low outgassing, temperature resistant and fit on the end of the manipulator comfortably. A design was produced which satisfied these elements, shown in Figure 2-14 and Figure 2-15. A stainless block was machined to form a recess to mount a small commercial off the shelf filament bulb with the glass removed to expose the filament (50W 12V halogen bulb, Osram). A tantalum heat shield was constructed around the

## 2.3 Material preparation and characterisation

---

filament with the glass body of the bulb providing an electrical break. A molybdenum reflector was added behind the filament, Mo was chosen instead of Ta as from experience Ta dulls with heating, reducing the effectiveness as a back reflector over time whereas Mo does not. This design is far more economical than commercial heaters and during the course of this research has only required one replacement bulb showing its robust qualities.

Provisions have been made for thermocouple connection. One UHV feedthrough is permanently used as a thermocouple connected directly to the sample receiver near the heater. The other thermocouple connection provides a second temperature measurement and can also be used to measure drain current as a method of X-ray alignment. An electrical feed through supplies current to the filament. By having heating and cooling on the same sample mount the temperature range is between 77 K (theoretically) and 1100 K (measured) giving a wide range to work with. On the rear of the sample stage heater two quartz crystals are mounted to provide deposition rate calibration and monitoring.

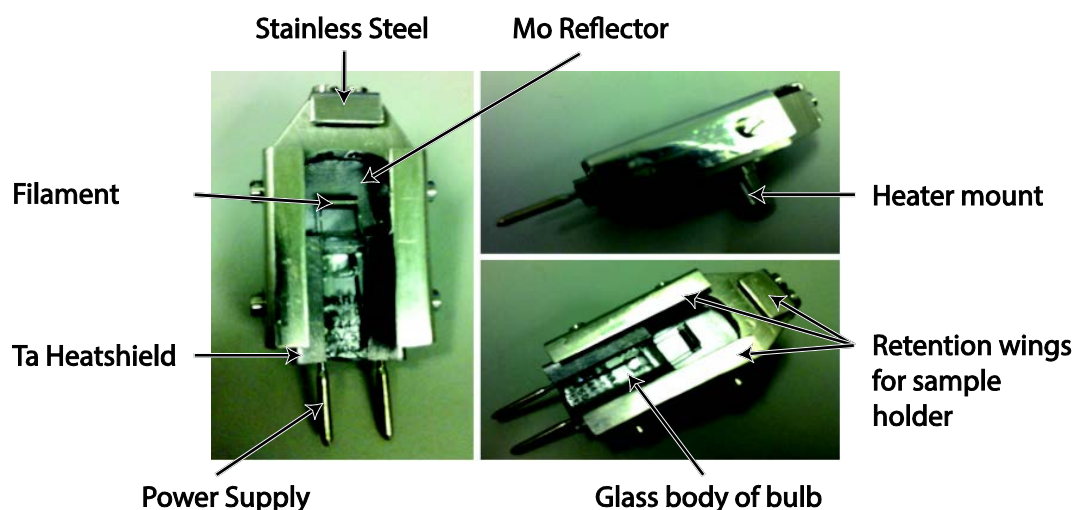


Figure 2-14 ApREES sample heater.

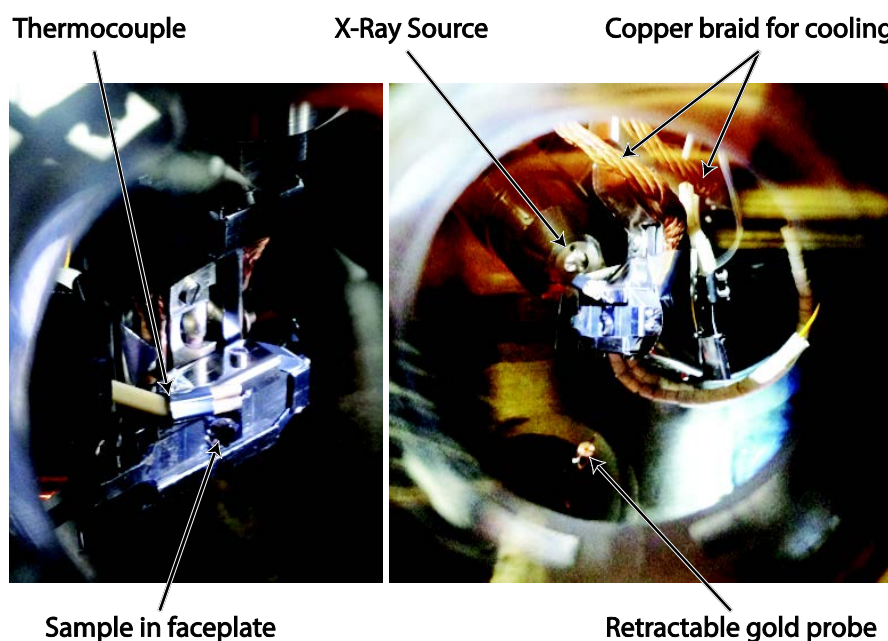


Figure 2-15 ApREES interior showing sample stage.

#### 2.3.1.1.2 Cooling

Sample cooling is provided by an open flow liquid nitrogen cryostat. The thermal losses from the cryostat through the copper braid to the sample mount, and the volume of liquid nitrogen ( $\text{LN}_2$ ) available for cooling, limits the lower bound of sample temperature achievable. Tests showed two litres of  $\text{LN}_2$  would result in a temperature of 190 K. To reach lower temperatures additional  $\text{LN}_2$  flow is required, however the infrastructure to store this on site was not available to the author at the time these tests were conducted therefore subsequent low temperature measurements were conducted using HeLIOS.

### 2.3.2 Deposition Techniques

The system was constructed to provide an environment for material characterisation of as loaded and processed surfaces. Sample heating and cooling have been previously discussed, here the deposition techniques incorporated into the system are presented and discussed.

#### 2.3.2.1 Knudsen Cell

Knudsen cells, or K-cells, are a method of UHV deposition. These are used to deposit pure, multi-layered structures. Used to evaporate a wide range of materials including metals and stable organic molecules. The ApREES is equipped with gold, iron and a copper phthalocyanine K-cells. The orientations of the cells have been chosen to allow deposition and characterisation at the same time. A shutter has been fabricated to prevent cross deposition of sources near each other. The technique provides a reliable means of film growth. For operation the material to be deposited is inserted into a small ceramic crucible surrounded by a Ta filament heater. On application of a current to the filament the sample is evaporated into a beam directly onto the substrate. By controlling the applied current to the heater the deposition rate can be accurately controlled and calibrated by means of a quartz crystal microbalance.

### 2.3.3 Excitation sources

#### 2.3.3.1 X-Ray Radiation

X-ray radiation can be used to excite a sample for measurement by a number of techniques including XPS and XEOL used here. The addition of a hemispherical electron analyser to the system will combine these two powerful techniques, more discussion on this can be found in Chapter 7. The X-rays are produced by thermionic electrons from a hot tungsten filament



being accelerated by high voltage onto the water-cooled anode. The ApREES X-ray source is a twin Magnesium and Aluminium anode with characteristic  $K\alpha_{1-2}$  X-ray emission at 1253.6 eV and 1486.6 eV respectively. The source is operated at a bias of 14.5 kV and a user selected flux (0 to 20mA) to determine the power.

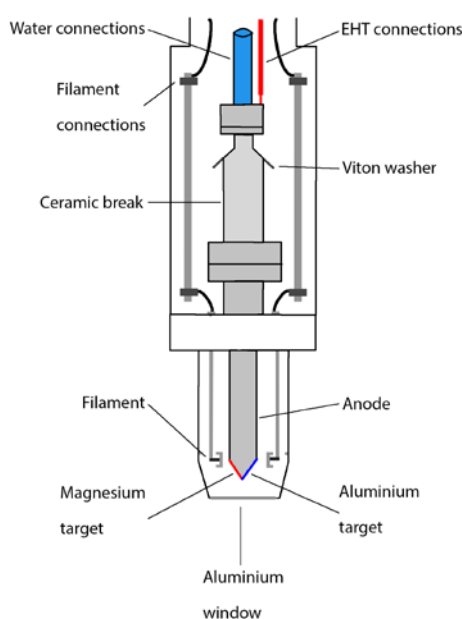


Figure 2-16 ApREES twin anode X-Ray source.

For the future XEOL work in HeLIOS a hard X-ray source has been adapted for use. The source is an Oxford Instruments 2kW Phillips PW2273/20 X-ray tube with a Cu target. This source produces bremsstrahlung radiation (limited to 30keV) and Cu  $K\alpha$  radiation at 8keV. The manufacturer estimates the total X-ray power at the sample to be  $70\mu\text{Wcm}^{-2}$ .

The source installation comprises of a number of safety interlock features: chamber pressure, X-ray housing temperature, and source alignment. These function to keep the user safe during

## 2.3 Material preparation and characterisation

---

operation and to satisfy the necessary requirements of the Ionising Radiation Regulations 1999 (Amended). The pressure interlock is linked to the cold-cathode gauge on the sample chamber; this prevents X-ray source operation if the chamber is at ambient pressure. This ensures the X-ray source cannot be operated during sample change over where the user may encounter stray X-ray radiation when opening the chamber.

The X-ray housing has been custom made by the Aberystwyth Mechanical Workshop to the authors requirements in order to improve the radiation shielding, it also incorporates a temperature sensor, which disables the source should the temperature exceed 55°C. The housing is lead lined throughout the length and additional lead shielding is located at the top where the electrical connectors emerge. This additional shield and the rotation of the source to a position where the connectors exited being pointed upwards, away from users, was required as it was found there was a strong  $\beta$  signal being emitted during use. The final, and most important interlock is that which prevents the source becoming detached from the chamber during operation. As the source operates in air, through an aluminized 100 $\mu$ m thick Mylar window into the sample vacuum chamber, additional precautions must be taken to ensure it can only operate when locked into place. A stainless steel collar with a micro-switch ensures that should the source come away from the chamber during operation it will be disabled immediately. During operation the X-ray shutter (Uniblitz XRS25) can be computer controlled or operated manually from the instrumentation rack. Steel apertures can also be inserted into the beam path to collimate and control the spot size. The X-Ray housing is illustrated in the diagram shown in Figure 2-17.

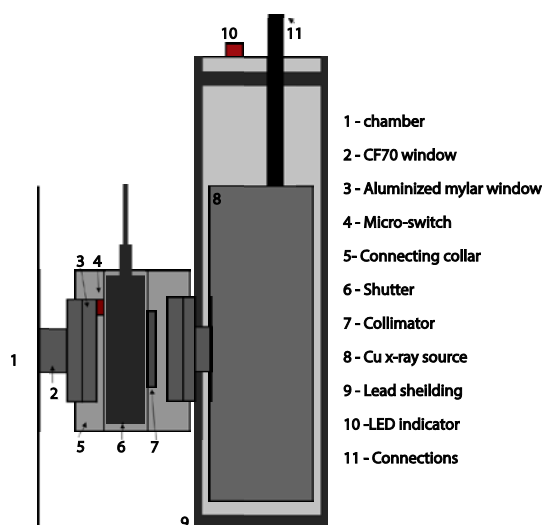


Figure 2-17 HeLIOS X-Ray source interlocked mount. Interlocks have been put into place to prevent operation of the source when not connected to the closed sample chamber.

### 2.3.3.2 Lasers and LEDs

A number of lasers have been employed in this work for photoluminescence and Raman spectroscopy studies. In initial ApREES measurements the Super-Head was used to deliver the Raman spectrometer's lasers (488 nm and 633 nm) and two standalone lasers (405 nm and 532 nm) into the vacuum chamber. In HeLIOS only the 405nm laser on a Thorlabs adjustable mount was used.

A 365nm UV LED in a custom mount with filter holder for a UG11 filter to remove the visible portion of the spectrum, allowing only the UV component to illuminate the sample. A UV lens is located within the mount to allow changes in the excitation spot size. The UV LED source used in this work was a Thorlabs mounted high-power LED M365L2-UV. The output is dominated at 365 nm at over 190 mW power. Due to the higher power the module is mounted

on a heat sink and driven using a Thorlabs controller. This source had a typical bandwidth of 7.5 nm.

### **2.3.3.3 Aberystwyth Tuneable Light Source (ATLS)**

To provide a spectrally stable source illumination for samples and calibration work a tuneable light source has been developed. The instrument consists of a laser driven light source (LDLS)(Energetiq), a Triax190 monochromator (Horiba) and a suite of optimised off axis parabolic (OAP) mirrors housed in a sealed nitrogen purged environment. A LDLS operates by focusing a continuous wave near infrared laser via a high numerical aperture lens into a fused silica bulb filled with high-pressure rare gas (in this case Xenon<sup>54</sup>). Once the gas in the bulb is ignited a plasma is formed by conventional arc lamp ignition absorbing the laser light, which heats it to above 10000K. The ignition arc is terminated and the plasma becomes self-sustained by the laser. The small size of the source (limited by the focus spot of the laser) enables the high spectral brightness and stability across its spectral range. The LDLS has advantages over conventional sources such as arc and deuterium lamps due to the small spot size of the output. The closer this is matched along the optical path to the monochromator and to the monochromator slit widths the more light is able to be utilised and the higher the resolution. A schematic of the instrument and annotated photograph are given in Figure 2-18 and Figure 2-19 respectively.

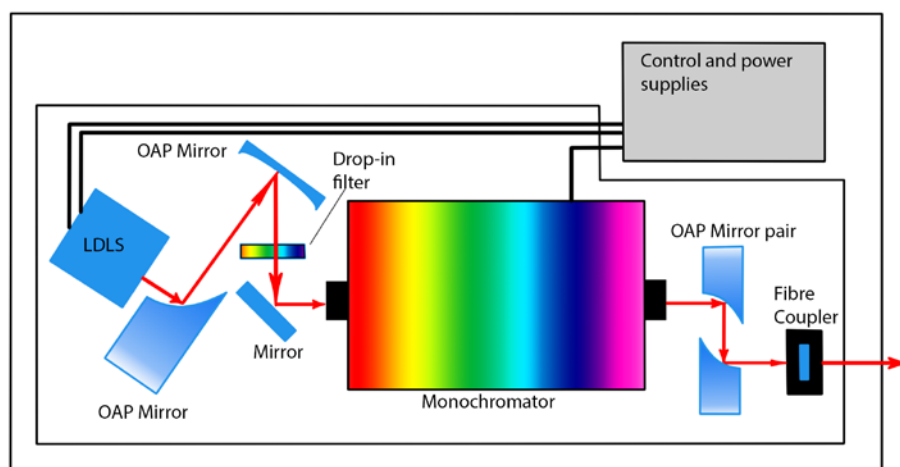


Figure 2-18 ATLS Optical block diagram illustrating key components.

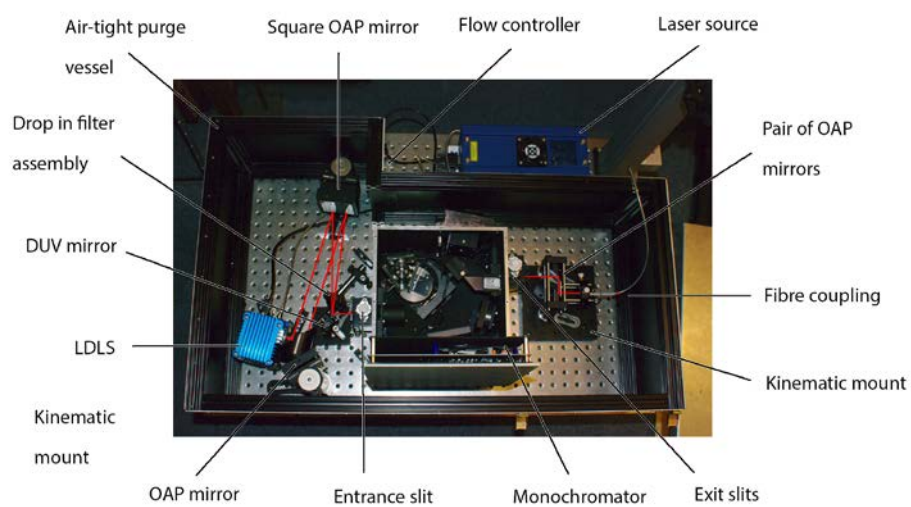


Figure 2-19 Annotated ATLS photograph, beam path illustrated in red.

## 2.3 Material preparation and characterisation

---

The diverging output from the LDLS is first collected by an Ø2" 90° off-axis parabolic (OAP) mirror. This mirror focuses the light onto another AOP mirror which in turn directs the light through an optional manual filter assembly to a flat Ø1" mirror. The flat mirror is held on a magnetic kinematic mount, enabling it to be replaced with a Ø1" 90° AOP mirror enabling the white light output from the LDLS to be coupled directly to an optical fibre for a high brightness light source or a broad band source when using the drop in filters. From the flat mirror the light enters a Horiba Triax 190 monochromator where spectral dispersion is controlled via a computer interface. On selection of the desired output wavelength and spectral width (by controlling the slit size) the desired light exits the monochromator and can be collected in a number of ways. For spectroscopy applications the light can be collected via a pair of matched Ø1" 90° OAP mirrors and focused onto a collimating lens coupled to an optical fibre. For calibration applications, the light can be allowed to exit the monochromator directly into an integrating sphere for maximum illumination. The properties of these components are summarised in the tables below:

| Source                  | Continuous wave (CW) plasma discharge   |
|-------------------------|---|
| Spectral range          | UV-Vis-NIR (170 – 2100nm)   |
| Numerical Aperture (NA) | 0.47 (max)  |
| Typical output          | Wavelength dependent; 10 mW.mm <sup>-2</sup> .sr <sup>-1</sup> .nm <sup>-1</sup> , broadband power of 0.5 W |
| Plasma size             | Continuous wave 100-200 µm Xenon  |
| Internal laser          | Class 4 IR 974 nm continuous wave (8 mW at aperture)  |

Table 2-2 Laser Driven Light Source (LDLS) technical specifications <sup>55</sup>

| <b>Optical layout</b> | <b>Corrected Cross Czerny Turner</b>  |
|-----------------------|---|
| Focal length          | 190mm   |
| Aperture              | f/3.9   |
| Grating size          | 50x50mm   |
| Resolution            | 0.3nm   |
| Dispersion            | 3.53nm/mm   |
| Accuracy              | $\pm 0.3\text{nm}$  |
| Repeatability         | $\pm 0.06\text{nm}$   |
| Step size             | 0.06nm (nominal)  |
| Wavelength range      | 185nm to FIR (with appropriate gratings)  |
| Turret                | Kinematically interchangeable, 3 per turret   |
| Slits                 | Motorised, 0-2mm in 2 $\mu\text{m}$ steps or 0-7mm in 6.35 $\mu\text{m}$ steps with interchangeable fixed slits |
| Dimensions            | 230 x 260 x 320mm   |

Table 2-3 Horiba Triax190 monochromator technical specification <sup>56</sup>

## 2.3 Material preparation and characterisation

| Specifications/ Item and reference | (1)<br>90° OAP Mirror | (2)<br>Square OAP Mirror | (3)<br>Precision DUV Mirror | (4)<br>Pair 90° OAP Mirrors | (5)<br>90° OAP Mirror |
|------------------------------------|-----------------------|--------------------------|-----------------------------|-----------------------------|-----------------------|
| Supplier                           | Edmund Optics         | Edmund Optics            | Edmund Optics               | Thorlabs                    | Thorlabs              |
| Size (mm)                          | Ø 50.8 (2")           | 60 x 60                  | Ø 25.0                      | Ø 25.4 (1")                 | Ø 25.4 (1")           |
| Parent Focal Length (PFL) (mm)     | 25.4                  | 275                      |                             | 25.4                        | 50.8                  |
| Effective Focal Length (EFL) (mm)  | 50.8                  | 279.10                   |                             | 50.8                        | 101.6                 |
| Substrate                          | Al 6061-T6            | Soda lime float glass    | Fused silica                | Al                          | Al                    |
| Surface accuracy                   | 1/8λ                  | ¼λ                       |                             |                             |                       |
| Surface roughness (Å)              | <50 RMS               |                          |                             | <100 RMS                    | <100 RMS              |
| Coating                            | Protected Al          |                          |                             | Protected Al                | Protected Al          |

Table 2-4 ATLS mirror specifications <sup>57,58</sup>

The system is mounted onto a 2" thick optical bench, constructed at table height on castors for mobility. Below the optical bench there is a slide-out shelf housing the monochromator's laptop PC. On a lower level a high resolution Horiba iHR320 spectrometer is located, also controlled from the laptop PC. This configuration provides flexible delivery of a source of fully tuneable, bright, stable light from 200 nm – 2000 nm and a high-resolution fibre couple spectrometer for data acquisition in a self-contained, portable system.

The optical path and components are encased in a light tight box with access via a top hatch for configuration changes. The box is air tight to allow nitrogen gas purging. This has two main benefits; maintaining clean optical surfaces, protecting the components from damage and also to purge ozone generated by the LDLS. Ozone is produced when air (i.e. oxygen) is exposed to UV radiation below 200nm. As the LDLS has output down to 170nm there are health and instrumentation implications. Ozone is hazardous to optical components as



hydrocarbons present in the atmosphere can be photodissociated by deep UV light. These materials can then become deposited on components, reducing their optical properties such as transmission and reflection. During this process ozone absorbs UV light and so in order to operate in that spectral region nitrogen purging is required. For applications where deep UV is not required, a blocking window can be placed on the LDLS window. In this situation there is no need to purge the optical path, however the LDLS itself must be internally purged to maintain maximum lifetime. In addition to providing a source of tuneable excitation for PL measurements in HeLIOS the Aberystwyth Tuneable Light Source (ATLS) shall be used for the spectral characterisation and calibration of the two wide angle cameras deployed on the PanCam instrument and the camera used in the concept development of the Hyperspectral Imager (SPEC-I, HIA and HyperCLUPI). The Aberystwyth University PanCam Emulator (AUPE) has been investigated using this light source, where initial calibrations have revealed ring artefacts in the images<sup>59</sup>. This was achieved by delivering light with a narrow spectral width into an integrating sphere with the camera to be calibrated directed into the sphere. The light can be delivered to the sphere by fibre or by allowing the light emerging from the monochromator's exit slits to directly enter the sphere. The latter option provides a higher brightness, however the former method is more suitable for applications where the camera is undergoing thermal testing as fibre coupling allows minimal intrusion into the thermal vacuum chamber and shall be applied to the engineering, flight spare and flight model of PanCam. The incident light can then be scanned over the sensor's detection range to collect flat field and photo-responsivity measurements.

#### **2.3.4 Atomic Force Microscopy**

Atomic Force Microscopy (AFM), a type of scanning probe microscopy, was used to measure the surface of two polycrystalline CVD diamond in order to assess which sample would be most suitable for future work and to assess the surface prior to Raman mapping. Surface

## 2.3 Material preparation and characterisation

---

texture influences the accuracy of Raman mapping as the signal is proportional to the quality of the laser focus. Variations in height can produce a false representation of peak area and intensity due to shifting focus and surface scatter. AFM is an imaging tool with a dynamic range, spanning that of optical and electron microscopes.

AFM probes the surface of a sample with an atomically sharp tip. The tip is located at the end of a cantilever approximately 125  $\mu\text{m}$  long (depending on the particular probe). Forces between the tip and the sample surface cause the cantilever to bend, or deflect. A detector measures the cantilever's deflection as the tip is scanned over the sample, or as the sample is scanned under the tip. These deflections are mapped to generate a topography map of the surface. This profile data is then used to generate 3D images. The dominant force contributing to the deflection is the van der Waals force.

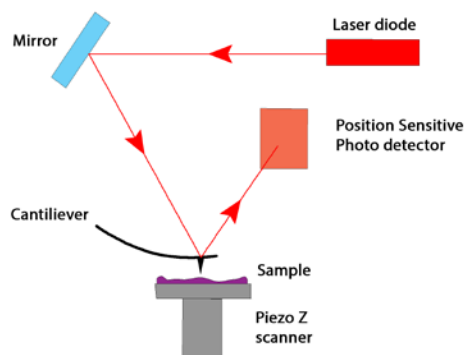


Figure 2-20 AFM Operation schematic. The cantilever is deflected the probe's interaction with the sample surface which in turn deflects the incident laser beam. This can then be detected on a position sensitive photodiode.

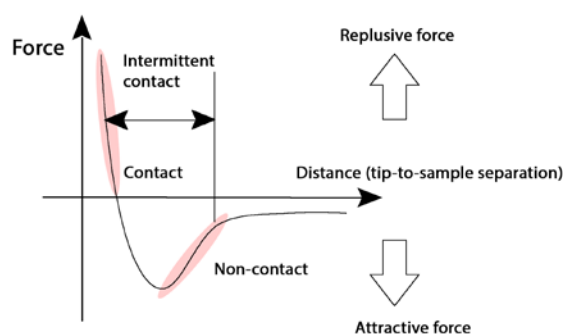


Figure 2-21 AFM force vs. distance curve illustrating the three modes of AFM available.

The cantilever may be operated in a number of modes, Figure 2-21 illustrates the three modes; contact, non-contact and intermittent. In contact mode, referred to as C-AFM, the cantilever is held less than a few angstroms from the sample surface where the interatomic force between the cantilever and the tip is repulsive. This is also known as repulsive mode due to the interatomic force involved. As the atoms are gradually brought together they first weakly attract each other, this causes the atoms to move closer together until their electron clouds begin to repel each other. The electrostatic repulsion progressively weakens the attractive force as the interatomic separation continues to decrease. The forces reaches zero when the distance between the atoms reaches a couple of angstroms; about the length of a chemical bond. In non-contact mode, NC-AFM, the cantilever is held tens to hundreds of angstroms from the sample surface and the interatomic force between the cantilever and the sample is attractive as a result of long range van der Waals interactions.

## 2.4 Chapter summary

This chapter introduced the theory of the interaction of radiation with matter, which underpins the characterisation techniques of luminescence and Raman scattering used in this

## 2.4 Chapter summary

---

work. The applications of PL, Raman and polarisation imaging have been discussed. Additionally a new system for in-situ UHV monitoring of sample processing by optical techniques has been presented.

## Chapter 3      Spectral Imaging

### 3.1 Introduction

This chapter provides an introduction to hyperspectral imaging and associated terminology. Before describing the hyperspectral imager constructed as part of this work, the key components and concepts shall be discussed in order to put into context the decisions made throughout the project. The question '*what is a hyperspectral image?*' is addressed by first considering spectral imaging, which combines the fields of spectroscopy and imaging. The combination of these creates a three-dimensional data set, also known as an image cube, in which a complete spectrum is available for each point in the spatial array. In HeLIOS, for example, its 512x512 pixel array gives rise to 262,144 individual spectra. In order to explain the use of hyperspectral imaging the fields of spectroscopy and imaging shall be discussed and it shown how spectral imaging provides a combined spectral and spatial approach to the analysis of inhomogeneous materials.

#### 3.1.1 Spectroscopy

Spectroscopy in itself is a wide field covering diverse applications, the work presented here concerns optical spectroscopy and so discussion shall be constrained to this.

Spectroscopy is a broad and well-established science, concerned with the acquisition and investigation of the spectral characteristics of matter. Spectroscopy is used to make direct measurements of the energy levels of materials at the molecular and atomic level. Broadly it is the study of the interaction of electromagnetic radiation with matter. There are three

### 3.1 Introduction

---

aspects to a spectroscopic measurement; irradiation of a sample with electromagnetic radiation, measurement of the interaction of the light with material (absorption, emission and scattering), and finally analysis or interpretation of these measured values. Further categories of reflectance, transmission, and absorption can then be broken down into how the material responds to the absorption of a portion of the EM spectrum. Chapter 2 introduced and reviewed the spectroscopy techniques used in this thesis.

At this point it is useful to set out a scheme for definitions of spectral regions to be used in this thesis. In the field of spectroscopy it is common to come across the terms UV, VIS, NIR etc. for the regions of the electromagnetic spectrum they concern. However quite often regions are quoted which overlap or miss out parts of the spectrum, a good example of this is in the field of remote sensing the 6-7  $\mu\text{m}$  region is not considered due to the absorption effects of the atmosphere. In this work the proposed discrimination between spectral regions by Dischler <sup>60</sup> have been used as this best aligns with literature concerning optical measurements of diamonds which form the bulk of the experimental data acquired in the course of this work. These are summarised in Table 3-1 below.

| Spectral region         | Energy (eV)          | Wavelength (nm)  |
|-------------------------|----------------------|------------------|
| Far infrared            | 0.04 – 0.18          | 30,000 – 7,000   |
| Mid infrared            | 0.18 – 1.24          | 7,000 – 1,000    |
| Near infrared           | 1.24 – 1.77          | 1,000 – 700      |
| Purple                  | 1.77 – 1.88          | 700 – 660        |
| Red                     | 1.88 – 2.03          | 660 – 610        |
| Orange                  | 2.03 – 2.10          | 610 – 590        |
| Yellow                  | 2.10 – 2.18          | 590 – 570        |
| Green                   | 2.18 – 2.43          | 570 – 510        |
| Blue                    | 2.43 – 2.58          | 510 – 480        |
| Ultramarine             | 2.58 – 2.75          | 480 – 450        |
| Violet                  | 2.75 – 3.10          | 450 – 400        |
| Near ultraviolet (UV-A) | 3.10 – 3.94          | 400 – 315        |
| Min ultraviolet (UV-B)  | 3.94 – 4.43          | 315 – 280        |
| Far ultraviolet (UV-C)  | 4.43 – 5.90 (-12.40) | 280 – 210 (-100) |

Table 3-1 Definition of spectral regions used in this thesis, after Dischler<sup>60</sup>

### 3.1.2 Imaging

Imaging is a method of acquiring spatial and temporal information of matter. Digital imaging is currently one of the most advanced methods of image acquisition, with data recorded by a CCD, CMOS or photodiode array.

A digital image is an array of I rows and J columns, called pixels, with individual elements displaying irradiance. A single number can represent these intensities. In the MathCAD data processing and analysis scripts used later, images were given the simplest treatment by displaying as an 8 bit image represented as  $2^8$  integer values, where 0 is the blackest black (no light) and 255 is the whitest white (saturation point) for initial interrogation. For colour imaging three images are required to contain red, green and blue information in order for the

### 3.1 Introduction

---

human eye to interpret colour. This can be achieved through taking three images and mixing or through the use of a sensor that acquires all three at once, such as a Bayer filter pattern<sup>61,62</sup>. For image reproduction, such as photocopying and printing, the three required colours are yellow, cyan and magenta. When taking a spectral image, this comprises of the additional wavelength component and so contains significantly more information than a single colour image and takes longer to acquire.

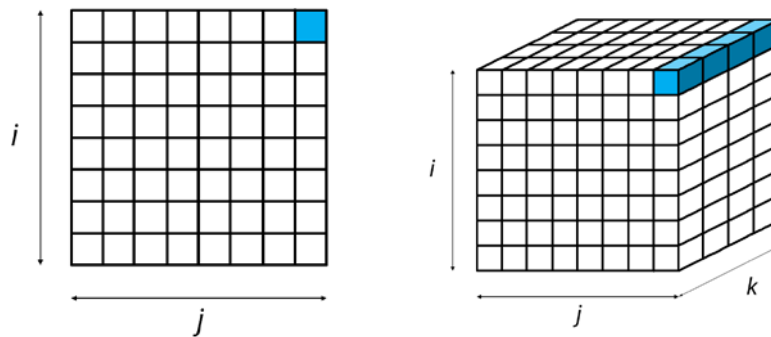


Figure 3-2 Pictorial representation of 2D and 3D arrays showing the extension from a single pixel to a spectrum.

Images have the benefit of conveying and interpreting large datasets in a manageable and easily digestible way. When properly calibrated an image can be used to convey qualitative and quantitative information. However a downside of extracting information from more complex datasets is the very large file size. Due to the nature of wishing to extract spectral data this last point is very pertinent as compression techniques and storage formats can have significant effects on the usability of acquired data.



### 3.1.3 Spectral and Hyperspectral Imaging

Spectral imaging integrates conventional imaging with spectroscopy, generating a three-dimensional data cube containing both spatial and spectral information of the target. When the wavelength dependent component is introduced to the 2D image array an additional dimension is added, transforming the pixel into a voxel. As in spectroscopy, hyperspectral imaging can be applied in different parts of the electromagnetic spectrum, such as UV, VIS, NIR and IR. In the selected region different physical interactions of the EM spectrum with the target can be investigated including reflectance, transmission, luminescence and Raman scattering. In Chapter 5 the results from hyperspectral imaging of photoluminescence, X-ray Excited Optical Luminescence and Raman spectroscopy are presented. The work in this thesis is focused solely on luminescence and Raman spectroscopy, however it has been demonstrated that HeLIOS can be used to collect reflectance data also. Reflectance data are not presented in this thesis.

The different types of sensors required to perform data acquisition are illustrated in Figure 3-3. These sensors are used to capture spatial, radiometric and spectral information from the instruments field of view.

### 3.1 Introduction

---

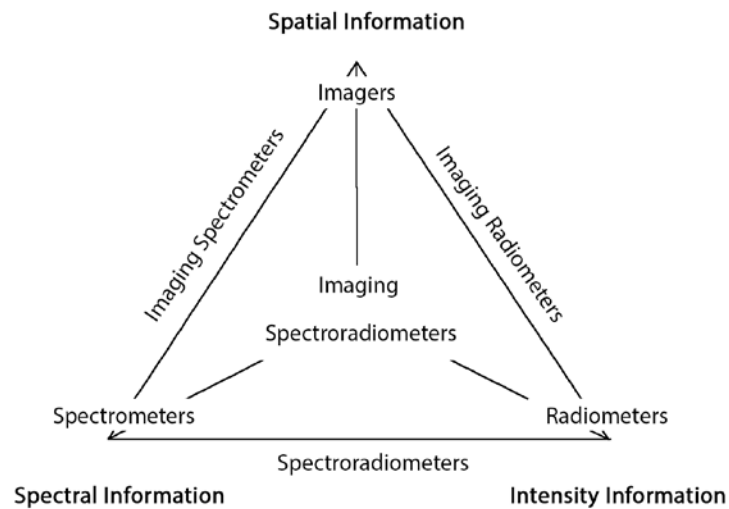


Figure 3-3 Illustration of the relationship between imaging and spectroscopy.

Figure 3-4 illustrates the concept of a spectral imaging system through the combination of 2D monochrome imaging with a spectroscopy component. A spectral image can be visualised by a data cube, where the face is a representation of two spatial components and the depth of the cube represents the wavelength component. The progression through the illustrations shows the addition of information, starting with a monochrome 2D image which alone can only provide spatial detail, extending this to three red, green and blue bands an image which the human eye can perceive colour is created. If a third wavelength component is introduced through multi or hyperspectral imaging a 3D data set can be generated which can be interrogated to provide spatial and spectral information.

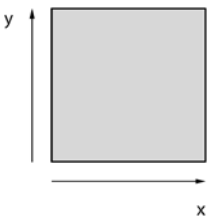
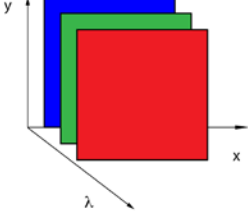

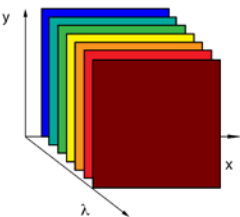
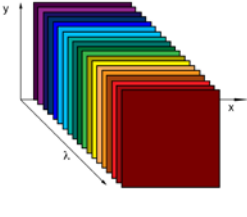
|                               | Monochrome  | RGB   | Spectroscopy   | Multispectral   | Hyperspectral   |
|-------------------------------|---|---|--|---|---|
| Feature                       |  |  |  |  |  |
| Spatial Information           | Yes   | Yes   | No   | Yes   | Yes   |
| Channels                      | 1   | 3   | Several to hundreds  | Several, can be contiguous or dispersed   | Tens to hundreds, but must be contiguous  |
| Spectral Information          | No  | No  | Yes  | Limited   | Yes   |
| Multi-constituent information | No  | Limited   | Yes  | Limited   | Yes   |

Figure 3-4 Comparison of monochrome, RGB, Spectroscopy, multi and hyperspectral acquisitions adapted from Li *et al*<sup>63</sup>.

Imaging spectrometers are designed to measure the energy or quanta collected from an object as a function of two spatial and one spectral dimension. This information is then used to generate a 3D data set, known as an object cube or data cube.

Spectral imaging technology is derived from early remote sensing applications that used satellite-imaging data of the earth, notably the LANDSAT programme. Goetz provides a useful reviews for those interested in the history of spectral imaging from a remote sensing perspective <sup>64</sup>. LANDSAT was the first remote Earth sensing satellite to use spectral imaging. The earliest version used only four wavelengths from filters – green, red and two IR bands. Later instruments in the series added additional wavelengths using diffraction gratings/prisms to give 100s of wavelengths, giving rise to the term '*hyperspectral imaging*' which was first used in a paper by Goetz <sup>65</sup>. The LANDSAT programme has provided the longest continuous space-based record of the Earth's surface and is still in operation since its launch in 1972. From these origins in remote sensing, hyperspectral imaging is now actively in use in many fields for numerous applications due to its flexibility, noncontact and non-destructive nature for the analysis of complex heterogeneous samples. These diverse applications include; the detection of defects in solar cells <sup>66</sup>; the study of historical manuscripts <sup>67</sup>; satellite and UAV studies <sup>68</sup>; biological applications such as gene mapping <sup>69</sup>, forensic applications <sup>13</sup> such as enhancement of fingerprints, crime scene recovery and document analysis <sup>70</sup>; agriculture for the identification of different crops and diseased plants; food science for quality control; medical for the saturation of haemoglobin oxygen in skin and identification of cancers; and geophysical research for example imaging of shells <sup>71</sup>. These examples present just a small fraction of the possibilities for hyperspectral imaging.

A literature search on the term "hyperspectral" shows the technique is predominantly used in remote sensing and food industry applications. From a search of the terms "hyperspectral" and "hyperspectral imaging" on the popular journal reference website Sciencedirect.com it can be seen that that there is an increasing number of publications in peer reviewed journals on the subject.

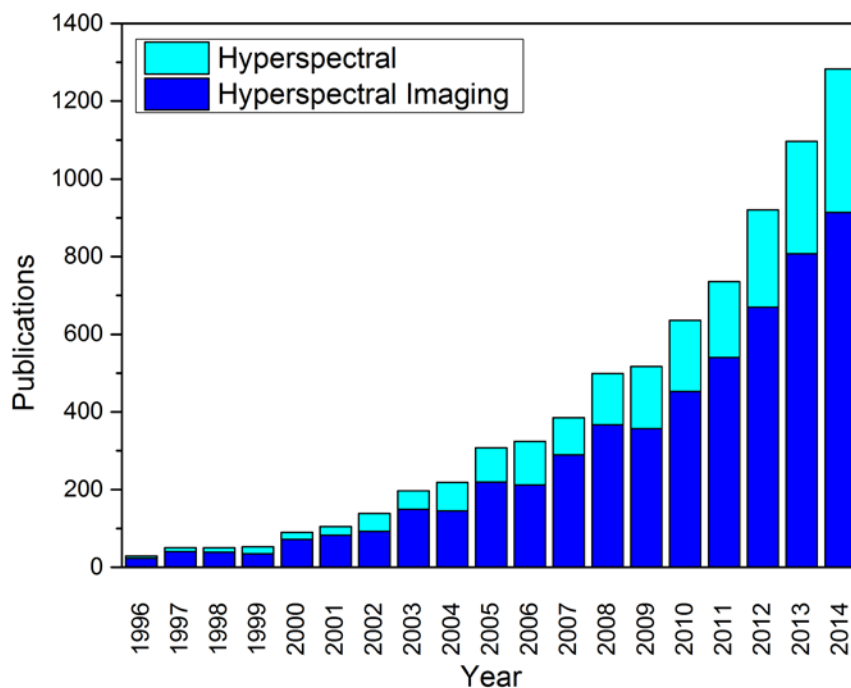


Figure 3-5 Graphic showing the increasing trend in the use of hyperspectral techniques.

Hyperspectral microscopy is a relatively new area of research predominantly concerned with life-science and is emerging in space exploration applications. Pilorget *et al*<sup>72</sup> describe the use of spectral imaging as “*one of the most promising ways to study remotely planetary objects.*” They also go on to discuss its applications for in situ analysis where such instrumentation is part of a lander. MicrOmega<sup>73,74</sup> is one such instrument planned for the ExoMars Pasteur<sup>75,76</sup> payload which hopes to exploit the technique of spectral imaging for sample composition analysis at the grain size scale. This aims to characterise the mineral and molecular composition of in-situ samples using microscopic spectral imaging. This instrument is based on an acoustic optically tuneable filter (AOTF) for spectral selection. The remote sensing applications for earth sciences and planetary exploration are predominantly

### 3.1 Introduction

---

reflectance measurements. In this work the instrumentation is detecting the emitted light from a sample when stimulated by a specific wavelength.

Hyperspectral imaging is an extension of spectral imaging, adding additional data points to the third dimension (wavelength). There is no definitive threshold for discriminating between a multi and hyperspectral imaging system accepted in literature. One criterion is found in remote sensing literature as 20-200 narrow bands or more for hyperspectral imagers <sup>77</sup>. Multispectral imagers are generally those where data is collected in a limited number of wide and non-contiguous spectral bands. In this section the different methods of hyperspectral image acquisition shall be discussed. Images can be acquired in a number of ways, a classification system proposed by <sup>78</sup> has been adopted as a standard across the field. Acquiring all three dimensions of a hypercube (a multi-dimension dataset) simultaneously is currently not feasible, temporal scanning is required to stack 2D data in a sequence. It should be noted that detectors are being developed which can sample multiple wavelength at a time, paving the way for future simultaneous one shot multispectral 3D data acquisition <sup>79,80</sup>.

Hyperspectral imagers come in many different forms, however as mentioned earlier they can be classified into one of four categories by their method of spatial discrimination; whiskbroom, push-broom, framing and windowing. Whiskbroom and pushbroom use dispersive elements that give the advantage of uniformly high efficiency, low scatter and low cost. However they can have complex optical design and long collection times. Air and space borne hyperspectral imagers are almost exclusively whiskbroom or pushbroom data capture systems.

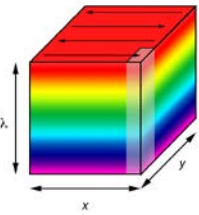
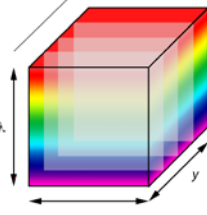
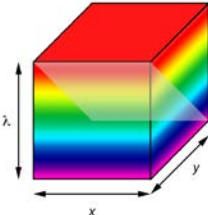
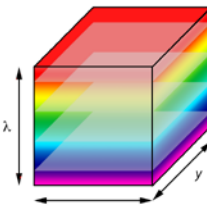
|                   | Whiskbroom  | Pushbroom   | Windowing  | Framing   |
|-------------------|---|---|--|---|
| <b>Spectral</b>   |  |  |  |  |
| <b>Filtering</b>  | Multiband radiometer  | No examples   | Filter array<br>Wedge filter<br>Linear variable filter                             | Band sequential<br>Filter wheel<br>Tunable filter (AOTF or LCTF)                    |
| <b>Dispersive</b> | Grating or prism  | Grating or prism  | Grating  | Image slicer<br>Tomographic   |

Figure 3-6 Classification of hyperspectral imagers adapted from <sup>81</sup>.

### 3.1.3.1.1 Whiskbroom

Whiskbroom imaging is a spatial scanning method; using conventional spectroscopy to build up an image by rastering over the target, acquiring a complete spectrum for each pixel. It is also referred to in literature as a point scanning method, an across-track imager, an across track scanner and a spotlight sensor due to the way a single image element is acquired which contains all the spectral information at once. In order to capture an image this must be repeated in both spatial directions to form a complete hypercube.

The technique was originally used for passive remote sensing from air and space on pioneering instruments such as the Landsat programme <sup>82</sup> and is one of the most common methods employed by remote sensing. Common whiskbroom instrument formats use rotating mirrors to scan a landscape, or other area, redirecting the reflected light to a single or small number of sensors. The reflected light is dispersed by a dispersive element (prism, grating, prism grating prism (PGP) and recorded on a linear array detector.

### 3.1 Introduction

---

By our definition of a spectral imager, a whiskbroom instrument is not technically an imager. In a similar manner to the Raman mapping work presented in chapter 5, a whiskbroom instrument is a single point spectrometer that forms a data cube through scanning over the desired spatial dimensions. Due to this scanning nature this type of instrument is very slow and more suitable to static scene measurement. Whiskbroom instruments have a complex set up and operation due to the need for two-axis motorisation to acquire the entire image cube. Advantages of the system include the wide wavelength range, high spectral resolution and ability to acquire large areas. An additional advantage of the system is that the user can control the depth of field by using a confocal set up with the majority of commercial available spectral confocal scanning instruments available belong to the whiskbroom class <sup>63</sup>, this is most useful when linking the whiskbroom imager to a microscope and using the inbuilt x-y stage to perform the sample translation. In comparison with pushbroom, a whiskbroom instrument has fewer sensor elements and so it is simpler to maintain the calibration. Examples of whiskbroom imagers include the Landsat Multispectral Scanner (MSS) and Thematic Mapper (TM) <sup>82</sup>, NOAA Advance Very High Resolution Radiometer (AVHRR) <sup>83</sup>, Airborne Visible Infrared Imaging Spectrometer (AVIRIS) <sup>84</sup>.

#### **3.1.3.1.2 Push-broom**

Pushbroom imaging is a line scanning method where complete spectra are acquired for one line of the target image simultaneously, also known as a spatial scanning method and along track imagers. In a typical pushbroom imaging system the dataset is acquired by scanning the sample line by line to form the hypercube with the light dispersed onto a 2D CCD. A 2D data matrix is obtained containing the spectral data, a complete spectrum for each line of pixels, for one spatial dimension and the sample (or imager) then moved and re-scanned in the perpendicular direction to add the third dimension. Movement is needed between the imager and the target, either by moving the imager or the target, which can introduce translation



and registration problems in the final hypercube. Similar to the whiskbroom, pushbroom imagers use a dispersive element (prism, grating, prism grating prism (PGP)). Providing a wide wavelength range and high spectral resolution. Pushbroom imagers tend to be smaller and lighter than their whiskbroom counterparts due to their simpler design and fewer moving parts, making them the most common method of data acquisition for earth and planetary remote sensing. They are used in airborne and satellite imaging where the travel of the instrument provides the second spatial component. Although they can be low cost due to their smaller and simpler design, pushbroom imagers have a complex set up and operation due to the higher number of detectors that make up a pushbroom imager their calibration can be very time consuming. The benefit of which provides better radiometric and spatial resolution. As with other prism or grating dispersion methods, pushbroom imager collects light more effectively than current tuneable filter options. Examples of pushbroom hyperspectral imaging include food quality inspection <sup>85</sup>, satellite imaging <sup>86</sup>, solar cell inspection <sup>66</sup> and the Terra Advance Space-borne Thermal Emission and Reflection Radiometer (ASTER) <sup>87</sup>.

#### **3.1.3.1.3 Framing**

The framing data acquisition method, also referred to as stare-down, band sequential method, 'point and stare', spectral scanning and area scanning, acquires a 2D data matrix at each wavelength band. The data cube is acquired by producing a stack of images taken at a contiguous range of wavelengths. A tuneable filter typically disperses the wavelength of the light impinging on the detector array, which is the method employed by HeLIOS. Framing instruments employ a 2D field of view (FOV), which remains fixed on the object during data acquisition. Framing acquires a 2D array, as with pushbroom, but in a more recognisable and conventional image format of two spatial axes providing the advantage of generating live images to aid in aiming and focusing. The term framing is used synonymously to staring in

### 3.1 Introduction

---

literature, as it is most suitable for stationary objects and hence most commonly found incorporated into a microscope.

Framing has short collection times and ease of coupling to other set ups and instrumentation. The user has full control of the spectral components, offering a flexible selection of spectral range for acquisition. Framing suffers from lower spectral resolution and transmission due to the dispersion method compared to the whiskbroom and pushbroom methods due to the lower throughput of tuneable filters and limit to the number of contiguous bands that can be resolved. Although there is an associated high cost of framing imager due to the spectral dispersion method selected, they are simple to use and set up, and by controlling the integration time and the selection of the 2D sensor a larger dynamic range can be preserved.

In Li's review of biomedical hyperspectral imagers <sup>63</sup>, the majority are framing incorporating filter wheels or LCTFs for wavelength dispersion. Filters wheels involve swapping narrow bandpass filters in front of the detector can also be used to generate the data, however these can introduce registry problems in the final image cube and hence errors in the spatially resolved spectral data. The use of filter wheels and interchangeable bandpass filters is far more common in multispectral imaging. A number of tests were conducted as part of this work to judge the effect of using such conventional filters, which highlighted the irreproducible nature of this method. A far more elegant and convenient method is via an electronically tuneable filter such as a liquid crystal tuneable filter (LCTF) or an acoustic optically tuneable filter (AOTF).

Figure 3-7 below shows the colour checker chart mounted onto a strip of photo-responsive paper for sample positioning on one of the HeLIOS copper sample mounts.

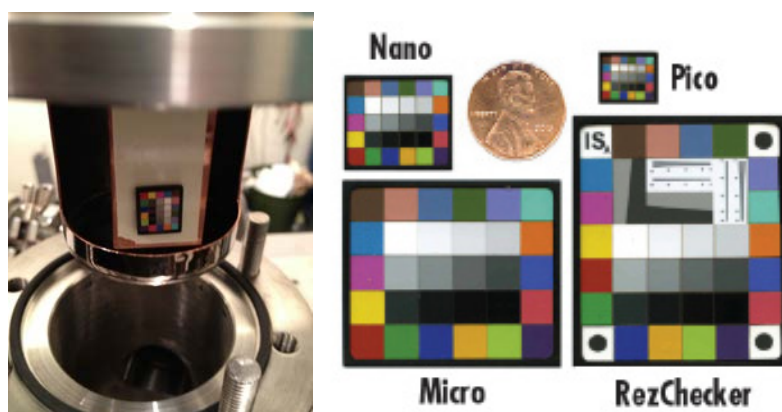


Figure 3-7 (l-r) Pico colour checker chart mounted onto photo-responsive paper in HeLIOS for sample and excitation alignment. Right, size comparison of chart the from Edmund Optics <sup>88</sup>.

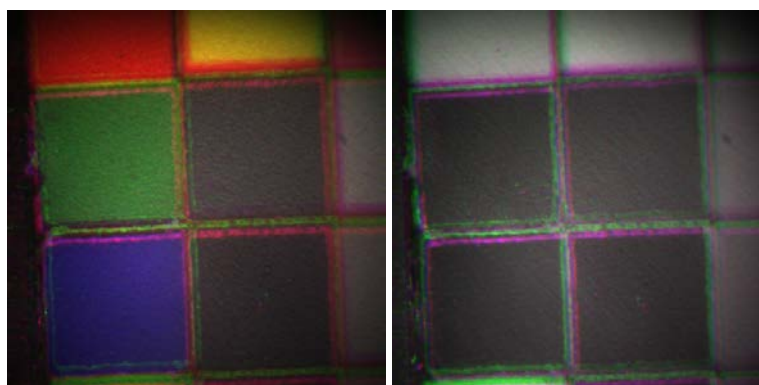


Figure 3-8 Manual acquisition using drop in filters showing registration problems.

Figure 3-8 above, is a region of the chart acquired with the 2x objective of HeLIOS. The image on the left shows a colour image reconstructed from a set of three images acquired with red, green and blue drop in bandpass filters. The resultant registration problems caused by small

### 3.1 Introduction

---

shifts in filter position when manually inserted are clear to see. To investigate if the registry problem was due to the filters themselves, or simply the act of changing them, three images were acquired with the same filter being repeatedly removed and reloaded. An RGB image was then constructed by assigning each image to a channel. This image is shown in the right hand pane of Figure 3-8 and clearly shows the registration problems caused by this method. This reaffirmed the use of a LCTF, which does not involve moving parts and so eliminates such registration problems.

Systems with a limited number of filters, such as multispectral instruments with a small number of filters mounted in filter wheel, can miss important spectral features. Work undertaken by the author as part of the Aberystwyth's joint proposal for a new hyperspectral imager for Mars<sup>9,89</sup>, HyperCLUPI, showed the advantages of hyperspectral imaging. By using a combination of two linear variable filters and long pass blocking filters a compact framing hyperspectral imager was designed to detect fine spectral detail. By comparing the spectral reflectance profiles of two minerals over the visible range as acquired by our breadboard and a simulation of the five MER (Mars Exploration Rover) Pancam filters it can be seen in Figure 3-9 the benefits of hyperspectral over multispectral when attempting to identify unknown materials.

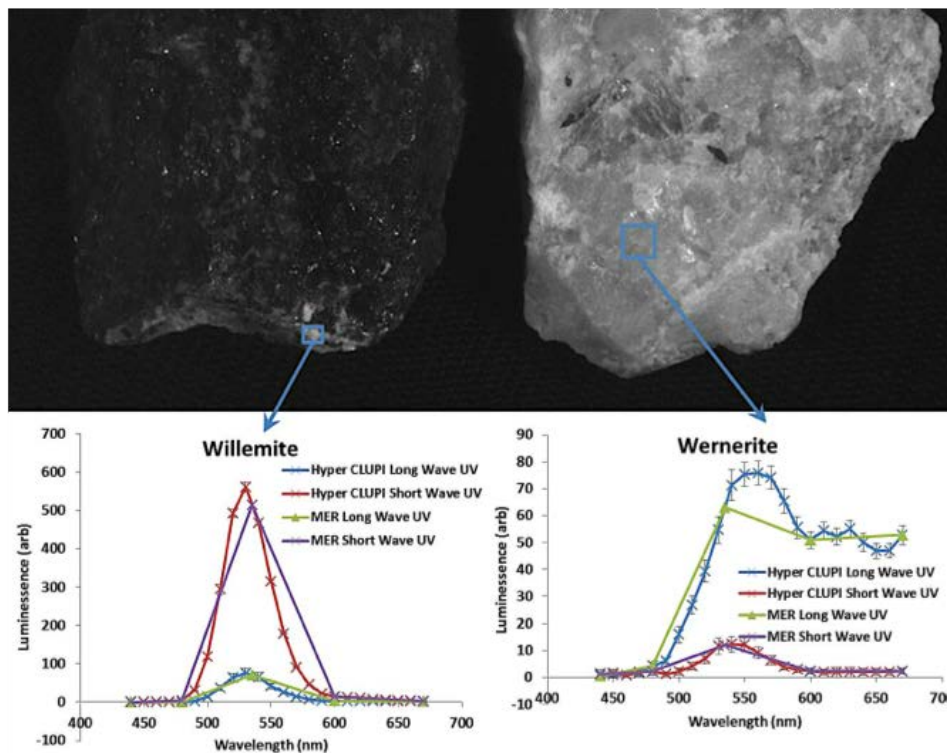


Figure 3-9 Comparison of MER and a HyperCLUPI breadboard data <sup>9,89</sup> illustrating the step change from multi to hyperspectral data collection.

New technology was needed to provide the hyperspectral element for framing instruments as filter wheels rapidly become large, cumbersome and impractical for most applications, introducing more technical difficulties, such as registration and corrections for thickness, than they solve. The large size of the CLASSIX <sup>34</sup> system led to long periods to move between filters and potential registration problems (no calibration test were conducted to the author's knowledge).

### 3.1.3.1.4 Windowing

Windowing is a hybrid of pushbroom and framing, capturing an image diagonally through the data cube. This image can be acquired along the spectral or spatial axis. Windowing is not very common and only included here for completeness of the Sellar and Boreman's classification <sup>78</sup>.

### 3.1.3.2 Hyperspectral microscopes

Hyperspectral microscopes are not yet widespread amongst the materials physics community; those researchers who loosely use the term 'hyperspectral' are often referring to Cathodoluminescence studies using an electron source. Flowdown instruments from remote sensing pushbroom technology have successfully made their way into biological and medical fields. Examples of pushbroom and whiskbroom hyperspectral microscopes include the PARISS hyperspectral microscopy system <sup>90</sup>, an imaging spectrometer that uses a prism with curved sides, translating the FOV with a computer controlled microscope stage. Uhr *et al*<sup>91</sup> describe a hyperspectral microscopic imaging platform for the identification of cancer cells. Their imager operates in a pushbroom method, using a grating for wavelength dispersion and a filter cube for excitation of the sample when prepared with fluorescent markers. CytoViva manufacture a very popular commercial whiskbroom VNIR spectrophotometer <sup>92</sup> that mounts directly onto a microscope for reflectance measurements. This system uses diffraction grating dispersion for higher resolution. Lower-tech and more cost effective hyperspectral microscopes such as that presented by Huebschman *et al* <sup>69</sup> are often however more accurately described as multispectral. Operating as a pushbroom, this system employs a linear variable filter, with a 22nm bandpass, far wider than that of CLASSIX and HeLIOS. With such a wide bandpass there is limited scope for the detection of fine spectral detail. A limit of current linear variable filters (LVF) is the range per filter; currently LVFs have a limited range. For example Huebschman's system is limited to the 400-800 nm

range. As with many fluorescence microscopes, it is designed to detect specific known fluorophores, limiting its wider application. Merging ideas, the MicrOmega instrument<sup>72–74,93</sup>, a NIR hyperspectral microscope to be flown as part of the planned Pasteur payload for the forthcoming ESA ExoMars mission, is an IR micro-imager. MicrOmega is based on AOTF, where an image is acquired of a sample under the illumination of contiguous spectral profiles in a framing method of the sample's reflectance. In the world of forensic material analysis a hyperspectral microscope has been developed for examining fibres from clothing using absorption spectroscopy<sup>94</sup>. This instrument employs a LCTF for wavelength discrimination operating in the framing method. With the development of new sensors it is hoped that soon hyperspectral instruments will be available to record the full spectrum at each pixel, therefore generating a hypercube in one shot. Hirvonen *et al*<sup>95</sup> introduce a wide range spectral imager for reflectance and luminescence. This makes use of new sensor technology to fuse three sensors together to produce an imager for 200–2500nm. However no data are present on actual samples, currently data are limited to a reflectance colour checker chart.

## 3.2 Instrumentation and Components

In this section the components used in hyperspectral imagers are discussed, introducing those items that were selected to build HeLIOS and the rationale behind the choices. Also presented are additional technologies that have become available and are considered for future upgrades. Instrumentation plays a pivotal role in the development of a new method for material characterisation. In this section those components used to form HeLIOS are discussed as are the excitation sources used in this work to stimulate luminescence.

### 3.2.1 Spectral dispersion

As seen so far, a hyperspectral imager has four methods of image acquisition. The differences in these are heavily influenced on the application and the method of spectral dispersion. Here the main types of spectral dispersion in use are presented and discussed. Figure 3-10 illustrates a number of common methods of spectral dispersion.

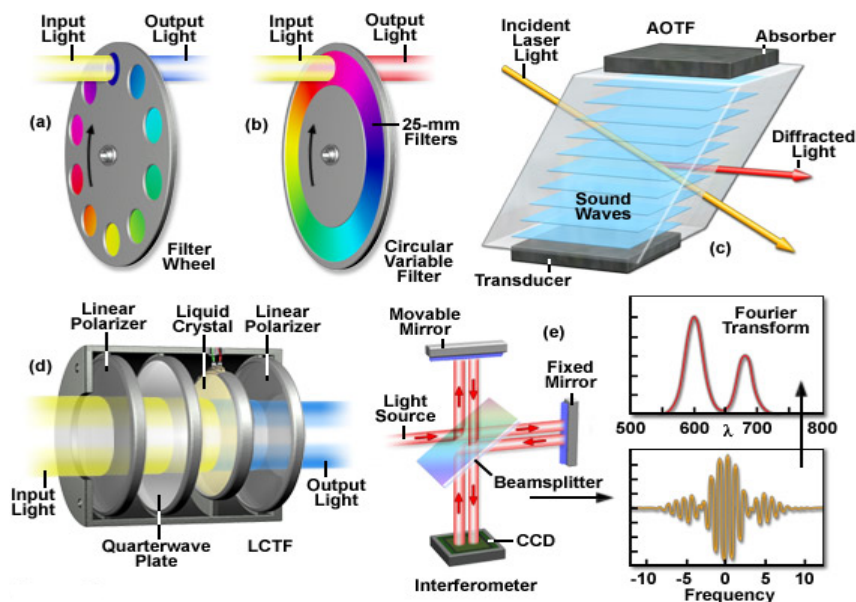


Figure 3-10 Methods of spectral dispersion available for hyperspectral imaging, reproduced from <sup>96</sup>.

#### 3.2.1.1 Liquid Crystal Tuneable Filter

Liquid crystal tuneable filters (LCTFs), illustrated in Figure 3-10, allow the spectral analysis of not only a single point, but of an entire object through combination with a 2D array sensor. This type of filter works on the principle of polarization dispersion and diffraction, using in phase retardation to pass a selected wavelength of light. These filters are of solid-state



construction with no moving parts and so easily integrated in different instrumental geometries. They have the highly desirable quality of being able to tune continuously across the filter's range, in the case of HeLIOS from 400-1000nm. LCTF are currently available which go out to over  $2\mu\text{m}$ <sup>97</sup> and are employed in the many diverse fields of hyperspectral imaging.

In a LCTF a sandwich of nematic molecules replaces conventional waveplates to pass only a narrow bandwidth of light while blocking all others within a designated spectral range. The construction of a typical nematic liquid crystal retarder is illustrated in Figure 3-11. A single retarder is constructed using two optically flat fused silica windows coated with transparent, conductive ITO. A thin dielectric layer is applied over the ITO and gently rubbed to create parallel micro-grooves to facilitate liquid crystal molecular alignment. The two windows are precisely aligned, spaced a few microns apart. This cavity is filled with birefringent nematic liquid crystal material, referred to as LC molecules in Figure 3-11. Finally this assembly has electrical contacts applied and is sealed. Figure 3-11 illustrates the LC alignment where no voltage is applied. Due to their nature they prefer to align themselves with their longest axis parallel to the assembly layers, providing maximum retardation. On the application of a suitable voltage the LC molecules rotate to align their tips to become perpendicular to the assembly layers, providing minimum retardation of the incoming light. In effect the electric field applies an external torque to each of the active liquid crystal molecules.

The finished LCFT filter is comprised of a stack of these individual retarders where incoming wavelengths of light are retarded by different amounts by Lyot (two parallel polarisers either side of a waveplate held at  $45^\circ$ ) stages, by stacking a number of these stages together they can work together to reduce the resulting transmitted light to only that of a desired range. Through the addition of Solc stages (multiple waveplates at varying angles between two parallel polarisers) the number of total optical stages in the final filter can be reduced. This has the benefit of increasing the transmission as most of the attenuation of the incoming light

### 3.2 Instrumentation and Components

---

is due to the polarisers. By varying the voltage applied to each element of the stack the wavelengths transmitted is controlled.

The pass band can be changed very quickly with the ultimate response time of the filter depending on a number of factors including the liquid crystal layer thickness, viscosity, temperature, surface treatment and driving waveform <sup>98</sup>.

The LCTF used in HeLIOS is a D4020 by Meadowlark Optics, employing Lyot stages, Solc stages and other proprietary stages to give optimum peak transmission with minimum of leakage. The filter is capable of tuning from 400-1000 nm via the provided Filterdrive 4000 software. This software has been integrated into the LabVIEW HeLIOS control software to provide a single point to operate the instrument from and enable automatic data acquisition and logging. The optical head contains the filter, consisting of multiple liquid crystal variable retarders and polarizers, heater and a temperature sensor. Temperature control is important, as the birefringence of the liquid crystal variable retarders is a function of temperature as well as voltage. The filter is contained in a light-tight housing, putting the heater and the filter under the least amount of thermal stress due to temperature fluctuations in the laboratory. Experience of using the filter out of the housing showed it took longer for the temperature to settle and cycled more frequently. The filter is thermally stabilised by a temperature feedback circuit to 40°C. The pass band can be shifted in milliseconds, with stabilisation times of approximately 20 ms, giving an instrument equivalent to hundreds or thousands of filters on a wheel, as used in the CLASSIX spectrometer <sup>34</sup>.

The transmission of a LCTF is wavelength dependent, hence it needs to be calibrated and corrected for in the final data set; this is discussed in more detail in Chapter 4 where an integrating sphere and calibrated light source have been used for measuring the transmittance of the filter under integrated instrument conditions.

Transmission of randomly polarised light is half that of the linearly polarised light in the maximum orientation. It is this maximum transmission that is quoted in literature and product details.

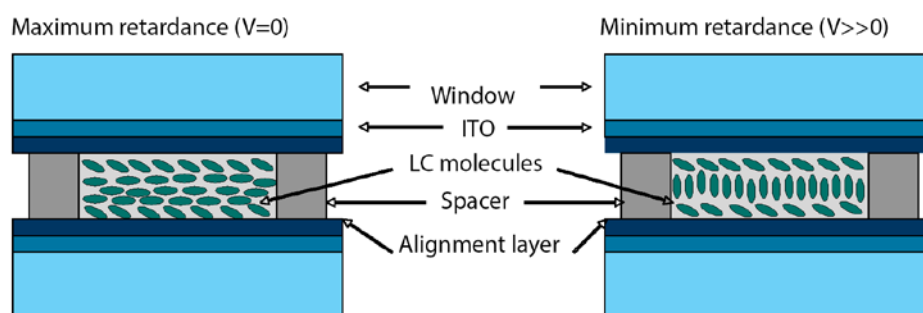


Figure 3-11 Principle of LCTF operation, adapted from Meadowlark LCTF manual <sup>99</sup>, illustrating the change in orientation induced by an applied voltage.

As shown in Figure 3-12 the transmittance of the HeLIOS LCTF is quite low due to the nature of the impinging randomly polarised light, this is especially evident when tuned to short wavelengths (400-450nm). An intense light source can help with this and is one of the reasons being the development of the Aberystwyth Tuneable Light Source (ATLS), which is discussed in Chapters 4 and 7.

For completeness and comparison, another commercial available and popular tuneable filter the acoustic optically tuneable filter (AOTF) shown in Figure 3-10, uses a crystal in which the wavelength of light passing is a function of the frequency of the radio wave applied to the crystal. AOTF can have high transmission and narrow bandpasses, however LCTFs have superior out-of-band rejection to an AOTF and do not suffer from the characteristic blur often observed with AOTF <sup>100</sup>, hence the LCTF was preferred to its superior imaging qualities.

### 3.2 Instrumentation and Components

---

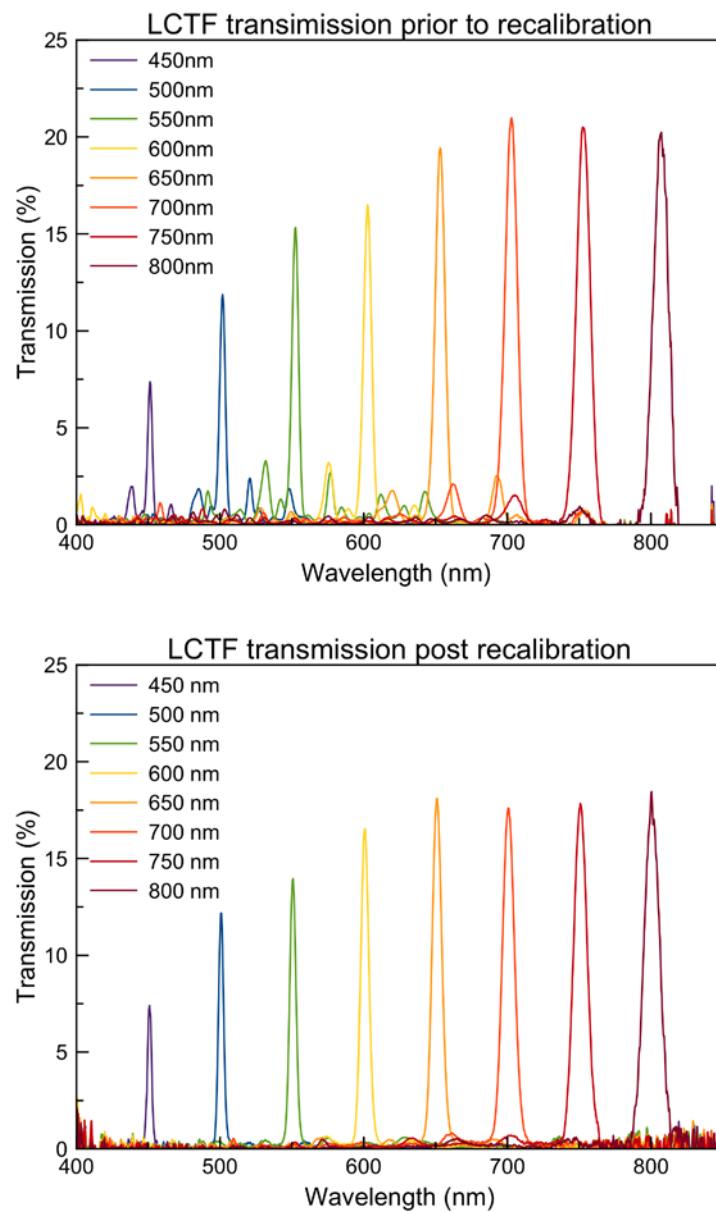


Figure 3-12 LCTF transmission, prior to recalibration (top) there was considerable out of band rejection, post calibration this has significantly improved, however the overall transmission was reduced in the process.

### **3.2.1.2 Filters**

Although a small and relatively minor component in the build of spectroscopy instrumentation, optical filters can be used to greatly improve image quality, perform selective measurements and in some cases, such as Raman spectroscopy, enable a technique to be performed at all. Optical filters from a number of sources (including Edmund Optics, Thorlabs, Laser2000, and Comar) have been used alongside the instrumentation developed as part of this work for image enhancement, wavelength selection and wavelength rejection. For completeness, and to stress the importance of filter selection, a brief overview of the types of filters used in this work and their applications is provided. Four main classes of filters have been employed in this work; long pass, short pass, band pass and neutral density filters. It should be noted that filters can be absorptive or reflective.

Long pass filters transmit all wavelengths longer than the specified cut in wavelength, blocking an undesired shorter wavelength range. Long pass filters have been employed in the acquisition of HeLIOS images and spectra and ApREES spectra to eliminate the unwanted reflected components of the excitation source. An edge filter has been utilised in Raman spectroscopy to transmit the wavelengths above the laser emission line with high efficiency due to the very weak Raman scattering. Figure 3-13, shows the combination of filters required for different Raman spectroscopy measurements.

Short pass filters transmit all wavelengths shorter than the specified cut in wavelength, blocking an undesired longer wavelength range. Such filters have been used with excitation sources to eliminate the visible component of UV sources such as the 365nm LED. These filters are either incorporated directly into the light source assembly (as in the 365nm LED) or in a customised drop in filter assembly positioned between the excitation source and the sample.

### 3.2 Instrumentation and Components

---

Band pass filters are commonly available with narrow band (<2nm to 10nm) or broadband (>50nm) transmittance. These can be either coloured glass or interference filters, which are angle sensitive due their multi-layer fabrication which combines bandpass ranges to achieve the desired result. These filters are used to selectively transmit a desired wavelength range. A notch, or rejection filter, is used to block a pre-selected bandwidth whilst transmitting all other wavelengths with the filter's range. Steep notch with high blocking at the desired wavelength are required for applications such as Raman and fluorescence excitation spectroscopy. A set of custom notch filters on interchangeable kinematic mounts is used here for Raman studies to block the incident laser from the spectrometer's path. A notch filter is typically a very narrow band block filter (a few nm), which is chosen to correspond with the laser excitation. This enables the laser line to be rejected and the Raman scattered light to be transmitted. Notch filters are needed where it is desirable to measure both Stokes and Anti-Stokes scattering. Figure 3-13 shows the use of these filters and their application to scattering spectroscopy is discussed in Chapter 2 in more detail.

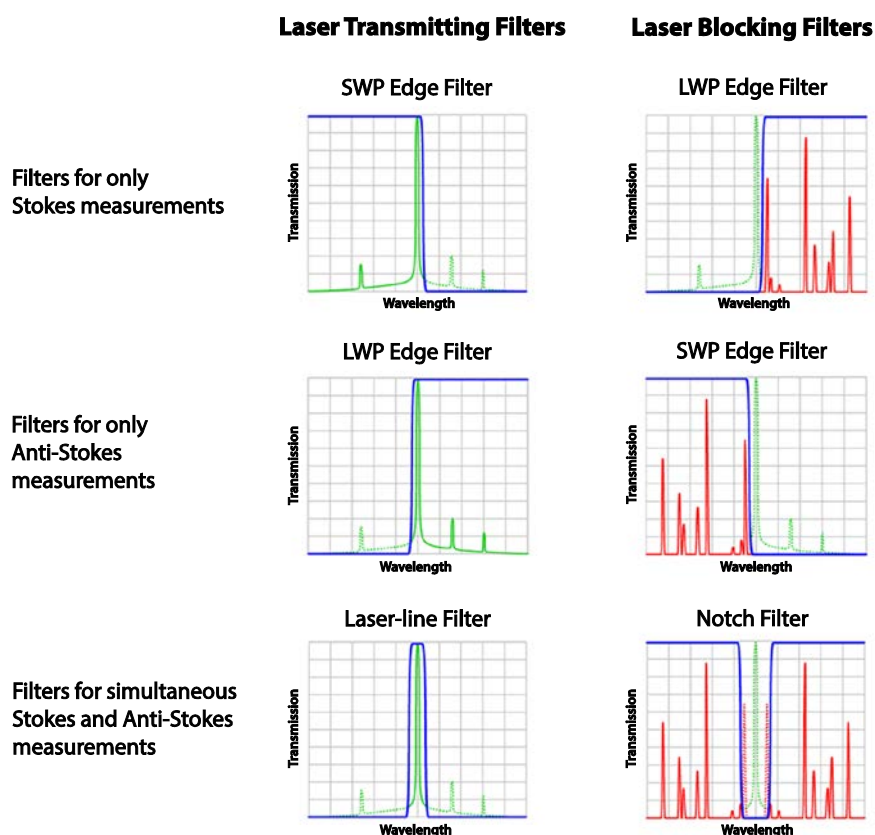


Figure 3-13 Filter selection plays an important role in the different types of scattering spectroscopy, adapted from Semrock.

The final category of filters used in this work is the neutral density filter. These are used to reduce transmission evenly across a portion of the spectrum having a nearly constant transmission, especially in the visible range. Neutral density filters have been used to prevent blooming or overexposure during sample set up for HeLIOS imaging, but not during data acquisition. They can be distinguished from other types of filter by their grey uniform colour.

Figure 3-14 Example of coloured glass filters taken from the Schott 2013 catalogue <sup>101</sup> below illustrates a number of absorptive glass filters available over the UV-VIS-IR range, showing the

## 3.2 Instrumentation and Components

cut in and bandwidths of some typical filters. Additionally Figure 3-13 illustrates the type of filters available for Raman spectroscopy.

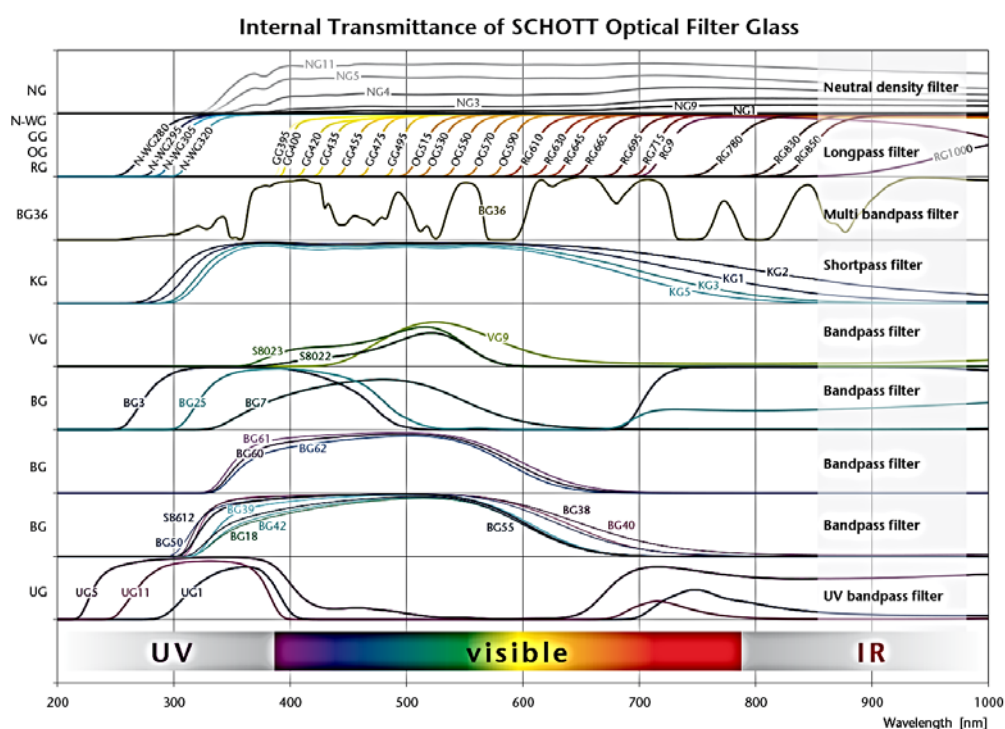


Figure 3-14 Example of coloured glass filters taken from the Schott 2013 catalogue <sup>101</sup>.

### 3.2.2 Objectives and lenses

A number of factors need to be considered when deciding on the optical components of an imaging system. These include sharpness, contrast, colour correction, relative illumination, spectral transmission, blocking factor and aberrations. In specifying objectives for HeLIOS it was necessary to look for those which provided the highest light collection and longest working distance do to the positioning of the objective turret to the sample chamber.



Before describing the individual components it is useful to provide definitions of quantities specific to optical systems as used in this thesis.

A lens' intensity varies from the centre to the edge of the image, with the centre being brighter than the edges. This can also be expressed as radial falloff. This non-uniformity can be caused by two factors; the natural decrease in illumination from the centre to the edge due to the  $\cos^4\theta$  effect and the effect of mechanical vignetting due to some light being physically obstructed. This can be corrected by taking a series of flat field measurements, but as each objective will have a different profile measurements should be taken for each. This effect is discussed in more detail in Chapter 4.

The f-number (F#) is the ratio of the effective focal length,  $f$ , for an object at infinity of the optical element or system to the diameter,  $D$ , of the entrance pupil:

$$f\# = \frac{f}{D} \quad \text{Equation 3-1}$$

Good optical systems fulfil the Abbe sine condition with a spherical wave-front converging at the focal point:

$$f\# = \frac{1}{2 \sin \theta_1} \quad \text{Equation 3-2}$$

The f-number and numerical aperture (NA) provide essentially the same information, however the numerical aperture is more frequently quoted when dealing with microscopy. NA is also an important parameter to consider when specifying optical components for an imaging system such as HeLIOS. It is the sine of the vertex angle (half angle) of the largest cone of meridional rays that can enter or exit an optical system or element, multiplied by the refractive index of the medium in which the vertex of the cone is located:

### 3.2 Instrumentation and Components

---

$$NA = n \sin \theta_{\frac{1}{2}} \quad \text{Equation 3-3}$$

The higher the NA, the smaller the width of the Point Spread Function (PSF). The degree of spreading of the PSF is used as a measure of the quality of an imaging system.

The solid angle,  $\Omega$ , links the f-number and NA to the throughput T (the geometrical extent or étendue) which is the product of the cross sectional area, A, of a beam and its projected solid angle. The solid angle can be expressed as:

$$\Omega = \frac{\pi}{4(f\#)^2} \quad \text{Equation 3-4}$$

$$\Omega = \frac{\pi(NA)^2}{n^2} \quad \text{Equation 3-5}$$

$$T = A\Omega \quad \text{Equation 3-6}$$

The microscope objectives used in HeLIOS are Mitutoyo infinity-corrected long working distance objectives. The benefits of these are the long working distances, required to allow sample imaging within the chamber and flat image surface over the field of view, reducing aberrations in the collected image on the CCD. The objectives are larger and longer than those one would find on a traditional microscope; enabling a higher NA at long working distances. To retain the infinity correction in HeLIOS a secondary tube lens has been employed. The tube adaptor functions as a secondary lens to form an image when used with the above infinity corrected objectives. It is necessary to match a suitable tube lens to the objective when switching between UV and UV-VIS.

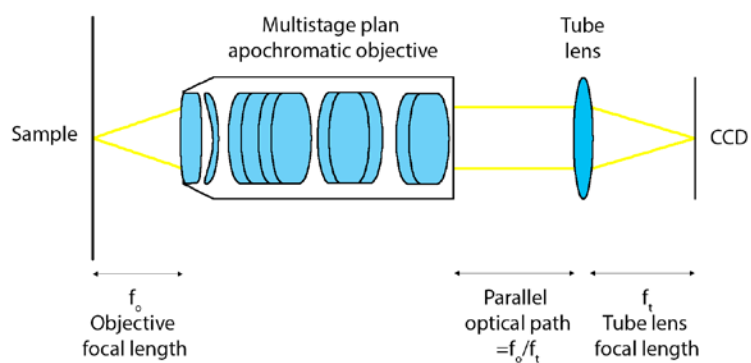


Figure 3-15 HeLIOS infinity corrected plan apochromatic lens diagram, illustrating the need for the additional tube lens for light collection.

| Magnification | NA    | Working Distance (mm) | Focal Length (mm) | Resolving Power ( $\mu\text{m}$ ) | Depth of Focus ( $\mu\text{m}$ ) | Transmission (nm) |
|---------------|-------|-----------------------|-------------------|-----------------------------------|----------------------------------|-------------------|
| <b>2x</b>     | 0.055 | 34.0                  | 100.00            | 5.0                               | 91                               | 380-1000          |
| <b>7.5x</b>   | 0.21  | 35.0                  | 26.27             | 1.3                               | 6.2                              | 380-1000          |
| <b>10x</b>    | 0.28  | 33.5                  | 20.00             | 1.0                               | 3.5                              | 380-1000          |
| <b>20x</b>    | 0.42  | 20.0                  | 10.00             | 0.7                               | 1.6                              | 380-1000          |
| <b>50x</b>    | 0.55  | 13.0                  | 4.00              | 0.5                               | 0.9                              | 380-1000          |
| <b>20x UV</b> | 0.36  | 15.0                  | 10.00             | 0.8                               | 2.1                              | 200-800           |
| <b>80x UV</b> | 0.55  | 10.0                  | 2.50              | 0.5                               | 0.9                              | 200-800           |

Table 3-1 HeLIOS objectives technical specifications, parameters taken from component datasheets <sup>57</sup>

## 3.2 Instrumentation and Components

| Magnification          | Image Field of View (mm) | Entrance Pupil (mm) | Focal Length (mm) | Design Wavelength (nm) |
|------------------------|--------------------------|---------------------|-------------------|------------------------|
| <b>1x tube lens</b>    | 24                       | 22                  | 200               | 355-1064               |
| <b>1x UV tube lens</b> | 24                       | 23                  | 200               | 266-620                |

Table 3-2 HeLIOS tube lens technical specifications

The Mitutoyo infinity corrected long working distance objectives were selected due to their high quality plan apochromatic design offering a flat image surface over the entire field of view. The advantage of an apochromatic lens over a standard achromatic lens is the former is corrected for red, blue and yellow where the latter is only corrected for red and blue. As seen in Equation 3-3, it is important to maximise the NA by bringing it as close as possible to the optical invariant. The larger format of these objectives allows for a higher NA and contrast.

UV objectives are  $\text{CaF}_2/\text{SiO}_2$ . Calcium fluoride has one of the highest Abbe numbers at 95.10. This high Abbe number results in less colour dispersion and reduces chromatic aberration. Fused silica has an Abbe number of 67.70. The low refractive indexes of these two materials at 1.434 and 1.458 respectively means they fall into the higher quality ‘crown’ glass category leading to lower dispersion and better transmission in the UV than those with higher refractive indexes, known as ‘flint’ glasses.

### 3.2.3 Detection

#### 3.2.3.1 Spectrometers

‘Spectrometer’ is a generic term which covers a class of instruments that can be used to collect, spectrally disperse and reimage an optical signal. There are a number of subsets to this generic term including monochromators, polychromators, spectrographs and imaging spectrographs. Spectrometers are used to measure the distribution of radiation of a source

in a specific wavelength region. Its basic operation consists of receiving radiant power through a narrow slit, dispersing this light to select a narrow spectral band to transmit, and transmitting this narrow band through an exit slit onto a photosensitive detector. The spectrometer can be used in two configurations; as a filter, where it is used to select a narrow bandpass to transmit light to irradiate a sample (as used in this work on the ATLS, or in analysis, where the photosensitive detector records the spectra of light being transmitted (as used here for Raman and PL spectroscopy).

There are a number of designs of spectrometer available, often optimised for specific applications and wavelength ranges, distinguished by their method of optical dispersion; prism or diffraction grating. Diffraction gratings are available in three types; classically ruled (CR), holographic surface relief (HSR) and volume holographic (VHG). Ruled diffraction gratings, such as the ones in the iHR320 used in this work for high resolution PL measurements, are optimized for maximum efficiency at a particular wavelength, known as the 'blaze'. 'Blazing' is designed to preferentially diffract the first order light of a selected range. When a grating disperses light, multiple spectra can be formed on the detector. Higher orders of diffracted light that make it to the detector can mix with the first order spectra, generating false peaks and hindering analysis. By incorporating filters on an automatic wheel into the spectrometer these higher orders can be eliminated. When using a tuneable filter such as an AOTF or LCTF this problem is avoided entirely, making the system simpler.

## 3.2 Instrumentation and Components

---

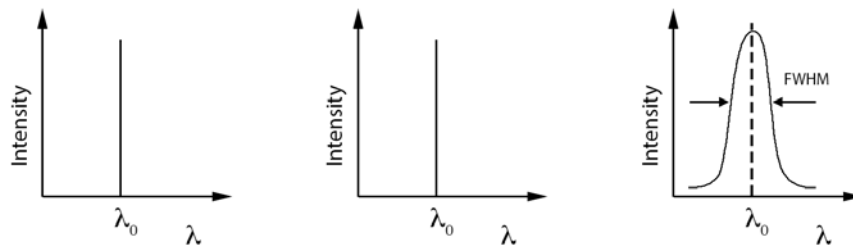


Figure 3-16 Comparison of an ideal spectrometer to real instrument for imaging monochromatic light, adapted from Lerner<sup>102</sup>. (l-r) The spectrum of a pure monochromatic light source, as recorded by a perfect instrument, and lastly as recorded by a real instrument.

Illustrated in Figure 3-16 a real instrument imposes an instrumental function onto the natural bandwidth of the monochromatic light, creating a finite bandwidth – represented by the full width half maximum (FWHM).

One popular spectrometer design, which has been used in this work, is the Czerny-Turner. This design features two concave mirrors and a plano diffraction grating. The two mirrors act to collimate the light source and focus the light dispersed from the grating respectively. The optical configuration is flexible in order to ‘fold’ the light, providing a compact yet high-resolution spectrometer.

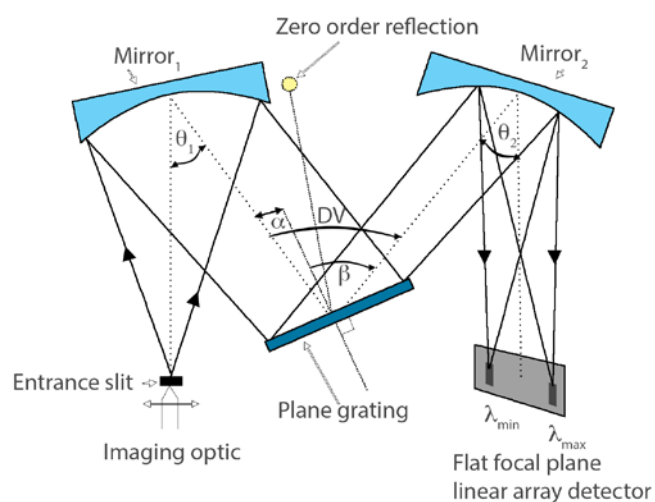


Figure 3-17 As used in this work for high resolution spectroscopy and calibration, an asymmetric Czerny Turner spectrometer design with incorporated array detector, adapted from Lerner<sup>102</sup>.

A conventional Czerny-Turner spectrometer, the Horiba iHR320, with enhanced capabilities for use with a CCD is employed in HeLIOS and the ApREES for spectral acquisition. This system acquires a single spectrum at a time from an acceptance angle of an optical fibre coupled to the objective turret in HeLIOS or the lens assembly in the ApREES. This type of spectrometer is most useful for the investigation of homogeneous samples, however when examining heterogeneous samples the individual spectral features are convolved into the final spectrum. By utilising the microscope objectives this convolution can be reduced by focusing in on areas of interest.

## 3.2 Instrumentation and Components

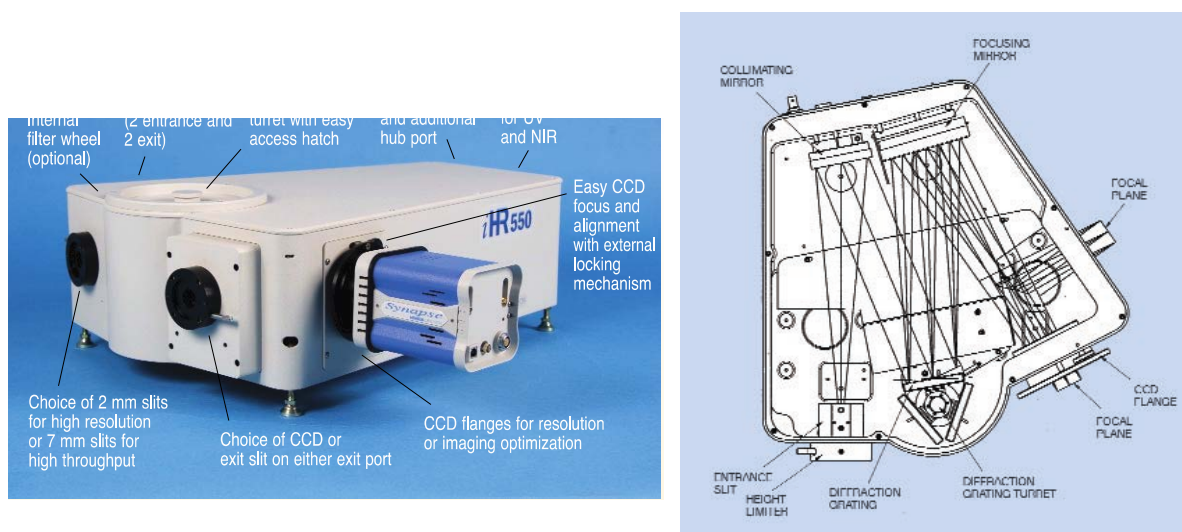


Figure 3-18 iHR320 spectrometer components and design, reproduced from Horiba manual <sup>103</sup>.

In contrast to this type of spectrometer, an imaging spectrometer can be operated in single, multi or hyperspectral mode, acquiring thousands of spectra rapidly to probe a sample spectrally and spatially. Following acquisition maps can be generated of specific features of interest, such as chemical maps. For spectral imaging a different approach to data acquisition is required. Where an absolute radiometric calibration is provided the spectrometer is referred to as a spectro-radiometer.

### 3.2.3.2 Charge Coupled Device (CCD)

For spectral imaging Charge Coupled Device (CCD) are one of the most popular choices. CCD detectors have been of interest to researchers since Willard S. Boyle and George E. Smith developed the technology in 1969 at the Bell Telephone Laboratories for which they later shared the Nobel Prize in Physics in 2009 <sup>104–106</sup>. With advances over the years in resolution, quantum efficiency, spectral response they process many desirable features for incorporation



into scientific instruments such as high linearity, increased sensitivity in the visible range and accessibility of data.

A CCD is an array of light-sensitive elements, pixel, arranged in the silicon substrate as a grid of narrow electrode strips. A common analogy for CCD operation is the comparison to measuring the spatial distribution of rainfall over a field by placing an array of buckets on the field <sup>107</sup>. After rainfall has occurred, a conveyor belt systematically transfers the buckets to a metering station where the amount of water in each bucket is measured. Each measurement represents the amount of rainfall at a particular location on the field. A CCD works in a similar way to measure the spatially distribution of light incident on a thin wafer of silicon. The underlying physical process is the photoelectron effect. When a photon of sufficient energy is incident on the P-N junction of the device it can be absorbed, causing electrons to be ejected, creating an electron-hole pair. These photoelectrons can then be collected at one of the many discrete collection sites. The positively charged gate electrodes then collect the negatively charged electrons. Each collection site is a thin layer of silicon dioxide, grown on the silicon, and a conductive gate structure is deposited on top. Applying a positive electrical potential to the gate creates the depletion region where the photoelectrons may then be stored. By integrating the photoelectrons in each individual collection site (counting the rain drops in a bucket) a spatial distribution over a fixed time interval is created. As one e-h pair is generated by one absorbed photon the charge collected by the electrode is linearly proportional to the number of incident photons. The light flux on a pixel can be determined by measuring the charge collected on the electrode. Charge coupling is used to move stored charge in a CCD, during which charge packets at a collection site are transferred from site to site by varying the gate potentials. Finally an image is readout by transferring the charge packets to a serial output register. This process repeats until all the collection sites in a two dimensional array have been read out.

## 3.2 Instrumentation and Components

---

CCDs are prominent in their use in radiometry for conducting measurements of heterogeneous objects and scenes. In the simplest radiometric terms a CCD can be calibrated by uniformly irradiating the array so that each individual element receives the same amount of optical radiation. There are a number of fundamental parameters which ultimately limit a CCD's performance <sup>108</sup>: read noise, fixed pattern noise (FPN), full-well capacity, charge-transfer efficiency (CTE), quantum efficiency (QE) and charge-collection efficiency (CCE). These measures of a camera's performance and the concept of camera irradiance are discussed in more detail in Chapter 4 where the measures taken to calibrate HeLIOS are discussed.

### **3.2.3.2.1 Electron Multiplying Charge Coupled Device (EMCCD)**

EMCCD technology has been commercially available since 2001 when Andor Technology Plc. first introduced the concept. Since its introduction a number of other manufacturers have developed CCDs with the same principles and the term 'EMCCD' has been adopted across the industry to signify a CCD that incorporates an additional gain register. EMCCDs have enabled advances in fields such as live cell imaging microscopy and single photon-counting astronomy. By using the principle of impact ionization to provide high gain an EMCCD can deliver performance with an equivalent input noise of less than 1 rms electron <sup>109</sup>. The detector used in HeLIOS is an Andor Technology Ltd. iXon DV887DCS-UVB. It is an ultra-sensitive CCD array capable of single photon counting over an operation range of 200-1000nm <sup>110</sup>. The EMCCD is comprised of a silicon-based semiconductor chip with a 2D matrix of pixels or photo-sensors, referred to as the image area. The EMCCD is identical in structure to a conventional CCD but the shift register is extended to include an additional section – the multiplication or gain register between the serial register and the output amplifier. At the point of readout this additional gain register multiplies the amount of charge in each pixel before it reaches the readout amplifier. By using a high multiplication gain the read noise can

be effectively eliminated, enabling sub-electron readout noise. It is this additional register that allows single photon counting and low light level applications. Although noise cannot be entirely avoided by using the multiplication gain it is introduced in another way, as the process is stochastic. CCD and EMCCD noise and characterisation are discussed in detail in the next chapter.

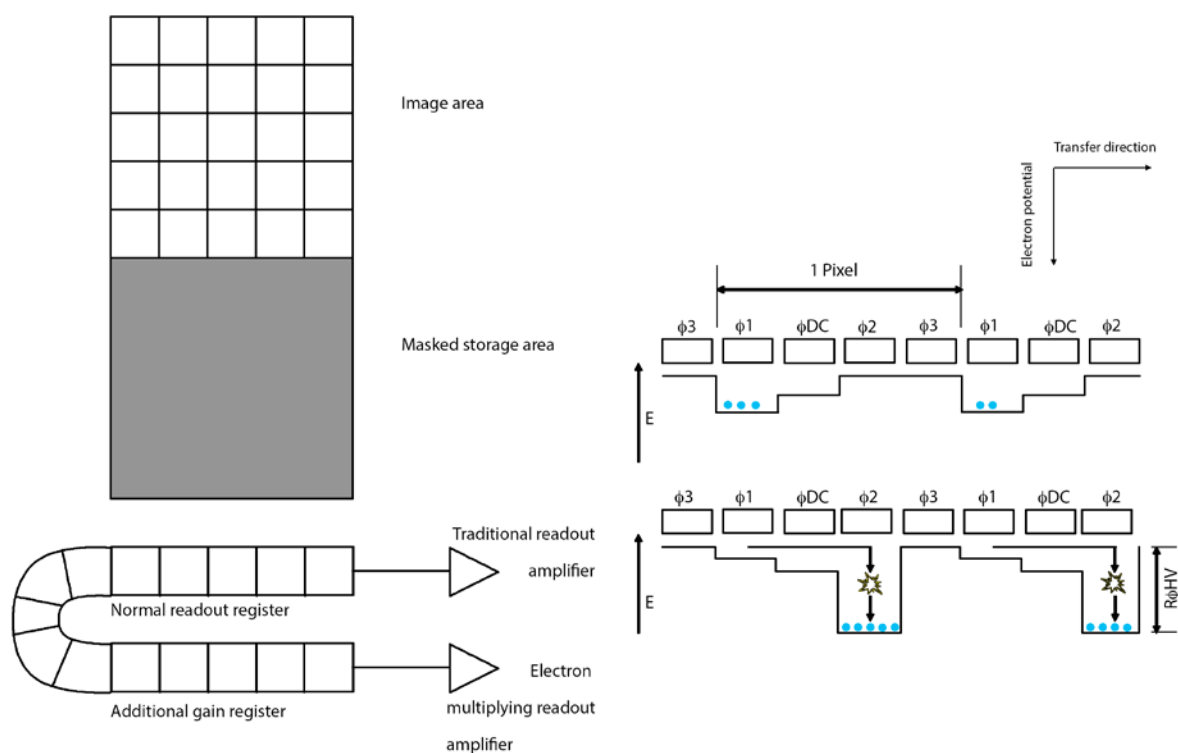


Figure 3-19 EMCCD and gain register operation, adapted from Andor <sup>111,112</sup>.

Figure 3-19 EMCCD and gain register operation above illustrates the operation of an EMCCD in conventional mode, akin to the standard CCD discussed in the previous section. The image area is exposed to light and an image is captured, this image, in the form of an electronic

### 3.2 Instrumentation and Components

---

charge, is then automatically shifted downwards behind the masked region of the chip before being read out. To read out, the charge is moved vertically into the readout register, then horizontally from the readout register into the output node of the amplifier. In an EMCCD the readout register is extended to include the multiplication or gain register. This additional register allows the detected signal to be amplified on the actual sensor itself before being read out through the amplifier and digitized. This negates the effect of any electronic noise that may be generated by the readout electronics.

The second illustration of Figure 3-19 shows the difference in well depth between a conventional CCD (top) and an EMCCD where impact ionisation is taking place. During the commissioning of HeLIOS the EMCCD was initially operated with the pre-amplifier set to 1x, using the EM range from 0-225 to prevent aging. However calibration data showed that the CCD's pixel wells were saturating but the shift register was not. Hence calibrations moved onto use the higher pre-amplifier setting of 2.4x. It was found for maximum dynamic range, whilst maintaining a suitable signal to noise, the EM gain should be equal to the read noise and the readout speed. The gain register pixels have a greater well depth than the imaging pixel well depth. If the lower pre-amplifier setting are used without EM gain applied the lower well capacity of the imaging pixels will saturate long before the gain register, thus imposing an upper limit on the charge which can be cascaded to the gain register. This is the cause of earlier tests where the full 16,384 counts for the 14-bit A/D channel could not be achieved without the application of EM gain. By increasing the signal with the pre-amplifier the signal has 'room to grow' so to speak.

The imaging of low light emission required relatively long exposures; hence the CCD must be cooled to a temperature at which thermal charges do not interfere with its operation. The EMCCD sensor is cooled using a thermoelectric (TE) cooler in air-cooling mode, where a small inbuilt fan forces air over the TE heat sink. Water-cooling is possible, but not employed in these studies.

### **3.3 Chapter summary**

In this chapter the origins of spectral imaging have been discussed, with the fundamental concepts presented. Hyperspectral imaging has been introduced, expanding on the four current classifications of hyperspectral imager. Current application of hyperspectral imaging in research have been illustrated. It has been shown how from spectral images of samples, be they via reflectance or luminescence, chemical information can be extracted enabling the users to examine wider differences, or go down to pixel level. From this introduction the components required to build a hyperspectral imager have been established and can now move onto the hyperspectral imaging spectro-radiometer constructed for this work – HeLIOS.

## Chapter 4 Helios

### 4.1 Introduction

This chapter details the primary instrument developed as part of this thesis along with the motivation behind its development and its current applications. Chapter 3 introduced the concept of hyperspectral imaging (what it is, why it's needed and how it is implemented) and gave the technical background to the key components and concepts required for an understanding of the instrument. Here its design, construction and calibration are covered.

Owing to its application, the instrument described in this thesis has been named HeLIOS (**H**yperspectral **L**uminescence **I**maging for **O**ptical **S**pectroscopy) and shall be referred to as such hereafter. HeLIOS can be operated in a number of modes, depending on the excitation source and the light dispersion method employed. HeLIOS builds upon the earlier work of MoLES (**M**obile **L**uminescence **E**nd-**S**tation)<sup>35,113–117</sup> and CLASSIX (**C**hemistry, **L**uminescence **A**nd **S**tructure of **S**urfaces via micro-**I**maging **X**-ray absorption)<sup>23,34,118,119</sup>.

When consulting the literature regarding vision systems, it is often assumed that the image brightness of a point directly depicts the scene radiance of that point. However in claiming this, a number of assumptions have been made which do not hold true due to artefacts in the image formation process which arise from the lenses, filters, and detectors used. This may not be an issue for some applications, however as here the wish is to accurately measure the light emitted from a sample and compare it with other systems a full characterisation and calibration of our system was required. In this, section parameters such as nonlinear camera responses, integration time, vignetting and noise have been investigated and accounted for

in the final image. A full radiometric calibration, which includes an estimation of the radiometric response function, camera linearity, dark current and LCTF response as a function of varying the integration time, microscope objective, EMCCD pre-amplifier and electron multiplier gains has been performed. The uncertainty in the acquisition of a science target image has been investigated and quantified using covariance error analysis.

## 4.2 System Development

The previous chapter laid the foundations for the construction of HeLIOS, giving details of many of the components used. Here these components are pulled together alongside custom fabricated pieces to form HeLIOS. The aim of this work has been to investigate heterogeneous samples via their luminescence, probing both spectrally and spatially. To satisfy this, a system for the hyperspectral imaging of emitted luminescence from target materials under a range of excitations has been developed. In this study the author has developed an instrument to advance the understanding of luminescence emission in materials, particularly wide band gap semiconductors, and develop calibration processing pipelines for space instrumentation. The overall aim is to correlate stimulated light emission with spatial features in a quantitative way.

HeLIOS consists of a cryostat sample stage mounted vertically into a UHV compatible chamber, with imaging optics, spectral dispersion elements and a 2D EMCCD detector array. A PC controls the spectral dispersion (when using the LCTF), cryostat temperature, microscope turret and data acquisition. The sample position (x,y,z) is controlled by a joy-pad interface. HeLIOS can be operated in XEOL mode when the custom housed X-ray source and aluminized Mylar window are in place. In PL mode excitation is provided by laser, LED or by coupling to the specially developed ATLS (Aberystwyth Tuneable Light Source) for tuneable excitation from UV to NIR. Hyperspectral images are collected using a cooled, 14-bit, monochrome EMCCD camera (Andor DV887) and LCTF (Meadowlark). Additionally high-

## 4.2 System Development

---

resolution area average spectra can be obtained by moving the linear drive mounted LCTF out of the optical path and inserting a custom SMA (Sub Miniature A) fibre coupler into the threaded port. From this the emission can be collected using a choice of the three objectives (2x, 7.5x, or 20x) or the clear aperture using a fibre-coupled spectrometer. A radiometrically calibrated Ocean Optics USB2000+ has been used for the collection of calibration data and a Horiba iHR320 spectrometer for the collection of high resolution data (0.06 nm per channel with a typical resolution of 0.18 nm).

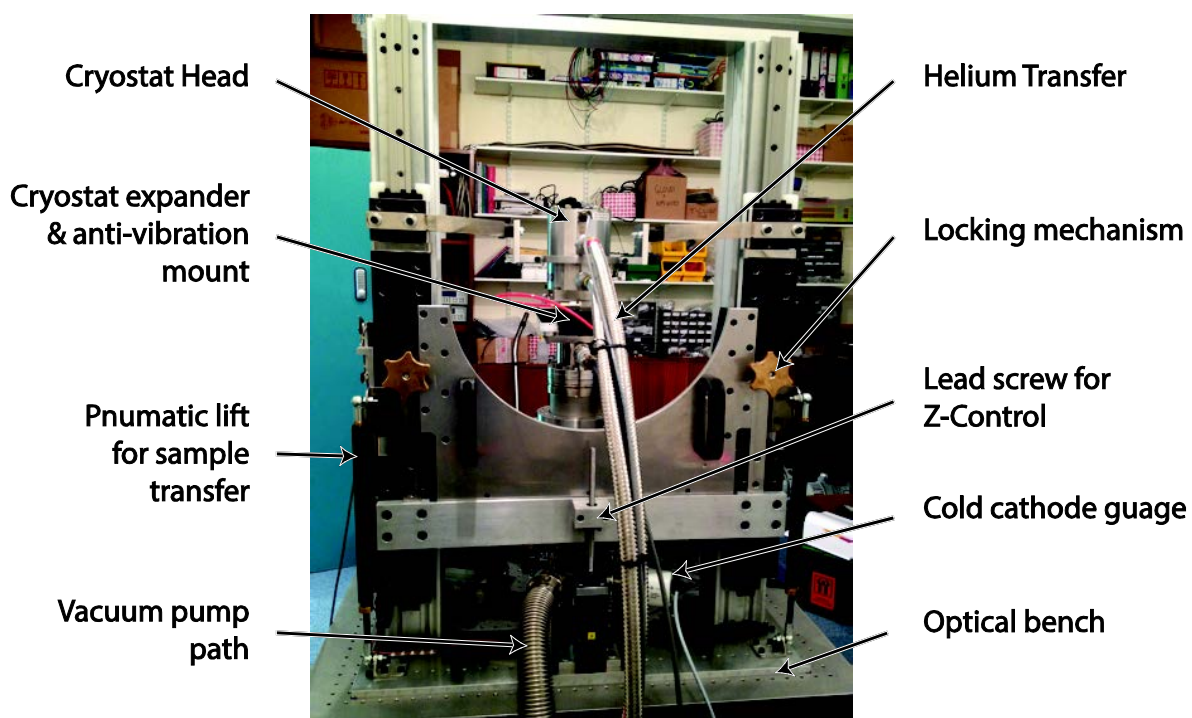


Figure 4-1 Photograph of the rear of HeLIOS showing the pumping path, He lines and stage pneumatics.



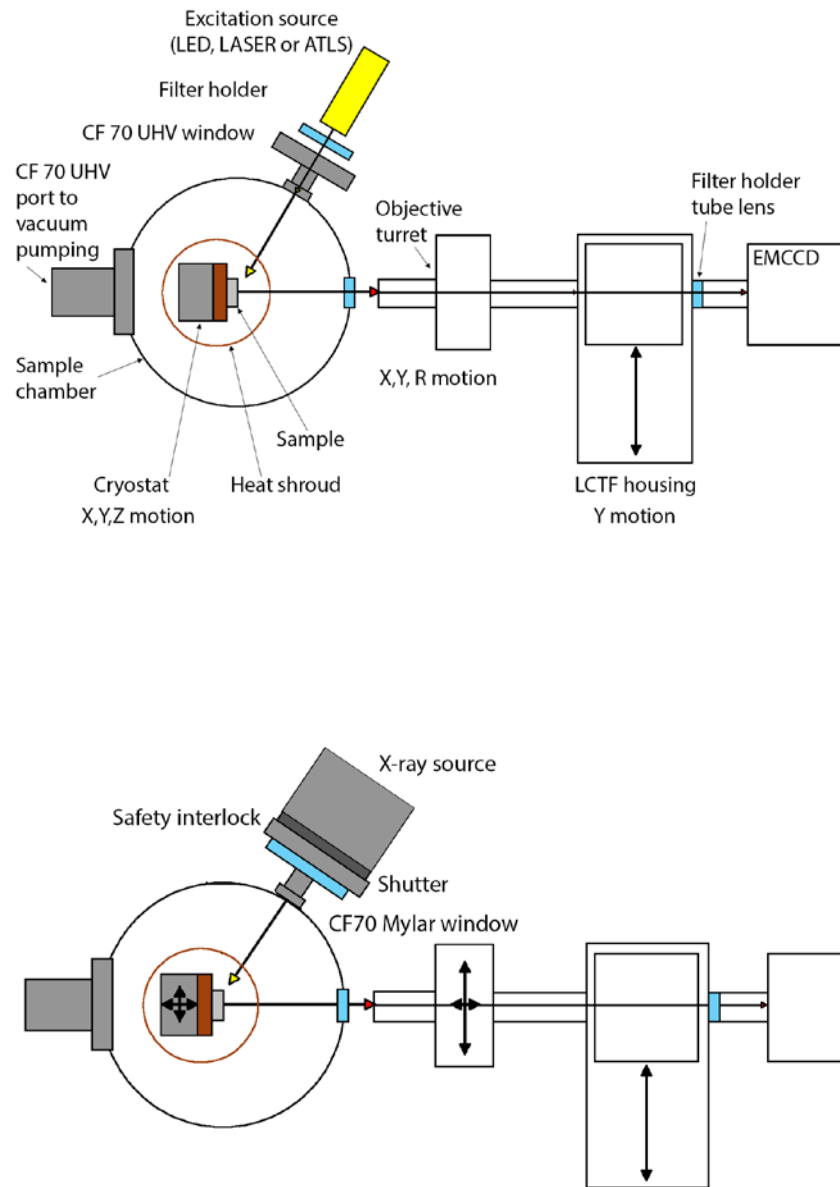


Figure 4-2 HeLIOS PL (top) and XEOL (bottom) hyperspectral experimental configurations.

## 4.2 System Development

---

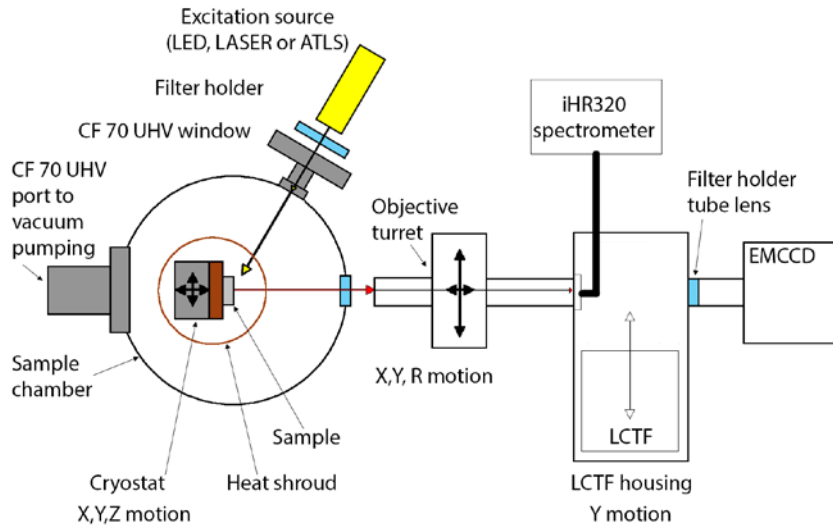


Figure 4-3 HeLIOS High-res PL experimental configuration.

Where the previous CLASSIX instrument<sup>34</sup> utilized a large filter wheel to provide the spectral discrimination, HeLIOS employs a liquid crystal tuneable filter to select the desired wavelength to image. There are advantages and draw backs of this modification. The LCTF has a very low throughput at shorter wavelengths and so image acquisition times must be increased to compensate for the lower light levels reaching the detector. However the ease of wavelength selection and speed of changing between wavelengths outweighs this. To overcome the long integration times, a laser driven light source has also been employed as an illumination source. The high radiance of this source enables sufficient light to be transmitted through the system to the EMCCD to reduce acquisition times to the order of seconds from tens of seconds.

As luminescence emission has a strong temperature dependence samples are cooled via a low vibration closed loop Helium cryostat (Advanced Research Systems) positioned in a small, custom fabricated UHV compatible chamber. The small volume allows rapid evacuation using the pumping system down to high vacuum at which point the cryostat can be initiated for sample cooling and additional pumping. The chamber is evacuated by means of a roughing/backing scroll pump and turbo-molecular pump. This system achieves vacuum better than  $1 \times 10^{-6}$  mbar in under two hours. During sample measurement this pumping system is isolated and shutdown with the vacuum maintained by an ion pump. This has the benefit of reducing system vibration during measurements, which is crucial when working at high magnifications. Chamber pressure is monitored during operation by a Pfeiffer cold-cathode gauge (to which the X-ray source can be interlocked, preventing its operation if the sample chamber is open to atmosphere) and the readout from the ion pump.

To increase thermal coupling, samples are directly mounted onto custom solid copper sample holders Figure 4-5. Sample temperature is controlled using a Lakeshore controller (Lakeshore Cryotronics) linked to two thermocouples in direct contact with the cryostat cold finger. A section of the heat shield around the end of the cold finger has been removed to allow sample imaging. The removal of a section of the heat shield unfortunately prevents the sample reaching its theoretical minimum temperature, however it was necessary in order to provide sample access for excitation and imaging. This configuration allows spectral imaging and conventional spectroscopy of a sample at temperatures ranging from 14K to 350K. A sample heater is located in the cold finger to control the sample temperature within this range. This range marks a significant advance on other liquid nitrogen cooled systems that are limited to 77K. Due to the closed loop nature of the cryostat system it is simple and economical to use with temperatures of 14K achieved within 3 hours of cooling initiation. Figure 4-4 shows an example of the temperature monitoring during Helios operation. In typical operation the

## 4.2 System Development

---

sample is loaded into the chamber and it is evacuated to a vacuum of at most  $1 \times 10^{-4}$  mbar (typically  $1 \times 10^{-7}$  mbar) at which point the cryostat can be safely initialised.

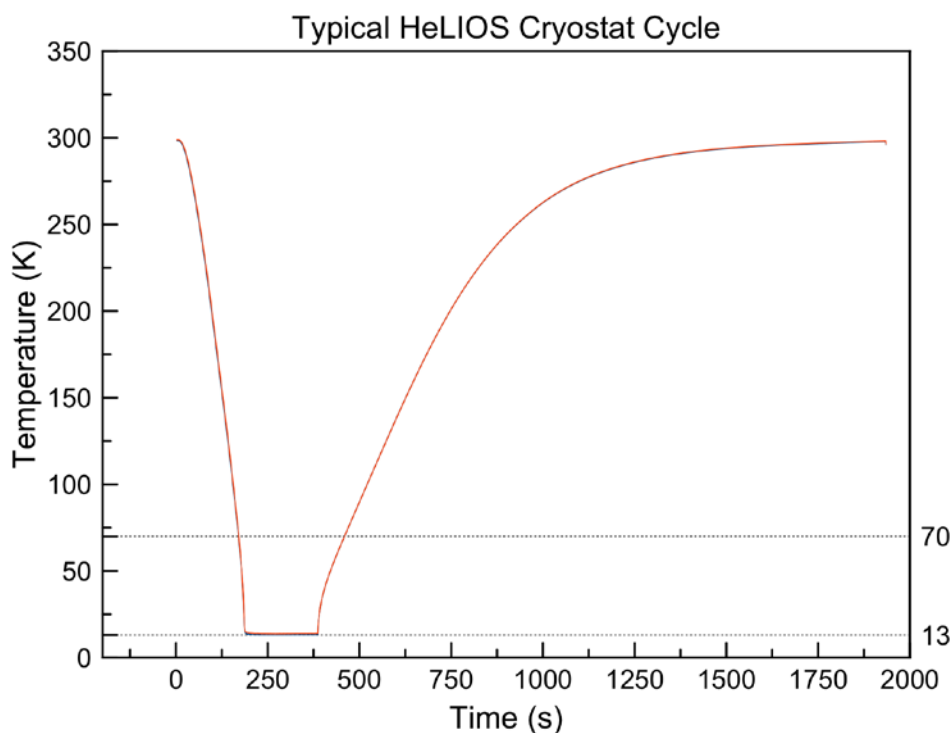


Figure 4-4 Example HeLIOS cooling curve illustrating the time taken to reach measurement temperature.

Figure 4-5 below shows an example HeLIOS sample mount; all are machined from solid copper bar to aid thermal conductivity. The holder pictured has been modified to take a recessed plate to enable a thicker sample (here  $\text{CaCO}_3$ ) to be imaged with the full depth of field of the objectives. Samples are directly mounted onto the mounts using conductive carbon tape, capable of withstanding the low temperatures and vacuum environment.

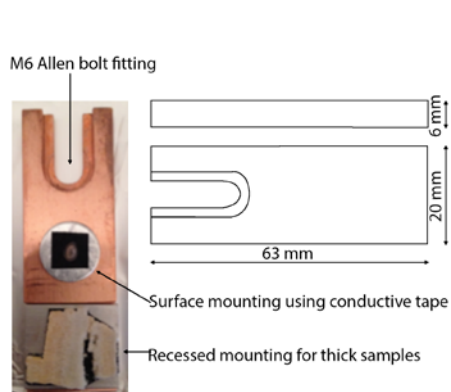


Figure 4-5 HeLIOS copper sample mount, pictured here with milled recess for larger samples.

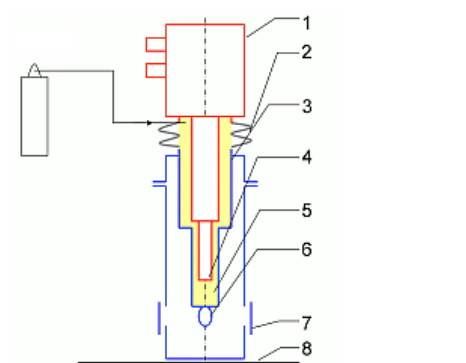


Figure 4-6 Low vibration cryostat helium gas exchange which allows decoupling to reduce vibration, reproduced from <sup>120</sup>.

### HeLIOS

Hyperspectral Luminescence Imaging and Optical Spectroscopy

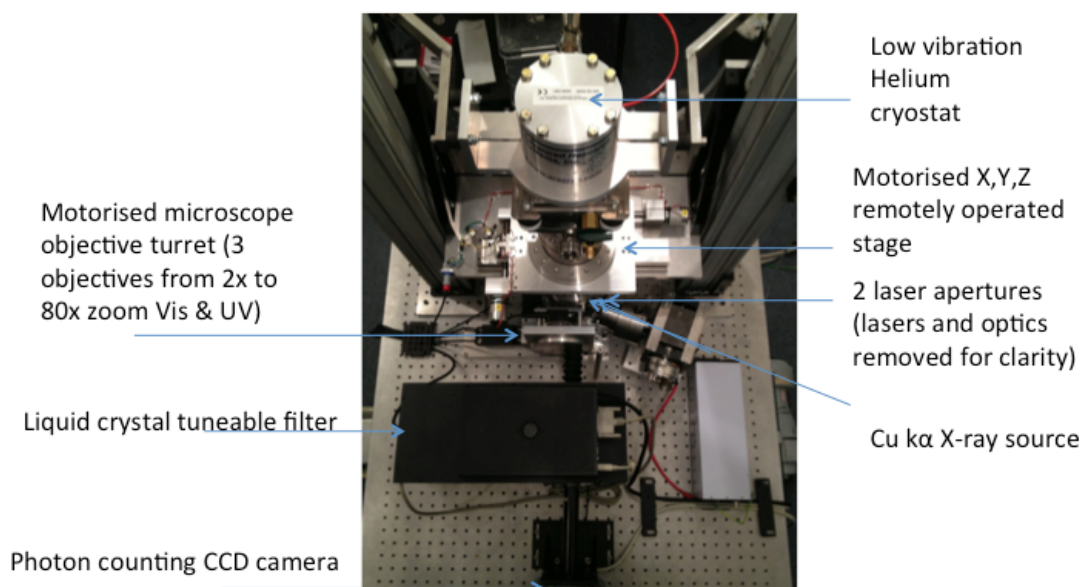


Figure 4-7 HeLIOS chamber from above illustrating the key components and optical path.

## 4.2 System Development

---

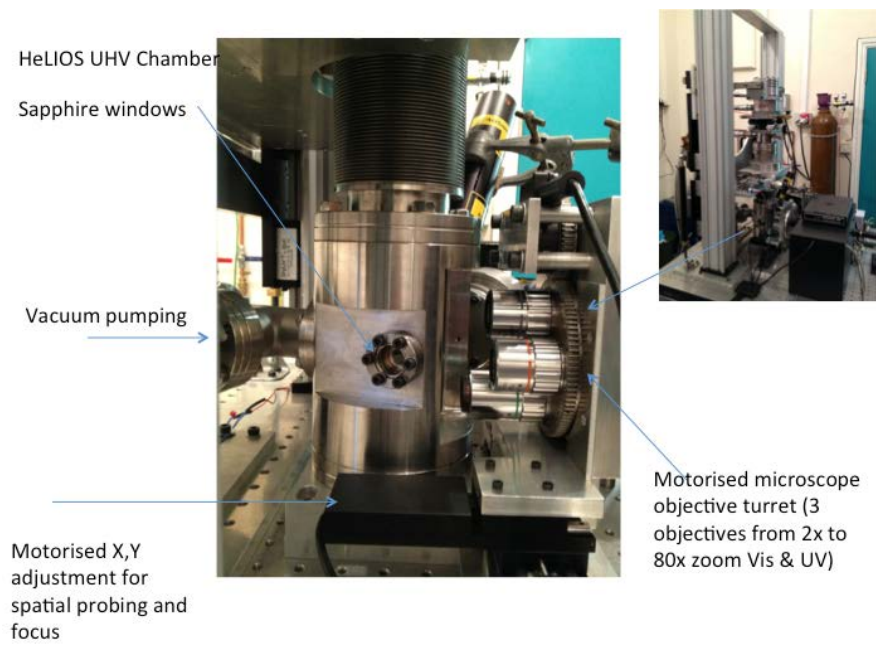


Figure 4-8 HeLIOS close-up photograph. Illustrated are the sample chamber and microscope objective turret.

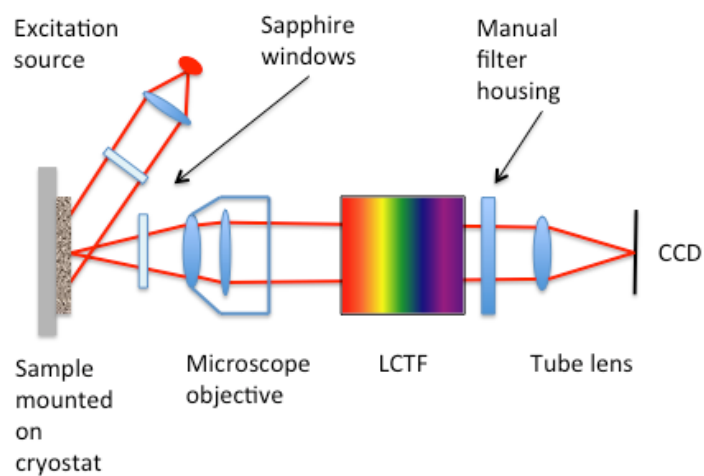


Figure 4-9 HeLIOS optical layout schematic illustrating the optical path from incident excitation, interaction with the sample, and path of the emitted light through the microscope, LCTF, long-pass filter, tube lens, and finally its incidence on the detector.

## 4.2 System Development

| Item                                | Details  |
|-------------------------------------|--|
| <b>Pumping</b>                      | Scroll pump<br>Turbo pump<br>Ion pump<br>Cold cathode gauge  |
| <b>Sample environment</b>           | Stainless steel chamber<br>View ports: sample imaging (20mm) $\varnothing$ sapphire window, (10 mm) $\varnothing$ alignment sapphire window, two angled excitation 10mm $\varnothing$ sapphire windows, 70mm CF window (choices of MgF <sub>2</sub> , Aluminised Mylar and quartz glass) |
| <b>Sample manipulation</b>          | Thorlabs servos for x, y, and z travel.  |
| <b>Optics</b>                       | Mitytoyo infinity corrected microscope objectives: 2x, 7.5x and 20x<br>Selection via Thorlabs rotation stage<br>Mitytoto 1x tube lens<br>SMA mounted lens and fibre to couple to iHR320  |
| <b>Spectral dispersion</b>          | Meadowlark LCTF<br>Driver: FilterDriver 4000<br>Position control: linear stage   |
| <b>Imaging</b>                      | Andor Xion EMCCD   |
| <b>High-resolution spectroscopy</b> | Horiba JY iHR320 Spectrometer  |

Table 4-1 HeLIOS components

As discussed in Chapter 3, hyperspectral applications are predominately concerned with reflectance data owing to the technique's origins in remote sensing. In this research, the detected light is due to the excitation of the sample by some part of the electromagnetic spectrum to induce light emission, most commonly the UV region. Spectral calibration of the camera and liquid crystal tuneable filter allows HeLIOS to obtain spectro-radiometric measurements of a material. In the acquisition of data using CCDs noise can have profound consequences, the effects of temporal and spatial noise on measurements shall be discussed next.



### 4.3 Characterisation and calibration

Radiometrically calibrated data are important if images and spectra from different sources are to be compared. For luminescence measurements users typically do not fully characterise and radiometrically calibrate their instruments, preferring to use manufacturers specifications. This can be for a number of reasons; the user may not need this level of information or may not possess the equipment or knowhow required perform such measurements. It should be noted that there is a difference between data that has been scaled radiometrically and data that has simply been scaled spectrally. By normalising data to their specific experimental arrangement they can work around this, expressing results as arbitrary values. Problems arise when data from different systems need to be directly compared. Although the principle use of HeLIOS is for the characterisation of materials via their luminescence, the instrument has attracted attention from the planetary exploration community, particularly astrobiologists. As a result HeLIOS is proposed as a Mars analogue test environment for the detection of life markers and fluorescent minerals<sup>9,10,12</sup>. In order to make direct comparisons with data received from future mission cross-referencing of analogue to field measurements is required. Presenting data in real, absolute units common to both systems is the most accurate way of achieving this. Such radiometry is applied in many diverse fields where it is important to know the signal in absolute units in order to make comparisons with other instruments or data. Examples include; astrophysics, atmospheric physics, clinical medicine, materials science, vision research and remote sensing. This is especially true for remote-sensing applications, where the user needs to make a link between ground based and airborne (aeroplane or satellite) observations. Such performance, characterisation and evaluation of an instrument require accurate radiometric measurements. In order to obtain such calibrated measurements, laboratory measurements

### 4.3 Characterisation and calibration

---

need to be correlated with specific values to give a relationship between the measured value and an absolute standard.

To put radiometric measurements into context and appreciate the need for them, the process of generation, transmission and detection need to be considered.

As discussed in the previous chapter, a perfect luminescence spectrometer is unachievable - such an instrument would have to incorporate; a light source which yields a constant photon output at all wavelengths, a monochromator which can pass photons of all wavelengths with equal efficiency and independent of polarisation, and a detector which can detect photons of all wavelengths with equal efficiency.

Beyer wrote in his 1992 paper <sup>122</sup>; *“Calibration of solid-state cameras is a prerequisite for the extraction of precise three-dimensional information from imagery in computer vision, robotics and other areas.”* Lack of precise specifications of the geometric properties and deviation from an ideal system make calibrations essential. Precision describes the statistical variability of the parameters estimated in the least squares adjustment, whereas accuracy determines how close the estimated parameters match the true values.

When detecting a signal optically, many things need to be considered. The optical path passes through a number of components and is affected by a number of experimental parameters. By characterising and calibrating HeLIOS, these variables can be accounted for and corrected to produce a measurement expressed in absolute units rather than arbitrary values. The ability to detect and quantify changes depends on the use of sensors that can provide calibrated and consistent measurements of desired features. In order to record high quality science data, which can then be used in further applications downstream, radiometric characterisation and calibration should be considered as a pre-requisite <sup>123</sup>. Converting data into physically meaningful and common radiometric units is necessary in applications where there is, or may be in the future, a need to compare to another instrument’s readings.

In this chapter a protocol for CCD calibration and the radiometric calibration for low-uncertainty measurements of the HeLIOS system is presented. This chapter provides an introduction to noise characteristics in CCD imaging systems and the processes involved in characterising and correcting for these parameters. A description of the experimental protocol and equipment used are presented alongside an analysis into the identified sources of uncertainty. Here it is shown that through rigorous calibration the related uncertainty in the irradiance can be computed when the CCD temperature is maintained at a constant (-65°C) and the field of view is constrained by the use of one of three characterised microscope objectives (2x, 7.5x and 20x). This protocol can then be applied in the future to additional experimental configurations, such as higher magnification objects and a higher number of wavelengths for example.

### **4.3.1 Instrumentation**

Prior to discussing the characterisation and calibration of HeLIOS, a brief introduction to the instrumentation used for the process is given. In this section the equipment essential for characterisation and calibration are introduced and discussed.

#### **4.3.1.1 Integrating spheres**

The integrating sphere is an invaluable piece of radiometry apparatus. Its primary function is to spatially integrate radiant flux, but has found many applications including use as a uniform light source, in uniform detection systems, transmission measurements, reflectance measurements, depolarization, acting as a cosine receiver, light source mixing and colour mixing. Integrating sphere theory originates from the theory of radiation exchange within an enclosure of diffuse surfaces. Jacquez *et al*<sup>124</sup> provides a sound understanding and discussion of the theory of integrating spheres and there is a large body of work dedicated to their design

### 4.3 Characterisation and calibration

---

and use. The integrating sphere was invented by British scientist W.E. Sumpner in 1892<sup>125</sup> and fully described by the German scientist R. Ulbricht some years later giving rise to the term 'Ulbricht sphere' being used.

An integrating sphere has been used in this work to provide a uniform light source for a number of characterisations including responsivity, linearity, photo-response non-uniformity, flat field and radiometric calibration. Figure 4-10 depicts the sphere geometry used in this work. The light incident into the sphere from a lamp creates a virtual light source by reflection on the highly diffuse surface. This light, which is used for characterisation and calibration, is the radiance of the sphere, expressed as the flux density per unit solid angle.

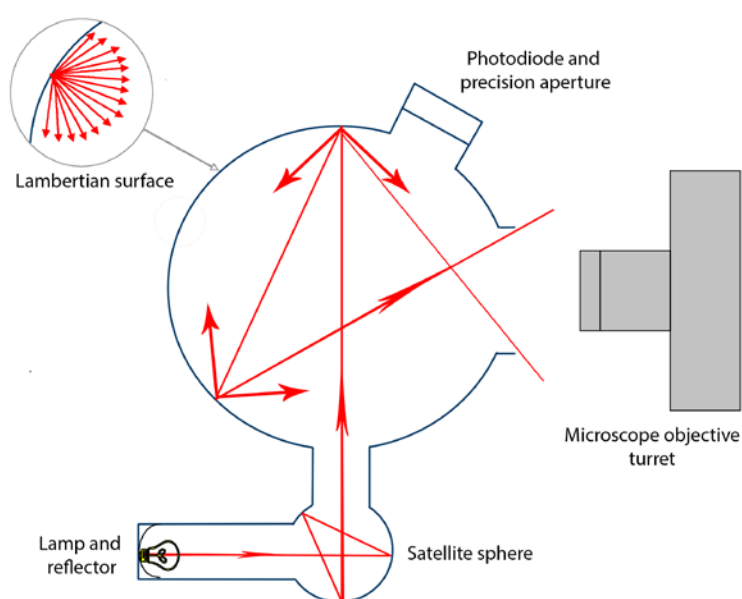


Figure 4-10 - Integrating sphere geometry. Light arrives to the main sphere via a small satellite sphere, on arrival at the sphere's internal surface this acts as a highly Lambertian surface efficiently scattering the light to provide a uniform light source for calibration.

The selection of a sphere's coating, or the material it is machined from, can make a significant difference to the radiance produced for a given sphere design. The sphere used in this work is made from Spectralon® which is an extremely Lambertian surface with over 99% diffuse reflectance. The material is chemically inert and thermally stable. Its porous surface produces multiple reflections in the first few tenths of a millimetre<sup>126</sup>. Spectralon® is most suited to use in the UV-VIS-NIR range, hence most appropriate for the measurements undertaken with HeLIOS. Spectralon® is considered superior to barium sulphate based materials as it is hydrophobic, preventing water absorption from its surroundings which could lead to water overtone bands in the NIR.

### 4.3 Characterisation and calibration

---

A Labsphere<sup>127</sup> general-purpose sphere with bespoke accessories has been used to provide a uniform light source for HeLIOS calibration measurements. This sphere is a 5.3" internal diameter Spectralon® integrating sphere with four ports (three used in these measurements) to enable a range of configurations. The ports are located as follows; single 2.5" diameter port at 0°, two 1" diameter ports at 90° and 180° on the sphere's equator and a single 1" diameter at the pole position. A Spectralon® baffle is located between the 0° and 90° ports on the equator to prevent light passing directly between these two ports. A single Labsphere 100 W tungsten halogen lamp, powered by stable Labsphere power supply illuminates the internal surface of the sphere. The lamp is coupled into the sphere via a small 2" diameter custom-made barium sulphate coated satellite sphere<sup>128</sup> mounted onto the 90° port. Where ports are not in use, Spectralon® plugs are inserted to maintain the surface reflectance.

Figure 4-11 and Figure 4-12 below show the experimental configuration for HeLIOS calibration. The HeLIOS sample chamber was removed to provide access for a Spectralon® integrating sphere to be positioned directly in front of the HeLIOS microscope objective turret to provide a uniform light source for calibrations. Light is delivered into the Spectralon® sphere from a tungsten halogen bulb coupled by a small satellite integrating sphere. This provides the most uniform source possible as the light has been scattered by two Lambertian surfaces prior to arriving at the instrument for imaging. Taking into consideration the working distances of objective the sphere was adjusted to ensure the acquired images were not focused onto the back of the sphere, as this would have introduced errors into the flat field corrections. As all optical components of HeLIOS are secured to the optical bench, it was assured that the calibration conditions reflected accurately the measurement conditions. For calibration data collection the lamp was powered for a minimum of 1 hour prior to acquisitions to allow it to stabilise.

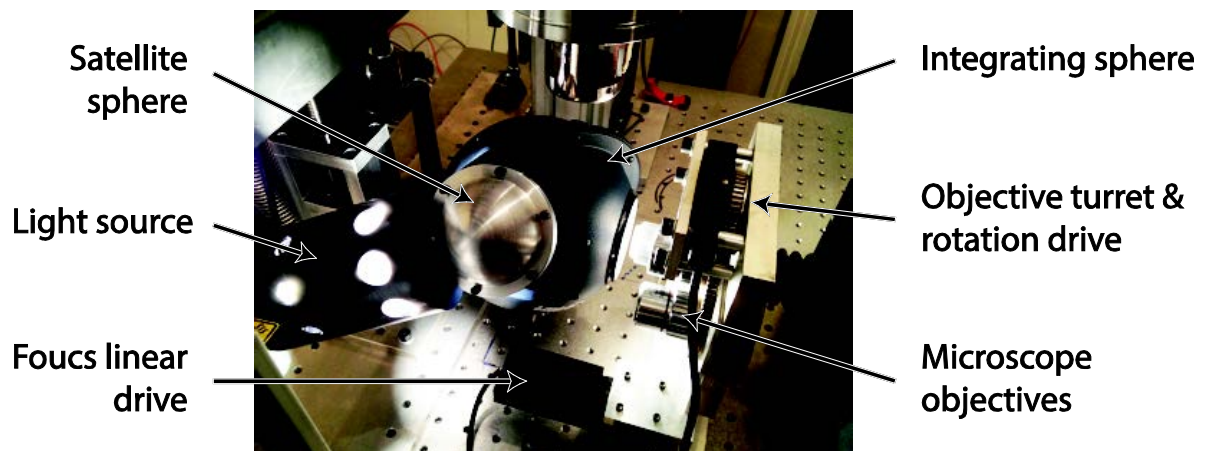


Figure 4-11 HeLIOS calibration configuration, the sample chamber is replaced with an integrating sphere. The light source can be seen on the left entering the main sphere via a smaller satellite sphere. The focus stage allows movement of the objectives to prevent focusing on the back surface of the sphere.

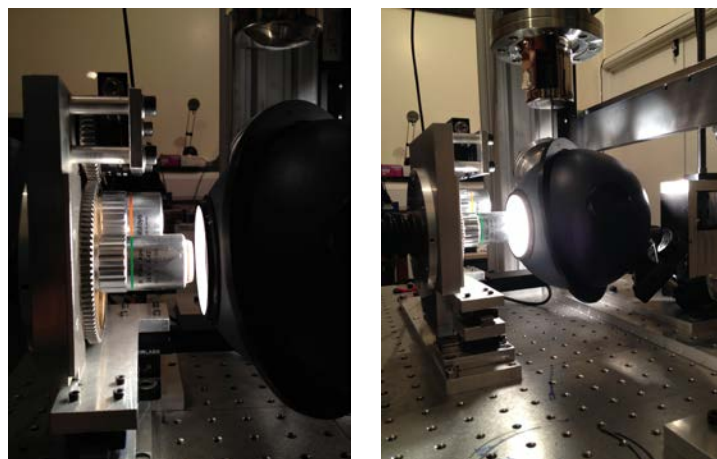


Figure 4-12 Alternate views of the HeLIOS calibration configuration showing the microscope turret directed in the sphere.

### 4.3.1.2 Cosine corrector

When measuring the absolute irradiance values to transfer the calibration from the NIST lamp to the USB 2000+ spectrometer to HeLIOS it is necessary to use a cosine corrector. The use of a cosine corrector minimises issues due to sampling geometry encountered that can arise when using a bare fibre. This is a step very often overlooked by investigators. The cosine corrector used was a CC-3-UV-S from Ocean Optics <sup>129</sup>, illustrated in Figure 4-13. The device comprises of a Spectralon® diffusing disk mounted in a SMA coupler, optimised for the 200-1100nm range. This is used for coupling to a SMA terminated fibre attached to a spectrometer to collect signal from 180° field of view to measure spectral irradiance of a plane surface.

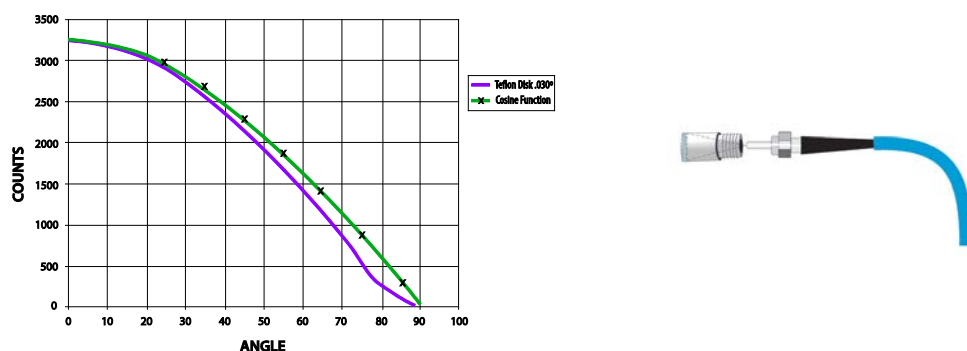


Figure 4-13 Cosine corrector response with angle (left) and illustration (right), images reproduced from Ocean Optics website <sup>130</sup>.

### 4.3.1.3 NIST traceable calibrated light source

As discussed earlier, in order to fully calibrate a system one must be able to trace that calibration back to an accepted national standard. For this work a NIST (National Institute of



Standards and Technology) traceable calibrated light source has been used from which to trace all measurements performed with HeLIOS back to. The source is a LS-I-CAL calibrated light source from Ocean Optics. It comprises of a tungsten halogen bulb housed in a unit that can accept a SMA terminated bare fibre or cosine corrector. The lamp itself has been calibrated by the manufacturer to provide traceability to NIST standards and is then used to calibrate the absolute spectral response of a system. It has a bulb life of 900 hours, however as previously discussed, due to the high temperature and spectral drift, the calibration is only valid for 50 hours before it must be recalibrated. This source is effective for calibrating the absolute spectral response of a system from 350-1050 nm. The lamp can be used for absolute spectral intensity measurements of a sample and measurements of its absolute irradiance and emissive colour. The calibration traceability works by providing a known absolute irradiance value at a number of wavelengths in  $\mu\text{Wcm}^{-2}\text{nm}^{-1}$ .

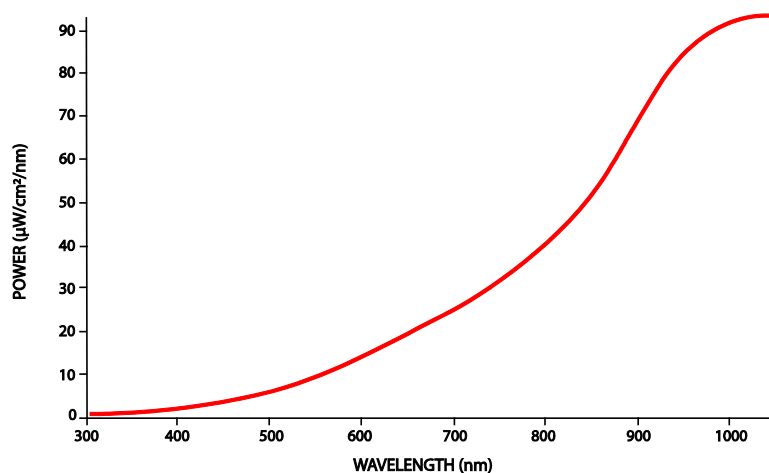


Figure 4-14 Irradiance measurement of the NIST calibrated light source used to transfer the calibration to HeLIOS.

### **4.3.1.4 Reference spectrometer**

The calibration from the NIST light source has been transferred to an independent spectrometer in order to make the necessary measurements of the integrating sphere whilst illuminated at different light levels to provide the radiometric calibration.

An Ocean Optics USB2000+ spectrometer was used for measuring the irradiance of the integrating sphere. The USB 2000+ is a miniature fibre optic f/4 crossed Czerny-Turner spectrometer comprising of a linear Si CCD array with 2048 pixels for measurements in the 350-1000nm range <sup>131</sup>.

### **4.3.2 Nomenclature of Characterisation and Calibration**

This section aims to clarify those terms that are of most importance to the task of characterisation and calibration of a spectral imager. Table 4-2 summarises key terminology of radiometric calibration.

| Term                                      | Definition   | Units                                 |
|---|--|---------------------------------------|
| <b>Radiometry</b>                         | The measurement of electromagnetic radiant energy over the optical spectrum (1nm-1000µm)                   |                                       |
| <b>Spectroradiometry</b>                  | The measurement of the spectral content of the radiating source.   |                                       |
| <b>Radiant energy</b>                     | The total energy emitted from a radiating source   | J                                     |
| <b>Radiant energy density</b>             | The radiant energy per unit volume.  | Jm <sup>-3</sup>                      |
| <b>Radiant power (flux)</b>               | The radiant energy per unit time   | Js <sup>-1</sup> or W                 |
| <b>Radiant exitance or Emittance, M</b>   | The total radiant flux emitted by a source / surface area of the source                                    | Wm <sup>-2</sup>                      |
| <b>Radiant incidence or Irradiance, E</b> | The total radiant flux emitted by a source divided by the surface area of the source                       | Wm <sup>-2</sup>                      |
| <b>Radiant intensity</b>                  | The total radiant flux emitted by a point source per unit solid angle in a given direction                 | Wsr <sup>-1</sup>                     |
| <b>Radiance, L</b>                        | The radiant intensity of a source % area of the source   | Wsr <sup>-1</sup> m <sup>-2</sup>     |
| <b>Luminance</b>                          | The power per unit area and unit solid angle, weighted by the spectral response of the human eye           | (lm) m <sup>-2</sup> sr <sup>-1</sup> |
| <b>Fluence, or scalar irradiance</b>      | Flux per unit area landing on a spherical detector at a given point, omitting the cosine component         | Wm <sup>-2</sup>                      |
| <b>Illuminance</b>                        | The power per unit area, weighted by the spectral response of the human eye                                | (lm) m <sup>-2</sup>                  |
| <b>Emissivity</b>                         | The ratio of the radiant flux density of a source to that of a blackbody radiator at the same temperature. |                                       |

Table 4-2 Key radiometry terms, definitions and units

Radiometry is the measurement of optical radiant energy. When the full optical radiation spectrum is considered, it extends far further than the human eye can detect. The visible portion is a rather small window spanning from 380 nm to 760 nm. Special designation is given to measurements in this region where the response of the human eye is involved – *photometric*. When considering optical radiation as a whole this extends from 1 nm to 100 µm, disregarding micro- and radio waves, which are not discussed in this work. Spectroradiometry is used to determine the intensity of the radiation from a source as a

### 4.3 Characterisation and calibration

---

function of its wavelength – its spectral power distribution. Here two key measurements, the radiance from the source and the irradiance at a surface, are of concern. In this work the radiance from a calibrated NIST lamp has been used to calibrate the irradiance at the detector.

Radiance,  $L$ , is a fundamental measurement in radiometry, defined as the power per unit area per unit projected solid angle or power per unit foreshortened area emitted into a solid angle by a surface. In the context of this work, radiance is associated with the active source of luminescence, rather than the passive reflective source often seen in hyperspectral imaging. An example of radiance is how a pixel collects light arriving at the lens from some solid angle. The aperture of the camera defines a small area. The pixel value is an estimate of flux per unit solid angle (in the pixel's ray direction) per unit area (at the aperture's position). Where surfaces are not perpendicular to the solid angle,  $\omega$ , the cosine factor needs to be included to measure radiance. The Lambertian approximation is used to describe the angular distribution of radiation from a source.

Radiant exitance, or emittance,  $M$ , is radiation that exits a source, it is the term for light leaving a surface. For example here the integrating sphere is used as a source of uniform light for calibrations, it has a radiant exitance. It is defined as power,  $\Phi$ , per unit area radiated into a hemisphere, expressed in  $\text{Wm}^{-2}$ , where in Equation 4-1  $A_s$  refers to the area of the source.

$$M = \lim_{\Delta A_s \rightarrow 0} \left( \frac{\Delta \Phi}{\Delta A_s} \right) = \frac{\partial \Phi}{\partial A_s} \quad \text{Equation 4-1}$$

Radiant exitance and irradiance are often confused. Irradiance, sometimes referred to as spectral radiant incidence,  $E$ , is the power per unit area incident on a surface, it is the term for light arriving at a surface. The surface area is the effective aperture, image area, area of the CCD or the area of a pixel. For example the irradiance incident on the cosine corrector

coupled to the USB2000 is measured in order to calibrate the HeLIOS system. As with radiant exitance, its units are  $\text{Wm}^{-2}$ . Where in Equation 4-2  $A_s$  refers to the area of the surface.

$$E = \lim_{\Delta A_s \rightarrow 0} \left( \frac{\Delta \Phi}{\Delta A_s} \right) = \frac{\partial \Phi}{\partial A_s} \quad \text{Equation 4-2}$$

Irradiance is a surface-orientated property. Taking a point  $x$  in a volume, specifying a surface normal  $n$  and giving irradiance as  $e(x,n)$  as the irradiance landing on a small surface element facing the direction of  $n$ . It is this which is expressed when measuring the light arriving at the flat surface of the cosine corrector passing into the USB200+ spectrometer. In HeLIOS, after passing through the lens of the system, in this case the microscope objectives, the power of the radiant energy falling on the image plane is called irradiance. This irradiance is then transformed into image brightness by the detector elements. Each point records a signal that is related to the density of photons landing near that point, but this value is invariant of the direction the light comes from. Fluence, or scalar irradiance, this is the flux per unit area landing on a spherical detector at a given point. An example of flux is a photodiode, it collects all the photons landing on it and is sensitive to angle.

#### 4.3.2.1 Calibrations

An absolute radiometric calibration is performed by relating the digital counts output from the CCD's sensor, in the linear region, to the value of an accurately known uniform radiance field at the entrance of the instrument. In contrast a relative calibration is where the output of a detector is normalised to a given average output. For example, a pixel is treated as a single detector and the entire array is normalised so that all the pixels output the same value when the detector is irradiated with a uniform radiance field. Here it is not necessary for the absolute radiance field to be known. This is also referred to in literature as interband

### 4.3 Characterisation and calibration

---

calibration as this method can be used to ratio the average outputs from several different bands of a sensor <sup>132</sup>. Relative calibration is used in applications such as scene classification where the user wishes to remove striping, in this case absolute calibration is not needed and to go to such lengths would be unnecessary.

Radiometric calibration has been chosen for this work, as it is desirable to express the detected luminescence in absolute units to enable comparisons between different instruments of the same samples in the future. This work is of vital importance when building a spectral database of analogue materials for comparison with science data acquired on future planetary exploration missions. Providing the instrument to be compared with has also received a radiometric calibration, the data should be directly comparable, removing (or quantifying) the artefacts and uncertainties created in its acquisition. When performing calibrations it is imperative to maintain consistency between the geometry, spectral radiance distribution and levels used in calibration with those used in the acquisition of science target images. This is to minimise differences between calibration/experiment measurement and use due to stray light, detector non-linearity etc. To allow for the widest range of science data acquisition it is important that calibrations are performed using full aperture, full field and over the full dynamic range of the sensor, with the sensor characterised as far as possible in the configuration it is to be used. Limits for the validity of the calibration should be made clear when expressing results in absolute units. Here HeLIOS has been calibrated in a number of configurations (objectives, integration times, EM gains and pre-amplifier gains), should this change, for example if the camera is moved, even slightly, or a different microscope objective or tube lens is introduced, a new calibration will be required. For this reason all components in HeLIOS are fixed as far as possible to the optical bench.

In the process of calibration or characterisation of an instrument consideration must be given to the sources of uncertainty in the measurement prior to conversion from raw digital

numbers (DN) to electrons to an expression of the absolute irradiance. The next section discussed noise sources in irradiance measurements using a CCD detector.

### 4.3.3 Noise

Measurements of irradiance by imaging detectors cannot be assumed noise free due to physical variations across the detector arising from manufacturing defects, the electronic behaviour during operation and the operating regime imposed by the user. Noise is an active research field in its own right, in this work efforts have been made to develop and perform a robust characterisation of the noise components present in the HeLIOS system. These procedures will become refined further over time through more use of the instrument and the development of future characterisation methods. Through thorough characterisation, the different elements of noise present can be removed or accounted for via a combination of image processing and thought out image acquisition.

Noise itself can be classified into two types: spatial and temporal. Photo response non-uniformity, dark current non-uniformities are examples of spatial noise. There are a number of methods which can be used to remove spatial noise from the system <sup>133</sup>, radiometric calibration has been used to minimise spatial noise in this work as it provides the most comprehensive method. Shot noise, output amplifier noise and dark current shot noise are examples of temporal noise. Temporal noise can be minimised by frame averaging to a degree, however corrections such as dark frame subtraction are more effective. Averaging has been showed to have a limited effect, in Figure 4-15 below López-Álvarez et al <sup>134</sup> show in their calibration investigations that noise is barely reduced when more than 100 images are averaged. For this work longer integration times of 10 s have been used owing to the low light levels. As seen in the figure below the longer integration times give rise to a higher noise, however the level plateaus quickly. This was repeated for the HeLIOS detector and similar

### 4.3 Characterisation and calibration

---

observations were made when plotting the noise against the integration time, illustrated in Figure 4-15.

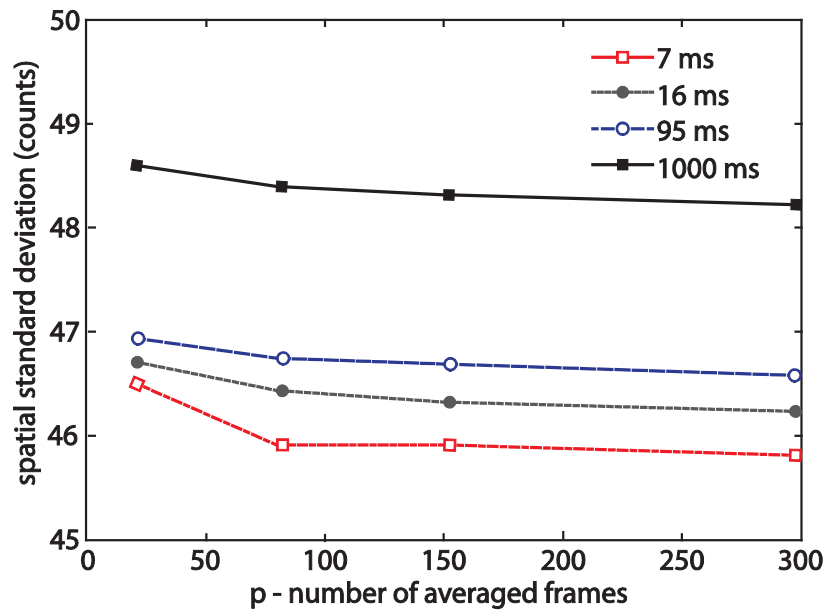


Figure 4-15 Effect of image averaging on spatial noise, reproduced from <sup>134</sup>, indicating for this sample the spatial standard deviation plateaus.

#### 4.3.3.1 Shot noise

Shot noise does not originate from the detector. It is a fundamental limit, a result of the quantum nature of light, inherent to the random arrival of a photon at the CCD and so cannot be experimentally eliminated. It is directly related to the input illumination; being proportional to the square root of that signal and it grows proportionally to  $Q^{1/2}$ ,  $Q$  being the total charge collected in pixel <sup>134</sup>. It is used to characterise the uncertainty in the number of electrons stored at a collection site as this follows a Poisson distribution; its variance equals



its mean. As it cannot be eliminated it determines the maximum signal to noise ratio for a noise free sensor.

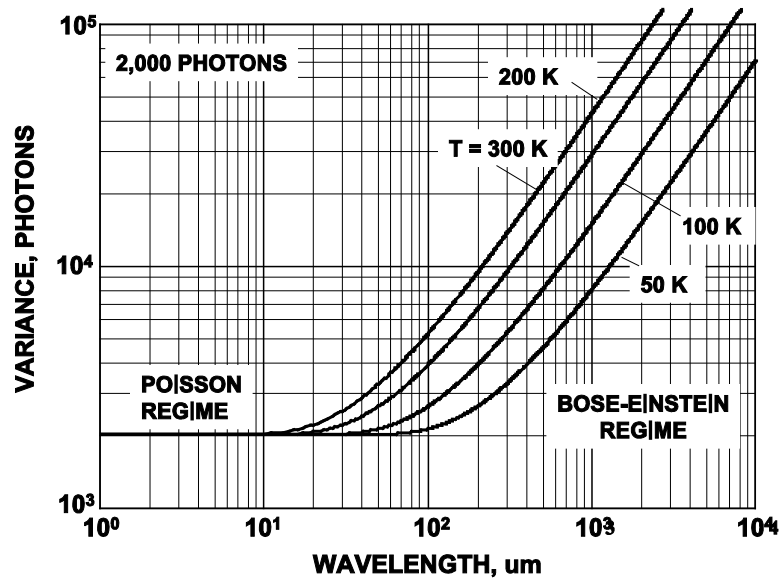


Figure 4-16 Illustration of photon shot noise variance as a function of wavelength, reproduced from 136. Moving into the infrared and longer wavelengths the photon behaviour departs from the Poisson regime.

Figure 4-16 illustrates the variance against wavelength at different temperatures. From this it can be seen that HeLIOS' detection range falls into the Poisson regime. As the time between photon arrivals is governed by Poisson statistics the uncertainty in the number of photons collected during a given period of time is given by the relationship:

$$\sigma_{shot} = \sqrt{S} \quad \text{Equation 4-3}$$

Where  $\sigma_{shot}$  is the shot noise and  $S$  is the signal, both are expressed in electrons. Shot noise is identified in photon transfer curves (PTCs) at the regime having a gradient of  $\frac{1}{2}$ . By taking a

### 4.3 Characterisation and calibration

---

number of images under the same conditions and averaging them, shot noise can be reduced and the signal to noise (S/N) improved.

Just as photon shot noise cannot simply be subtracted out nor can the dark current shot noise. The dark current shot noise is equal to the square root of the dark signal:

$$\sigma_{dark} = \sqrt{D} \quad \text{Equation 4-4}$$

Shot noise and thermal noise are linked, as the dark current stored at a collection site will increase the mean and therefore the variance in the number of electrons. A relationship between the shot noise and dark current is given by:

$$KI + N_{DC} + N_S \quad \text{Equation 4-5}$$

Where  $N_{DC}$  is the number of electrons due to dark current and  $N_S$  is the zero mean Poisson shot noise with a variance which depends on the number of collected photoelectrons ( $KI$ ) and the number of dark electrons ( $N_{DC}$ ).

#### 4.3.3.2 Dark noise

Dark noise, or thermal noise, refers to the number of electrons generated thermally as the stored electrons move along the CCD and associated electronics within the device. As with many other noise forms, this value is proportional to temperature and integration time. It is a result of imperfections or impurities in the depleted bulk silicon or at the silicon dioxide interface of the detector. These sites introduce electronics states in the forbidden gap which act as steps between the valence and conduction bands, providing a path for valence electrons to move into the conduction band, and in doing so add to the signal measured by the individual pixel. Variations in signal can also be caused by potential bumps in barrier

phases preferentially directing charge to different pixels. Electrons use thermal energy to move to an intermediate state from where they can be excited into the conduction band however thermal energy in the silicon detector also generates free electrons, which can subsequently be stored at collection sites and therefore become indistinguishable from photoelectrons. This thermal energy adds a constant offset and a small Gaussian noise contribution to the measured signal, dependent on the integration time and gain. Regardless of the quality of the CCD, a background charge is present which is independent of the illumination level. It is this dark current which limits low light applications such as single photon counting<sup>135</sup>. The predicted number of dark electrons generated is proportional to the integration time and is highly temperature dependent. By acquiring many identical exposures at constant temperature under the same experimental acquisition parameters this component can be treated as an offset and subtracted from subsequent data. Dark noise is intrinsically linked with two other types of noise, dark current non-uniformity and dark current shot noise. The random component of the dark signal depends on the mean level of dark current (temperature and integration time) it can be expressed as the RMS noise:

$$\sigma = \sqrt{N_t} \quad \text{Equation 4-6}$$

As dark current is a thermal process the most effective way to reduce it is to cool the CCD. Andor states that cooling the detector below 0°C on fast exposures (less than a few seconds) will generally remove most of the shot noise caused by dark signal. For this reason, a Peltier cooled EMCCD has been used in this work, held consistently at -65°C with a variation better than 1°C. The relationship between the bulk dark current and temperature is given Equation 4-7, where  $D$  is the dark current (e/pixel/s),  $A$  is the pixel area (cm<sup>2</sup>),  $I_d$  is the dark current measured at 300K (nA/cm<sup>2</sup>),  $E_g$  is the band gap at temperature  $T$  (K). The band gap of silicon varies with temperature and is given by Equation 4-8 and is tied into integration time using Equation 4-9, where  $V_g$  is the gap voltage and  $A$  is a constant.

$$D = 2.5 \times 10^{15} A I_d T^{1.5} e^{-\frac{E_g}{2kT}} \quad \text{Equation 4-7}$$

$$E_g = 1.1557 - \frac{(7.021 \times 10^4) T^2}{1108 + T} \quad \text{Equation 4-8}$$

$$S = A T^{\frac{3}{2}} e^{-V_g q(2kT)} \quad \text{Equation 4-9}$$

To account for the variety of permutations needed when acquiring an image a simple dark correction protocol has been written in MathCAD. The processing pipeline is illustrated as a flow diagram in Figure 4-17. This process to generate a set of master dark images for use throughout the processing chain took the following steps. A series of images were acquired with the CCD held at a constant -65°C and the shutter to the sensor closed at combinations of pre-amplifier gains, electron-multiplier gains and integration times selected to best represent the needs of image acquisition of the samples to be studied in this work. Data were acquired for two pre-amplifier settings (1x and 2.4x), five EM gains (0, 50, 100, 150 and 200) and eight integration times (0.1, 1, 5, 10, 20, 30, 60 and 120 seconds). For each permutation five images were acquired. These five images were then read into the MathCAD script “Master Dark” for processing. In this script the images are compared and the minimum pixel value for each pixel are taken to form a “Master Dark” image. By taking the minimum pixel value of the five this prevents a negative number arising when the master dark is subtracted from data further in the processing chain. This also has the effect of eliminating dark fixed pattern noise. This master dark image is then exported as a comma separated variable (.csv) file for later use. The image is also exported as a bitmap (.bmp) file for visual inspection, examples of which are shown below in Figure 4-22. The script then goes on to perform statistical analysis on the data. The average pixel value and the standard deviation of the master dark are calculated. To investigate for spatial anomalies and highlight hot or dark pixels, further images are

generated to display those pixels above and below the mean and RGB images are generated to reflect a pixel's deviation from the mean by a user-defined number of standard deviation. Finally an image of the read noise is generated from the standard deviation of the data.

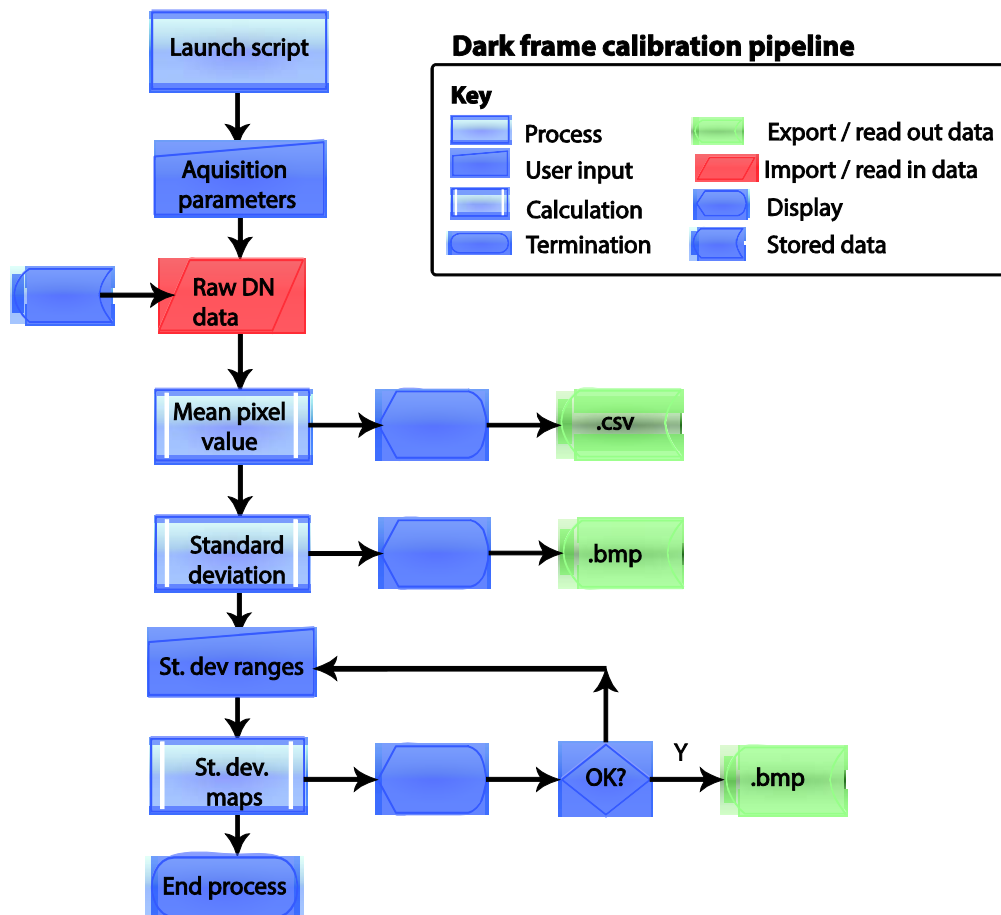


Figure 4-17 Dark frame calibration image generation pipeline.

### 4.3 Characterisation and calibration

---

Through the outputs from the dark image processing pipeline the camera's dark frame response to integration time and the application of gain can be explained. A series of image are displayed below which are typical of those generated.

Figure 4-18 shows the relationship between the average dark signal (average of all pixels in image in DN) and integration time using different camera gain settings. As expected the signal intensity increases with gain application and the dark signal noise (the standard deviation) also increases. When using the pre-amplification of 2.4x (using the shorthand of PA2.4 in figures) and EM gain of 200 (using shorthand of EM200 in figures) the noise (the standard deviation) is seen to increase and then plateau. This plateau region between 5 and 10 seconds has been chosen as the integration time for data acquisition due to its consistency.

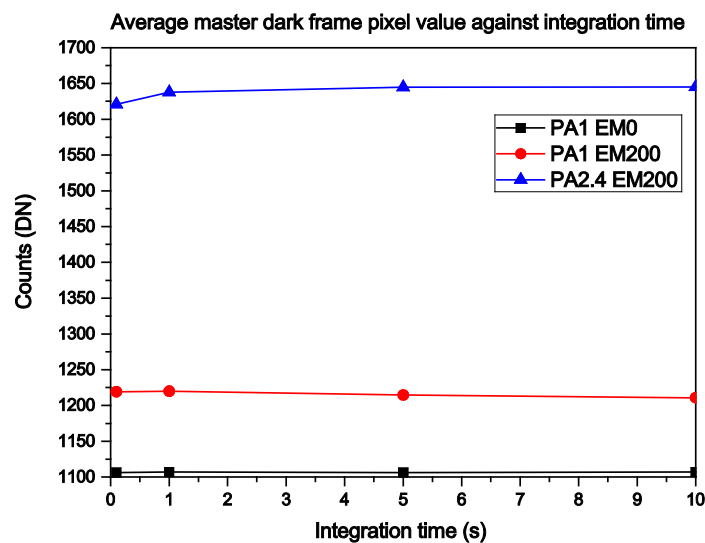


Figure 4-18 Plot of the average pixel value of selected master dark frames against integration time of acquisition.

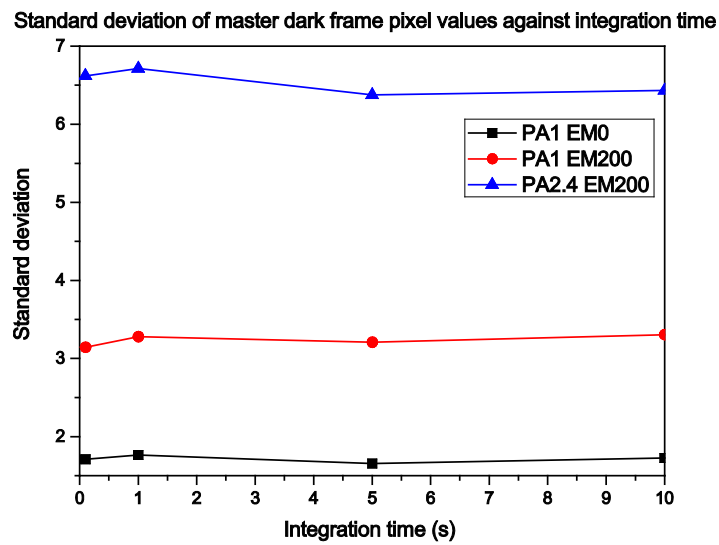


Figure 4-19 Plot of the standard deviation of the master dark frames against integration time. It can be seen that with the increased pre-amplification and electron multiplication levels there is a far lower standard deviation compared to the un-amplified signal.

Figure 4-20 and Figure 4-21 illustrate a line plot taken across the centre of the pixel array, corresponding to pixel row 256. Here some variation in the signal is seen, however this is proportional to the applied gain. Figure 4-23 to Figure 4-27 show the variation in the dark images by viewing the signal as a function of pixel position in the x and y direction (pixel row 256 and pixel column 256).

### 4.3 Characterisation and calibration

---

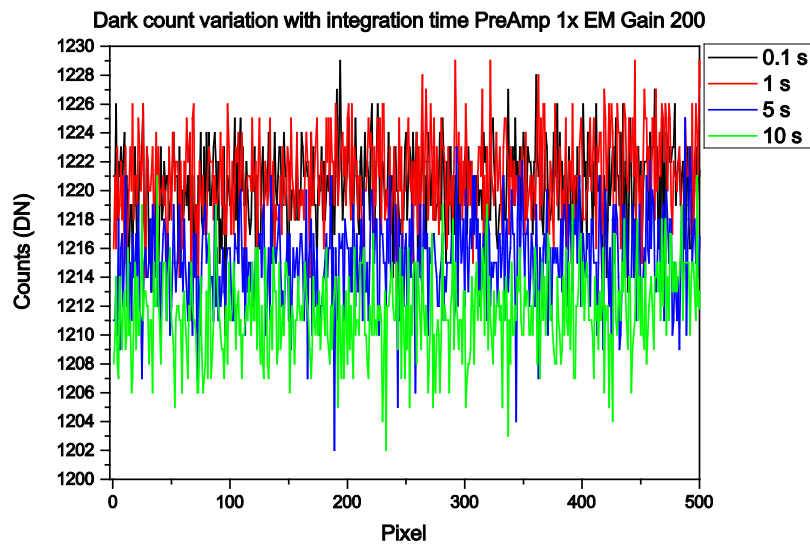


Figure 4-20 Plot of signal (in DN) against integration time showing the noise floor when applying only EM gain of 200.

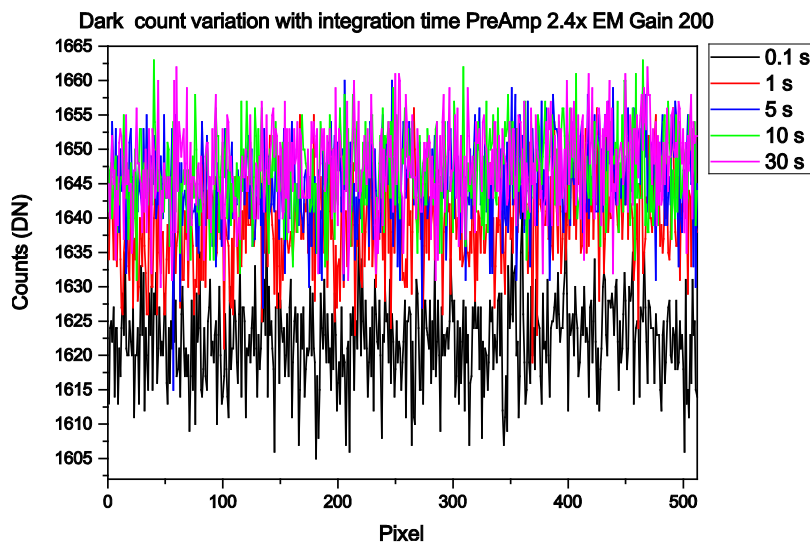


Figure 4-21 Plot of signal (in DN) against integration time showing the noise floor when applying pre-amplification of 2.4x and EM gain of 200.



From the images in Figure 4-22 below column defects become apparent in the move between conventional CCD mode (PA=1, EM=0) to where both the pre-amplifier and a high EM gain are applied (PA=2.4, EM=200). The standard deviation images (blue and red) highlight this further. When inspecting the dark noise component in the dark signal (the standard deviation) of the conventional CCD image it can be seen that this is very even across the image, with very few red pixels indicating those that are hot or cold. The distribution remains consistent in the images acquired with additional amplification, with low incidents of pixels over  $3\sigma$  from the mean. These data give confidence in the use of the detector with additional pre-amplifier and EM gains as the pattern is fixed, scaling with the applied gain.

### 4.3 Characterisation and calibration

---

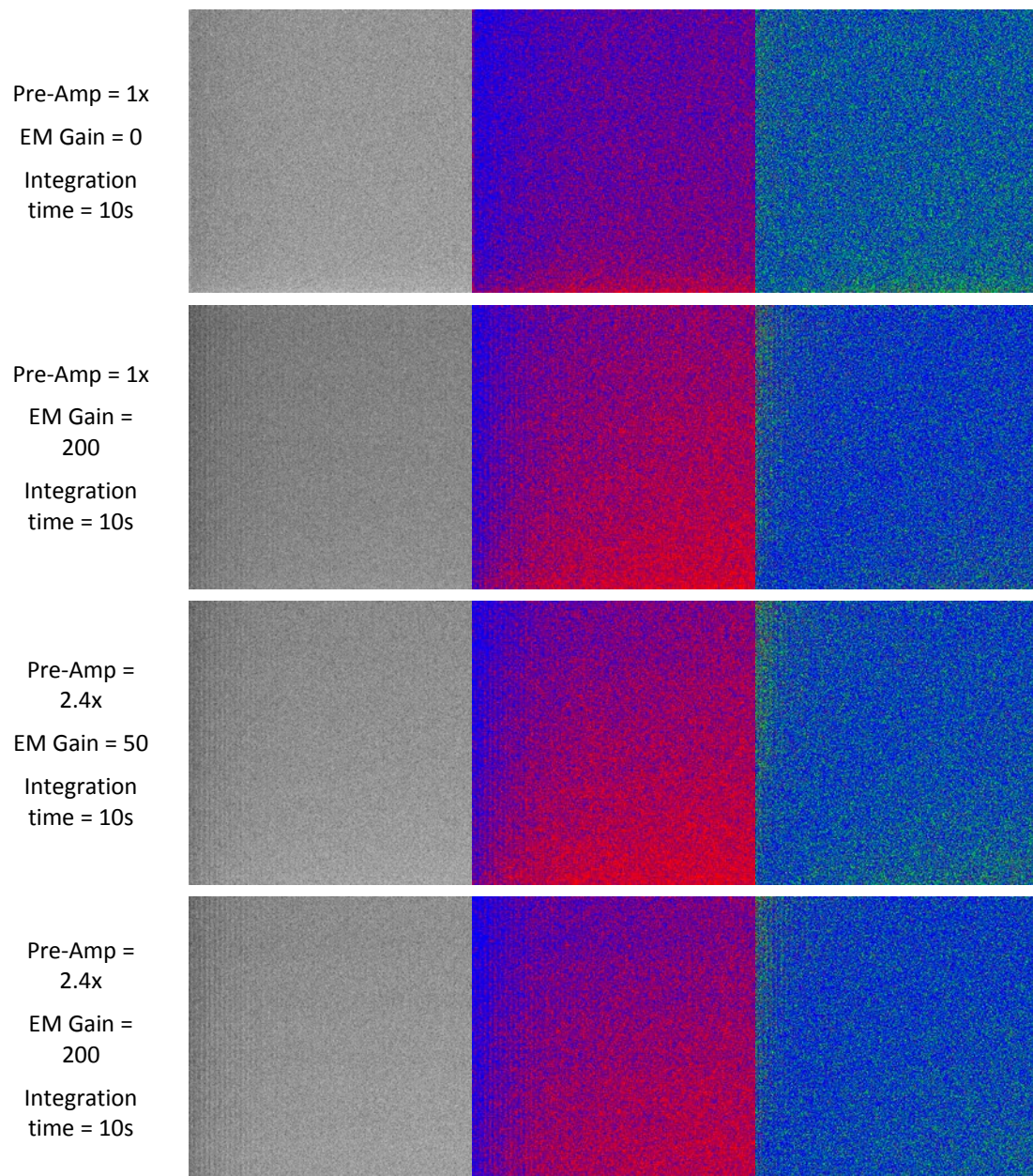


Figure 4-22 Standard deviation maps showing the deviation for the mean of the signal (DN) across the array for different pre-amplifier and gain permutations (512 x 512 pixels). (l-r) master dark image, standard deviation (red = above, blue = below), and variation of standard deviation (red  $> 3\sigma$ ,  $3\sigma >$  green  $< 1\sigma$ , blue  $\leq 1\sigma$ ).

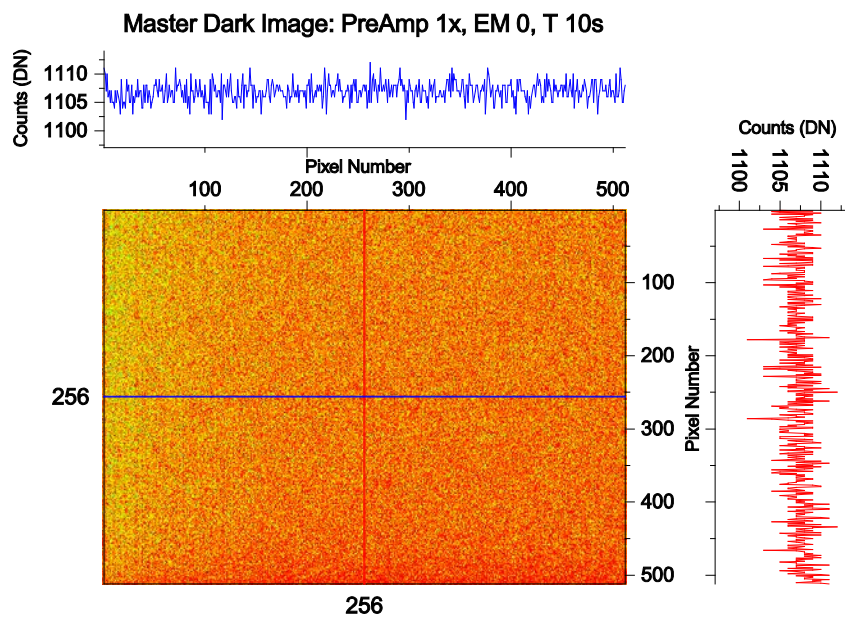


Figure 4-23 Master dark image used in the data processing pipeline. In conventional CCD mode (no pre-amplification or EM gain) there is minimal variation across the detector.

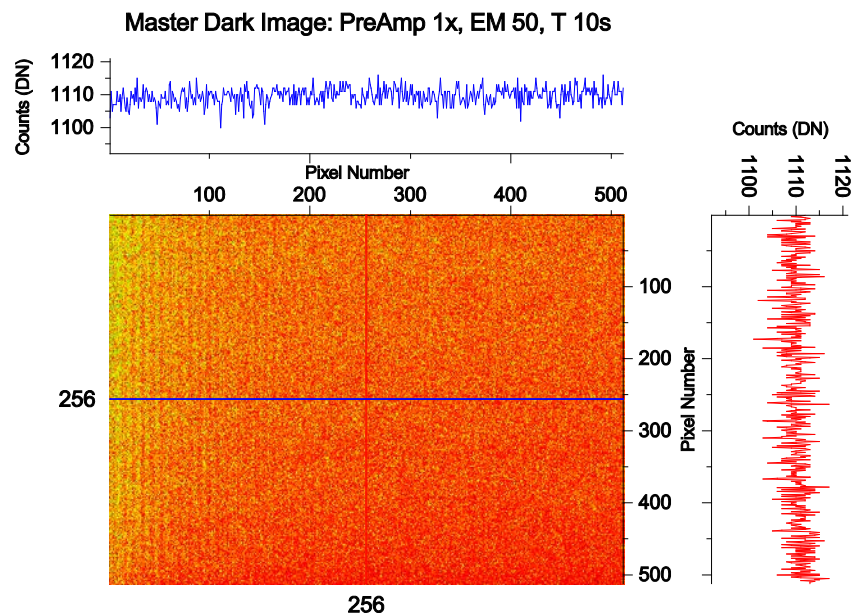


Figure 4-24 Master dark image used in the data processing pipeline. In conventional CCD mode (no pre-amplification) with a small amount of EM gain column defects begin to emerge on the left hand side.



### 4.3 Characterisation and calibration

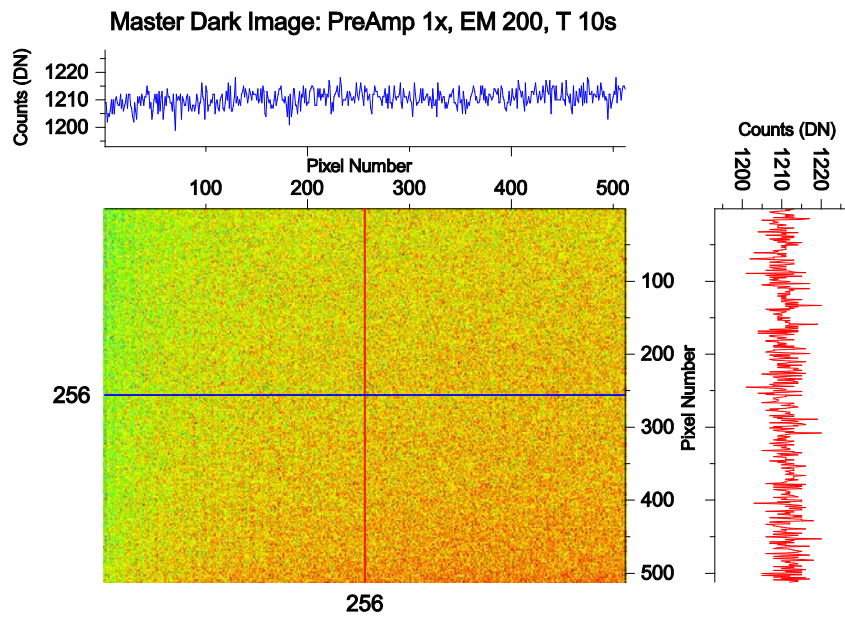


Figure 4-25 Master dark image used in the data processing pipeline. In conventional CCD mode (no pre-amplification) with increasing gain the noise floor increases as expected.

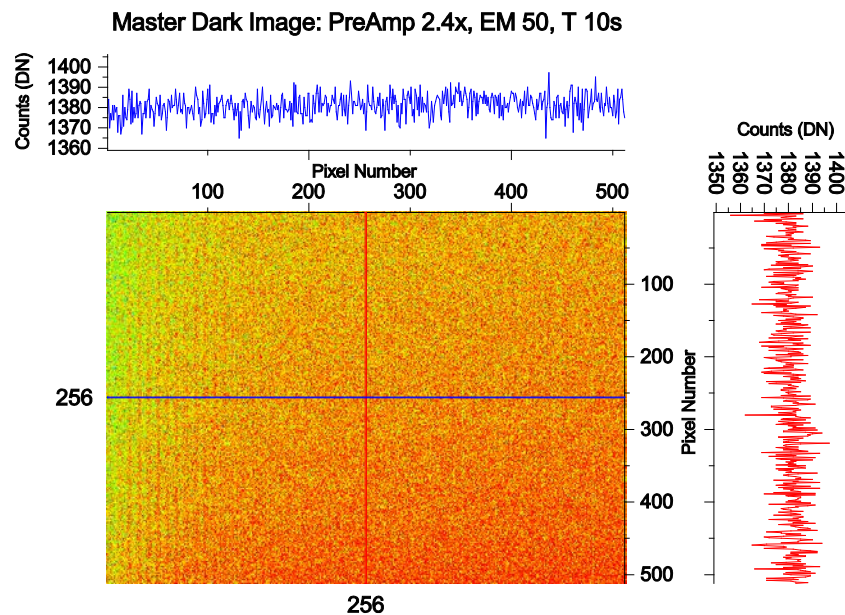


Figure 4-26 Master dark image used in the data processing pipeline. In EMCCD mode (pre-amplification and EM gain) the noise floor is raised and column defects are present on the left hand side.

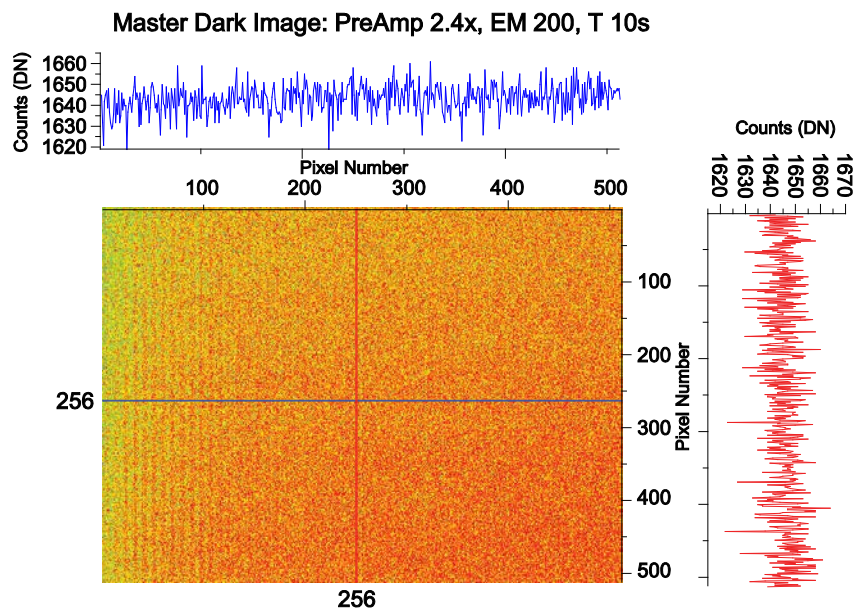


Figure 4-27 Master dark image used in the data processing pipeline. In EMCCD mode (pre-amplification and EM gain) the noise floor is raised and column defects are present on the left hand side, however there is less variation with the addition of a higher EM gain.

#### 4.3.3.3 Pixel Non-Uniformities

Pixel non-uniformity comprises of fixed pattern noise (FPN) and photo-response non-uniformity (PRNU). Pixel non-uniformity is a measure of how signal charge is distributed across a detector. In an ideal detector when a fixed level of uniform light is incident on its elements each should output an identical voltage. In real devices manufacturing errors such as variations in the boundaries that define a pixel caused due to lithography errors, inclusion of defects in the silicon and non-uniform oxide layer growth lead to variations in the signal detected across a device. Pixel non-uniformity factors express these differences in output signal from pixel to pixel. Although the sources of FPN and PRNU are different, many

publications treat them collectively as scene noise, pixel noise, pixel non-uniformity or pattern noise. Pattern noise is the sum of FPN and PRNU. Pixel non-uniformity is linked to charge collection, i.e. the ability of the CCD to efficiently collect charge on a pixel when struck with incident photon; it is a measure of the variation in charge collection efficiency in a group of pixels. Clock bias can also influence pixel-to-pixel non-uniformity, however this has been kept constant during this work as so shall not be discussed. Frame averaging will not reduce FPN and PRNU, differencing is required. Pixel non-uniformity dominates a detector's dynamic range as it sets the lower and upper bounds of detection.

FPN is a fixed pixel-to-pixel offset due to a combination of variations in pixel geometry, substrate material and dark current. FPN becomes dominant at relatively high levels of illumination. It is directly proportional to the input signal strength. FPN, also called pixel non-uniformity is the variation in sensitivity from pixel-to-pixel. Processing errors which can result in pixel to pixel variation (FPN) include differences in the pixel size during manufacture, differing doping densities of the Si substrate and the inclusion of contaminants on the sensor during fabrication and assembly <sup>62</sup>. FPN consists of the differences in values read out from individual pixels, even if no light is falling on the detector. This response remains constant from read to read. These differences are due in part to a variation in the dark signal produced by each pixel (the dark shot noise) and in part due to small irregularities in the CCD fabrication. FPN is temperature, integration time and gain dependent. The temperature relationship is due to its link to dark signal noise, but as it is a spatial noise this component can be completely removed from measurements by background subtraction. If the temperature is set constant for the measurements, this noise can be removed simply by taking away a dark frame taken under the sample condition. As all sample images acquired with HeLIOS were taken at -65°C, this method was chosen to remove the FPN component. Background images were acquired for the data correction; these are made up of FPN and any signal due to dark current. These images are referred to as "Master Dark" in the MathCAD processing. FPN can be identified in

photon transfer plots by the separation of random and fixed noise. The linear region where the gradient is equal to one identifies FPN as it is directly proportional to the incident light level. In order to estimate FPN it is necessary to consider a series of images of a uniform reflectance target illuminated by a spatially uniform source. The relationship between FPN and signal is given by:

$$P_N = \frac{\sigma_S(DN)}{S(DN)} \quad \text{Equation 4-10}$$

Considering the sources of noise, thermoelectric cooling of the CCD array reduces the dark current component to a negligible amount, and hence the FPN, leaving PRNU to dominate the pattern noise. The PRNU is the standard deviation in the flat field image after having removed image defects. PRNU is caused by the physical properties of the CCD. This was calculated by taking a flat field and dark current map. The mean intensity of the image is then calculated, followed by the standard deviation. As with FPN, not all pixels demonstrate the same sensitivity to light. PRNU is a result of sensitivity differences between pixels. These can be caused during fabrication, resulting in pixels with different responses. PRNU can be seen to vary with integration time and gain. It can be removed by subtracting two images pixel by pixel that were acquired under the same conditions, as PRNU is not governed by statistics as other sources of noise are. The noise comes from the CCD sensor itself, dependent on pixel illumination. PRNU is the standard deviation in the flat field image, having removed defects first. Hot and dark pixels, column defects etc. are removed first. The mean intensity is calculated, followed by the standard deviation. PRNU can be thought of as an expression of the variation between pixel's average values. Holst <sup>62</sup> summarises the most common array defects which contribute to PRNU which include: point, hot point, dead pixels, pixel traps, column defects and cluster defects. Point defects are defined as those pixels that have an output that deviates by more than 6% compared to adjacent pixels when illuminated to 70%

saturation (i.e. in the linear region of the PTC). Hot pixels are defined as those with very high dark currents – in the order of 10 times higher than the average dark current. On the other end of pixel response dead or cold pixels, these are characterised by low output voltages and/or poor responsivity. These can be identified as those pixels with under half the output of its neighbours when approaching full well conditions. Pixel traps interfere with the charge transfer process resulting in partial or full column defects, these are observed as saturated (white) or nonresponsive (black) columns in the array output. Column defects can also be due to a group of point defects affecting a single column. Groups of point defects can be dispersed randomly across the array, or form clusters.

Just as photon shot noise has its counterpart of dark shot noise, PRNU has dark current non-uniformity (DCNU). DCNU arises as each pixel can generate a different amount of dark current. This noise is minimised by subtracting a dark reference frame from each image acquired. It is important for the reasons discussed above that this reference is acquired under the same conditions as the science image, i.e. temperature and integration time <sup>136</sup>. Dark current non-uniformity (DCNU) is a measure of the expected dark current generated by thermal energy at every pixel in the array and is independent from PRNU.

### 4.3.3.4 Flat field measurements

The radiance arriving at an image plane varies spatially due to a number of factors, one of which is vignetting. This is characterised as the gradual falloff and darkening of an image towards its peripheries due to the blocking of a part of the incident light's path by the effective aperture size. The effects caused by vignetting vary with the size of the aperture; increasing with larger apertures and vice versa. The cosine-fourth law ( $\cos^4$ ) defines the relationship between the radiance  $L$  and the irradiance  $E$ . From this relationship the irradiance can be seen to be proportional to the radiance, however it decreases as the cosine fourth of the angle  $\theta$



that a ray makes with the optical axis.  $R$  is the radius of the lens and  $d$  is the distance between the lens and the image plane.

$$E = \frac{L\pi R^2 \cos^4 \theta}{4d^2} \quad \text{Equation 4-11}$$

Flat field images correct for vignetting, blemishes on the CCD and optical components. For these reasons it is of the upmost importance to perform flat field measurements with all the microscope objectives and filters in place, as they would be during experimental data acquisition. The noise associated with PRNU can be removed by differencing flat-fielded images. This process removes the PRNU, however it introduces an  $\sqrt{2}$  increase in the shot noise due to the subtraction of images. A flat field calibration (FFC) protocol has been used to minimize, and attempt to eliminate, the effects of fixed pattern noise (FPN), photo-response non-uniformity (PRNU) and illumination and optical non-uniformities.

During FFC the microscope objectives were defocused so not to inadvertently image the surface texture of the integrating sphere. The exposure level was carefully controlled at approximately 75% saturation to prevent over saturation of hot pixels and unwanted effects such as blooming. Flat field data was then collected for a large number of operating permutations and used to generate calibration files for the experimental data processing pipeline to call upon when processing science images, which can be seen in Figure 4-53.

The FFC calibration image generation pipeline, illustrated in Figure 4-33, is as follows. Images were acquired for each microscope objective used (2x, 7p5x and 20x), at a nominal EM gain, adjusted to recorded approximately  $\frac{3}{4}$  full well capacity (i.e.  $\frac{3}{4}$  of the saturation value). The images were acquired at a range of integration times over the full spectral range of the LCTF and without the filter in place. On examination of the individual images it was concluded that

### 4.3 Characterisation and calibration

---

averaging over the 61 images could generate average flats for each objective without compromising the quality or introducing any additional error.

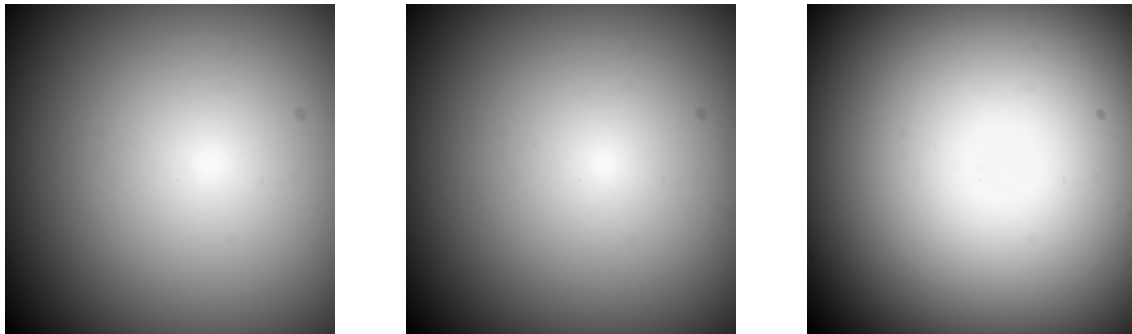


Figure 4-28 Master flat field images (l-r) 2x, 7.5x and 20x magnification. The radial fall off can clearly be observed, with pronounced darkening at the corners. A small blemish on the CCD can be observed in the top right of the images.

The master flat images used for radiometric calibration are shown in Figure 4-28 above. From these images correction factors can be determined to apply to science images to correct for the radial fall off and pattern noise. In addition to these features flat fielding also corrects for introduced artefacts such as the smudge on the CCD visible in the top right hand side of the images. By plotting these images as 3D surfaces (Figure 4-29 to Figure 4-31) with the same colour scale the radial falloff becomes more obvious. Figure 4-32 below illustrates the line profile showing the radial falloff across a typical flat field image. The flat field calibration pipeline is illustrated as a flow chart in Figure 4-33.

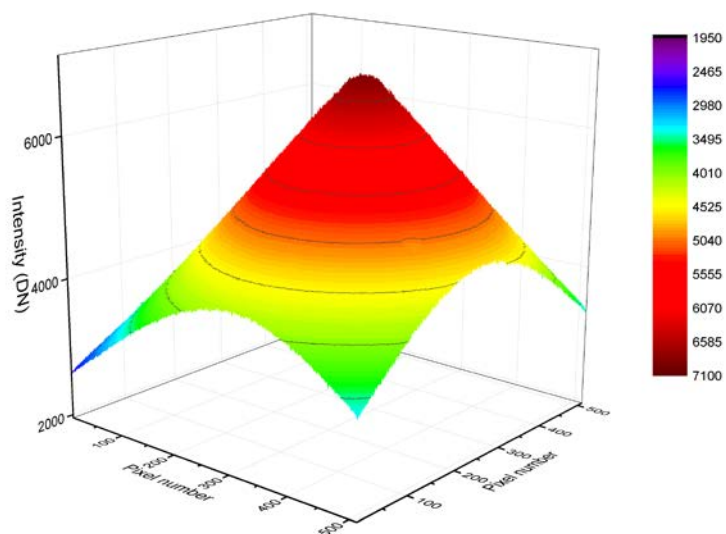


Figure 4-29 3D radial falloff plot for the 2x microscope objective.

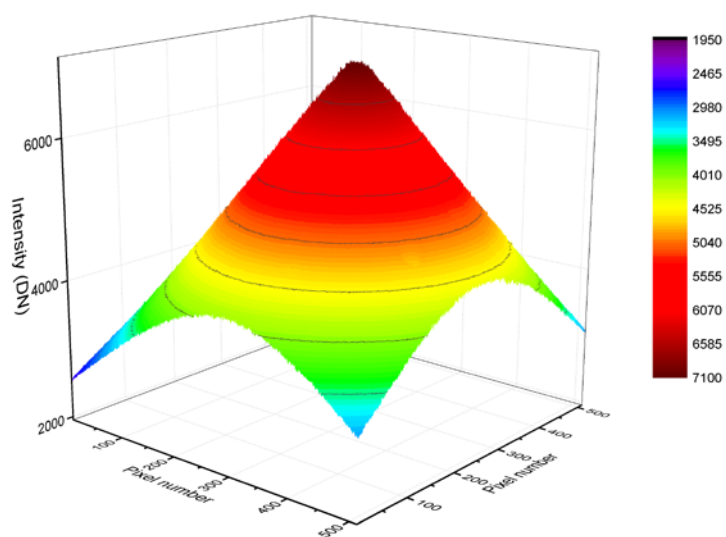


Figure 4-30 3D radial falloff plot for the 7.5x microscope objective.

### 4.3 Characterisation and calibration

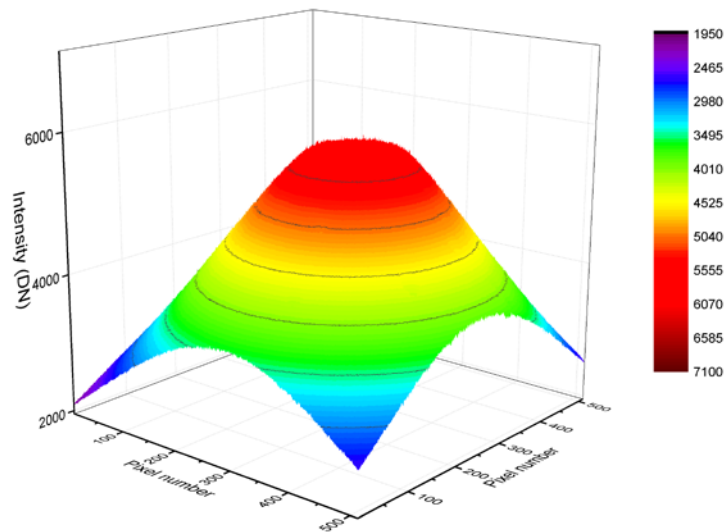


Figure 4-31 3D radial falloff plot for the 20x microscope objective showing a wider saturated area in the centre of the image.

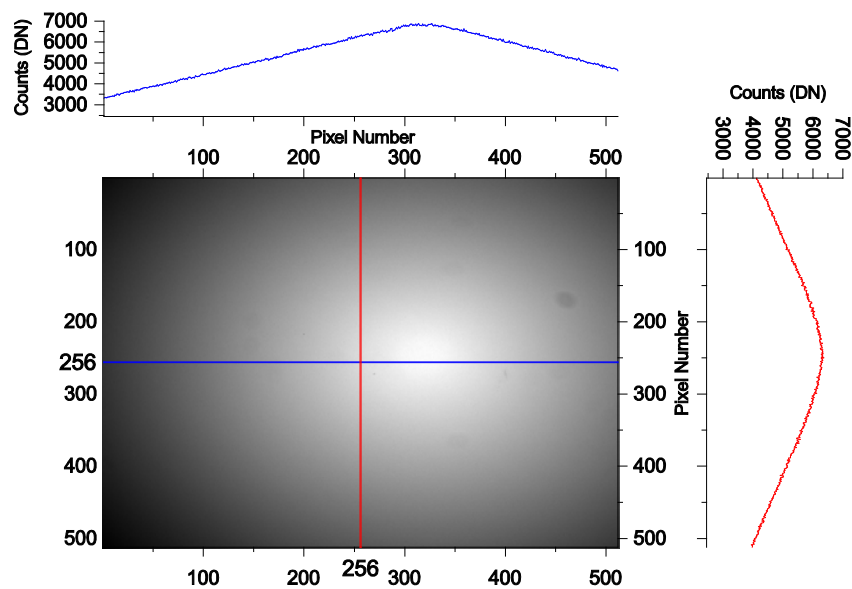


Figure 4-32 Radial falloff profile for a typical flat field measurement illustrated with two cross-sections from the central pixel rows and columns respectively. It can be seen that in this image the fall off is not uniform across the detector.

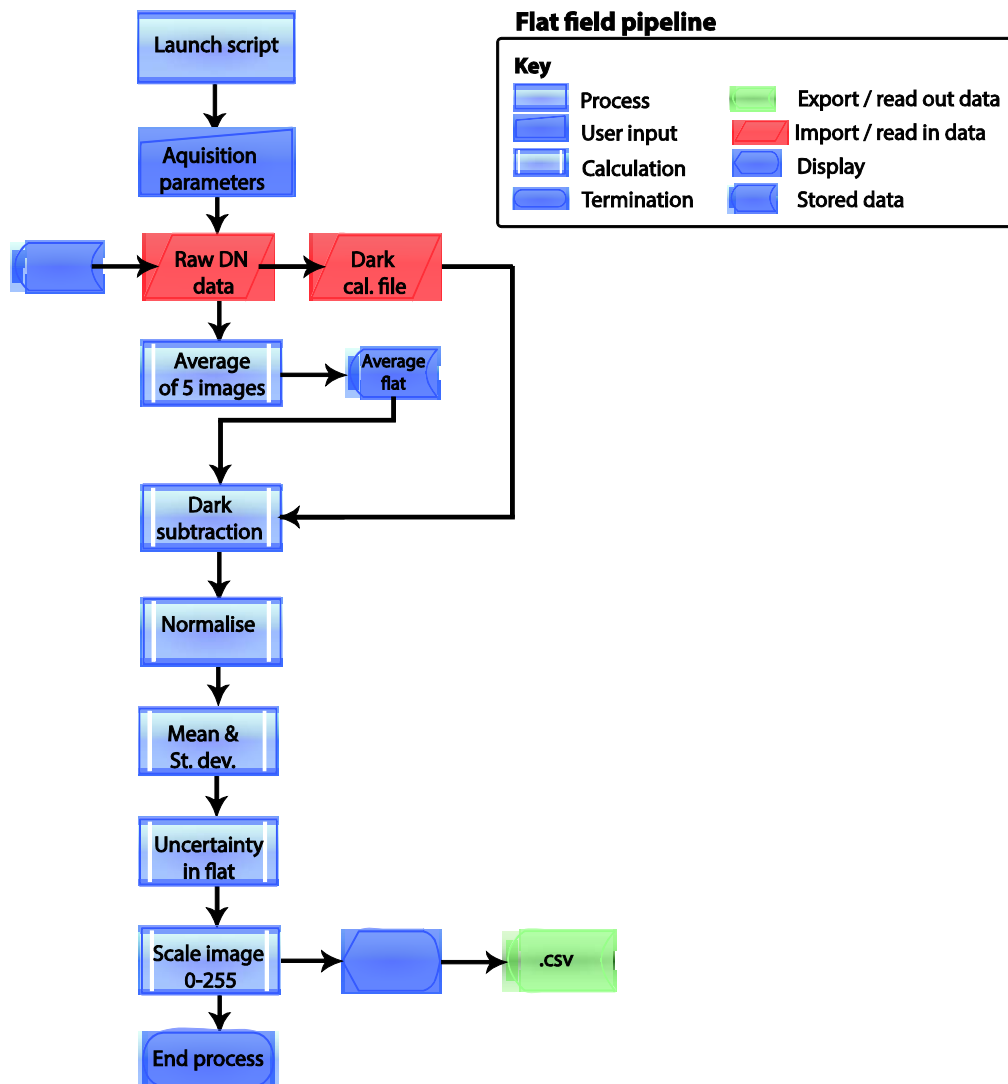


Figure 4-33 Flat field calibration image generation pipeline.

#### 4.3.3.5 Output amplifier noise

A number of noise sources are associated with the output amplification process. Two important sources to consider when working with CCDs are Johnson and flicker noises.

Johnson noise or white noise is a classification given to types of thermal noise. Its magnitude is independent of frequency. Thermal noise and shot noise are considered to be white noise as they are equally intense for every exposure time and impose a noise plateau on the signal. Flicker noise is generated by surface interface states and the tunnelling of electrons in the silicon oxide surface of the CCD detector. When electrons become trapped in these states they are later released with a wide range of emission times. Flicker is therefore related to traps in the detector material and can be reduced through improved manufacturing conditions. It is also referred to as  $1/f$  noise as it has an approximately inverse dependence on frequency. This  $1/f$  relationship is due to fluctuations in the long time constant states contributing to a greater fluctuation in the output than the shorter time constant states. The longer time constant state corresponds to lower frequencies, hence the higher the frequency or pixel rate the lower the noise. The read noise floor can be quantified using the photon transfer curve.

### 4.3.4 Photon Transfer (DN to $\lambda$ )

Janesick, one of the highest cited authors in the area of photon transfer, comments on photon transfer <sup>137</sup>; “Photon transfer is a valuable testing methodology employed in the design, operation, characterisation, optimisation, calibration, specification, and application of solid state imagers and camera systems.”

The technique was developed in the 1980s by Janesick for the characterisation and calibration of CCD and has since been extended to CMOS detectors <sup>138</sup>. It comprises of a collection of curves that provide information about a CCD’s characteristics, which are used to optimize and calibrate the cameras performance. The photon transfer curve (PTC) itself is the most extensively used of the collection. The PCT is an elegant and simple way of investigating three important CCD characteristics: read noise (horizontal area, gradient is zero), shot noise

(where the gradient is  $\frac{1}{2}$ ), and fixed pattern noise (where the gradient is one). The curve is generated by plotting noise (the standard deviation) as a function of signal for a sub-array of pixels. A theoretical plot is given below.

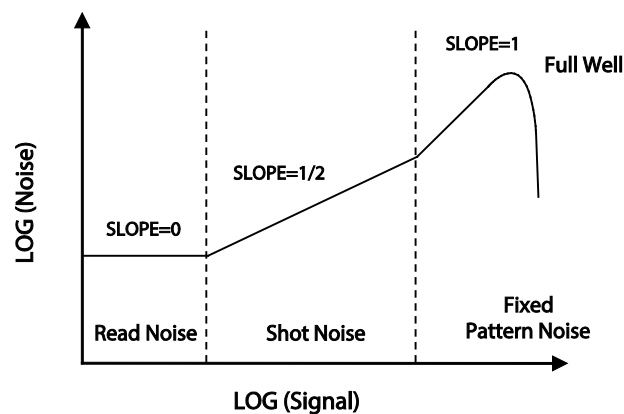


Figure 4-34 Photon Transfer theoretical plot, reproduced from <sup>137</sup>, highlighting the read noise, shot noise, and fixed pattern noise limited regions of the plot. The full well is denoted by the point at which the detector becomes saturated.

The photon transfer technique arose from observations by NASA of changes in the noise floor near saturation during planetary imaging missions in their vidicon tubes <sup>137</sup>. Researchers then began to investigate the imager's noise characteristics and with the introduction of CCD array imagers it became possible to characterise the different forms of noise, such as the noise floor and shot noise. The raw data acquired by a CCD as relative digital numbers (DN) is physically meaningless, in order to use this data a constant is needed to convert this into something meaningful - absolute electron units ( $e^-$ ).

### 4.3 Characterisation and calibration

PTC is a measure of a CCD camera's response, used for noise measurement characterisation and allowing direct comparison of data between systems and cameras. PTC provides the sensor's noise floor, full well and conversion constant ( $e^-/\text{DN}$ ) at selected acquisition parameters. These are calculated by effectively using noise to measure noise. The input to the system is light, which has inherent noise due to the quantum nature described above, and therefore any difference between the noise at the input and the noise at the output is due to the camera. Figure 4-34 below shows an example classical PTC, classical in that the pattern noise component has been removed prior to plotting to leave only the read and shot noise.

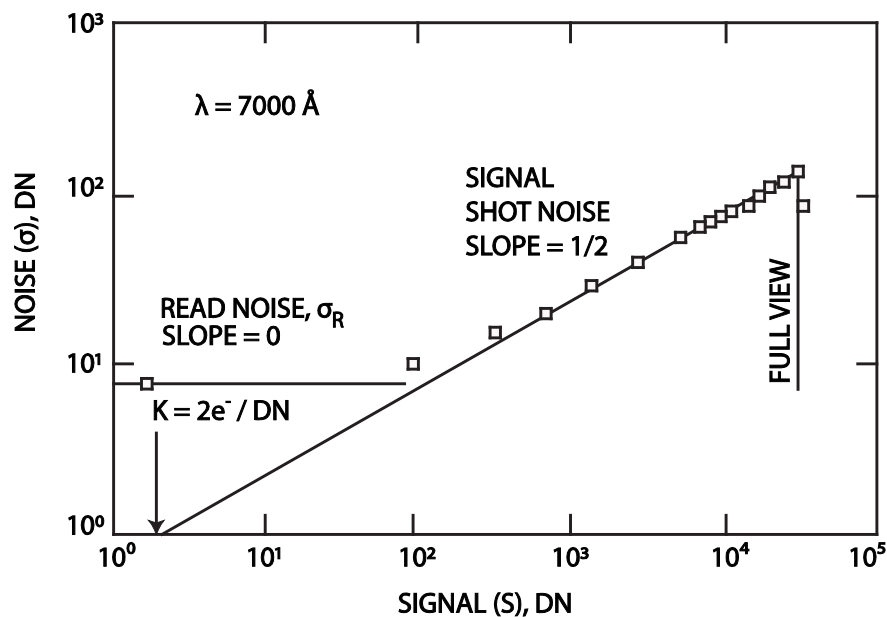


Figure 4-35 Example of a classical photon transfer curve of a CCD under 700 nm illumination, reproduced from <sup>108</sup>. Here the FPN noise element has been removed via frame differencing. Using this method key parameters can be calculated including the read noise and the digital numbers to electron conversion factor.



In the examples above of photon transfer curves it can be seen that from a few simple measurements of a uniform area of the CCD many useful characteristics of the detector can be obtained. The curve can be generated through adjusting the exposure, this can be done by changing the integration time or changing the light level intensity entering the integrating sphere using a precision aperture. The parameters found are:

- Read noise, in DN – the value can be read off the graph where the curve intercepts the y-axis
- Gain, in  $e^-DN^{-1}$  – the gain of the detector can be read from the graph at the point at which the straight-line region of the curve is extrapolated, or by substitution into the total noise equation
- Fixed pattern noise (FPN) – can be calculated through substitution and graphed. At the point of intercept the FPN can be read off. This is usually expressed as a percentage.
- Full well, in DN or  $e^-$  – by examining the point at which the detector saturates and reading down to the x-axis, the full well of the detector can be calculated. This can then be converted from DN to electrons and compared with the manufacturer information.

HeLIOS has been investigated by both methods of examining the photon response; using a precision aperture and varying the integration time for consistency. To estimate the DN to  $e^-$  conversion factor,  $K$ , plotting the log Signal against the log Noise produces the photon transfer curve. By identifying the shot noise limited region where the gradient is equal to  $\frac{1}{2}$  and extrapolating to the x-axis intercept  $K$  can be found. The figures below illustrate the effect on photon transfer curves when the detector is operating in conventional CCD mode, EMCCD without pre-amplifier and EMCCD with pre-amplifier. In these plots the total noise is used, hence a fixed pattern noise component is present in the higher signal region near saturation

### 4.3 Characterisation and calibration

---

point. Pixel values are averaged together and the fixed electrical offset is subtracted to give the signal,  $S(DN)$ : where  $S_i(DN)$  is the signal value of the  $i^{th}$  pixel (DN) and  $N_P$  is the number of pixels sampled and the signal offset,  $S_{off}(DN)$ , is found.

$$S(DN) = \frac{\sum_{i=0}^{N_P} S_i(DN) - S_{off}(DN)}{N_P} \quad \text{Equation 4-12}$$

Noise,  $\sigma_s(DN)$ , is calculated from the variance of the pixels:

$$\sigma_s^2(DN) = \frac{\sum_{i=1}^{N_P} (S_i(DN) - S(DN))^2}{N_P} \quad \text{Equation 4-13}$$

The total noise,  $\sigma_s^2(DN)$ , is comprised of the three source shown in the photon transfer curve: read noise,  $\sigma_R$ , photon shot noise,  $\sigma_{shot}$ , and pixel non-uniformity or fixed pattern noise,  $\sigma_{PN}$ .

$$\sigma_s^2(DN)^2 = \sigma_R^2(DN)^2 + \sigma_{shot}^2(DN)^2 + \sigma_{PN}^2(DN)^2 \quad \text{Equation 4-14}$$

The shot noise limited region can be clearly identified in Figure 4-30 for the detector in conventional CCD mode. Here the active area pixel well depth limits the signal, as the gain register is not utilised. The estimate of the full well depth of approximately 235,000  $e^-$  agrees well with the literature estimation of an average pixel value of 220,000  $e^-$ <sup>110</sup>.

With the application of the electron multiplier the full well can be seen to increase, as the detector is now using the additional gain register's pixel depth, which can reach of up to 800,000  $e^-$ <sup>110</sup>. This can be seen to rise to an estimated 314,956  $e^-$  with the addition of the pre-amplification. Read noise is also reduced with the addition of the pre-amplification as the signal is amplified prior to read out.

In the read noise region the read noise can be read from the y-axis intercept, in the shot noise region of the plot the curve has a slope of approximately 0.5 on average which represents the dynamic range over which its operation is shot noise limited. A comparison of the PTCs using individual frames and differenced frames can be used to measure PRNU. The final FNP region shows where the camera is linear, where the curve rises to a maximum and falls rapidly off shows where the saturation point is for the detector, giving an approximation of the full well depth.

A CCD needs to generate an output voltage in proportion to the charge contained in a pixel; this is expressed as the linearity of the detector. The non-linearity for the detector used in this work is given by Andor as less than 5%, where the degree of linearity is expressed as the deviation from a straight-line fit of the signal from the integration time plot. As Andor does not measure the linearity for each detector, an estimation of the linearity has been made to check it is within specification and many of the calibration measurements rely on the detector operating linearly. Figure 4-40 shows the plot of the detector's linearity along with a least squares linear regression fit. The non-linearity is calculated as 1.26% to 2 s.f..

### 4.3 Characterisation and calibration

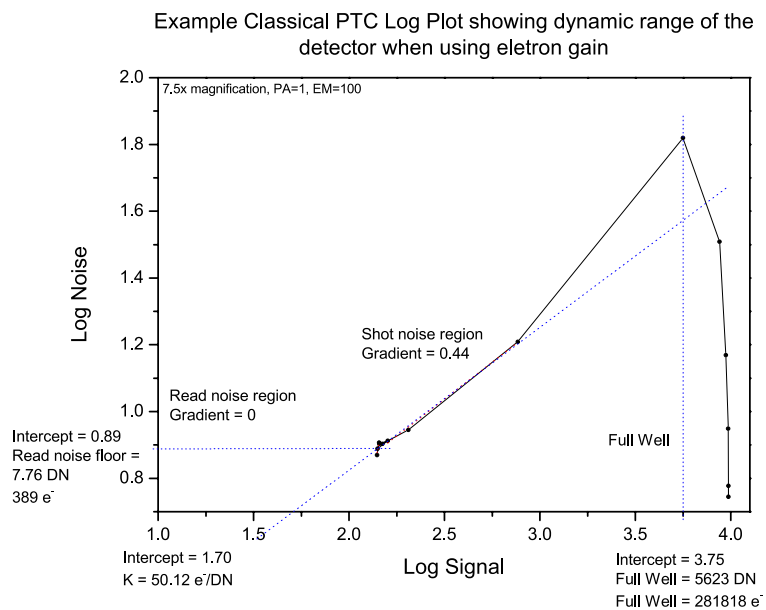


Figure 4-36 Photon Transfer Curve in conventional CCD Mode (no EM gain or pre-amplifier).

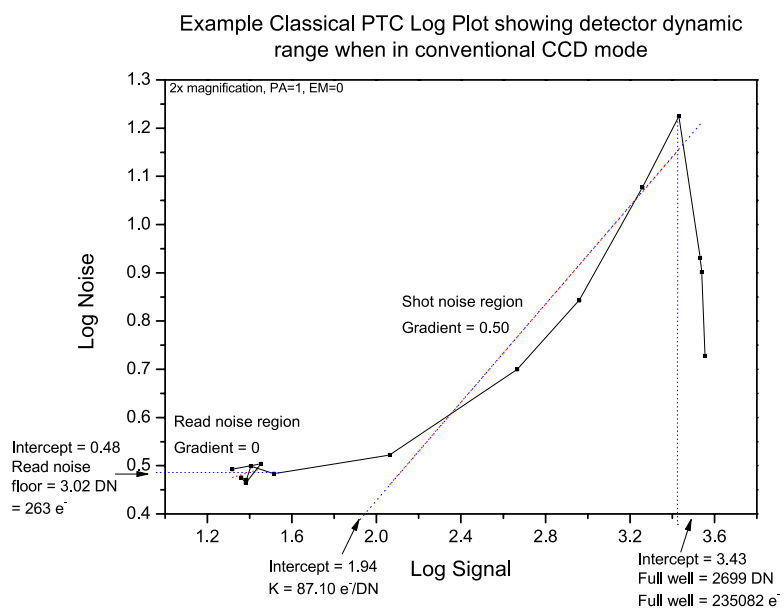


Figure 4-37 Photon Transfer Curve for detector in EMCCD mode without additional pre-amplification.

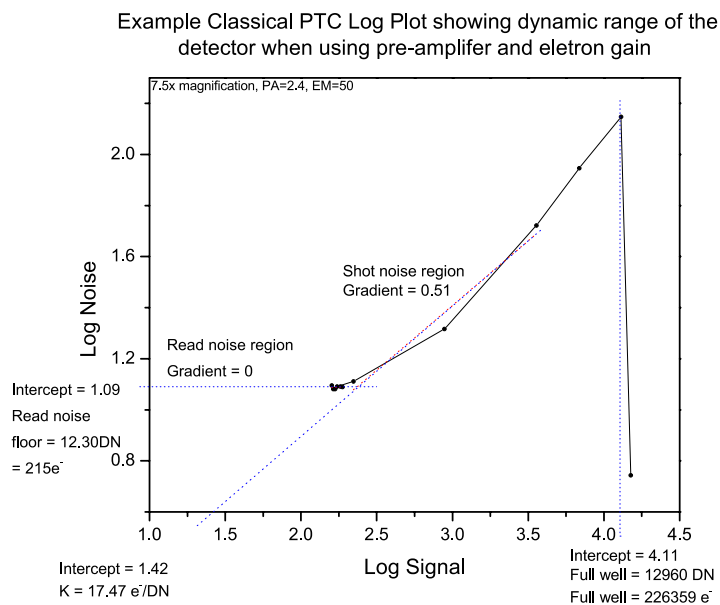


Figure 4-38 Photon Transfer Curve for detector in EMCCD mode with additional pre-amplification.

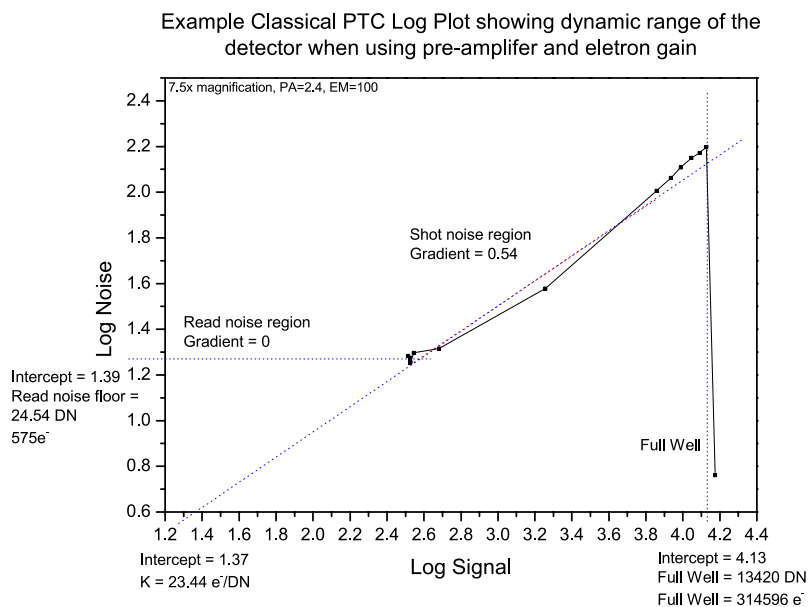


Figure 4-39 Photon Transfer Curve for detector in EMCCD mode without additional pre-amplification.

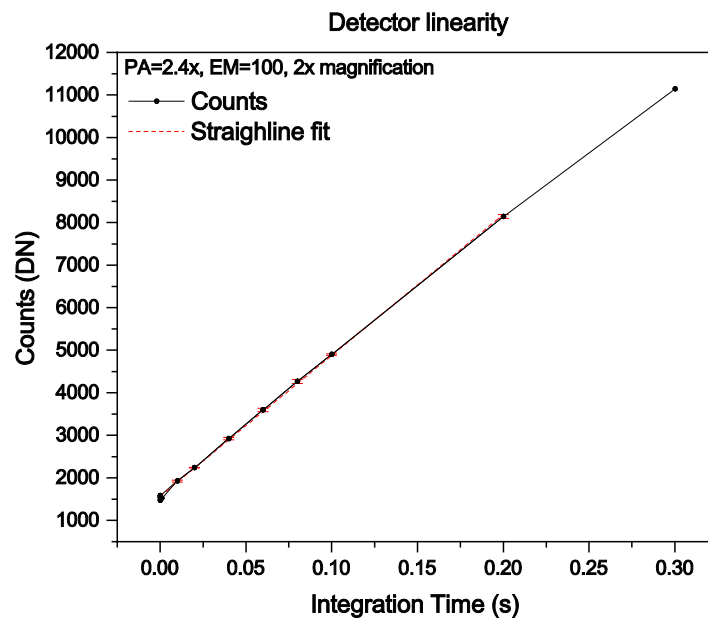


Figure 4-40 Detector linearity, the red dashed line shows the line of best fits for the linear region of the CCD (that between read noise and near saturation). Fitting of a straight line in the form of  $y=mx+c$  provides and  $R^2$  of 0.99947.

#### 4.3.5 Photometric response and calibration uncertainties

As discussed in the previous chapter, multispectral and hyperspectral techniques allow spectral radiance of an illuminant, reflectance of an object or combined colour signal at every pixel to be recovered <sup>134</sup>. CCD detectors produce digital images with inherent artefacts such as vignetting or radial falloff. Such effects arise from non-uniformities in the sensitivity across the field of view of the imaging instrument. A number of these non-uniformities have been illustrated so far in this chapter. Once a system is characterised, and experimental parameters

decided upon, the system can be radiometrically calibrated. As discussed standard calibration is a process of quantitatively defining a system's response to known, controlled inputs and radiometric calibration is the process of determining the functional relationship between the incoming radiation and the instrumental output. In an ideal system each pixel in the image would display the same digital number of counts (DN), i.e. every pixel would respond to the uniformly illuminated surface in the same manner. Radiometric calibration has been used to correct the DN readout of an image taking into consideration factors such as the integration time, flat field corrections, dark current, system bias and CCD operating regime (electron multiplier gain and pre-amp gain). In HeLIOS the additional factors of the different microscope objectives and the response of the LCFT have been also accounted for. A radiometrically calibrated image has irradiance values in radiometric units proportional to the brightness of the scene. For absolute calibration the spectrometer used to measure the uniform light of the integrating sphere used for calibrations has itself been calibrated to a NIST traceable light. The resulting data measuring the emitted light from a sample under excitation can now be expressed as irradiance; the electromagnetic radiation emitted from an area in  $\text{Wm}^{-2}\text{nm}^{-1}$ , as the luminescence output is small the irradiance has been expressed in  $\mu\text{Wcm}^{-2}\text{nm}^{-1}$  or  $\mu\text{Wcm}^{-2}\text{eV}^{-1}$  when investigating spectral features. After radiometric calibration the system is able to present accurate reconstructions of natural spectra and render data instrument independent (for a given selected bandpass/resolution). This provides a means of standardization when accurate background or illumination data is not available or heterogeneous.

During the transfer of the NIST calibration the spectral response (Quantum Efficiency curve) of the CCD is multiplied by the spectra from the NIST traceable lamp providing a reference instrument-acquired spectrum of the lamp. This instrument-acquired spectrum is then multiplied by a correction curve to return values equal to the NIST reference spectrum of lamp. Hence by using HeLIOS to measure a traceable lamp, with a calibration file of

### 4.3 Characterisation and calibration

---

wavelength versus power curve (Watts per unit area per wavelength (nm)) that calibration is transferred to HeLIOS. This is illustrated in Figure 4-41 below.

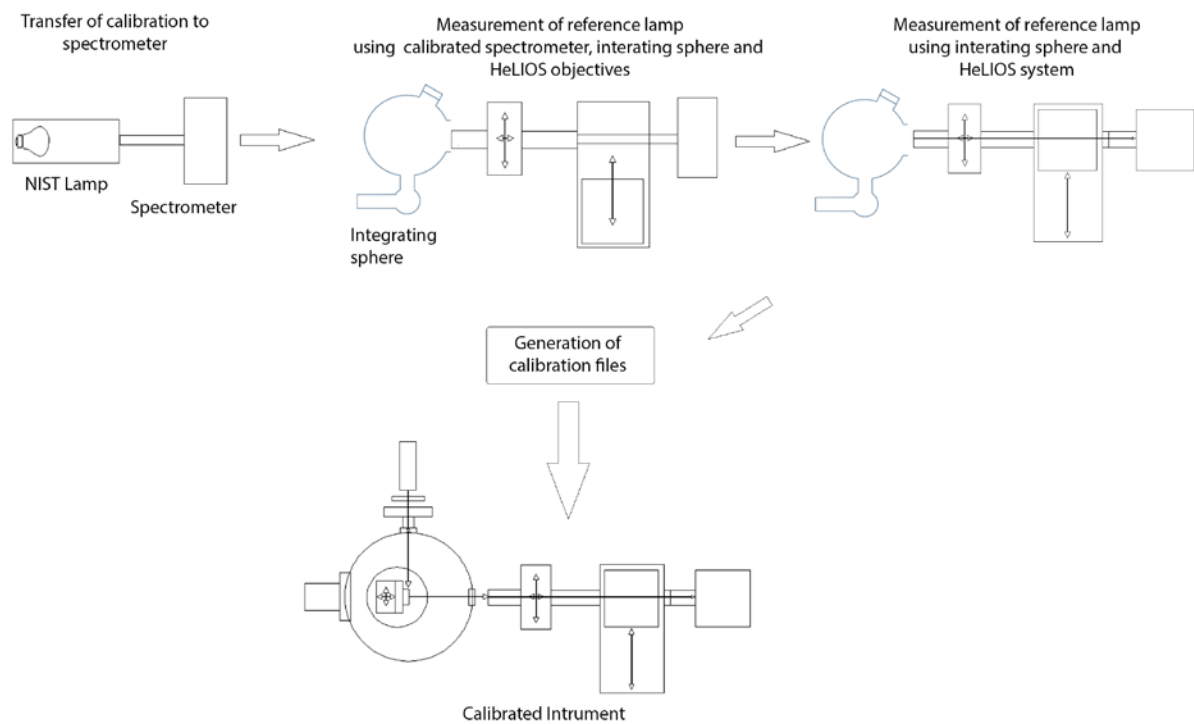


Figure 4-41 Illustration of the transfer of a NIST calibration across the system. A NIST lamp is used to calibrate a reference spectrometer, this is used to measure a reference uniform light source and calibration files generated. The same uniform source is measured using the HeLIOS system and the calibration applied.



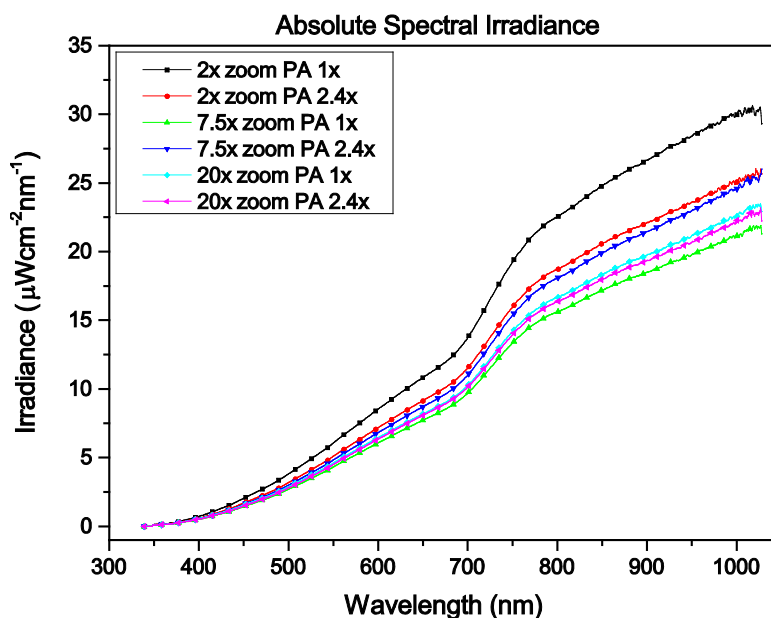


Figure 4-42 Absolute spectral irradiance measurements of the uniform light source in the six configurations used in this work. Here it can be observed there is a change in the irradiance measured over time.

An absolute spectral irradiance measurement is required for each operating configuration. Figure 4-42 above shows the absolute spectral irradiance recorded through the three objectives used in this work. For each objective configuration two sets of data were taken to correspond to calibration data acquired with those pre-amplifier settings, these were then averaged to provide a representative figure to use in the calibration chain. As calibration data acquisition is a time consuming process, the stability of the light source to the integrating sphere can be taken in to account more consistently by recording data in this way. It can be seen in Figure 4-42 above that there is some variation in the irradiance recorded at different times. These data were acquired using a USB 2000+ spectrometer, calibrated against a NIST traceable lamp. A single 400 $\mu\text{m}$  fibre was connected to the SMA connection installed at the

### 4.3 Characterisation and calibration

rear of the objective. The calibration procedure is summarised in the processing pipeline, Figure 4-43 below.

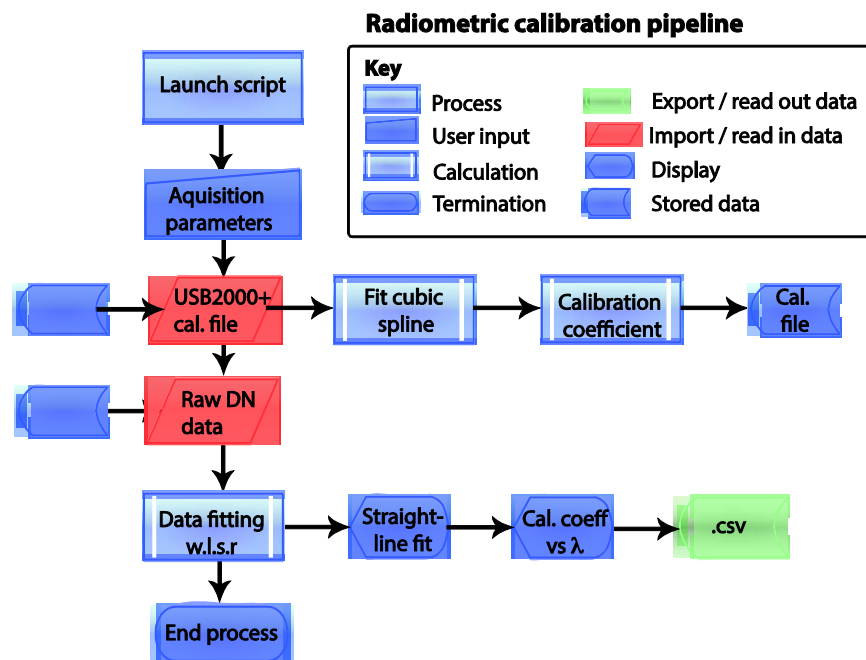


Figure 4-43 Radiometric calibration file generation pipeline.

This procedure demonstrates that the calibrated lamp curve can be reproduced, meaning subsequent data will be independent of the CCD's QE and artefacts of the system.

Figure 4-44 to Figure 4-47 below illustrated the progression from uncorrected, raw data to radiometrically calibrated. In plot a) the raw data is dominated by the spectral response of the LCTF, where there is a higher throughput in the central visible portion of the spectrum. This is to be expected when the transmission response of the filter in Figure 3-12 is considered. Plot b) shows the same profile shape, but has now been corrected for dark signal, flat field and integration time. Plot c) shows the calibration curve, which corresponds to the data acquisition. The response of the filter and detector are incorporated at this stage. Finally plot d) shows the data corrected using the processing pipeline, revealing the true spectra acquired from a region of interest (20 x 20 pixel selection) in meaningful absolute units of irradiance.

### 4.3 Characterisation and calibration

---

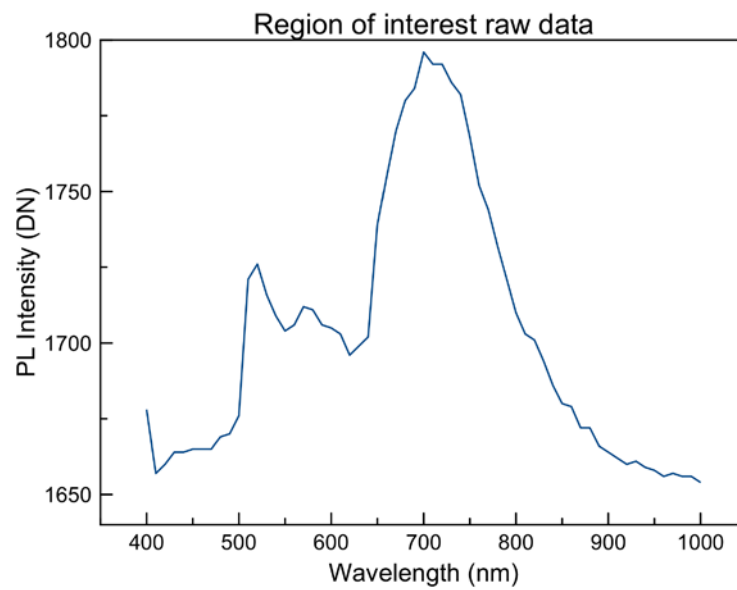


Figure 4-44 Raw photoluminescence data convoluted with the response of the instrument (LCTF, detector and optics).

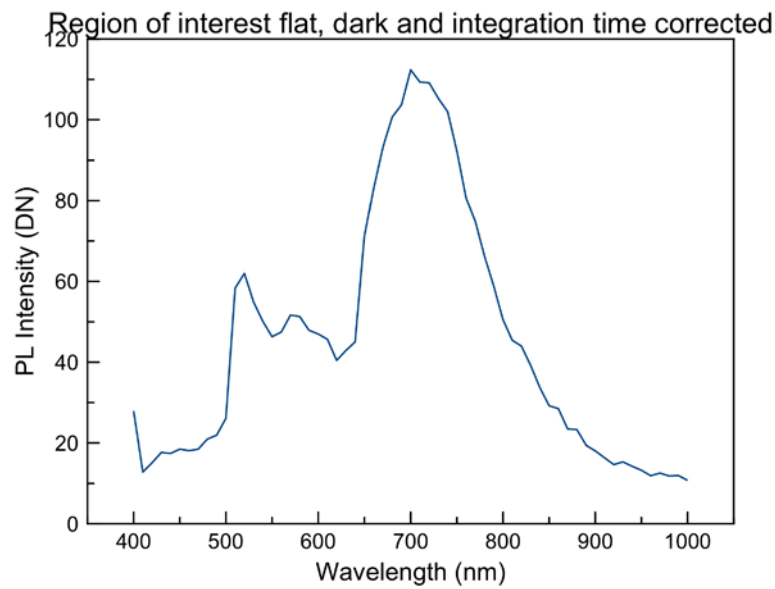


Figure 4-45 Raw photoluminescence data with the flat, dark and integration time corrections applied.

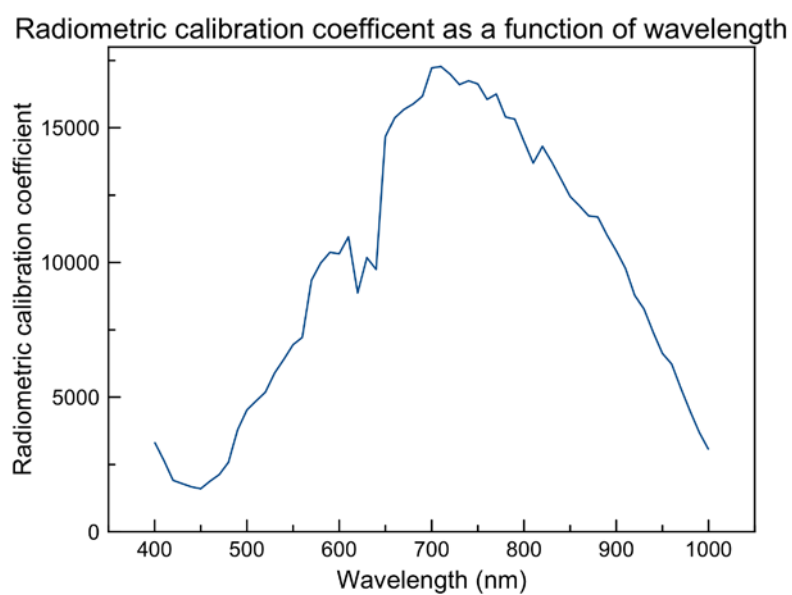


Figure 4-46 Radiometric calibration coefficient specific to the experimental set-up.

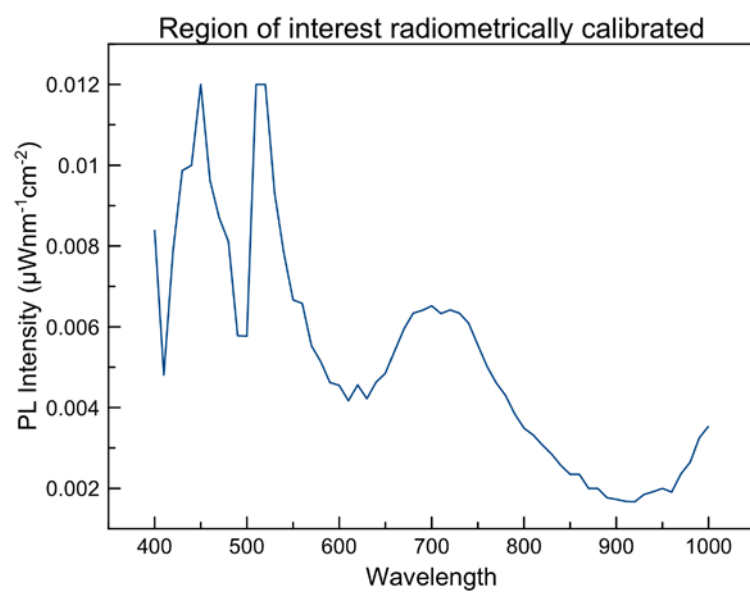


Figure 4-47 Final data set presented in units of irradiance corrected for the response of the instrument.

### 4.3 Characterisation and calibration

---

During calibrations a number of assumptions have been made and calibration files generated for which the uncertainty has been computed in order to plot data with meaningful error bars. These have the benefit of helping identify spurious data such as the overcorrection of short wavelengths (400-450 nm) that show larger error bars due to the lower signal. In the first instance a least squares weighted fit has been applied to calculate the error in the intercept and gradient for the photometric response data, using the straight-line expression:

$$y = mx + c \quad \text{Equation 4-15}$$

Here the terms are substituted for the relative irradiance at each wavelength,  $R$ , the signal in digital numbers,  $S$ ,  $m$  and  $c$  remain as the slope and intercept respectively. Rearranging to make irradiance the subject gives:

$$R = \frac{S - c}{m} \quad \text{Equation 4-16}$$

The slope and intercept, with their respective errors, can then be expressed as follows:

$$m = \frac{\sum \frac{1}{\sigma_i^2} \sum \frac{x_i y_i}{\sigma_i^2} - \sum \frac{x_i}{\sigma_i^2} \sum \frac{y_i}{\sigma_i^2}}{\Delta} \quad \text{Equation 4-17}$$

$$\sigma_m = \left( \frac{\sum \frac{1}{\sigma_i^2}}{\Delta} \right)^{\frac{1}{2}} \quad \text{Equation 4-18}$$

$$c = \frac{\sum \frac{x_i^2}{\sigma_i^2} \sum \frac{y_i}{\sigma_i^2} - \sum \frac{x_i}{\sigma_i^2} \sum \frac{x_i y_i}{\sigma_i^2}}{\Delta} \quad \text{Equation 4-19}$$

$$\sigma_c = \left( \frac{\sum \frac{x_i^2}{\sigma_i^2}}{\Delta} \right)^{\frac{1}{2}} \quad \text{Equation 4-20}$$

Where  $\Delta$  is expressed as:

$$\Delta = \sum \frac{1}{\sigma_i^2} \sum \frac{x_i^2}{\sigma_i^2} - \left( \sum \frac{x_i}{\sigma_i^2} \right)^2 \quad \text{Equation 4-21}$$

As the raw luminescence images have been corrected for bias, dark, flat field and expressed in terms of seconds by dividing through by the respective integration times in the data processing pipeline, it can be assumed that a signal,  $S$ , of zero should be obtained for zero luminescence. The EMCCD sensor temperature is known accurately as  $-65^\circ\text{C}$  and this is monitored during data acquisition to ensure its stability. The stability of the EMCCD during measurements is observed to be better than  $\pm 1^\circ\text{C}$ . The dark frame and signal depend on temperature and so by maintaining a steady state it can be assumed that the uncertainty in the dark and bias corrections will be significantly smaller than the uncertainty in the luminescence measurement. The method used to calculate the uncertainty in the irradiance measurements is based on that used by the MER Pancam team<sup>139</sup> and by Gunn<sup>128</sup> which works on these assumptions to force the straight-line fit through zero. Testing by the MER team showed that this is a justified method. To confirm this holds true, this treatment and

### 4.3 Characterisation and calibration

---

one using data recorded with the aperture fully closed have been compared. The total uncertainty in the luminescence data can now be expressed as a combination of uncertainties. By calculating the partial derivatives and correlation coefficients from each combination the total uncertainty can be calculated using matrix algebra.

$$\sigma_{R^*} = \begin{bmatrix} \frac{\partial R^*}{\partial S} & \frac{\partial R^*}{\partial c} & \frac{\partial R^*}{\partial m} \end{bmatrix} \begin{bmatrix} \sigma_S^2 & 0 & 0 \\ 0 & \sigma_c^2 & 0 \\ 0 & 0 & \sigma_m^2 \end{bmatrix} \begin{bmatrix} \frac{\partial R^*}{\partial S} \\ \frac{\partial R^*}{\partial c} \\ \frac{\partial R^*}{\partial m} \end{bmatrix} \quad \text{Equation 4-22}$$

Returning to the straight-line fit of Equation 4-14, the partial derivatives can be calculated and substituted into Equation 4-22.

$$\frac{\partial R^*}{\partial S} = \frac{1}{m} \qquad \frac{\partial R^*}{\partial c} = -\frac{1}{m} \qquad \frac{\partial R^*}{\partial m} = -\frac{S - c}{m^2}$$

$$\sigma_{R^*} = \begin{bmatrix} \frac{1}{m} & -\frac{1}{m} & -\frac{S - c}{m^2} \end{bmatrix} \begin{bmatrix} \sigma_S^2 & 0 & 0 \\ 0 & \sigma_c^2 & 0 \\ 0 & 0 & \sigma_m^2 \end{bmatrix} \begin{bmatrix} \frac{1}{m} \\ -\frac{1}{m} \\ -\frac{S - c}{m^2} \end{bmatrix} \quad \text{Equation 4-23}$$

The correlation between the components can then be assessed. Correlation between the signal  $S$  and the gradient  $m$  is found to be -0.269, between the signal and the intercept 0.418, and between the gradient and the intercept -0.579. This shows that as expected that the



strongest correlation is between the gradient and the intercept. From this the correlation coefficient,  $\rho(m,c)$ , for this relationship is introduced into the matrix:

$$\sigma_{R^*} = \begin{bmatrix} \frac{1}{m} & -\frac{1}{m} & -\frac{S-c}{m^2} \end{bmatrix} \begin{bmatrix} \sigma_S^2 & 0 & \rho(m,c)\sigma_m\sigma_c \\ 0 & \sigma_c^2 & 0 \\ 0 & \rho(m,c)\sigma_m\sigma_c & \sigma_m^2 \end{bmatrix} \begin{bmatrix} \frac{1}{m} \\ -\frac{1}{m} \\ -\frac{1}{m} \end{bmatrix} \quad \begin{array}{l} \text{Equation} \\ 4-24 \end{array}$$

Equation 4-24 above gives the uncertainty in the radiometrically calibrated data and has been implemented in the MathCAD data processing pipeline illustrated in Figure 4-53.

During data acquisition using HeLIOS a number of additional factors can influence the recorded luminescence signal including contributions from scattered and reflected excitation light, scatter from the copper sample holder, scatter from the cryostat heat shield, stray light, light from outside the focal plane and contamination which may also luminesce (such as fragments of tissue from cleaning, dust etc.). Experimental experience has minimized these as far as reasonably practicable but these have not been computed.

## 4.4 Experimental data acquisition

On acquisition of hyperspectral imaging data there are a number of ways to interrogate and present it. Three potential ‘views’ of data are described by Landgrebe<sup>140</sup>, these are image space, spectral space and feature space. Figure 4-48 illustrates these possible ‘views’. How pixels relate to one another can be information bearing, image space provides a picture of the data for a human viewer to interact with. For this reason image space is very useful in providing an overview of data, as the old saying goes - “a picture is worth a thousand words”.

## 4.4 Experimental data acquisition

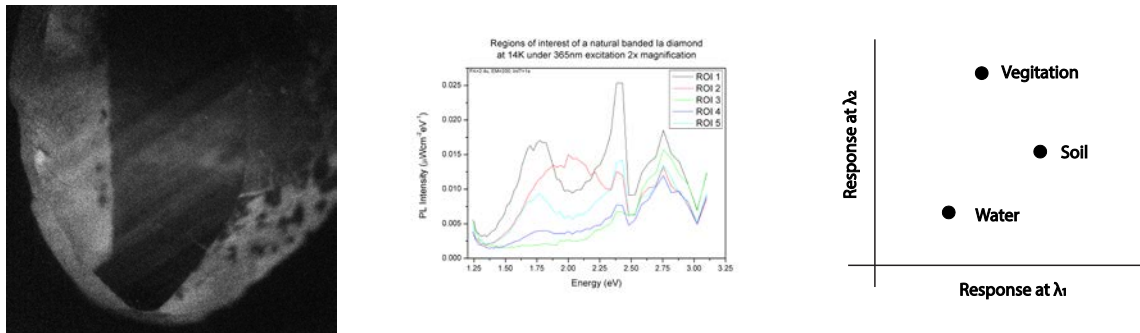


Figure 4-48 Examples of image, spectral and feature space. (l-r) 8 bit image of a sample; resolved hyperspectral data showing the spectral variation across the image; and example of feature space used in remote sensing for classification, reproduced from <sup>140</sup>.

This simple image however, does not convey all the information acquired by multi- or hyperspectral means. Data can be viewed in one or three bands at a time i.e. black and white or colour. Image space shows the relationship of spectral response to its spatial position; it is a way to associate each pixel to a location on the sample under investigation. Where multispectral and hyperspectral data is acquired, the response of an individual pixel as a function of wavelength can be expressed in the form of spectral space. From a stack of images each pixel can be processed individually to give a measure of spectral information linked to spatial information. By using this method where there is sufficient spectral detail, such as hyperspectral imaging, the characteristics of each pixel can be related to a physical property. This technique of relating the spectra acquired at each pixel is most often seen in remote sensing applications, where reflectance data acquired by satellite and airborne multispectral systems are used to acquire spatially resolved data on land use. However even this does not give the full information available. As in remote sensing, radiometric calibration is required to take into consideration other variables present and allow direct comparisons between pixel-

to-pixel and dataset-to-dataset. Spectral space, when conducted appropriately, enables a relationship to be found between a given spectral response and a material that can later be used for classification and identification. The third method illustrated above is feature space, which provides a representation useful to computer processing for feeding into pattern recognition and automated image classification. Feature space has not been explored as part of this work.

Figure 4-49 illustrates the products that can be extracted from a HeLIOS hyperspectral dataset. The simplest is a grey scale image of the sample under excitation, with only a filter to block the reflected component (i.e. images acquired using 365nm excitation are taken using stacked 395 and 400nm long pass filters). This provides an image for visual inspection, sample positioning and focusing. After LCTF insertion and hypercube acquisition an image of the sample at any of the acquisition wavelengths can be viewed and on selecting a pixel, or region of interest, a full spectra can be displayed. Finally by selecting up to three wavelengths and assigning those as RGB channels an image can be created to display contrast between the channels in the sample.

## 4.4 Experimental data acquisition

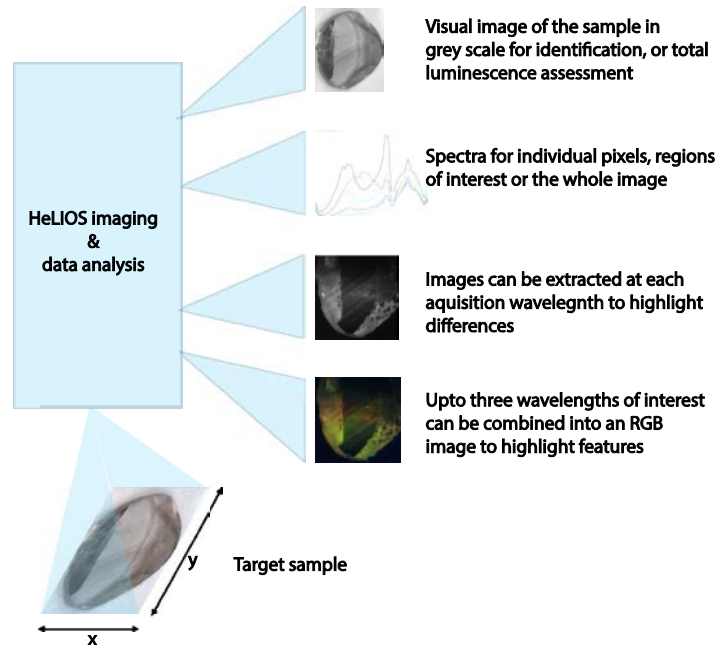


Figure 4-49 Illustration of the data products which may be extracted from a hypercube acquired with HeLIOS.

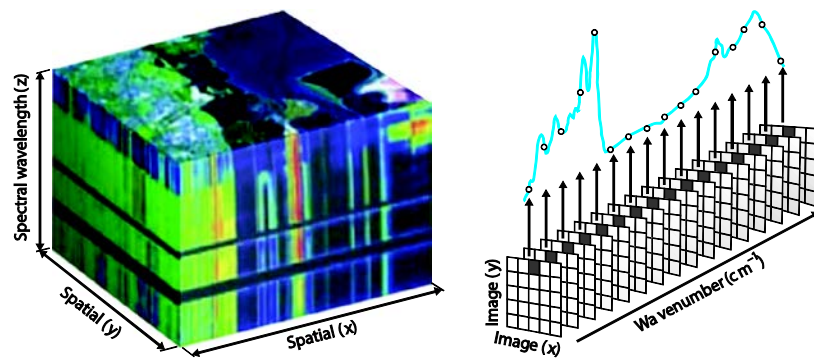


Figure 4-50 Illustration showing how a spectrum from region of interest is extracted from a data cube, such as that acquired with HeLIOS, reproduced from <sup>141</sup>.

Figure 4-51 displays a raw image acquired by HeLIOS of a type Ia banded natural diamond, taken at 14K under 365nm LED excitation. This image is an extract from the hypercube; the filter is set to 700nm. A gradient filter has been applied using Origin to highlight the features. The conversion from digital numbers (DNs) to meaningful units of  $\mu\text{Wcm}^{-2}\text{nm}^{-1}$  has been achieved through the application of radiometric calibration. In Figure 4-52 the raw data have been corrected for dark noise, received a flat field calibration, which can be seen by the reduction in intensity at the centre of the image over the banded region, and the data has been corrected for the filter transmission and detector response. The shape of the LED excitation is clear from these images as a long spread out beam, shown by the dark area above. This shape is due to the large beam size and oblique angle of incidence onto the sample surface.

## 4.4 Experimental data acquisition

---

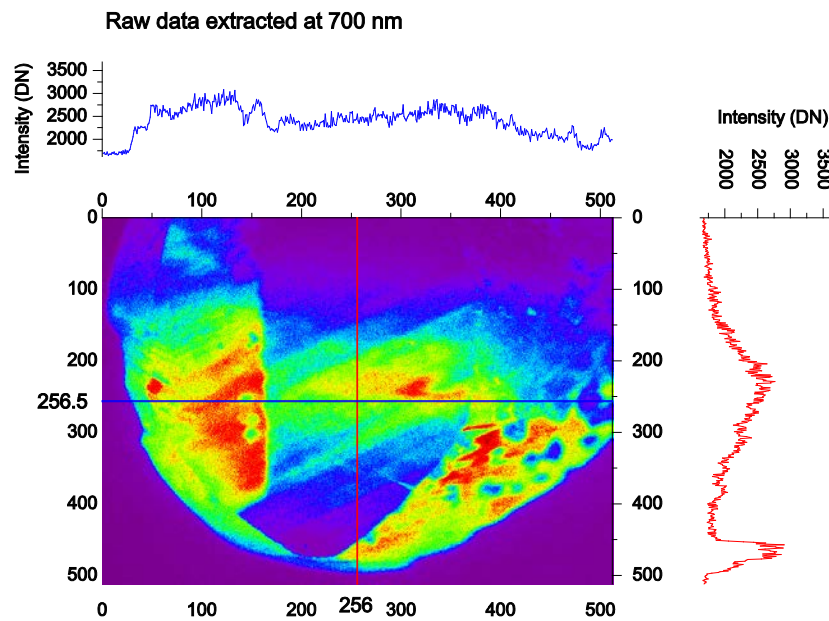


Figure 4-51 Example of a raw image extracted from the hypercube.

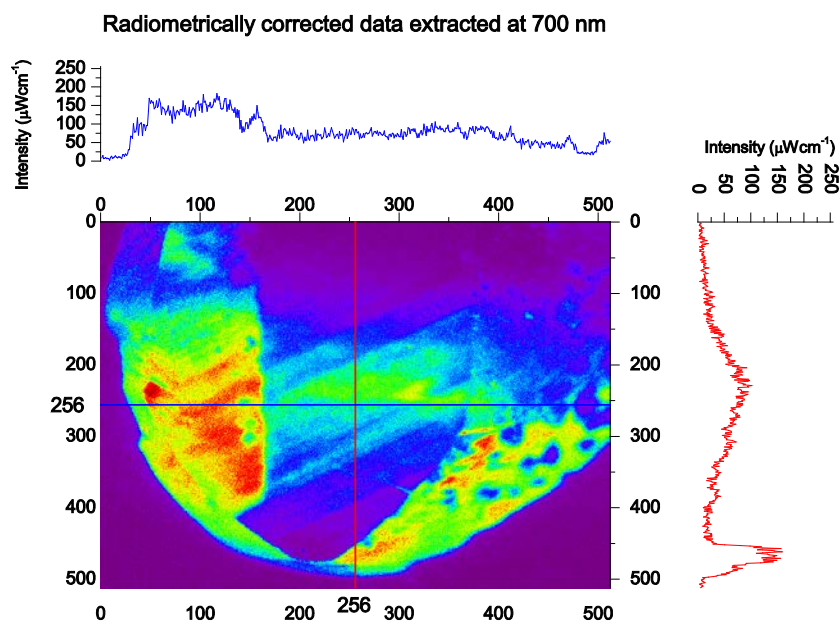


Figure 4-52 Example of a corrected image. The flat field correction has corrected the shape of the profile reducing the vignetting and intensity in the centre of the image enabling the banding to be observed.

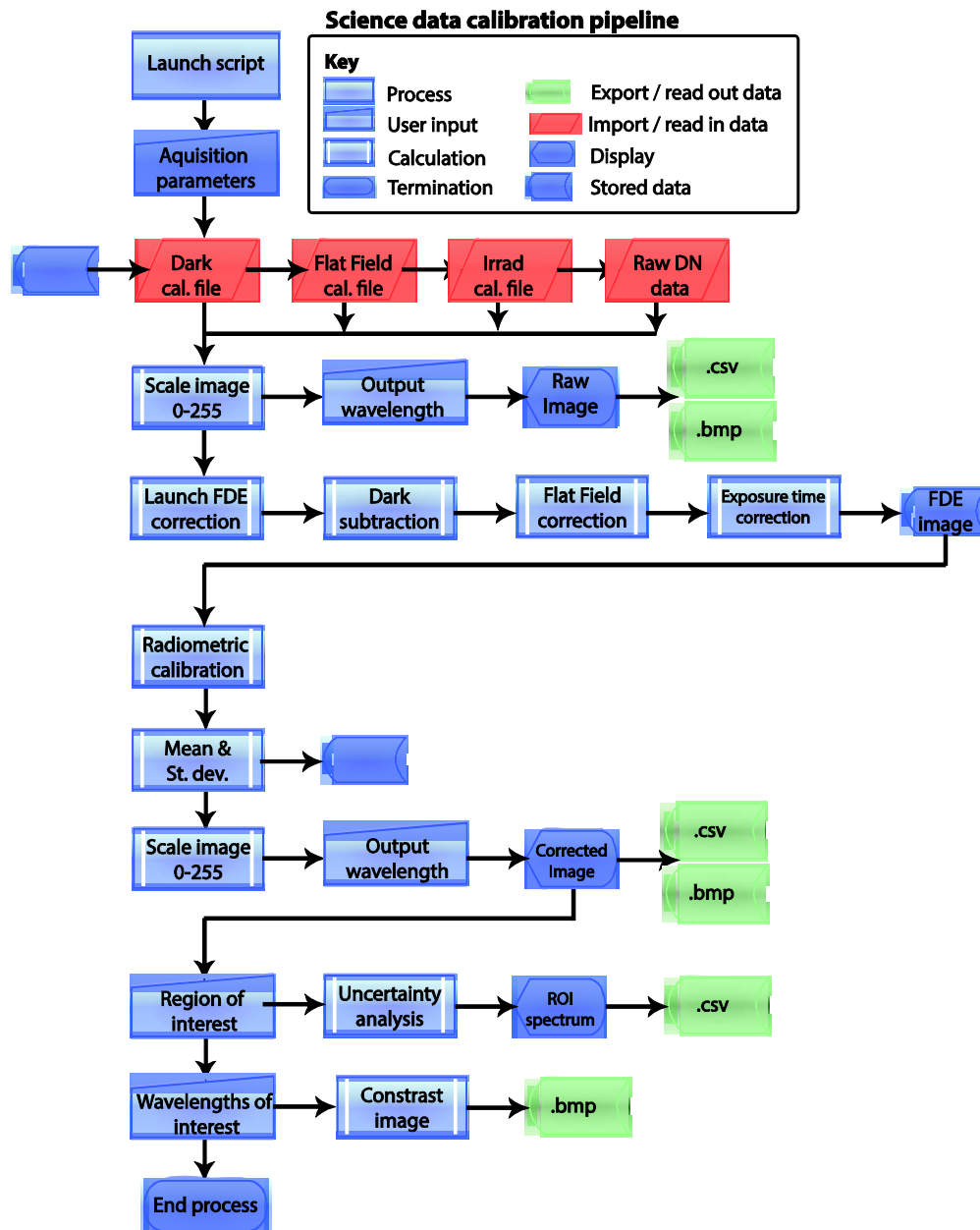


Figure 4-53 Flow chart illustrating the science data processing pipeline.

### 4.5 Chapter Summary

This chapter provided an introduction to the HeLIOS instrument that has been used to acquire the spatially resolved photoluminescence data presented in the next chapter. Here its development has been discussed along with a presentation of its radiometric calibration. The experimental configurations of HeLIOS have been presented, illustrating how both area averaged high resolution PL and calibrated spatially resolved PL can be acquired. A comprehensive calibration and data processing chain has been developed and introduced, along with background information of key terms and concepts. Calibrations have been performed for three microscope objectives (2x, 7.5x and 20x) over a five EM gain and two pre-amplifier values at a constant CCD temperature of -65°C in 10 nm increments of the LCTF. A NIST calibrated lamp has been used to trace an absolute radiometric calibration of HeLIOS back to and to convert acquired data in absolute units. The ability to express data in physical units has enabled the instrument to be selected for use in future investigations of Mars analogue samples and to develop camera characterisation and calibration processing pipelines for use in the calibration of PanCam.



## Chapter 5      Experimental Results

### 5.1 Introduction

This work has focused on the design and development of an instrument for the optical characterisation of wide band gap materials. The ability to relate a material's optical properties to its structure and composition are important to the field of condensed matter physics and the development of new optoelectronic devices. Timely, non-destructive characterisation techniques are beneficial for monitoring the growth of such materials and their commercialisation.

The materials chosen for study here have been selected carefully to represent a common thread and an element of diversity. Diamond has been chosen as the primary wide band gap material for study as natural and synthetic materials can be compared, representing interests from condensed matter to Earth Science. Diamond represents a straightforward system, with a limited number of substitution elements due to the small atomic size of carbon and there is a wealth of literature to compare data acquired with the new HeLIOS system.

A sample group containing a clear natural type Ia with brown banding, two synthetic single crystals, and a synthetic polycrystalline diamond were selected for study. Natural diamond is geologically ancient (3.3 Ga), originating from deep within the Earth's mantle <sup>142</sup>. As an ultra-high pressure mineral, <sup>143</sup> the trace elements present can provide insight into the process which brought them to the surface and where they formed. Shigley *et al* <sup>144</sup> discusses the

## 5.1 Introduction

---

need for further research into natural diamond as a mechanism for understanding the deep Earth. In such research those samples such as the banded diamond studies here are far more interesting due to their inclusions and defects. Diamond acts as protection for such inclusion to some degree, protecting them from the high pressure high temperature environment on their way to the surface. Optical techniques such as photoluminescence Raman are ideally placed to investigate inclusions and residual stress within diamonds.

The extreme properties of diamond make it a desirable material for many applications, however the supply of suitable natural diamonds is constrictive. This has led to the development of synthetic diamonds. Three synthetic samples produced by Chemical Vapour Deposition (CVD) have been selected for study. These include two single crystal diamonds, one a uniform, high quality boron doped sample which gives it a characteristic pale blue colour, the other a largely uniform brown sample with an area of damage to one corner. These were selected to contrast the brown colouration in natural and synthetic diamonds and to contrast single crystal samples of different colours. The final diamond sample selected for study is a polycrystalline CVD with visible graining. This sample is included in the study to investigate the cause of colouration at the grain boundaries. This sample contains a high degree of spatial variation, requiring spatially resolved techniques.

Raman spectroscopy has been used investigate to examine the relationship between stress and colouration in the diamond samples. High-resolution and spatially resolve photoluminescence have been used to investigate the relationship between defects and brown colouration.

In addition to diamond samples a small number of other wide band gap have been included to demonstrate the instrumentation's cross-disciplinary applications and future directions of HeLIOS. A complimentary wide band gap optoelectronic material, ZnO, has been included as a single crystal to compare spatially resolved and high-resolution photoluminescence as due

to its quality there is no spatial variation and intense luminescence. To investigate the potential applications for studying more complex natural materials, a slice of calcium carbonate displaying strong PL under UV excitation with a high degree of spatial variation has been included. Finally, representing one of the most complex systems, a snail operculum has been included to investigate the potential for utilising spatially resolved PL to determine growth structures and mineral inclusions to date and place samples. The added complexity arises from the convolution of PL from mineral and bio-material.

In this chapter each sample is introduced along with a brief review of the associated literature. The data acquired using the optical techniques discussed in chapter 2 are presented for each sample in turn, identifying significant spectral features. Data fitting and presentation of photoluminescence and Raman data have been performed using OriginPro (versions 8 and 9), MagicPlotPro and Labspec6. Spectroscopic transitions, such as those examined here, are associated with specific amounts of energy,  $E$ . When this is measured by a spectroscopic technique, such as photoluminescence and Raman, the line is not infinitely sharp but forms a distinct shape or profile. The maximum possible line width can be determined by considering the lifetime broadening. From the uncertainty principle, the uncertainty in energy  $\Delta E$  and the lifetime of the excited state  $\Delta t$  of an excited state are related by Equation 5-1 below.

$$\Delta E \Delta t \approx \frac{\hbar}{2} \quad \text{Equation 5-1}$$

As the excited state decays exponentially this produces a Lorentzian shape, hence this line shape has been used in the fitting of photoluminescence and Raman data. The expression for this is given by Equation 5-2, Where  $L$  is the standardised Lorentzian function and  $x$  is a subsidiary variable given by Equation 5-3.  $P^0$  is the position of the peak maximum which corresponds to the transition energy  $E$  and  $w$  is the FWHM.

$$L = \frac{1}{1 + x^2} \quad \text{Equation 5-2}$$

$$x = \frac{p^0 - p}{w/2} \quad \text{Equation 5-3}$$

MagicPlot's non-linear curve fitting and decomposition functions have been used for the fitting of all high-resolution spectra. This software utilises an implementation of the Levenberg-Marquardt nonlinear fitting algorithm<sup>145</sup> in which fit function partial derivatives are computed numerically using central difference formula. The profile is characterised by three parameters: location (peak position), height (intensity), and line width (FWHM). Manual selection of peak locations were made to provide the initial guess to the algorithm in conjunction with the peak finding function. Suspected peak locations were identified by examining the second derivative of the spectrum as minima are identified as potential peak locations. The number of peaks included in the fit were gradually added, until a fit was converged upon. The peak positions were then fixed with the height and FWHM set as variables. The fully automatic peak finding and fitting option was not utilised as it was found that although exceptionally good fits could be obtained, this was often due to a large number of peaks, making them effectively meaningless.

## 5.2 Diamond samples

The sixth element in the periodic table, carbon exists in a diverse number of phases and structures. Carbon can be thought of as existing in two primary forms; diamond-like and graphitic-like, each with many allotropes. The neutral carbon atom has a ground state

electronic configuration of  $1s^2 2s^2 2p^2$ , where the core electrons occupy an s-orbital and the four valence electrons are distributed with two in each of the s and p orbitals. When the atom is in a three-fold coordinate configuration the valence orbitals hybridise giving three equivalent  $sp^2$  orbitals, referred to as graphitic-like carbon. Diamond-like carbon arises where the carbon atom is in a four-fold coordinate configuration, with four equivalent  $sp^3$  hybrid orbitals, each with one electron. These form a stable tetrahedral network and are the source of diamond's extreme hardness. These allotropes possess very different properties in electrical conductance, mechanical strength and brittleness to name a few, which are currently being exploited in forms such as carbon nanotubes and graphene. Diamond, both natural and synthetic, is a crystalline wide band-gap semiconductor with an indirect band gap of 5.47 eV at 300 K <sup>146</sup> consisting of carbon atoms, bounded over tetrahedral  $sp^3$  hybrid orbitals in a face centred cubic (FCC) crystal system, illustrated in Figure 5-1. Diamond has a crystalline structure, cubic edge length of 3.567 Å <sup>147</sup>. Diamond is one of the hardest known materials, with the lowest coefficient of thermal expansion, is chemically inert, highly wear resistant, and highly thermally conductive, can be electrically insulating and can be optically transparent in the UV-FIR range. The graphitic phase on the other hand consists of planes of threefold-coordinated atoms, making it the strongest two-dimensional material and leading to it behave as a lubricant due to weak bonding between planes.

## 5.2 Diamond samples

---

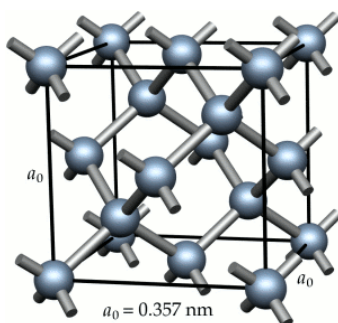


Figure 5-1 Diamond unit cell, spheres representing carbon atoms, reproduced from Sque<sup>148</sup>.

Bulk diamond can be monocrystalline (single crystal) or polycrystalline (crystals are separated by grain boundaries). Both types have been included in this work. In order to make use of diamond in electronic applications, it is necessary to provide n- and p-type varieties. Boron doping is one method of providing a p-type material and as such a boron-doped sample has been included in this work.

Although in this work the samples under investigation are diamonds, graphitic material cannot be neglected, as it is a key parameter to be monitored in the investigation of the origin of brown colouration in diamonds. In this work Raman and PL data are presented owing to Raman's ability to detect and characterise carbon materials and PL's ability to identify defects in the crystal structure.

In nature diamond is formed where carbon is present under high pressure and high temperature conditions deep within the Earth's crust. The history of the formation and life of a natural diamond is reflected in its structure and colour, with inclusions, defects and impurities giving indications of age and conditions of formation. As a result diamond is an interesting material to Earth Sciences <sup>149–154</sup>. An additional, rarer form of diamond is hexagonal lonsdaleite, found only in meteorites <sup>155</sup>. On the realisation of diamond's exceptional properties, research began into synthesis of artificial samples by mimicking

nature via high-temperature high-pressure (HPHT) synthesis. Diamonds of known impurities and concentrations are now able to be grown in volume as large single crystals and polycrystalline samples via chemical vapour deposition (CVD), the conditions of growth are illustrated in Figure 5-2.

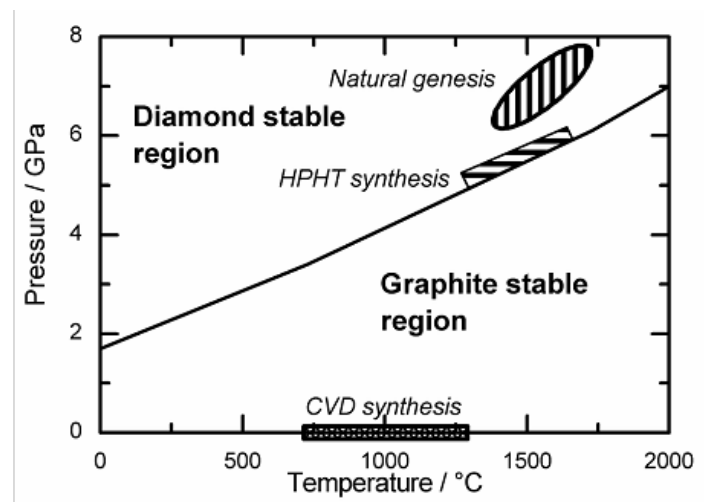


Figure 5-2 Carbon phase diagram, reproduced from Balmer *et al*<sup>156</sup> illustrating the main regions of pressure-temperature space in which diamond growth occurs.

Bundy's phase diagram<sup>157,158</sup>, shown in Figure 5-3, expands on the relationship between pressure and temperature of the carbon phases. In the diagram, solid lines represent equilibrium phase boundaries. The labelled regions can be discussed in turn. *A* represents the region of commercial synthesis of diamond from graphite by catalysis, also referred to as the T, P region used for HP commercial synthesis of diamond from graphite. *B* locates the P/T threshold of very fast (less than 1 ms) solid-solid transformation of graphite to diamond, which yields cubic-type diamond. *C* locates the P/T threshold of very fast transformation of diamond to graphite. It is this region in which diamond crystals are compressed after being embedded in a graphite rod and flash heated to graphitise. *D* represents the region in which

## 5.2 Diamond samples

---

single crystal hexagonal graphite transformation to retrievable hexagonal-type diamond is achieved. E and F locate the upper ends of shock compression/quench cycles that convert hex-type graphitic particles to hex-type diamond and hex-type diamond to cubic-type diamond respectively. The dashed line labelled *H, I, J* represents the path along which a single crystal hex-type graphite compressed in the *c*-direction at room temperature loses some graphite characteristics and acquires properties consistent with a diamond-like polytype, but reverses to graphite upon release of pressure.

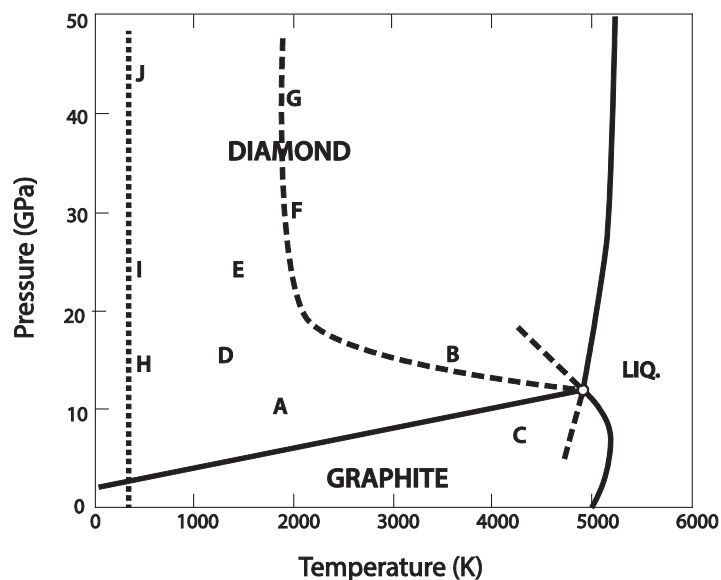


Figure 5-3 Bundy's phase diagram for carbon, reproduced from <sup>157,158</sup>.

As a number of different diamond samples have been investigated is useful to provide a brief explanation of their classification and origins. The physical classification of diamonds is based on their optical absorption features. This system, illustrated in Figure 5-4 below, shows the classification, first posed by Robertson *et al* <sup>159</sup>. It is divided into two branches: type I material in which impurity-related optical and paramagnetic absorption are dominated by nitrogen



defects; and type II diamonds which show no optical and paramagnetic absorption due to nitrogen related defects. Type II diamonds are rare in nature, the majority encountered are synthetic. These two branches are further divided into types Ia, Ib, and Ic. Briefly, type Ia are type I diamonds that do not show absorption due to single substitutional nitrogen atoms. This class can be further broken down into subsets IaA, IaB, IaB', IaB' regular, IaB irregular and IaB without B'. More detail on the features that form these sub-classes can be found in Zaitsev<sup>46</sup>. Type Ib diamonds are type I diamonds that contain paramagnetic single substitutional nitrogen atoms as the dominating defects. Type Ic diamonds are those diamonds containing a high concentration of dislocations. Finally type IIa diamonds are those type II diamonds which do not show specific IR optical absorption due to boron and hydrogen impurities in the one-phonon region.

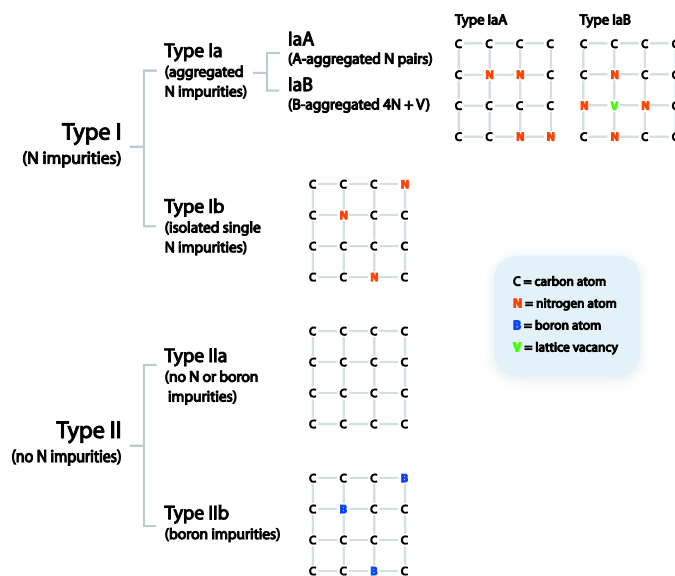


Figure 5-4 Diamond classification figure reproduced from Breeding and Shigley<sup>160</sup>.

## 5.2 Diamond samples

---

As mentioned, diamond possesses very desirable mechanical, thermal, chemical and optical properties making it a candidate for numerous application in which a material is required to operate in extreme conditions of mechanical wear, chemical environments and temperatures. Much focus to date has been on diamonds for mining applications, such as polycrystalline diamond coatings to drills, and to optics such as windows that can dissipate high laser powers. Although much research continues in these areas, research into the use of diamonds as biological carriers for medical applications, such as the delivery of cancer drugs and fluorescence markers is gaining momentum <sup>161–164</sup>. Diamond as an optoelectronic material had been somewhat neglected as other wide band gap semiconductors, such as GaN <sup>165</sup>, came to the forefront. However it is more recently benefiting from resurgence due to new applications. For example diamonds are now at the forefront as the future of quantum computing using the isolated nitrogen vacancy <sup>166–169</sup>.

When produced by synthetic means diamond can be grown to include dopants to alter the electrical properties. With refined techniques large crystals with very low defect densities and atomically smooth surfaces <sup>170,171</sup> can be produced. Nitrogen is an electron donor for diamond, which results in n-type conductivity, however the activation energy is very large resulting in very low room temperature conductivity. Hence useful n-type diamond does not exist in nature, however diamond can be doped by phosphorus to become n-type <sup>172</sup> and by boron to be p-type.

A large number of optical centres can be observed in diamond due to its wide optical transparency range and hardness. There are some two thousand lines currently identified <sup>60</sup>, however this is far larger than the number of centres identified as the majority of zero phonon lines (ZPL) have several phonon or vibrational sidebands. PL spectroscopy has been shown to be sensitive to a number of defects in diamonds <sup>46</sup>. Defects, such as the NV<sup>-</sup> centre, behave as luminescent centres and can be observed as defined spectral features. A large number of defects in diamonds have been attributed in literature to date, and the reader is directed to

a handbook by Dischler <sup>60</sup> for further information. However there are far more spectral features that have been identified, but not ascribed. PL can be used to measure the band gap energy of diamonds, however it is more useful to use it to measure impurities and defects. By determining these, progress can be made to understand the causes of colouration in diamonds. Photoluminescence can be used to discriminate between natural and HPHT-treated diamonds <sup>173</sup> and between natural and synthetic gem-quality diamonds <sup>174</sup>. Performing luminescence measurements at low temperatures is beneficial to reveal fine spectral transitions. This is done through immersing the samples in liquid nitrogen or mounting on a temperature controlled cryostat stage. Examining the literature on diamond and diamond-like material luminescence the majority of studies are performed at 77 K, liquid nitrogen temperature. When cooled, spectral features which could not be resolved at room temperature can be enhanced sufficiently for detection.

Defects cause interruptions in the lattice periodicity; these can be surface, line or point sources. There are three categories of point defects in diamond.

- Impurities; (also known as a substitutional) where a non-carbon atom occupies one of the regular lattice sites. Optical centres from 25 impurities are observed in diamond, with resolved DAP transitions being observed <sup>60</sup>.
- Vacancies; a carbon atom is missing in a lattice site. Vacancy defects affect the optical properties of a material in a number of ways, they can form deep energy levels in the band gap and consequently act as charge carrier recombination or generation centres.
- Interstitials; an atom (carbon or another element) is located at a site other than a substitutional lattice site.

Aberystwyth Materials Group has a strong heritage in the investigation of wide band gap materials, predominately diamonds, through a number of techniques <sup>3,175–178</sup>; therefore

## 5.2 Diamond samples

---

diamonds were a natural choice for the first testing of HeLIOS. Many of the samples studied in this work have previously been studied by members of the group and so serve a baseline for comparison of HeLIOS data with that published by the group. Individual crystals, rather than films, have been studied to avoid the associated stresses that can cause additional shifts and broadening of features when studied using Raman spectroscopy. The diamond samples studied here have not, to the knowledge of the author, undergone any treatment via irradiation, high temperatures or high pressures. They have been studied in their as received state, prepared solely by solvent cleaning protocols prior to examination unless stated. As discussed in chapter 2, Raman spectroscopy is a powerful technique for the study of carbon materials such as diamond and graphite. Diamond has a relatively large Raman scattering cross-section, the probability of Raman scattering, at  $r_{sp3} = 9 \times 10^{-7} \text{ cm}^{-1}\text{sr}^{-1}$ <sup>46</sup>. However this is far smaller than that of graphite at  $r_{sp2} = 5 \times 10^{-5} \text{ cm}^{-1}\text{sr}^{-1}$ <sup>46</sup>. The ratio of diamond to graphitic material can be calculated by taking ratios of the  $1332 \text{ cm}^{-1}$  (diamond) and  $1550 \text{ cm}^{-1}$  (graphitic) peaks. The  $1550 \text{ cm}^{-1}$  band is fitted with contributions from the D and G peaks ( $1345 \text{ cm}^{-1}$  and  $1560 \text{ cm}^{-1}$ ) and a low intensity band at  $1470 \text{ cm}^{-1}$  due to tetrahedral bonded diamond precursor. The respective amounts are calculated by considering the Raman cross sections of diamond and graphite which is given by 1:50<sup>46,179,180</sup>. This relationship is expressed in Equation 5-4 where  $A_d$  and  $A_i$  are the respective areas under the fitted curves corresponding the diamond peak and the graphitic bands<sup>181</sup>.

$$C_d = \frac{100A_d}{\left(A_d + \frac{\sum A_i}{50}\right)} \quad \text{Equation 5-4}$$

The spectral position of the first order diamond Raman line is not seen to change with varying excitation wavelengths in the 244-780 nm range <sup>182</sup>. These data have been acquired in this window allowing comparison with literature on the assignments of peaks.

Raman mapping can be used to probe the inhomogeneous distribution of carbon allotropes, for example to investigate non-sp<sup>3</sup> bonded carbon distribution <sup>183</sup>.

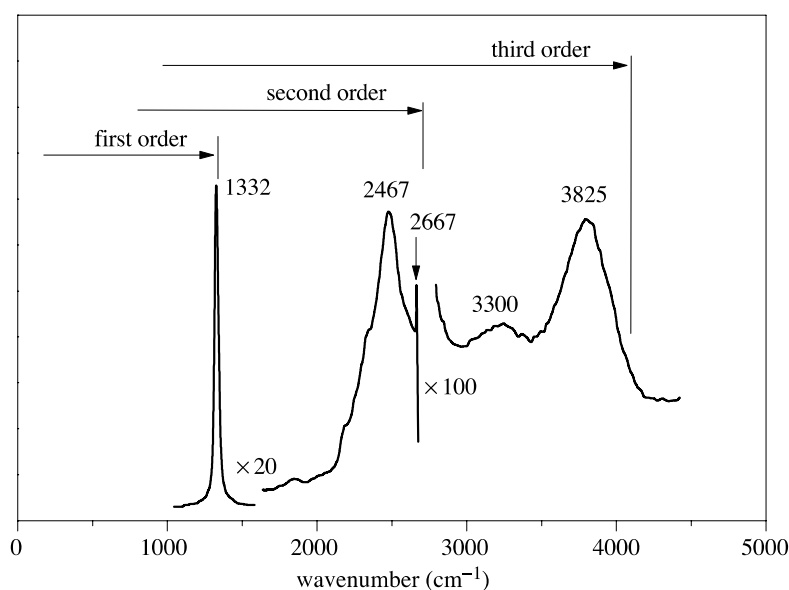


Figure 5-5 Example Raman spectrum of a gem-quality diamond illustrating the first, second, and third order Raman features. Reproduced from Praver *et al* <sup>45</sup>.

## 5.2 Diamond samples

| Position (cm <sup>-1</sup> ) | Typical FWHM (cm <sup>-1</sup> ) | Details  |
|------------------------------|----------------------------------|--|
| 520                          | 3-5                              | First order silicon Raman peak   |
| 1100-1150                    | 40-80                            | Grain boundary defects   |
| 1332                         | 1.5-10                           | First order diamond Raman line   |
| 1345                         | 250                              | D-Peak, sp <sup>2</sup> amorphous carbon   |
| 1430-1470                    | 80                               | Grain boundary defects   |
| 1520-1580                    | 100                              | G-Peak, sp <sup>2</sup> amorphous carbon. Ordered graphitic material present a band centred around 1580 cm <sup>-1</sup> , corresponding to the in-plane vibration of aromatic carbons |
| 1620                         |                                  | D'-peak, sp <sup>2</sup> amorphous carbon  |

Table 5-1 Characteristic Raman spectral feature of diamond

Internal stress in synthetically grown diamonds accumulated either during or after deposition can have significant effects on the material's properties. Those with tensile stress are prone to splitting and spalling, where those in compression are prone to peeling and delamination<sup>147</sup>. Raman spectroscopy can be used to analyse the internal stress of diamonds and has been extensively used by many authors to investigate the chemical composition, inherent stress and crystallinity of a wide range of diamond samples<sup>181,184–193</sup>. Distortion from a perfect cubic lattice by variations in bond length and angle influence the position and width of the first order Raman line, located at 1332.5 cm<sup>-1</sup><sup>194</sup>. This peak acts as a very sensitive indicator for applied stress, shifting to higher frequencies under compressive stress and to lower frequencies in response to tensile stress<sup>147</sup>. Wang *et al*<sup>147</sup> proposed a method for measuring stress in polycrystalline diamond films based on Raman stress analysis of silicon grown on a sapphire substrate as the basis for quantitative measurements. Assuming biaxial stresses are present, the degree and nature of stress can be estimated using Equation 5-5 below:

$$\sigma = -1.08 \frac{\text{GPa}}{\text{cm}^{-1}} \Delta\nu \quad \text{Equation 5-5}$$

where  $\Delta\nu$  is the magnitude of the Raman peak shift from the strain-free position at 1332  $\text{cm}^{-1}$ . The magnitude of the coefficient term is a source of disagreement between authors; Ferreira *et al*<sup>181</sup> use a far smaller value of -0.345 and Wang *et al*<sup>147</sup> suggest the figure above of -1.08. On review, it is considered more accurate to use the coefficient for uniaxial stress, 2.88, as used by a number of authors including Collins<sup>52,195,196</sup>. The quantification of stress or strain in diamonds by Raman spectroscopy is further complicated by domain size, temperature, non-hydrostatic stress, degeneracy lifting and multiple peaks<sup>197</sup>.

The diamond samples studied in this work are summarised in Table 5-2.

## 5.2 Diamond samples



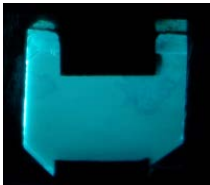
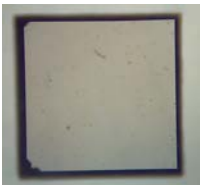

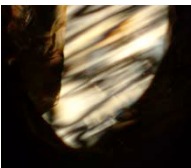
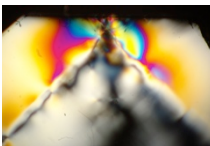

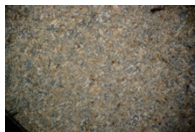
| Sample                                | A65-40-03   | A65-40-04   | 0473904-O  | 0473906-T   | 980134 EDGE   |
|---------------------------------------|---|---|--|---|---|
| Photograph<br>(White light)           |  |  |  |  |  |
| Photograph<br>(Cross polarised light) |   |  |  |  |  |
| Type                                  | Ia<br>Natural   | Ia<br>Natural   | Single crystal CVD   | Single crystal CVD  | PCD CVD fine  |
| Orientation                           | (110)   | (110)   | (100)  | (100)   |   |
| Dimensions                            |   |   |  |   |   |
| Appearance                            | Clear with diagonal brown banding   | Clear with diagonal brown banding   | Uniform pale blue  | Uniform brown with chip to one corner   | Fine brown speckles throughout  |
| Weight (ç)                            | 0.26  | 0.37  | 1.9  | 0.7   |   |
| Techniques applied                    | ApREES PL, XEOL   | HeLIOS PL Raman   | HeLIOS PL Raman  | HeLIOS PL, Raman  | HeLIOS PL, Raman  |

Table 5-2 Diamond samples studied in this work

### 5.2.1 Natural diamonds

Natural diamonds are found to be predominantly from peridotitic and eclogitic domains deep in the subcratonic lithospheric mantle<sup>149</sup>. The most straightforward method of diamond formation is the isochemical conversion of graphite into diamond. For this high activation energies are needed to cross the phase boundary (seen in Figure 5-2 and Figure 5-3), which can occur under high pressure, high temperature conditions (HPHT). Redox reactions are proposed as alternatives to this direct conversion<sup>149</sup>. Of the 25 observed photoluminescence centres in diamonds, only six



of are observed in natural diamond (H, B, N, Si, Ni, and Al). The remainder are introduced during synthetic growth, doping or ion implantation.

#### **5.2.1.1      Ia Banded Natural Diamond**

Two type Ia banded natural diamonds were available for study during the course of this work, kindly provided by Diamond Trading Company. The two samples were cut from the same stone and polished to provide (110) faces for study with the banded regions near the surface. The first, A65-40-03, was only used for PL in the ApREES as it was necessary to maintain a clean surface for other experiments which the author was not involved in. The second, A65-40-04, was used for HeLIOS and Raman investigations as it was available for mounting on carbon tape to allow transfer between instruments.

Samples such as these are of interest for spatial resolved measurements due to their variegated nature. By sampling on and off the brown-banded regions spectral features attributed to the different regions can be resolved, adding to the current understanding of the colouration in diamonds. Such diamonds containing clear and coloured banded regions have been referred to in literature as ‘zebra’ diamonds due to their characteristic stripes <sup>198,199</sup>. Figure 5-6 below, taken using a DSLR mounted to an optical microscope, illustrates the brown-banded regions on the cut and polished (110) face.



Figure 5-6 Ia banded natural diamond photographed via microscope, 4x magnification, using white light. The polished (110) face is shown with brown banding near the surface. Image width is 4mm.

### 5.2.1.1.1 Cross-polarisation

Prior to study by PL and Raman, cross-polarisation images were acquired using the method detailed in Chapter 2. In Figure 5-7 below, birefringence patterns are clearly visible when viewed between cross-polarisers, a) and c), and with the addition of a  $\frac{1}{4}\lambda$  filter to provide additional contrast, b) and d). A high degree of internal stress can be observed in the sample from the birefringence patterning in the same direction as the brown bands. When the colour intensity generated when using the  $\frac{1}{4}\lambda$  filter is compared to the standard Michel-Levy chart<sup>200</sup> the lighter green-turquoise regions correspond to the largest birefringence.

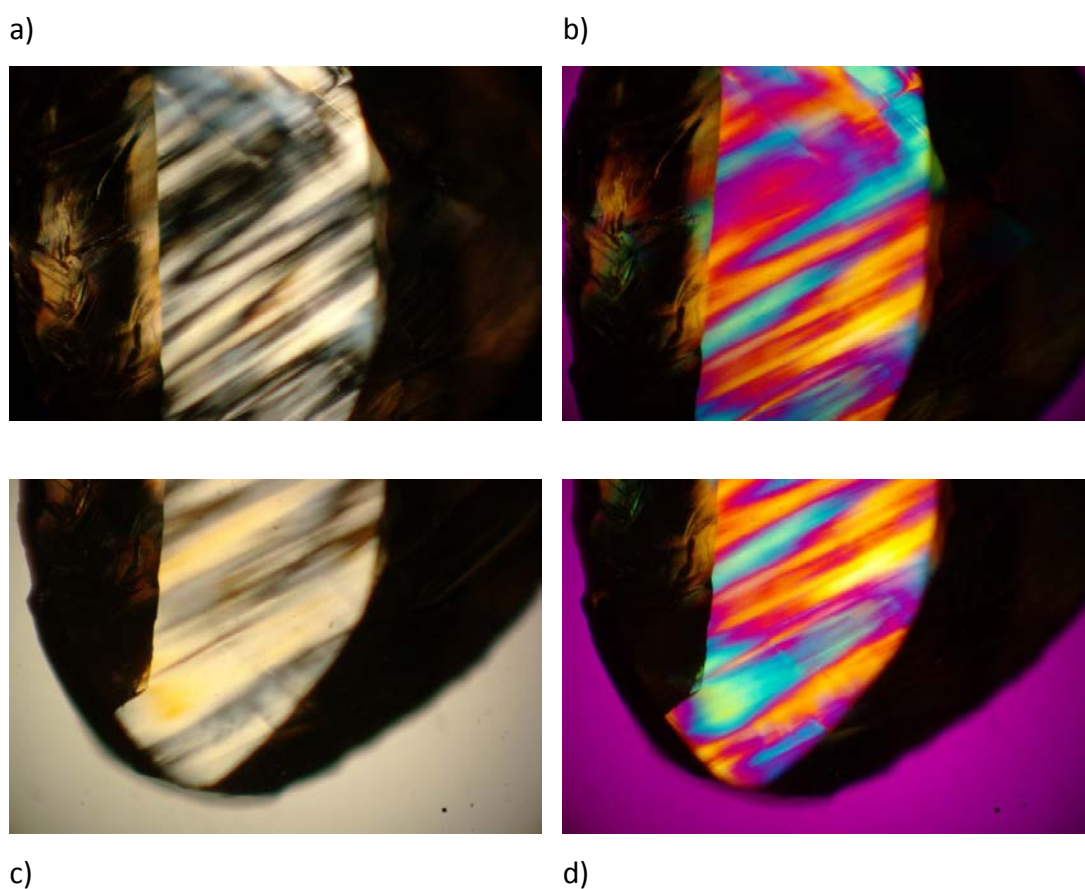


Figure 5-7 Ia banded natural diamond cross-polarisation microscopy under 4x magnification; a) and c) imaged between cross polarisers, b) and d) with the addition of  $\frac{1}{4} \lambda$  filter. The tatahi pattern is clearly observed in the polished face aligned with the direction and location of the brown banded area. Image width is 4mm.

#### 5.2.1.1.2 HeLIOS high-resolution PL

The data presented in this section were acquired using HeLIOS and an iHR320 spectrometer at 2x magnification, with additional 395 and 400 nm long pass filters to block reflected light from the excitation source. The experimental configuration can be seen in Figure 4-3. The full acquired range and fitted peaks corresponding to characteristic defects of interest to this work are presented here.

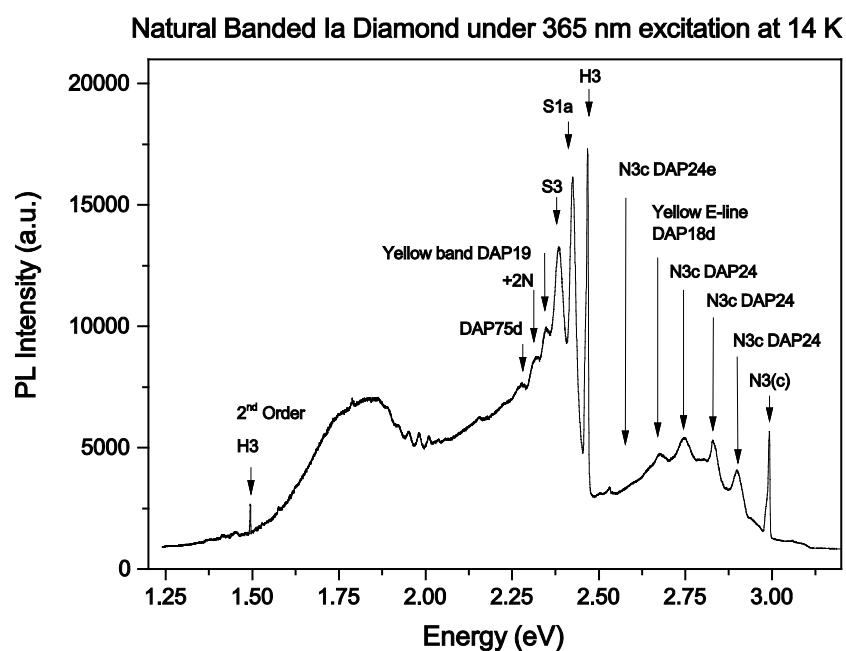


Figure 5-8 Hi-resolution PL of the natural type Ia banded 'zebra' diamond under 365 nm LED excitation at 14K.

Figure 5-8, above, shows an example spectrum acquired of the natural Ia banded diamond. Held at such low temperatures during measurement (14K), this sample exhibits many strong spectral features, which is expected for a natural diamond of mixed composition due to the variegation.

The following figures focus on the different regions of the spectrum that can be fitted to allow identification of spectral features by their position, shape and relationship to each other. The identified features are presented in table form with reference to published literature. Some variation is present in the published values hence identification has been made by comparison with literature (experimental and theoretical) and accounting for the relationship between features to identify families of lines associated with donor pair acceptors (DAPs) or zero phonon lines (ZPLs) and their vibrational sidebands.

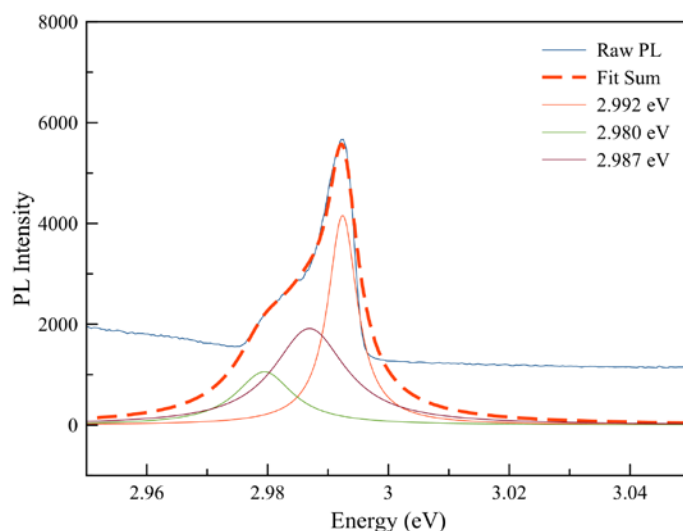


Figure 5-9 Ia natural banded diamond fitted violet region of PL spectrum.

Table 5-3 lists the features identified by curve fitting of the violet portion of the PL spectrum shown in Figure 5-9 and their assignments.

| Observed<br>eV |       | Description   | Reference  |
|----------------|-------|---|------------|
| 2.992          | 414.6 | 2.990 eV is DAP22e $V_1N_3^+$   | 201,202    |
|                |       | 2.991 eV luminescence line in natural diamond, DAP113 ZPL seen in Si rich natural brown diamond associated with $V_1Si_1^-$   |            |
| 2.980          | 416.0 | 2.980 eV 2Ni-DAP105b, $(V_3N_2)^+$  | 203        |
| 2.987          | 415.1 | 2.985 eV is N3a (also referred to as N3c) centre $V_1N_3^0$ ZPL of DAP24a-q, the excited state splitting $D_0$ . It is associated with the addition of 3 nitrogen atoms and corresponds with DAP 23a-p/24 which was formerly referred to as just 'N3' centre. It has three ZPL transitions; 2.297, 2.680, and 2.985 eV with sideband structure. Only this last ZPL is observed as the other two are only visible in delayed luminescence. The overall structure comprises of many sidebands. It is most commonly seen in type I and IIa insulating diamonds | 60,204–207 |

Table 5-3 Ia natural banded diamond identified PL features

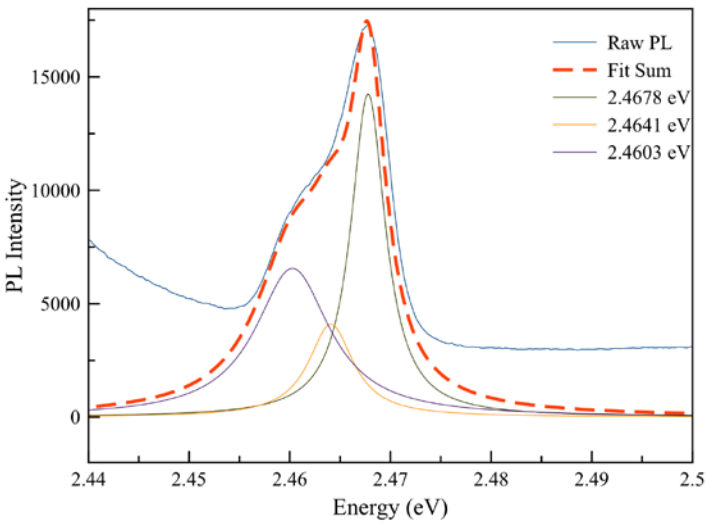


Figure 5-10 Ia natural banded diamond fitted blue region of PL spectrum.

Table 5-4 lists the features identified by curve fitting of the blue portion of the PL spectrum shown in Figure 5-10 and their assignments.

| Observed<br>eV |       | Description  | Reference |
|----------------|-------|--|-----------|
| 2.468          | 502.4 | 2.467 eV a feature observed in natural brown diamond (NBD)   | 208,209   |
| 2.464          | 503.2 | 2.464 eV H3a centre $V_1N_2^0$ , which can be seen to vary between 2.462-2.465 eV, it is a ZPL of DAP51a-f, observed in both natural and synthetic diamonds. H3 is a fundamental defect, arising from the inclusion two nitrogen atoms. It is also a ZPL of DAP 50.<br><br>There may also be a contribution from a feature at 2.463 eV observed in NBD due to the $\beta$ -line of the S1 centre, S1b, which is a ZPL of DAP43a-g corresponding to $V_1N_2^+$ observed in natural Ia and Ib diamond. | 46,210    |
| 2.460          | 504.0 | 2.460 eV associated with diamond-like carbon (DLC) in non-diamond phases   | 46,211    |

Table 5-4 Ia natural banded diamond identified PL features

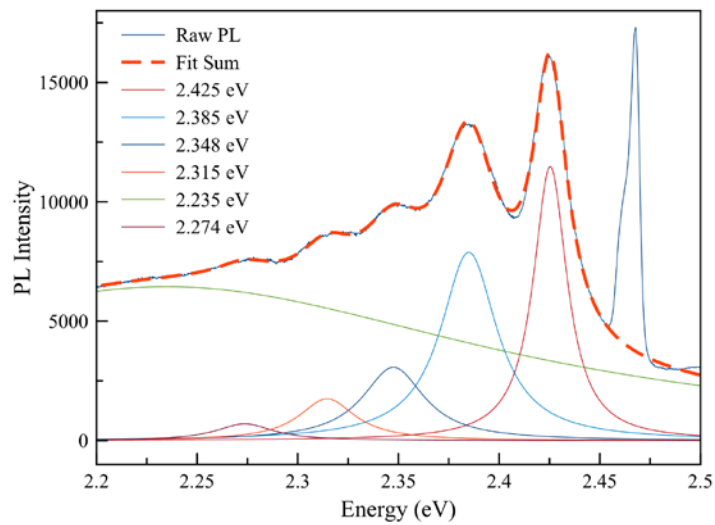


Figure 5-11 1a natural banded diamond fitted green region of PL spectrum.

Table 5-5 lists the features identified by curve fitting of the green portion of the PL spectrum shown in Figure 5-11 and their assignments.

## 5.2 Diamond samples

| Observed<br>eV |       | Description  | Reference      |
|----------------|-------|--|----------------|
|                | nm    |  |                |
| 2.425          | 511.3 | The S1a centre is located at 2.429 eV $V_1N_1^0$ , and calculated to be at 2.422 eV. 2.429 eV is the $\alpha$ -line and ZPL of the S1 centre, which is common to natural diamonds of the mixed Ia and Ib types. The $\beta$ -line at 2.463 eV (503.2 nm) is the main line of the S1 centre. This doublet is due to the splitting of the excited state. The S1 centre is seen in brown natural diamonds exhibiting no yellow luminescence under 365 nm excitation. Energy transfer between the S1 and H3 centres decreases the luminescence intensity of the S1 centre<br><br>There is also an unassigned feature observed at 2.424 eV in NBD, however considering the spectrum as a whole it is more like the S1 centre above. | 46,210,212–214 |
| 2.385          | 519.9 | A feature observed in natural diamond is that at 2.382 eV of DAP76i tentatively attributed to $V_1N_3^-$ observed in natural brown diamond<br><br>2.383 eV S3 ( $V_2Ni_1$ ) $N_2^+$  | 214            |
| 2.348          | 528.0 | 2.347 eV DAP19f $N_2^0+B_1^-$ observed in natural brown diamond. DAP19a-j is made of ten PL lines superimposed on the 2.35 eV broad band or the 'yellow band'  | 215 195        |
| 2.315          | 535.6 | 2.312 eV S1b-DAP43e $V_1N_1^0$<br><br>2.31 eV sideband of DAP75 ( $V_3Si_2$ ) $^-$   | 215 46         |
| 2.235          | 554.7 | 2.239 eV DAP1d $N_1^0+B_1^0$   | 202            |
| 2.274          | 545.2 | 2.270 eV DAP9w $N_1^++B_1^0$ , part of the B band / DAP19 'yellow' band family   | 195            |

Table 5-5 Ia natural banded diamond identified PL features



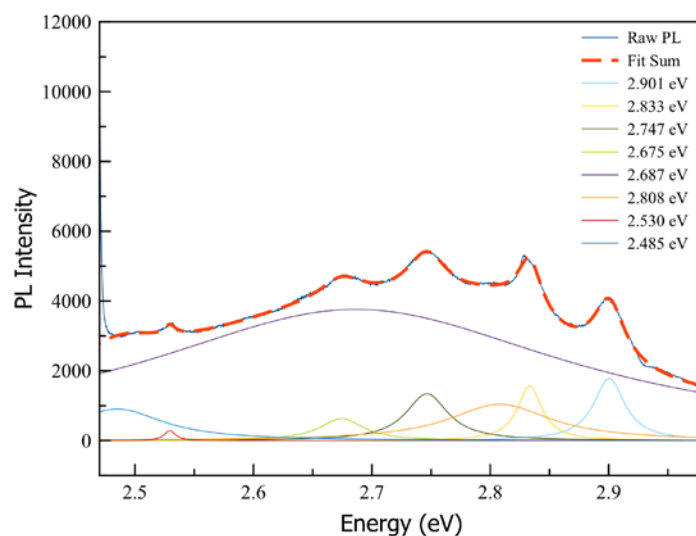


Figure 5-12 Ia natural banded diamond fitted blue-violet region of PL spectrum.

Table 5-6 lists the features identified by curve fitting of the blue-violet region of the PL spectrum shown in Figure 5-12 and their assignments.

| Observed<br>eV |        | Description   | Reference |
|----------------|--------|---|-----------|
| 2.901          | 427.53 | 2.91 eV (426 nm) weak centre observed in some natural grey diamonds   | 216       |
| 2.833          | 437.15 | 2.834 eV (437.5 nm) N3c-DAP24j $V_1N_3^0$<br>2.836 eV (437.2 nm) N3c-DAP24k $V_1N_3^0$<br>A natural diamond luminescence line is observed at 2.827 eV, related to N3c-DAP34i $V_1N_3^0$ |           |
| 2.747          | 451.41 | A natural diamond luminescence line is observed in natural brown diamond at 2.748 eV related to DAP18d, referred also as the yellow E line  |           |
| 2.687          | 462.98 | 462.9cm N3cDAP24e $V_1N_3^0$  |           |
| 2.530          | 490.16 | Nearest feature is that at 2.526 eV DAP76z $V_1N_3^-$ , a ZPL of that DAP   |           |

Table 5-6 Ia natural banded diamond identified PL features

## 5.2 Diamond samples

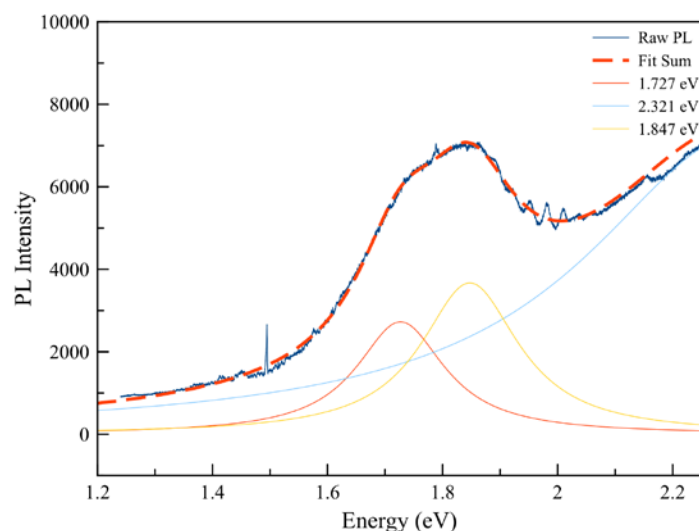


Figure 5-13 Ia natural banded diamond fitted NIR-yellow region of PL spectrum.

Table 5-7 lists the features identified by curve fitting of the NIR-yellow region of the PL spectrum shown in Figure 5-13 and their assignments.

| Observed<br>eV |        | Description  | Reference |
|----------------|--------|--|-----------|
| 2.009          | 617.03 | Feature observed in natural diamond DAP9p $N_1^+ + B_1^0$ at 2.007 eV  | 217       |
| 1.981          | 625.73 | Nearest feature to link to is that at 1.980 eV DAP20f due to $N_2^0 + B_1^0$   | 60        |
| 1.951          | 635.46 | Feature at 1.951 DAP9m due to $N_1^+ + B_1^0$  | 60        |
| 1.818          | 682.0  | This broad band feature can be attributed to the band observed in natural diamond known as the B band, DAP9 due to $N_1^+ + B_1^0$ this feature is reported to have a structure of twenty lines over the range 1.743 eV to 2.138 eV which agrees with the set of features observed in this region. | 60        |
| 1.494          | 830.0  | This feature is a 2 <sup>nd</sup> order of the high energy features as there was no higher order blocking in use during measurement.   | 60        |

Table 5-7 Ia natural banded diamond identified components

The two broad bands centred at 1.847 eV and 1.727 eV make up the large feature in this region, with smaller, narrow luminescence lines on top. The majority of features in this region, which form the band at approx. 1.8 eV, are attributed to nitrogen and boron DAPs. The broad B-band of DAP9 ( $N_1^+ + B_1^0$ ) and the red-band are also present in this region. The smaller features on top of this broad band can be mostly attributed

to DAP9. The 1.8 eV B-band, broad band seen in natural brown diamonds, may be related to dislocations<sup>212</sup>. Wight<sup>217</sup> and Reinitz<sup>216</sup> propose this as being boron related,  $N_1^+ + B_1^0$  and comprised of 20 lines (DAP9).

#### **5.2.1.1.3 HeLIOS spatially resolved PL**

Hyperspectral PL data has been acquired of the sample, focusing on the chipped corner of the sample displaying darker colouration. These data have been processed using the calibration protocols discussed in Chapter 4 to provide radiometrically corrected, spatially resolved PL data from regions of interest (ROIs) of different sizes. Figure 5-14 provides an example of an image, 700 nm, extracted from the hypercube. The brown-banded region is more clearly visible as bright diagonal lines in the data. The remainder of the polished face displays less intense luminescence. The brightest region across the centre of the images corresponds to the oblique excitation beam across the sample.

## 5.2 Diamond samples

---

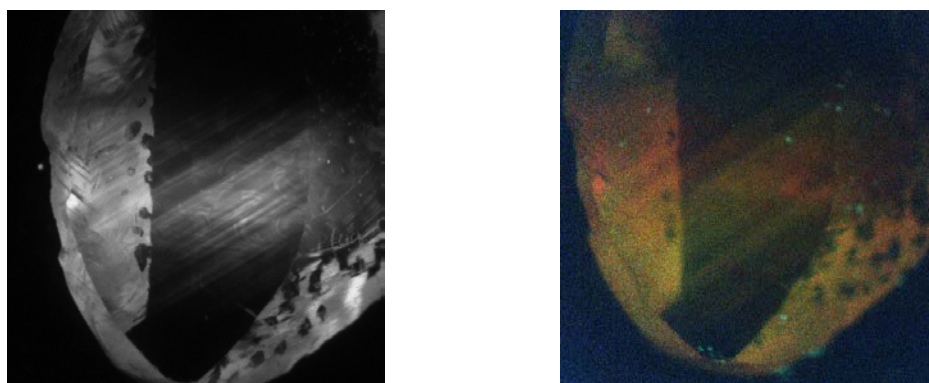


Figure 5-14 Corrected PL image of natural banded diamond at 700 nm, 2x magnification under 365 nm excitation at 14K, (left), and composite RGB image R=700, G=510, and B=450 nm, (right).

Taking three such extracted images and assigning to an RGB channel (Red, Green, and Blue) these can be combined into a colour image to highlight the photoluminescence distribution, illustrated on the right of Figure 5-14.

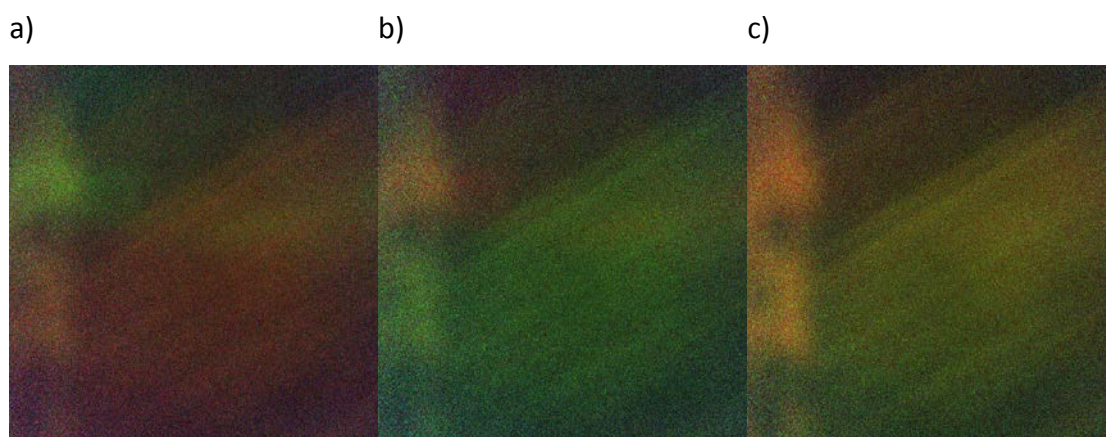


Figure 5-15 composite RGB images under 365 nm excitation, at 14K 7.5x magnification; a) R=510, G=580, and B=430 nm, b) R=580, G=510, and B=430 nm, and c) R=710, G=510, and B=450 nm.

Figure 5-15 above applies the same technique to images acquired at a higher magnification.

Selecting ROIs from an examination of the individual images of the data cube corresponding spectra can be extracted. Figure 5-16 illustrates such data. ROI2

corresponds to a bright area in the banded region, showing a clearly different spectra profile. ROIs 1-3 are generated from 10 x 10 pixel sections, and ROIs 4 and 5 are generated from 5 x 5 pixels selections. The uncertainty in the radiometrically calibrated PL intensity is illustrated with error bars. It can be seen, as expected, that in regions of weak emission, such as ROI 1, the error bars are far larger in the higher energy region. This corresponds to the low transmission at short wavelengths of the LCTF and the effects of overcompensation by the flat field correction on a weak signal. As the data presented here are in units of  $\mu\text{Wcm}^{-1}\text{eV}^{-1}$ , the PL intensity from different sized regions can be compared.

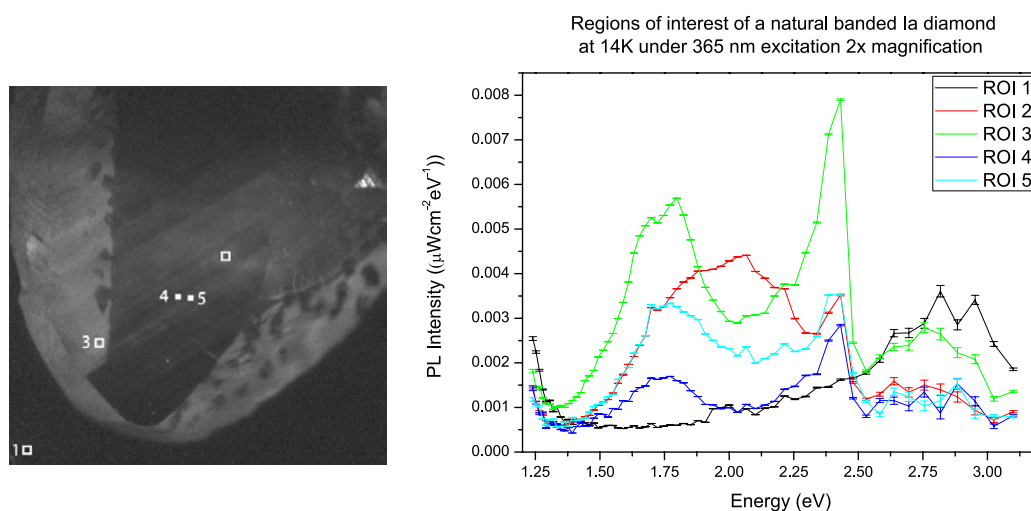


Figure 5-16 Radiometrically corrected ROI spectra of natural banded diamond imaged at 2x magnification under 365 nm excitation at 14K. ROIs 1-3 are comprised of 10x10 pixel selections and ROIs 4-5 of 5x5 pixel selections.

## 5.2 Diamond samples

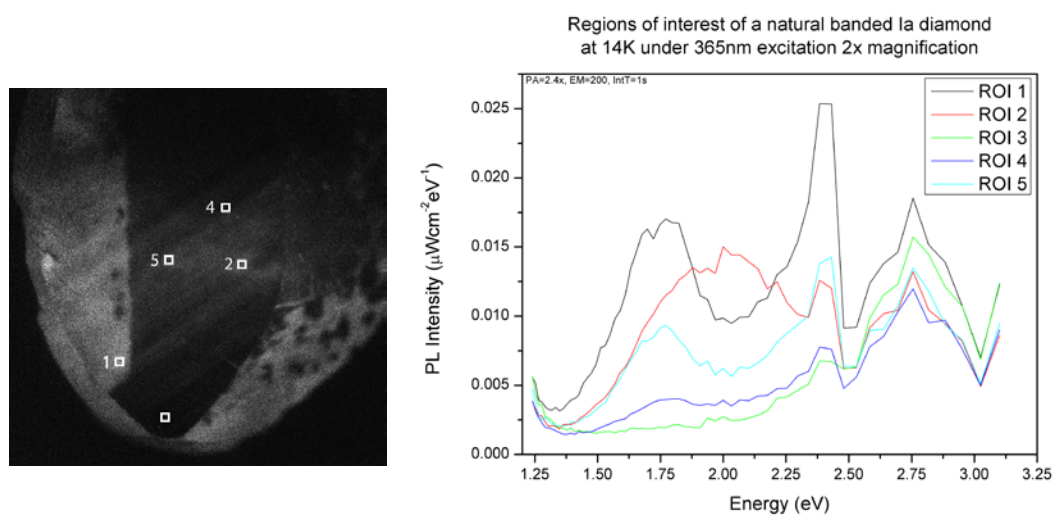


Figure 5-17 Radiometrically corrected ROI spectra of natural banded diamond imaged at 2x magnification under 365 nm excitation at 14K. All ROIs are comprised of 10x10 pixel selections.

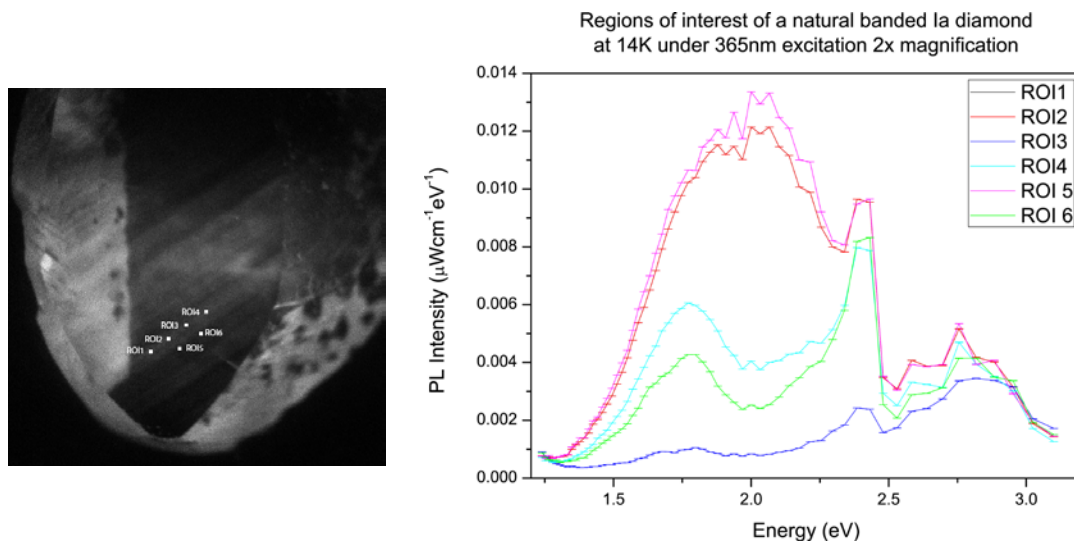


Figure 5-18 Radiometrically corrected ROI spectra of natural banded diamond imaged at 2x magnification under 365 nm excitation at 14K. All ROIs x are comprised of 5x5 pixel selections.

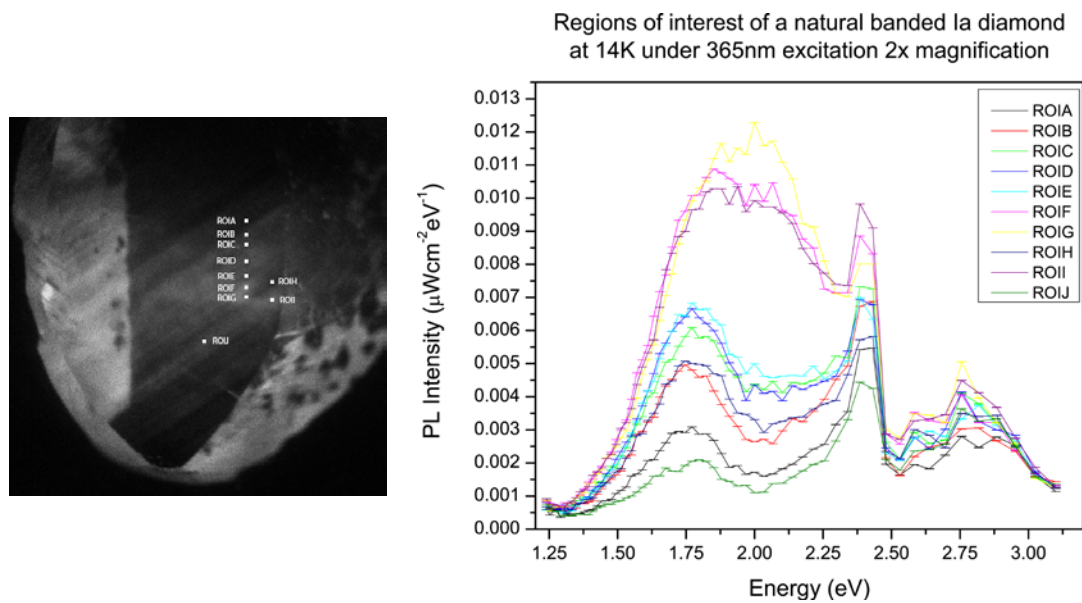


Figure 5-19 Radiometrically corrected ROI spectra of natural banded diamond imaged at 2x magnification under 365 nm excitation at 14K. ROIs x are comprised of 5x5 pixel selections.

## 5.2 Diamond samples

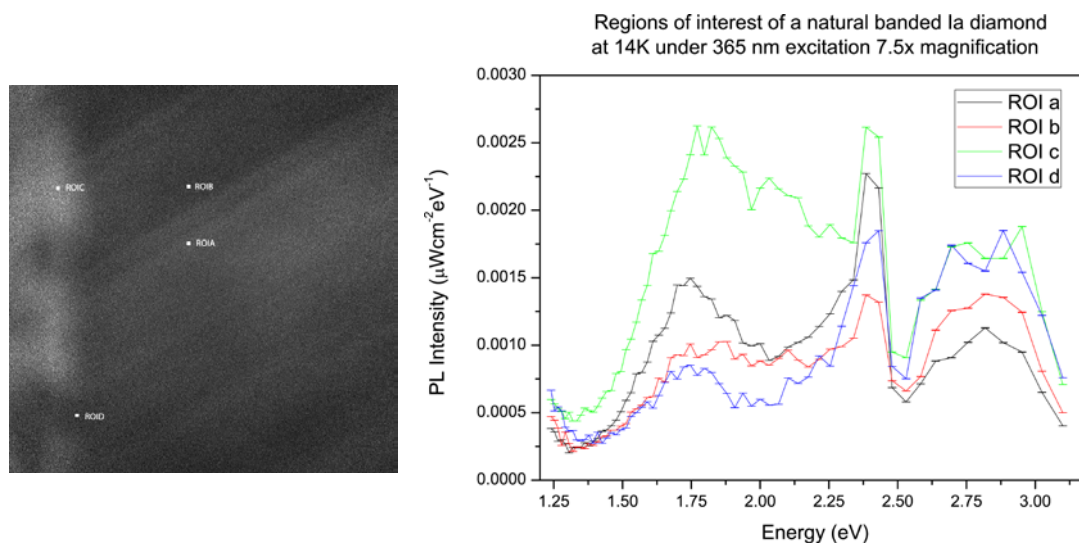


Figure 5-20 Radiometrically corrected ROI spectra of natural banded diamond imaged at 7.5x magnification under 365 nm excitation at 14K. All ROIs are comprised of 5x5 pixel selections.

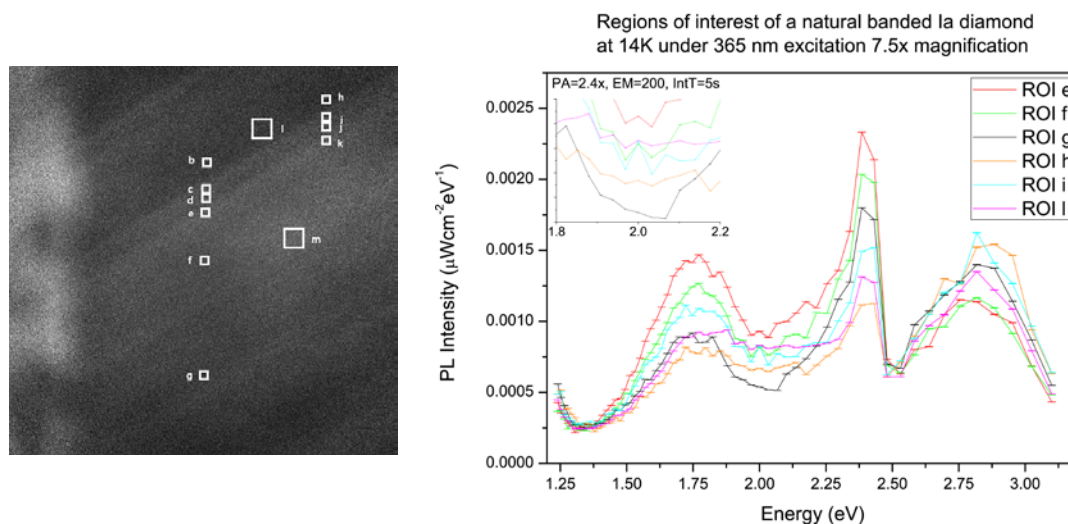


Figure 5-21 Radiometrically corrected ROI spectra of natural banded diamond imaged at 7.5x magnification under 365 nm excitation at 14K. ROIs l and m are comprised of 20x20 pixel selections and the remainder of 5x5 pixel selections.



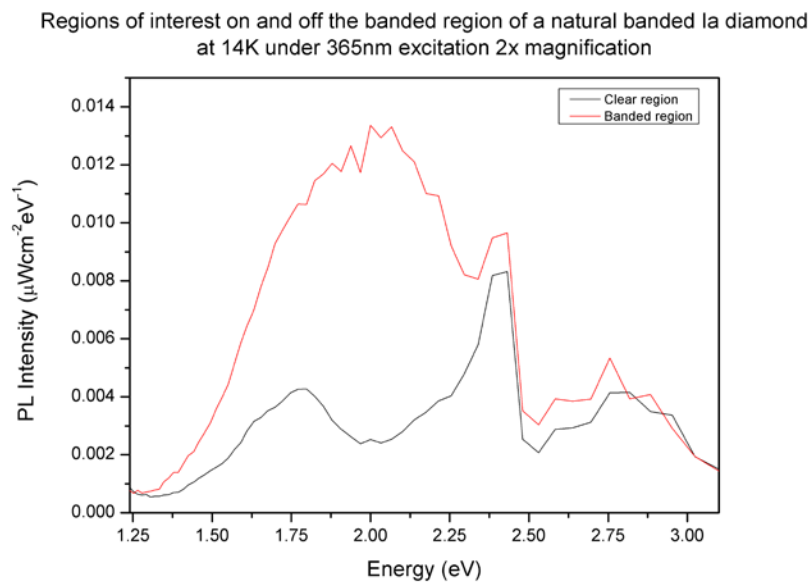


Figure 5-22 Spatially resolved ROI on and off banded region.

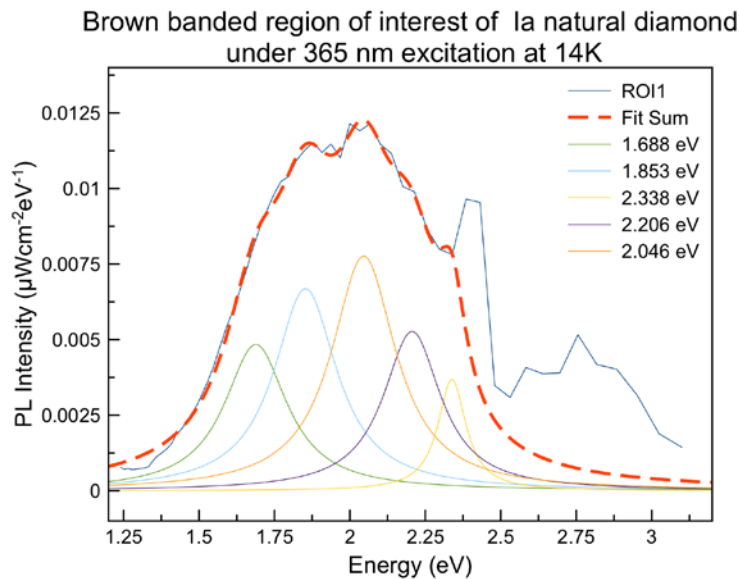


Figure 5-23 Fitted ROI of the spatially resolved data from a brown banded region.

## 5.2 Diamond samples

| Observed |       | Description  | Reference                          |
|----------|-------|--|------------------------------------|
| eV       | nm    |  |                                    |
| 1.688    | 734.5 | 1.681 eV is the Si centre, common in CVD diamonds and observed in a small number of type I natural diamonds. Formation of this centre leads to a reduction in the PL intensity, and has been seen to correlate with the Raman line intensity. It is a complex centre comprising of a large number of features<br><br>Natural diamond luminescence feature DAP4b located at 1.689 (734.0 nm) attributed to a N <sub>2</sub> related defect.   | 46,60,180                          |
| 1.853    | 669.1 | 1.85 eV B-band   | 218                                |
| 2.046    | 606.0 | Natural diamond luminescence feature at 2.041 eV (607.4 nm) DAP75a (V <sub>3</sub> Si <sub>2</sub> ) <sup>-</sup> comprising of ten lines (a-j)<br><br>Natural diamond luminescence feature at 2.049 eV (605.1 nm) DAP55b V <sub>1</sub> N <sub>3</sub> <sup>0</sup> (a)   | 219<br>207                         |
| 2.206    | 562.0 | Luminescence features in this region for natural diamonds<br><br>2.202 eV (563.0 nm) DAP1c N <sub>1</sub> <sup>0</sup> +B <sub>1</sub> <sup>0</sup><br><br>2.205 eV (562.3 nm) unattributed feature observed in natural brown diamond<br><br>2.206 eV (562.0 nm) S1b-DAP43c V <sub>1</sub> N <sub>1</sub> <sup>0</sup><br><br>2.207 eV (561.7 nm) DAP55e V <sub>1</sub> N <sub>3</sub> <sup>0</sup> (a)<br><br>Broad band centred at 2.200 eV (563.5 nm) DAP73 band V <sub>1</sub> B <sub>1</sub> <sup>0</sup> (a) | 201<br>210,215<br>46<br>207<br>220 |
| 2.338    | 530.3 | 2.331 DAP1f N <sub>1</sub> <sup>0</sup> +B <sub>1</sub> <sup>0</sup><br><br>2.335 DAP75e (V <sub>3</sub> Si <sub>2</sub> ) <sup>-</sup><br><br>2.337 S1b-DAP43f V <sub>1</sub> N <sub>1</sub> <sup>0</sup><br><br>Green band B component   | 201<br>219<br>46,210,221           |

Table 5-8 Features fitted from the ROI spectra of the brown banded regions

ROI 5 and 6 corresponding to 10 x 10 pixels on the clear region, can be fitted with three Lorentzians centred at 1.776 eV, 1.622 eV and a contribution to the small peak at 2.006 eV. These correspond to the broad features in the area average high-resolution PL spectra.

### 5.2.1.1.4 Raman spectroscopy

Raman spectroscopy has been used to map a region of the sample containing brown banding, illustrated in Figure 5-24. These data have been processed using MathCAD scripting (Appendix) by extracting a spectrum from each coordinate sampled, fitting of the first order Raman line using a Lorentzian function and exporting the following

data products; a) total intensity minus the first order peak to give the background intensity, b) the position of the first order peak, c) its FWHM, and d) the intensity of the peak. The peak intensity is heavily influenced by sample measurement conditions such as fluctuations in temperature, room lighting and sample surface texture/slope.

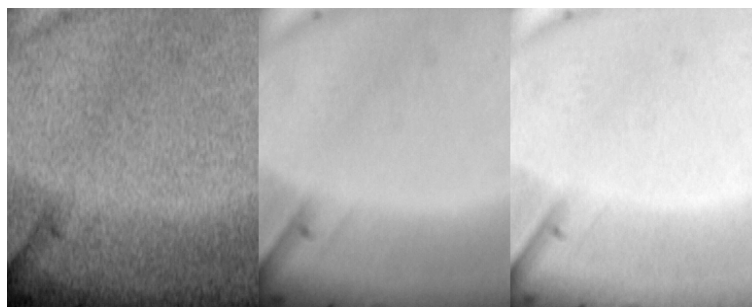


Figure 5-24 Mapped region in RGB profile to highlight banded region. The bright ring is an artefact of the microscope.

In images a) and c) of Figure 5-25 the bright almost horizontal lines show growth striations in the crystal. Image b) shows the first order diamond peak is more pronounced in the clear regions. The darker banding corresponds to the brown banding of the sample. The horizontal gradient effect is an artefact of the rastering method of mapping the sample.

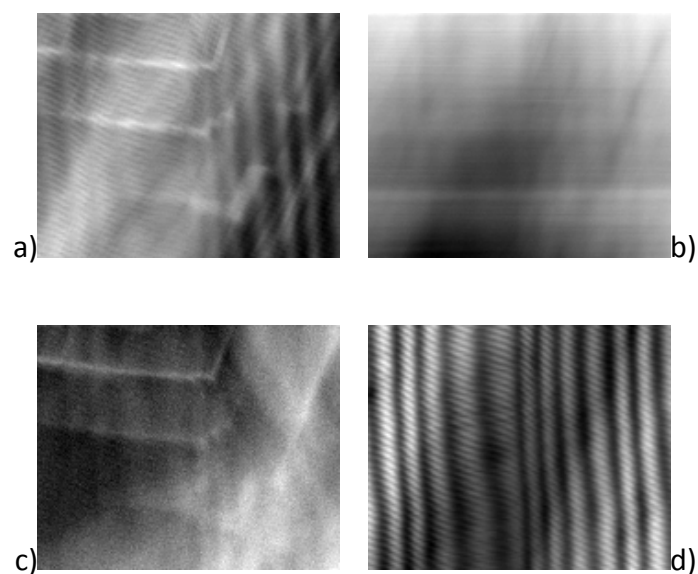


Figure 5-25 Maps of the first order Raman line ( $1332\text{ cm}^{-1}$ ) of Ia natural banded diamond scaled 0-255 to show contrast; a) background, b) peak position, c) FWHM, and d) peak intensity.

The contributions from a number of key Raman features have been plotted to investigate their correlation with the banded region, shown in Figure 5-26. In image a) of Figure 5-26 contour plot the region where the peak is broader contributes to a greater peak area, represented by the red colour. This corresponds to the brown banded region as the first order peak (a measure of a diamond's perfection) has been broadened due to the different composition of the brown band.

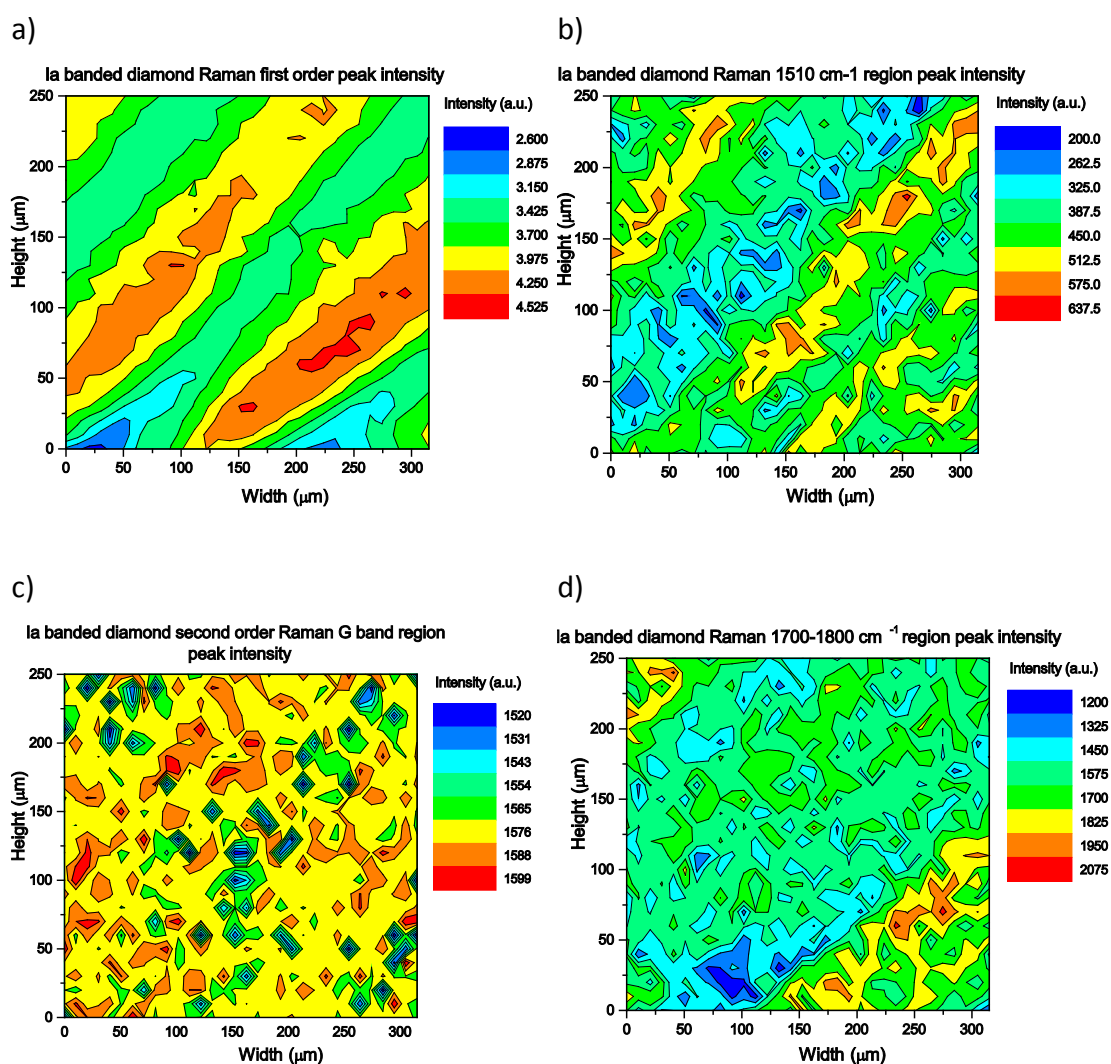


Figure 5-26 Ia banded diamond Raman mapping peak area plots; a) first order Raman line, b) 1510  $\text{cm}^{-1}$  feature, c) second order G-band, and d) 1700-1800  $\text{cm}^{-1}$  region.

Using the relationship between the peak shift of the first order Raman line and the coefficient of stress for uniaxial diamond, discussed in Chapter 2, the internal stress can be calculated and plotted as a surface, Figure 5-27. The stresses in the sample were calculated to be negative, showing tensile stress. These values are found to range from 5.9 MPa to 104.2 MPa. From the plot the stress is centred at a single point and radiates outward.

## 5.2 Diamond samples

---

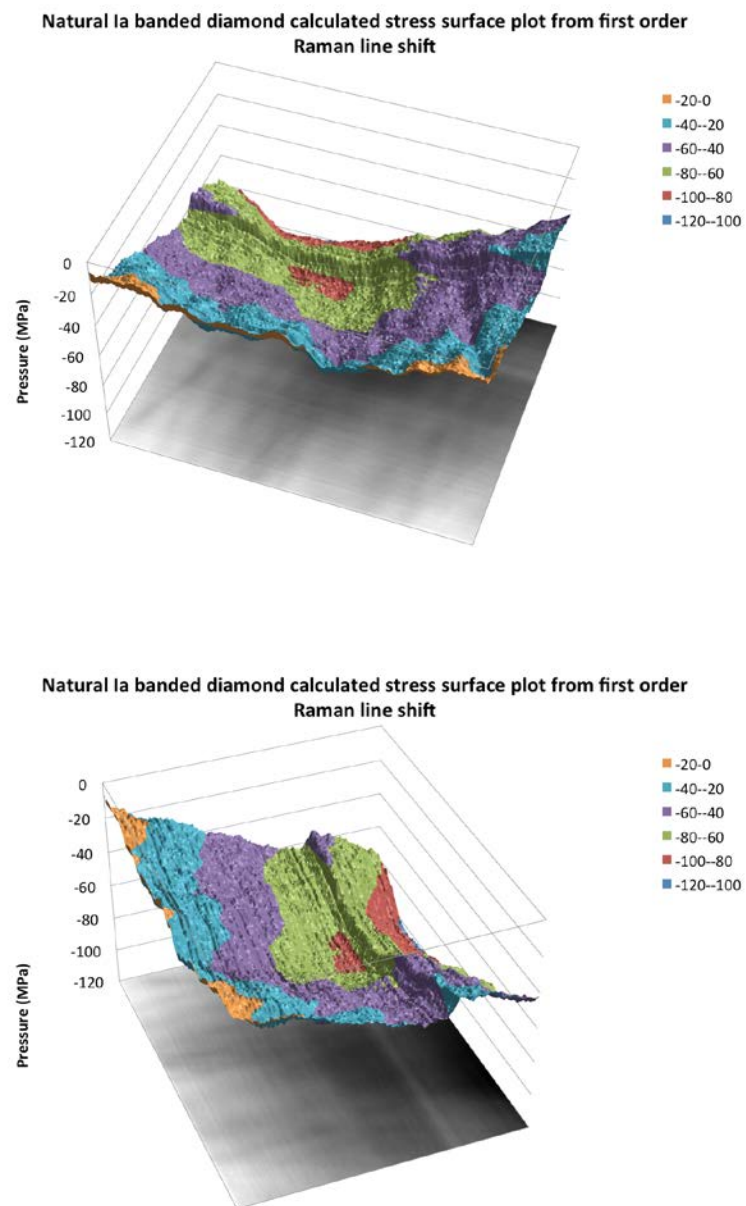


Figure 5-27 Ia banded natural diamond calculated stress map illustrating the tensile stress present in the sample.

### 5.2.2 Synthetic diamonds

First synthesised in the 1960s, shrouded in post war secrecy, the complete story of the first synthesis remains outstanding. For further reading the reader is directed to the review by one of the pioneers of CVD growth Angus <sup>222</sup>. Today CVD diamonds are produced via a chemical reaction inside a gas-phase and deposition onto a suitable substrate. The process has been developed over the years by a number of commercial and research institutions. The process is flexible with a number of parameters including the gases, energy sources for chemical activation and substrates. Figure 5-28, reproduced from the comprehensive review of CVD synthesis by Schwander *et al* <sup>223</sup>, illustrates the variables possible.

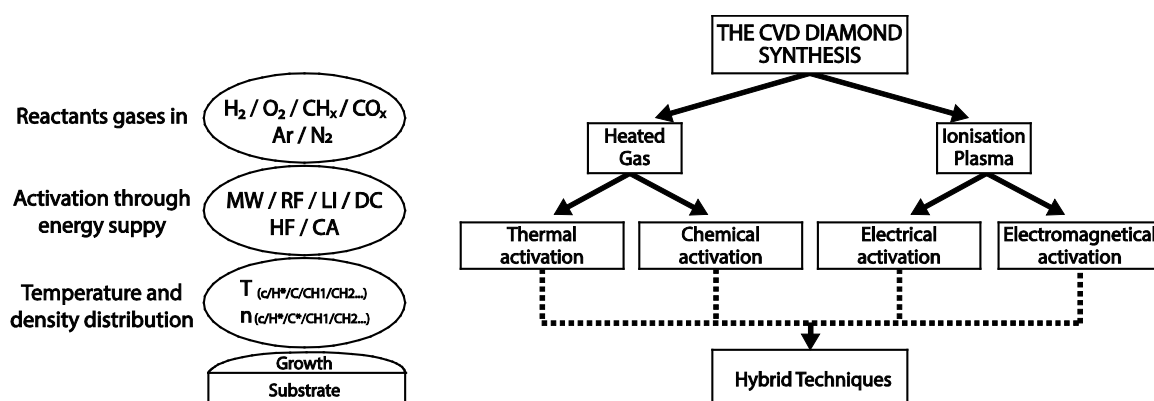


Figure 5-28 Illustrations of the mechanism for CVD diamond growth reproduced from Schwander *et al* <sup>223</sup>.

The production of synthetic, engineered, diamonds has opened up the material to a wider range of applications through the provision of large area, high quality, and reproducible material at industrial volumes. Coe *et al* <sup>224</sup> provide an informative review of the optical, thermal and mechanical properties of CVD diamond. CVD diamond is most commonly grown

## 5.2 Diamond samples

---

heteroepitaxially on lattice mismatched substrates such as silicon, silicon carbide and metals. These result in polycrystalline morphologies. Under optimised conditions highly orientated single crystals can be produced.

It is common to see contributions from silicon and boron in CVD diamond spectra, arising from the substrate the sample was grown on<sup>37</sup> and impurities in the chamber. Similarly, nickel can also be present from the growth vessel as can contributions from tantalum or tungsten from the hot filament in the growth chamber.

Synthetic diamonds produced by chemical vapour deposition (CVD) have been examined using the techniques applied the natural sample in the previous section. Three synthetic samples have been chosen for study; a uniform pale blue boron doped single crystal, a brown single crystal with uniform and damaged regions of colouration, and a polycrystalline sample.



### 5.2.2.1 Boron doped CVD diamond

Boron, like nitrogen, is a common impurity or dopant in diamond due to its positions in the periodic table next to carbon, making it compatible to be incorporated into the diamond lattice. After nitrogen, it is the second most abundant impurity found in natural diamond and there is considerable interest in boron-doped diamond as an electrode material as it has a wide potential window in aqueous solution<sup>225</sup>, low background currents and corrosion stability. Boron is added as a dopant to synthetic diamond for a number of reasons, commonly to modify the diamond to display p-type semiconductor characteristics. This is due to the shallow acceptor centre; isolated substitutional boron has a ground state 0.37eV above the valance band<sup>60</sup>.

According to Dischler<sup>60</sup>, there are six types of boron centres in diamond, these are:

- The  $B_1^0$  acceptor, isolated substitutional boron
- Standard Donor Acceptor Pairs (DAP) of boron with nitrogen (DAP1) and phosphorus (DAP2)
- Those associated with a lattice vacancy
- Associates of  $B_1$ ,  $B_2$ , or  $B_3$  with the (100)  $(N_1C_1)_i$  split interstitial
- Associates of  $B_1$  with the (100)  $(N_1C_1)$  split interstitial in three charge states
- Boron-bound exciton lines

The addition of boron can affect the crystal morphology<sup>226</sup>. The most pronounced effect – the Fano effect<sup>227</sup>, causes an asymmetry of the ZPLs due to Fano-type interference between the discrete zone-centre phonon and the continuum of electronic states induced by the present of the dopant<sup>45</sup>. In Raman spectra an asymmetry of the one phonon band is also related to this interference, affecting the Raman frequency shift, profile and band width<sup>226</sup>.

## 5.2 Diamond samples

---

Diamonds grown by CVD method doped with small boron concentration (<400ppm) and nitrogen have the effect of increasing and narrowing the first order Raman line compared to those grown with high concentrations ( $> 4 \times 10^{20} \text{ cm}^{-3}$ ) show weakening of the first order line <sup>46</sup>.

The sample studied in this work is a high quality, free-standing, polished, optically transparent, boron doped sample grown by CVD method and provided by the Diamond Trading Company (DTC). The sample was provided highly doped ( $\sim 10^{16}$  atoms per  $\text{cm}^3$ ). The sample is visually uniform with a pale blue colour and shows negligible strain patterning when viewed under a cross-polarising microscope.

When initially received for this work the sample was patterned with circular metal contacts (Pt/Ti/Au). The sample was used as received for early testing with HeLIOS to examine spectra recorded on and off the diamond/metal regions and for assistance in depth focusing and alignment. However, for acquiring experimental data, the metallic pattern proved problematic as it was not strongly bound to the surface leading to flaking in places causing light scatter and reflections. As the work required the sample for comparison with the brown CVD diamond for investigations into the colouration, it was agreed to remove the contacts via an acid clean and have the sample polished (kindly performed by E6). This provided a clean surface to examine using HeLIOS hyperspectral PL, hi-res PL, Raman spectroscopy and mapping, and cross polarisation microscopy.

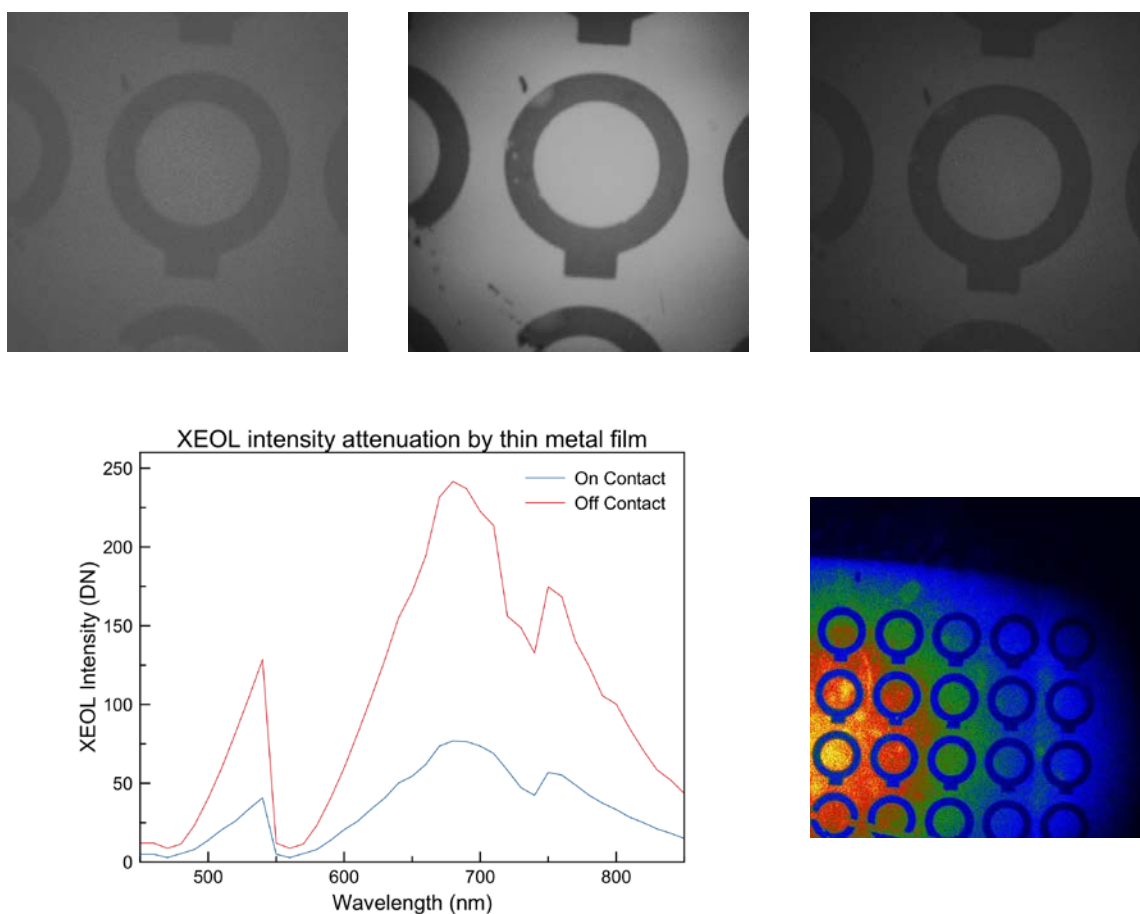


Figure 5-29 Boron doped CVD diamond as received with metal patterning deposited in UHV under Cu  $K\alpha$  irradiation in HeLIOS; a) 450 nm 7.5x magnification, b) 600 nm, c) 750 nm, d) raw data comparison of signal on and of the patterning, and e) false colour image of sample under irradiation at 2x magnification.

When examined under natural light the sample exhibits a pale uniform blue colour due to the boron's ultraviolet absorption from daylight. In natural IIb diamonds the blue colour is due to the natural inclusion of boron impurities in the lattice. Boron is a very effective colour centre in diamond, with concentrations as low as 1 ppm causing blue colouration. The blue

## 5.2 Diamond samples

---

colouration is growth sector dependant in CVD diamonds, with the (110) and (113) growth sectors becoming blue with low doping which does not affect the (111) sector <sup>213</sup>.

### 5.2.2.1.1 Cross-polarisation imaging

The sample has been examined by cross-polarisation microscopy using the method detailed in Chapter 2. Figure 5-30 shows the sample under white light illumination. Under examination between cross-polarisers, the sample shows typical growth patterns with little in-grown strain. There are also a number of small number petalled features present, seen in image b) of Figure 5-31. Examination of the cut edge revealed a darker growth region and striations which are also visible in the cross polarised images but did not appear to introduce any additional strain.

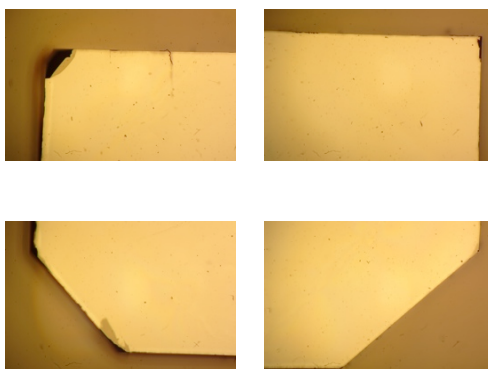


Figure 5-30 Boron doped CVD diamond under white light illumination at 4x magnification. Image width 4mm.

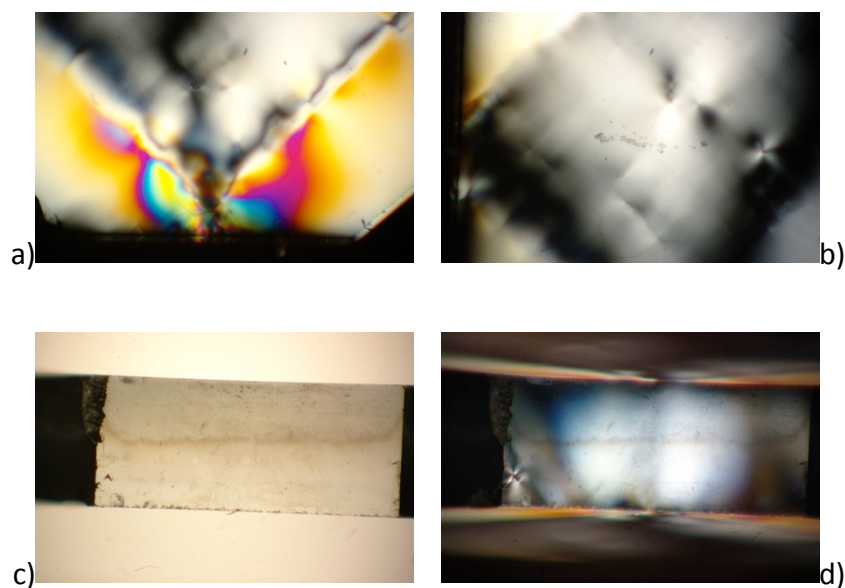


Figure 5-31 Cross polariser images of blue CVD diamond; a) sample imaged between two crossed polarising filters at 10x magnification; b) with the addition of a  $\frac{1}{4}\lambda$  filter, c) white light edge of the sample 10x, and d) with cross polarising filters. Image size 1.5mm.

#### 5.2.2.1.2 HeLIOS high-resolution PL

The data presented were acquired using HeLIOS and an iHR320 spectrometer at 2x magnification, with additional 395 and 400 nm long pass filters to block reflected light from the excitation source. The experimental configuration can be seen in Figure 4-3.

These data have been fitted and presented using LabSpec6, Origin Pro v8 and v9, and MagicPlot. The full acquired range and fitted peaks corresponding to characteristic defects of interest to this work are presented here.

## 5.2 Diamond samples

---

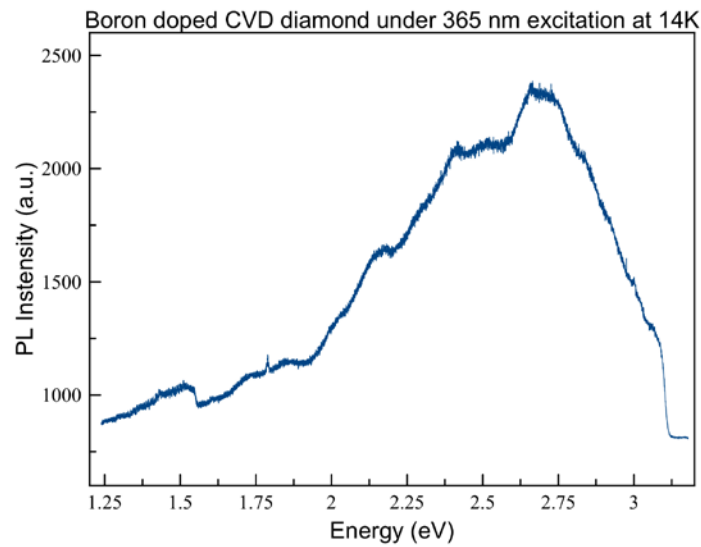


Figure 5-32 Boron doped CVD diamond high resolution PL spectra.

Figure 5-32 shows an example high resolution photoluminescence spectra acquired in the HeLIOS chamber at 14K. The broad shape has a large contribution from the boron-related band centred at 2.48 eV. The uniform nature of the sample leads to it emitting a broad continuum with less intense, narrow features that the natural diamond previously examined.

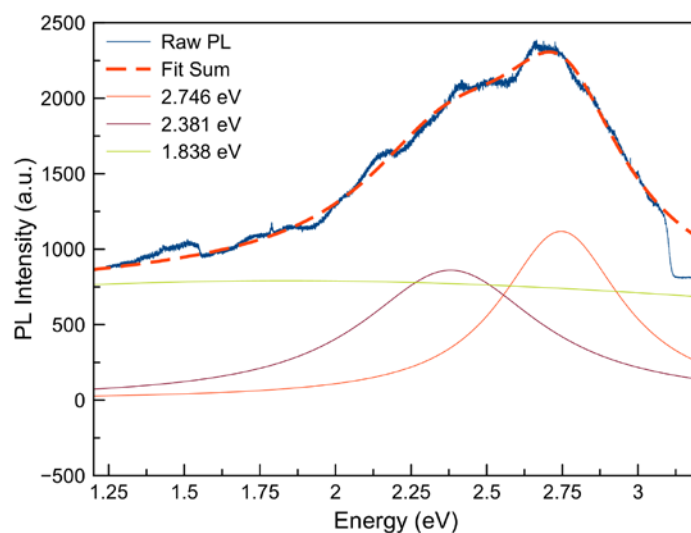


Figure 5-33 Boron doped CVD diamond fitted region.

The spectrum's broad shape can be fitted with a number of Lorentzian curves corresponding to broad features observed in boron doped CVD diamond. Table 5-9 lists the features identified in Figure 5-33.

| Observed<br>eV |       | Description  | Reference      |
|----------------|-------|--|----------------|
| 1.838          | 674.6 | Broad luminescence band in CVD around 1.8 eV is associated with boron incorporation, referred to in literature as the B-band. It is made up of a structure of 14 lines ranging from 1.742 – 2.138 eV and corresponds to DAP9 | 228            |
| 2.381          | 520.7 | The Green(c) or Green B centre associated with boron is located at 2.39  | 229 230        |
| 2.746          | 451.5 | PL band at 2.740 eV which is unattributed  | 229 228        |
|                |       | The Blue(a) band associated with boon is accepted to be located at 2.730 eV, with variations over the range 2.56-2.86 eV as it comprises of five bands   | 231,232<br>208 |

Table 5-9 Boron doped CVD diamond fitted components

## 5.2 Diamond samples

---

In addition the features listed in Table 5-9 The small, sharp feature at 1.789 eV and its sidebands located on the broad background correspond to DAP65 ( $V_3Si_2$ )<sup>0</sup>.

DAP99 lines a-h ( $N_1C_1$ )<sub>i</sub>B<sub>1</sub><sup>0</sup> contributes a number of features visible in this sample's PL spectrum<sup>233</sup>. These can be seen at 2.1417, 2.467, 2.512, 2.582, 2.612, 2.657, 2.687, and 2.696 eV with a ZPL at 2.792 eV. These are known to have been observed in boron containing CVD diamond with the  $V_1N_1$ <sup>0</sup> (2.156 eV) centre<sup>46</sup>, which is very faint in these data. The 1.84 eV broad PL band observed in synthetic boron doped diamond is attributed to boron and nitrogen complexes by Frittas *et al*<sup>234,235</sup>.

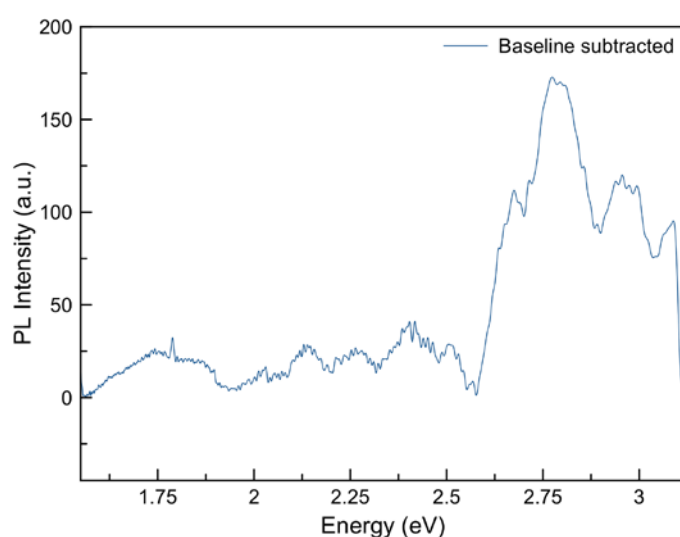


Figure 5-34 Baseline subtracted boron doped CVD diamond PL spectrum under 365 nm excitation at 14 K.

By performing a baseline subtraction in LabSpec6 these spectral features are more readily observed. In Figure 5-34 above a number of boron-related features can be observed, a number of which are listed in the Table 5-10 below.



| Observed<br>eV |       | Description<br>nm  | Reference  |
|----------------|-------|--|------------|
| 2.64           | 470.0 | 2.646 eV $V_1Si_1^0$ DAP110 ZPL                            | 46,229,236 |
| 2.65           | 467.9 | 2.657 eV DAP99f $(N_1C_1)_iB_1^0$                          | 233        |
| 2.68           | 462.6 | 2.687 eV DAP99g $(N_1C_1)_iB_1^0$ and $(N_1C_1)_iB_1^-$    | 233        |
| 2.69           | 460.9 | 2.692 eV DAP17c $O_1^0+B_1^0$                              | 46,237     |
|                |       | 2.963 eV DAP98f $(N_1C_1)_i^+$                             | 238        |
|                |       | 2.696 eV DAP99h $(N_1C_1)_iB_1^0$ and DAP17d $O_1^0+B_1^0$ | 46,233,237 |
| 2.71           | 457.5 | Unidentified   |            |
| 2.77           | 447.6 | 2.792 eV DAP99z ZPL $(N_1C_1)_iB_1^0$                      | 233        |

Table 5-10 Boron doped CVD diamond identified component

#### 5.2.2.1.3 HeLIOS spatially resolved PL

Hyperspectral photoluminescence data was acquired of the sample using excitation from a 365 nm LED source. Regions of interest were selected from across the sample, displayed in Figure 5-35. These show variations in the emitted light across the sample, due to the positioning of the excitation source, however the spectral shape remains consistent, confirming the uniform colouration of the sample. The ROI spectra are the product of 20 x 20 pixel areas. ROI 1, corresponds to the entire image. The sample emitted a very weak blue luminescence observed by eye. Due to the low throughput of the LCTF in the shorter wavelength range little was detected. The radiometric processing corrected for this as far as reasonably practicable to give a spectral shape comparable to that of the high resolution data. The ROIs are illustrated on an RGB image comprising of R=730, G=560, and B=450 nm to show maximum contrast. The bright region to the left corresponds to the edge of the sample, indicating the PL is preferentially emitted from this face.

## 5.2 Diamond samples

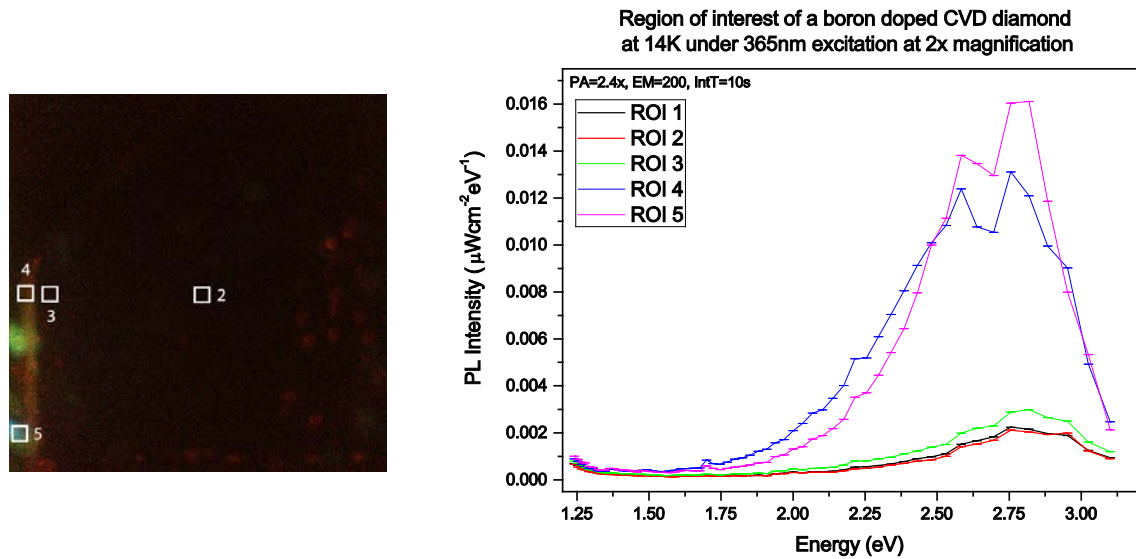


Figure 5-35 Radiometrically corrected ROI spectra of Boron doped CVD diamond imaged at 2x magnification under 365 nm excitation at 14K. All ROIs are comprised of 20x20 pixel selections.

### 5.2.2.1.4 Raman investigations

In this work, as in Ushizawa *et al* <sup>226</sup>, studies have been performed on a single crystal sample, rather than polycrystalline films to avoid local stress fluctuation. Low power excitation was used to prevent peak shifts or broadening due to local heating effects. Spectra were acquired of the (100) face.

The Raman line dominates the spectrum with no contributions at lower frequencies as seen in the literature for those samples with very high boron concentrations. Here it can be seen that the concentration is in the happy medium where the addition of boron causes the sharpening of the first order line. The line does not show any asymmetry due to Fano interference <sup>227</sup>, confirming the order of boron concentration.

Raman maps were acquired of a strain free area (as viewed under cross-polarising filters). Figure 5-36 shows those data presented as maps of Raman line peak height, Raman line FWHM, background and the shift from stain-free diamond (taken to be  $1332.5\text{ cm}^{-1}$ ). These maps show there is very little spatial variation, confirming the previous work by Jones<sup>239</sup> that the sample is of high quality. As with previous sample the shift from ideal undisturbed diamond has been converted into stress which yield and interesting undulating curve across the sample, Figure 5-37. The data show the region samples to be under compressive stress ranging from 98.6 MPa to 300.3 MPa.

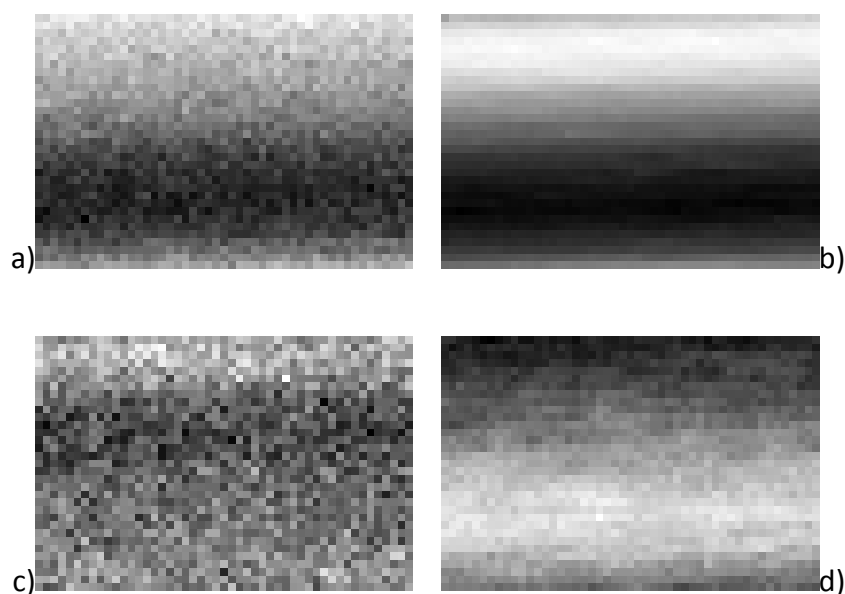


Figure 5-36 Maps of the first order Raman peak of boron doped CVD diamond, scaled 0-255 to show contrast; a) background, b) peak position, c) FWHM, and d) peak intensity.

## 5.2 Diamond samples

---

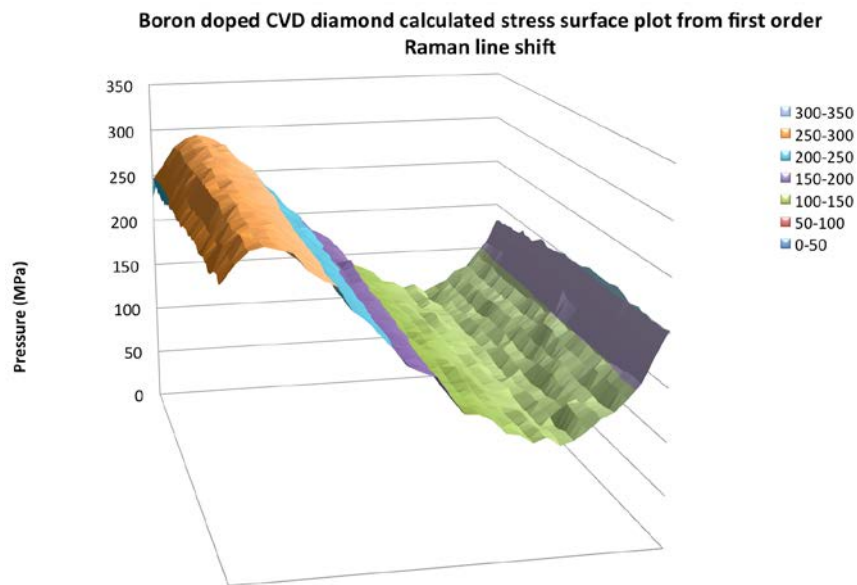


Figure 5-37 Boron doped CVD diamond stress map.

The peak centre for the 1<sup>st</sup> order phonon peak in the boron doped CVD sample has been fitted with a Lorentzian centred at  $1333.0\text{ cm}^{-1}$  and FWHM of  $1.90\text{ cm}^{-1}$ . This sample has been grown with a high doping concentration of approximately  $10^{16}$  atoms per  $\text{cm}^3$ . Brunet *et al* <sup>240</sup> showed that at higher boron concentrations, this first order Raman peak has been observed to positively shift by up to  $1.8\text{ cm}^{-1}$  towards higher wavenumbers, as seen here. If the boron concentration had been higher, a sharp downshift would have been observed due to Fano interference. Substitutional nitrogen has also been shown to cause a small up shift of the 1<sup>st</sup> order line of  $1\text{-}2\text{ cm}^{-1}$  <sup>241</sup> which could have contributed to the up shift. From the narrow FWHM it can be confirmed that this sample was grown homeoepitaxially on an (100) orientated substrate <sup>242</sup>.

The high quality of the sample is confirmed by the presence of second order features. As shown in the inset of Figure 5-39, this sample displays a relatively intense band in the two

phonon region. In ideal, undisturbed diamond this band ranges from 2176 to 2668  $\text{cm}^{-1}$ . Here the band is located between approximately 2140 and 2675  $\text{cm}^{-1}$ , showing a slight broadening. The most intense peak at 2464  $\text{cm}^{-1}$  corresponds to the doubled energy of the densest optical phonon region<sup>46</sup>.

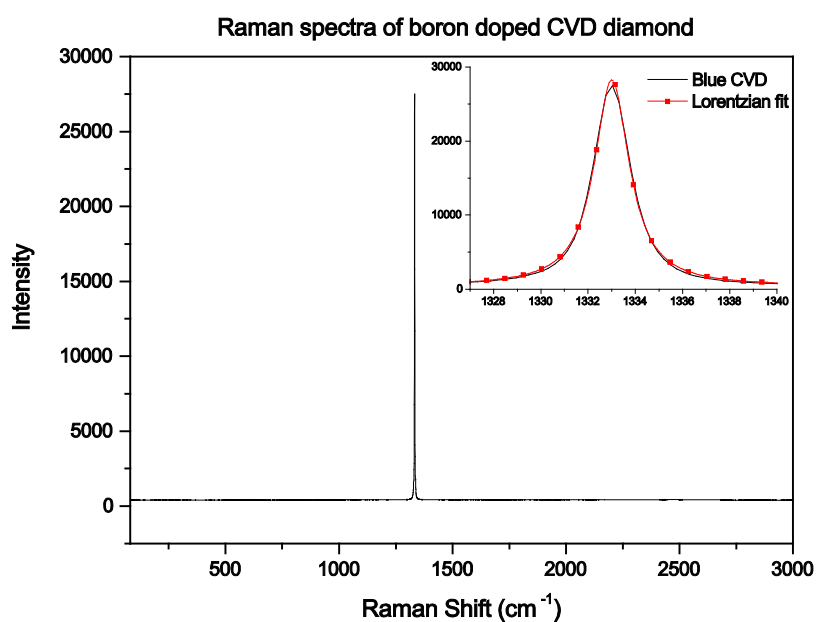


Figure 5-38 Boron doped CVD diamond Raman spectra, inset Lorentzian fitted first order peak giving peak position of 1333.0  $\text{cm}^{-1}$  with FWHM of 1.9  $\text{cm}^{-1}$ .

## 5.2 Diamond samples

---

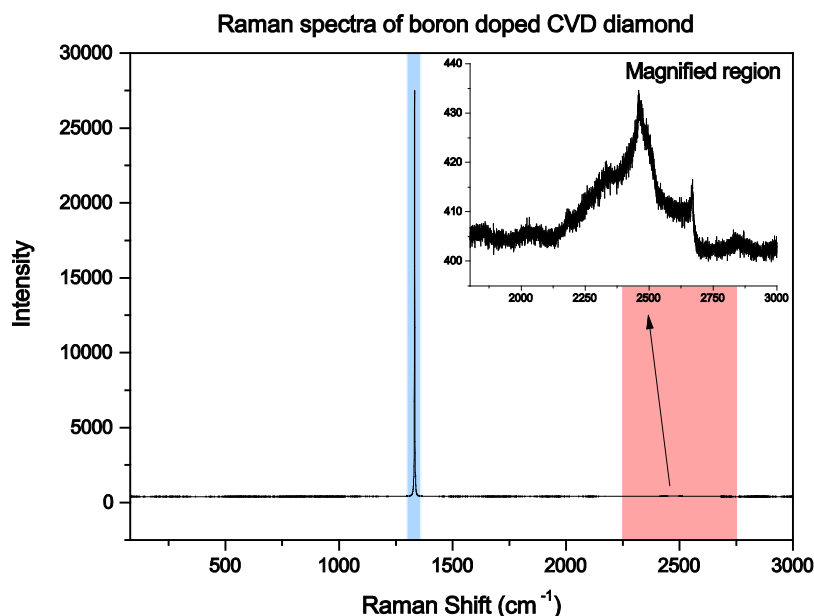


Figure 5-39 Boron doped CVD diamond Raman spectra, first order peak highlighted in blue, second order region highlighted in red. Inset magnification of the second order region.

### 5.2.2.2 Brown CVD diamond

This sample was kindly provided to the research group for investigation by the Diamond Trading Company. The sample is of high quality owing to the sharp, intense first order Raman peak acquired at the centre of the sample. The sample was originally to be used as a comparison for the boron doped CVD diamond as a uniform coloured sample, however on closer visual inspection the brown colour did not appear to be uniform. Examination under a cross-polarising microscope showed the sample contained significant strain and colour zoning that has been examined using spatially resolved PL and Raman mapping.

The sample contained interesting growth features in its profile, illustrated in Figure 5-40 by white light photographs. The coarser texture corresponds to the surface of growth in contact

with the substrate. On examination of the (100) face darker regions can be seen in the bottom left corner. The sample also contained small, darker flecks in its bulk.

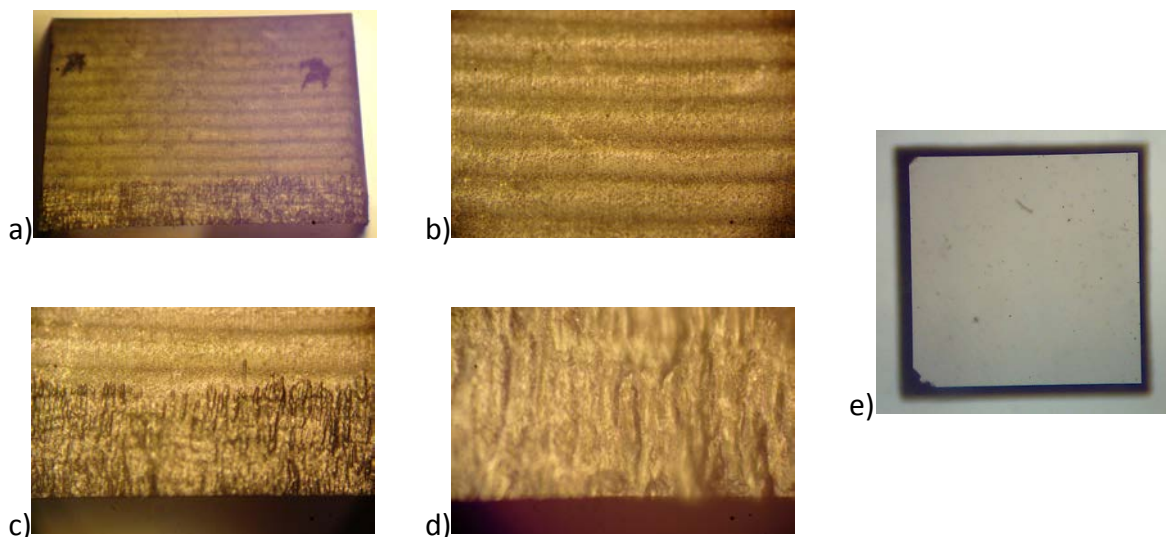


Figure 5-40 Brown CVD white light sample images, a) – d) show the growth layers with the substrate interface illustrated in c) and magnified in d), image e) shows the full sample, the chipped darker region studied is located at the bottom left corner.

#### 5.2.2.2.1 Cross-polarisation images

To investigation the darker corner cross polarisation images were taken using the equipment details in Chapter 2, presented in Figure 5-41. These images highlighted the strained region near the corner of the sample and a number of additional petal birefringence patterns in an otherwise relatively unstrained lattice. The lighter yellow – pale green – turquoise regions in images with the addition of the  $\frac{1}{4} \lambda$  filter correspond to high area of birefringence and strain when compared with the Michel-Levy chart <sup>200</sup>. Images a) and b) were acquired at 4x magnification, the remainder at 10x to focus on the strained corner region.

## 5.2 Diamond samples

---

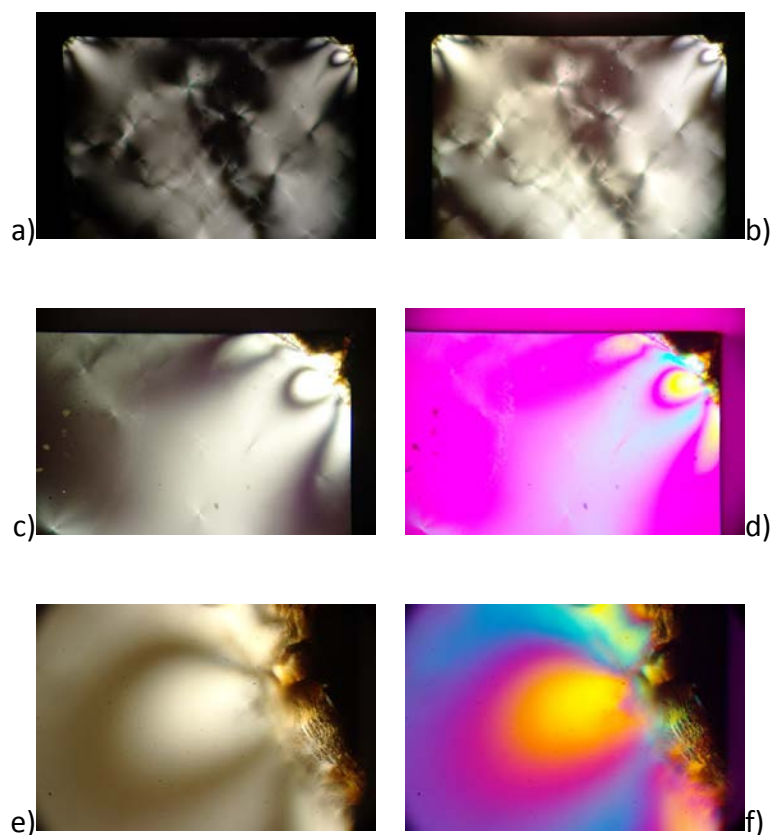


Figure 5-41 Brown CVD cross-polarisation images; a), c), and e) show the sample imaged between cross-polarisers; b), d), and f) show the sample with the addition of a  $\frac{1}{4}\lambda$  filter. Images a) and b) taken at 4x magnification, 4 mm image width, and the remainder at 10 mm, 1.5 mm image width.

### 5.2.2.2.2 HeLIOS high-resolution PL

The data presented were acquired using HeLIOS and an iHR320 spectrometer at 2x magnification, with additional 395 and 400 nm long pass filters to block reflected light from the excitation source. The experimental configuration can be seen in Figure 4-2.



These data have been fitted and presented using LabSpec6, Origin Pro v8 and v9, and MagicPlot. An example of the acquired spectra and fitted peaks corresponding to characteristic defects of interest to this work are presented here. Figure 5-42 shows a high resolution spectra acquired using the HeLIOS 2x objective.

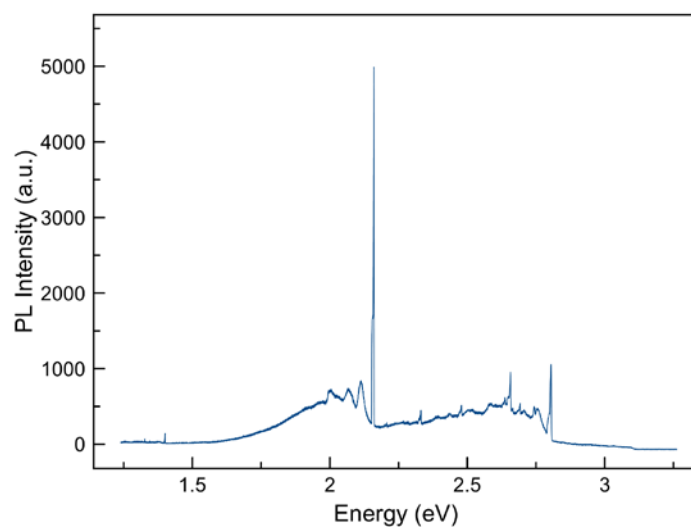


Figure 5-42 Brown CVD diamond PL spectra under 365nm excitation at 14K. The dominant feature is the neutral nitrogen vacancy.

5.2 Diamond samples

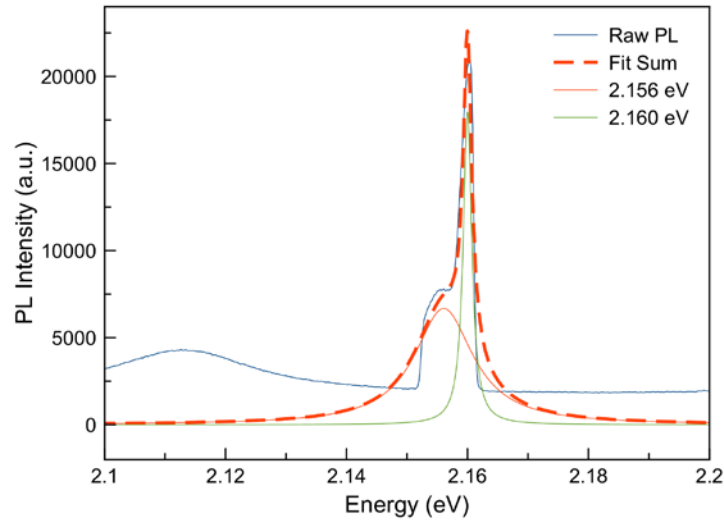


Figure 5-43 Brown CVD diamond under 365 nm excitation at 14K, magnified to show neutral NV centre splitting.

| Observed |       | Description  | Reference |
|----------|-------|--|-----------|
| eV       | nm    |  |           |
| 2.156    | 575.1 | NV centre (575.5nm)<br><br>The centre is observed between 2.154 to 2.156 eV, it is the ZPL of DAP47a-i and QLVM calculated to 1N +3C and DAP46a-f. DAP46 and DAP47 form a sideband mirror image on both sides of the NV ZPL<br><br>574.8 nm PL ZPL observed in brown diamonds exhibiting a yellow luminescence under 365 nm excitation | 46,243    |
| 2.160    | 574.0 | Associated with Ni impurities  | 46,60     |

Table 5-11 Brown CVD diamond PL features

The 2.156 eV centre naturally occurs in nitrogen-containing natural and synthetic diamonds. It can also be created by plastic deformation of the crystal – the intensity of the feature in this

brown CVD sample was acquired in a region over an area of stress and its intensity has been shown to be quenched via a high concentration of dislocations<sup>244,245</sup>. It is preferably located at grain boundaries in CVD diamonds<sup>246</sup>. It can be formed by a single substitutional nitrogen through irradiation and annealing. It comprises of five non-bonded electrons in the neutral state – two from the nitrogen atom and three from adjacent carbon atoms. It has a single allowed transition in the visible, with vibrational sidebands.

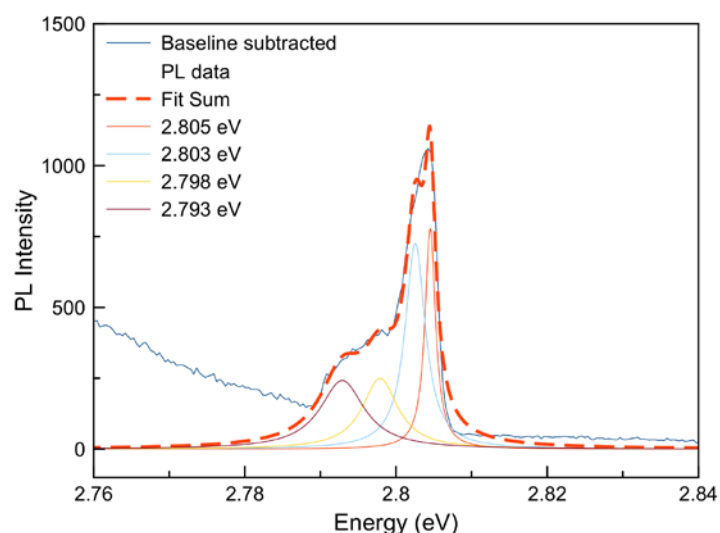


Figure 5-44 Brown CVD PL fitted region.

The second most prominent feature of the spectrum is that located around 2.8 eV. Subtracting a baseline and fitting with a number of Lorentzians yields a number of features.

## 5.2 Diamond samples

| Observed<br>eV |       | Description  | Reference |
|----------------|-------|--|-----------|
| 2.803          | 442.3 | Fundamental defect in diamond, associated with vacancies located at 2.80 eV ( $V_2Ni_1$ ) DAP58 S3= $+N_{2+0+0}$   | 60        |
| 2.805          | 442.0 | 2.807 eV ( $C_1N_1$ ) <sub>i</sub> <sup>+</sup> DAP98 ZPL. A very stable centre seen in as-grown synthetic diamond (both HPHT and CVD) consisting of the split interstitial, where one interstitial carbon is replaced by nitrogen ( $C_1N_1$ ) <sub>i</sub> . It is observed here in the positive charge state as the 2.807 eV centre. This is classed as an intrinsic defect. This centre has a number of sidebands. | 232 238   |
| 2.798          | 443.1 | 2.798 eV ( $V_1Si_1$ ) <sup>0</sup> DAP109b  | 46 247    |
| 2.793          | 443.9 | 2.792 eV ( $(N_1C_1)_iB_1$ ) <sup>0</sup> DAP99, fundamental defect with split (100) interstitial. Observed in boron contaminated CVD diamond. Seen with $V_1N_1$ <sup>0</sup> (2.156 eV) and ( $N_1C_1$ ) <sub>i</sub> <sup>0</sup> (3.188 eV). This boron can be introduced intentionally, or be present as a contaminant through unintentional transfer from boron-doped silicon substrates                         | 60 233    |

Table 5-12 Brown CVD diamond PL features

A large number of features are visible between the two strongest peaks of the neutral NV centre and that of the S3 centre ( $V_2Ni_1$ ) of DAP58, shown in Figure 5-45. These have been tentatively identified in Table 5-13.

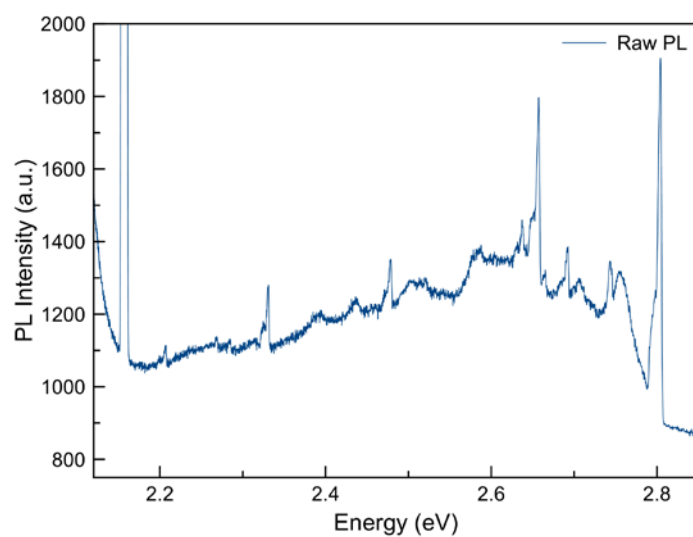


Figure 5-45 Brown CVD PL spectral region.

| Observed<br>eV |       | Description   | Reference          |
|----------------|-------|---|--------------------|
| 2.208          | 561.5 | 2.207 eV DAP55e, $V_1N_3^0(a)$  | 207                |
| 2.335          | 531.0 | 2.329 eV, a nitrogen related defect seen to split in regions of low quality diamond as seen here into a 2.322 and 2.335 eV doublet  | 46,231,232,236,248 |
| 2.481          | 499.7 | 2.480 eV, DAP113d, $V_1Si_1^-$  | 46,248             |
| 2.638          | 470.0 | Fundamental defect with split interstitial, $(C_2)_i^-$   | 60                 |
| 2.659          | 466.3 | Boron related feature, N10+B10 DAP1m, seen in low pressure CVD diamond. This is the first of the DAP structures, features range from 2.070-2.668 eV which can be seen in the weaker regions of the spectrum | 233 238            |
| 2.693          | 460.4 | Boron related features, possibly a line of DAP99, $(N_1C_1)_iB_1^0$ , at 2.696 eV or DAP17d, $O_1^0+B_1^0$ , also at 2.696 eV   | 46,233,237         |
| 2.742          | 452.2 | 2.741 eV N3c-DAP24f, $V_1N_3^0$   | 46,231             |

Table 5-13 Brown CVD PL features

5.2 Diamond samples

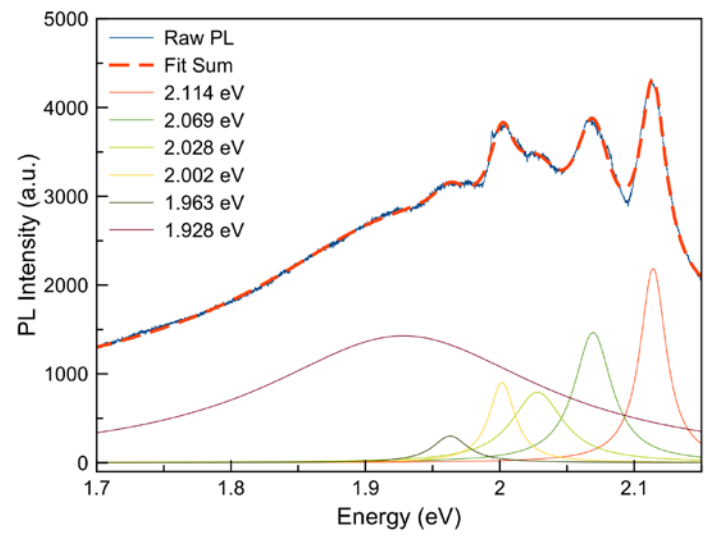


Figure 5-46 Brown CVD diamond PL features.

| Observed<br>eV | Description<br>nm                                    | Reference |
|----------------|--|-----------|
| 2.114          | 586.5 Green(a) band present in CVD diamond at 2.1 eV | 46        |
| 2.069          | 599.2 2.07 eV DAP1a $N_1^0+B_1^0$ one of 13 lines    | 243, 46   |
| 2.028          | 611.4 2.023 eV DAP47f $V_1N_1^0$                     | 243, 46   |
| 2.002          | 619.3 2.002 eV NV-DAP47e $V_1N_1^0$                  | 243, 46   |
| 1.963          | 631.6 1.965 eV S7-DAP11d $(V_2Ni_1)N_x^0$            | 229, 46   |

Table 5-14 Brown CVD diamond PL features

5.2.2.2.3 HeLIOS spatially resolved PL

Hyperspectral PL data have been acquired of the sample, focusing on the chipped corner of the sample displaying darker colouration. These data have been processed using the

calibration protocols discussed in Chapter 4 to provide radiometrically corrected, spatially resolved PL data from regions of interest (ROIs) of different sizes. Figure 5-47 provides an example of three images extracted from the hypercube, showing the contrast when the sample is imaged at different wavelengths. The darker, chipped region is visible in the bottom left corner.

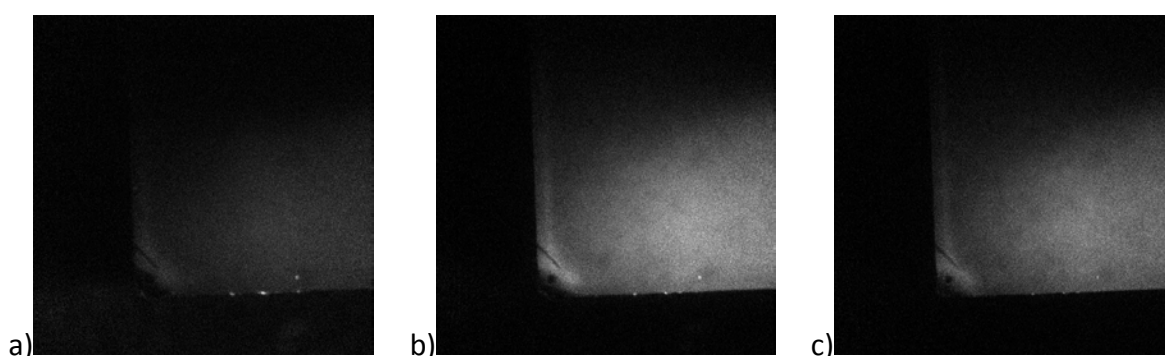


Figure 5-47 Extracted hypercube images of the brown CVD diamond at 2x magnification focused on the region of interest under 365 nm excitation at 14K. Corrected images extracted from the hypercube at a) 500 nm, b) 600 nm, and c) 700 nm.

Figure 5-48 below plots the radiometrically corrected data from five regions of interest, each 10 x 10 pixels. Selecting the entire 512 x 512 array generated the spectrum for ROI 1, this not pictured in the image. ROI 3, located over the darkest region shows very little PL emission. ROI 4, located at a defined crack, shows a change in the PL spectrum with an increase around

## 5.2 Diamond samples

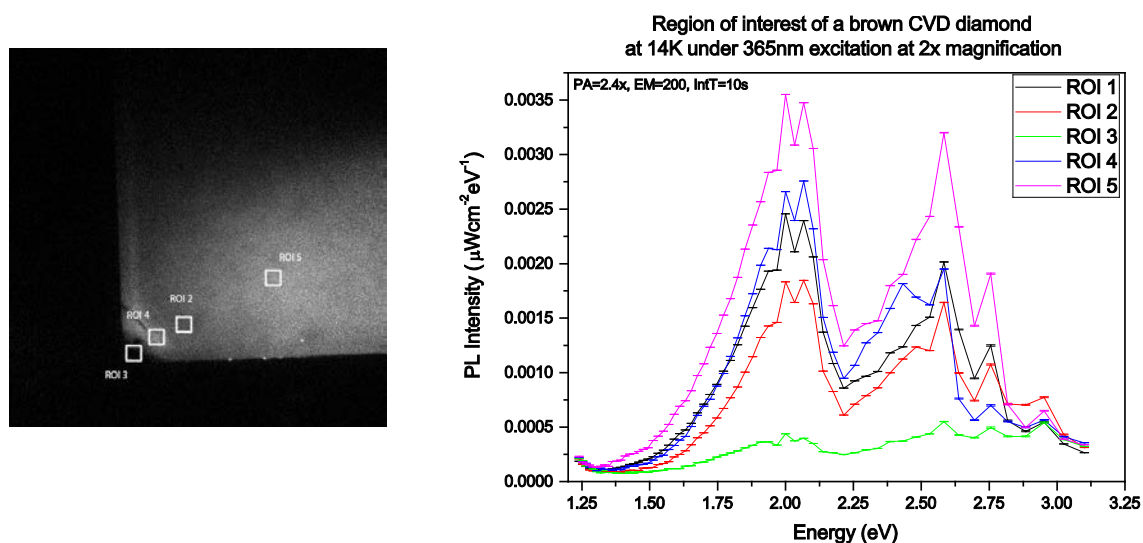


Figure 5-48 Spatially resolved PL of the damaged region of a brown CVD diamond under 365 nm excitation at 14K under 2x magnification.

Figure 5-49 below shows plots radiometrically corrected data from eight regions of interest. Regions 1-3 are 50 x 50 pixels, region 5 represents the whole array, and regions 6-8 are 10 x 10 pixels. The ROIs are illustrated on two images, 600 nm and 550 nm, to better show their locations. ROI 1 exhibits the most intense PL, acquired from the central, uniform region of the sample. There is little variation in the lower energy part of the spectrum shape, however differences are observed in the higher energy region.



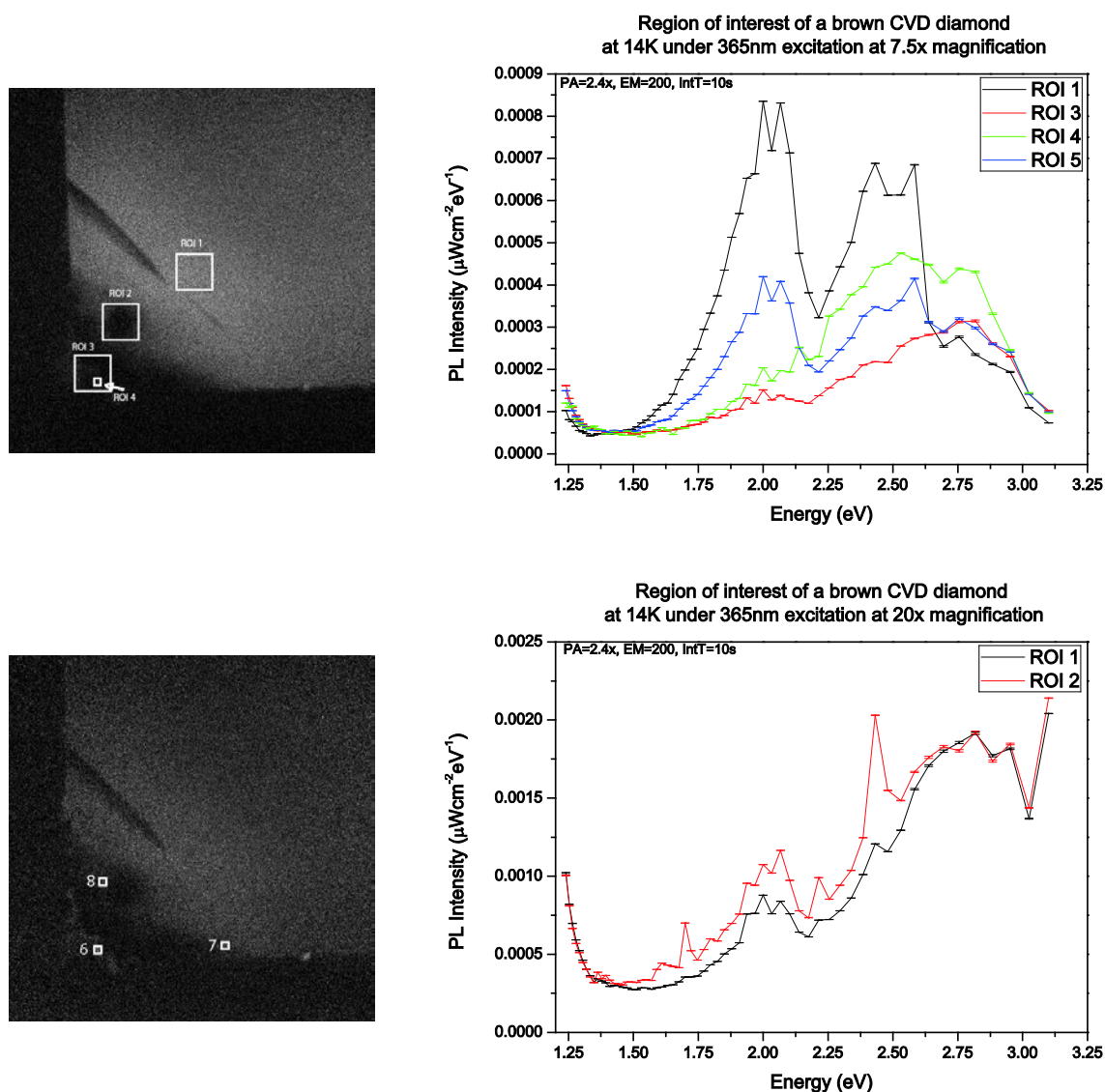


Figure 5-49 Spatially resolved PL of the damaged region of a brown CVD diamond under 365 nm excitation at 14K under 7.5x magnification.

## 5.2 Diamond samples

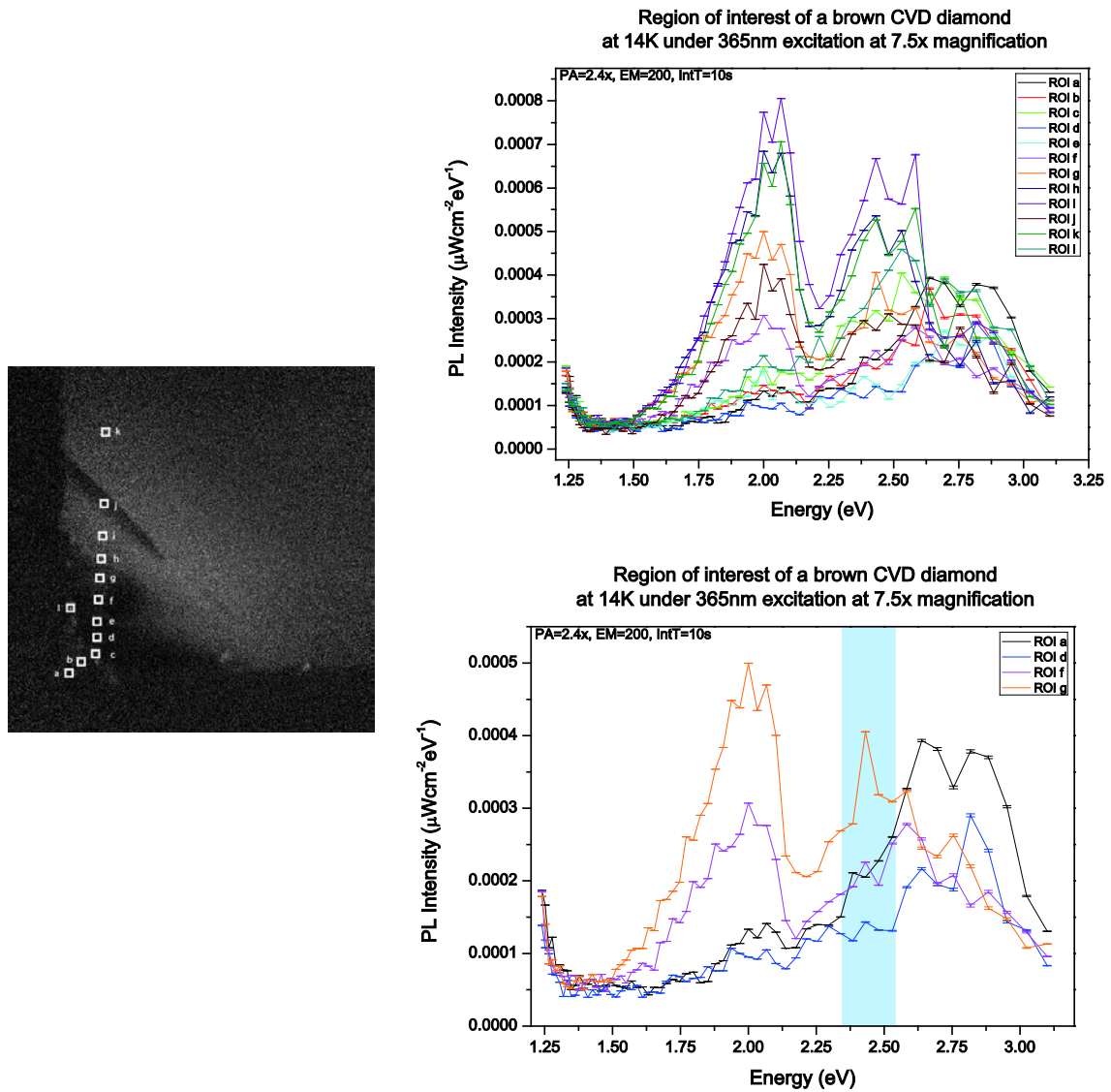


Figure 5-50 Spatially resolved PL of the damaged region of a Brown CVD Diamond under 365nm excitation at 14k under 7.5x magnification.

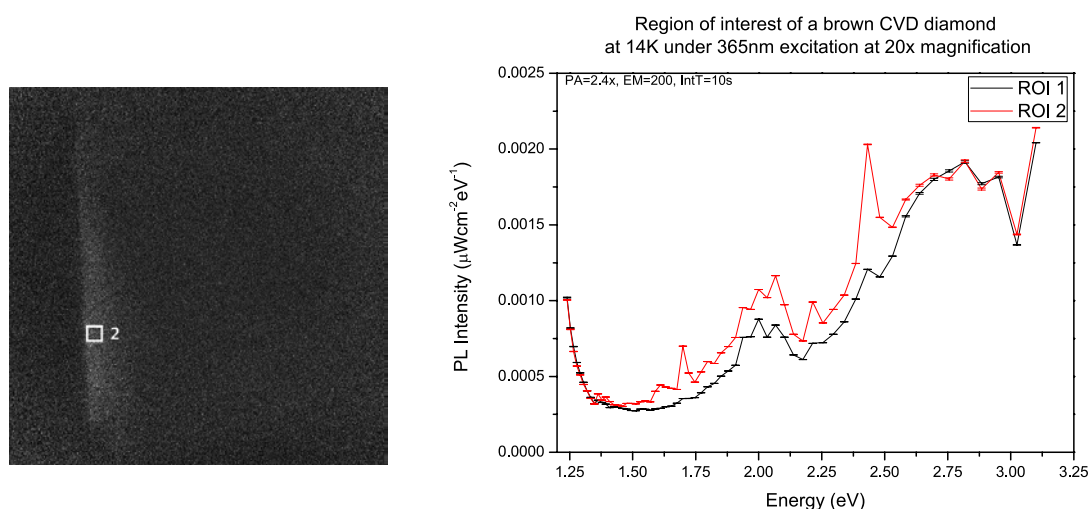


Figure 5-51 Spatially resolved PL of the damaged region of a brown CVD diamond under 365 nm excitation at 14K under 20x magnification.

This sample did not produce intense luminescence under 365 nm excitation. The spatially resolved data show agreement with the high resolution data in the detection of two distinct regions – that of the NV centre and nearby peaks and of the system of peaks at higher energies. ROI 1 is the whole array. ROI 2 is 20 x20 pixels, peak is at 2.43 eV as previous plots

The selected regions of interest correspond to areas around the strained region, discussed further in the next section on Raman spectroscopy. The chipped edge did not exhibit the same luminescence as the centre of the sample. The extracted data from ROI4 of Figure 5-49 can be fitted with three Lorentzians to investigate the profile: 2.57, 2.45 and 2.31 eV.

## 5.2 Diamond samples

| Observed<br>eV |       | Description   | Reference |
|----------------|-------|---|-----------|
| 2.57           | 482.4 | 2.562 eV ( $V_3Ni_2$ ) <sup>0</sup> and ( $V_3Ni_2$ ) <sup>+</sup> (a) ZPL of DAP106, this has an excited state at 2.588 eV | 60        |
|                |       | 2.580 DAP113g $V_1Si_1^-$   | 248, 46   |
| 2.45           | 506.1 | 2.464 eV $V_1N_2^0$ H3 centre DAP50/51/52, a fundamental defect of a vacancy with two nitrogen.                             | 46        |
|                |       | 2.496 eV $V_2Ni_1$ S3 centre DAP58  | 46        |
|                |       | 2.462 eV DAP86 3H centre ( $C_2$ ) <sub>i</sub> <sup>+</sup>  | 46        |
|                |       | 2.430 eV DAP113c $V_1Si_1^-$  | 248, 46   |
|                |       | 2.440 eV 1si-DAP110e $V_1Si_1^0$  |           |
| 2.31           | 536.7 | Unresolved  |           |

Table 5-15 Brown CVD PL Features

### 5.2.2.2.4 Raman spectroscopy

As discussed the sample was intended to be a uniform colour reference for brown colouration in CVD diamonds, however on closer inspection the bottom left corner had not been cut sharply, but had a darker, chipped appearance. Raman spectroscopy has been applied to investigate this darker colouration's relationship to strain.

The background PL intensity in CVD Raman spectra is seen in literature to increase with reduction in the growth temperature, reaching maxima when non-crystalline structure appears.

Single point measurements were made in three distinct regions of the sample, illustrated in Figure 5-52 below. Region a) is the centre of the (100) face, b) is located next to a cut edge, and c) is located in the darkened region where the diamond appears to be damaged. Region b) was chosen to compare with the other two check for stress introduced through cutting of

the finished sample from its rough grown form, an example of which is illustrated on the right of Figure 5-52 where only the top and bottom surfaces have been cut and polished.

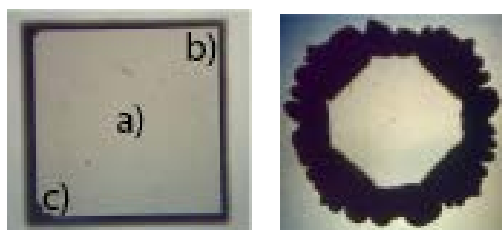


Figure 5-52 (left) Brown CVD diamond studied in this work labelled to show the three regions studied using Raman spectroscopy; (right) Example of a CVD diamond which has only been cut and polished top and bottom, leaving its grown state intact.

The Raman spectrum from the centre of the sample is shown in Figure 5-53. It comprises of a very sharp first order Raman peak corresponding to  $sp^3$  bound carbon, when fitted with a Lorentzian a peak position of  $1332.92\text{ cm}^{-1}$  is found, with a FWHM of  $1.83\text{ cm}^{-1}$ . These values are close to that of ideal undisturbed diamond ( $1332.5\text{ cm}^{-1}$  peak and  $1.7\text{ cm}^{-1}$  FWHM). These data, as with all the Raman data presented here, were acquired with the incident  $632.81\text{ nm}$  line of a HeNe laser. In this wavelength range any  $sp^2$  bound carbon will be enhanced due to its preferential scattering over  $sp^3$  bound carbon. The data show one additional peak in the second order region, centred around  $2257\text{ cm}^{-1}$ , however this is not linked to  $sp^2$  bonded carbon. This feature is ascribed to the luminescent Si-centre ( $738\text{ nm}$ ). It is thought this centre is present due to the incorporation of silicon from the sample's growth substrate.

## 5.2 Diamond samples

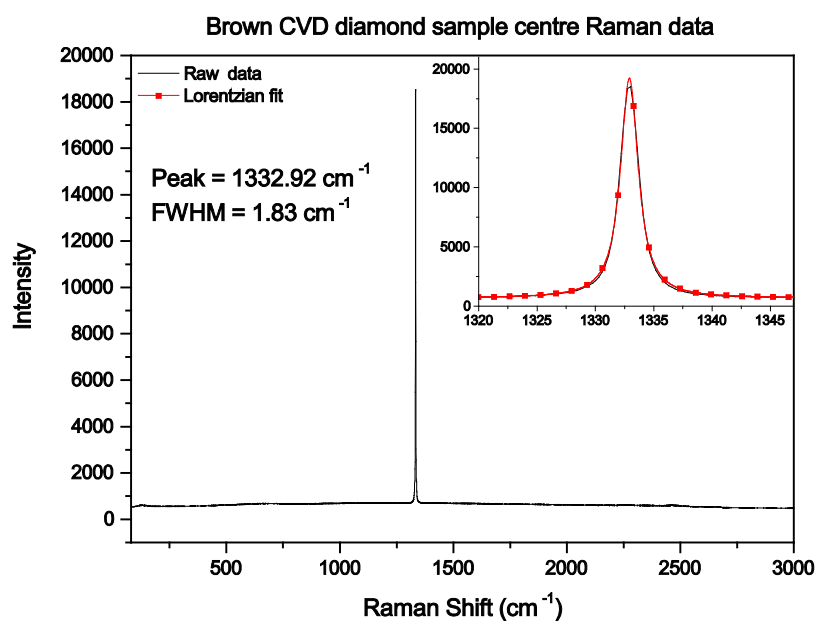


Figure 5-53 Raman spectra acquired from the centre of the Brown CVD diamond (100) surface.

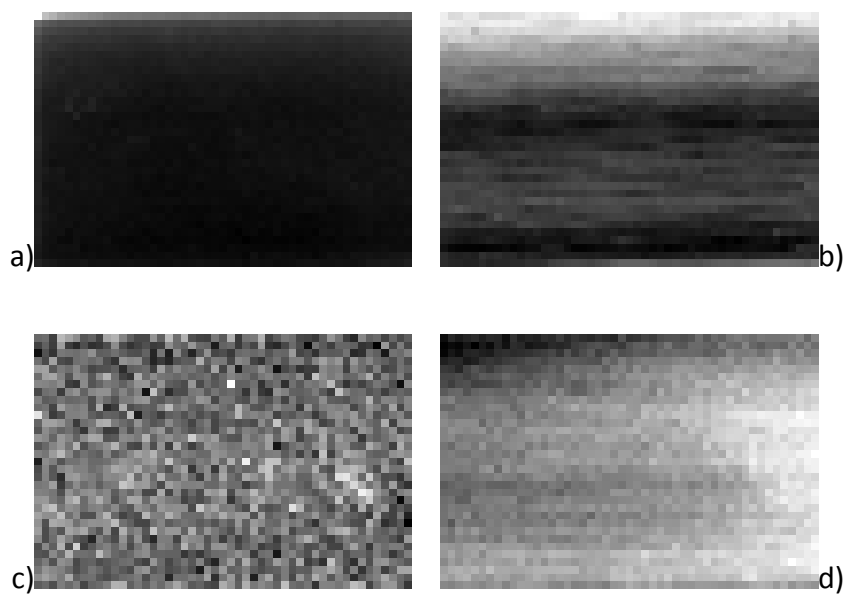


Figure 5-54 Brown CVD maps of the first order Raman line acquired over the central region of the sample; a) background, b) peak position, c) FWHM, and d) peak intensity.

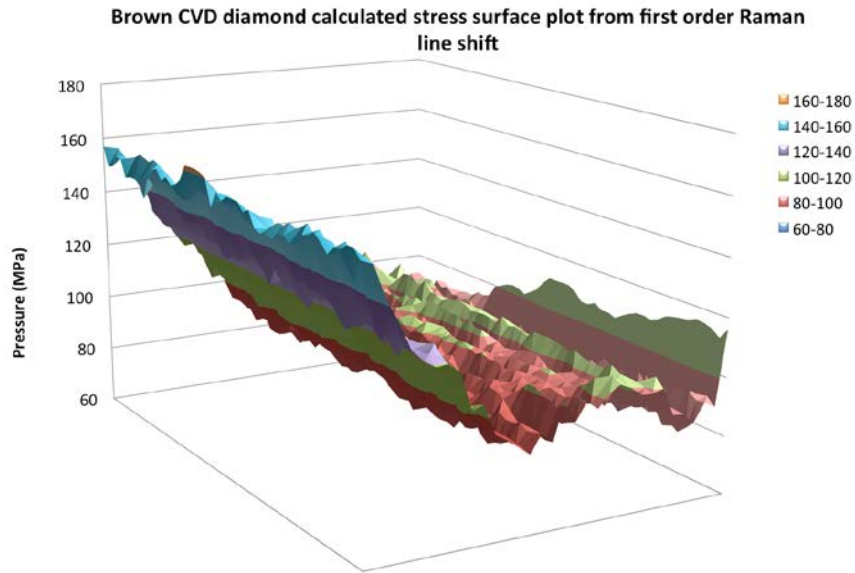


Figure 5-55 Brown CVD diamond central region stress.

The Raman spectra of the intact cut edge, labelled b) in Figure 5-52, are shown below in Figure 5-56. As with the spectrum acquired at the centre of the sample, it comprises of a very sharp first order Raman peak, which, when fitted with a Lorentzian a peak position of  $1332.98\text{ cm}^{-1}$  is found with a FWHM of  $1.83\text{ cm}^{-1}$ . At this location the peak in the second order region at  $2257\text{ cm}^{-1}$  is not as intense as the central spectrum. The calculated stress is in the range of  $78.98\text{ MPa}$  to  $162.3\text{ MPa}$ .

## 5.2 Diamond samples

---

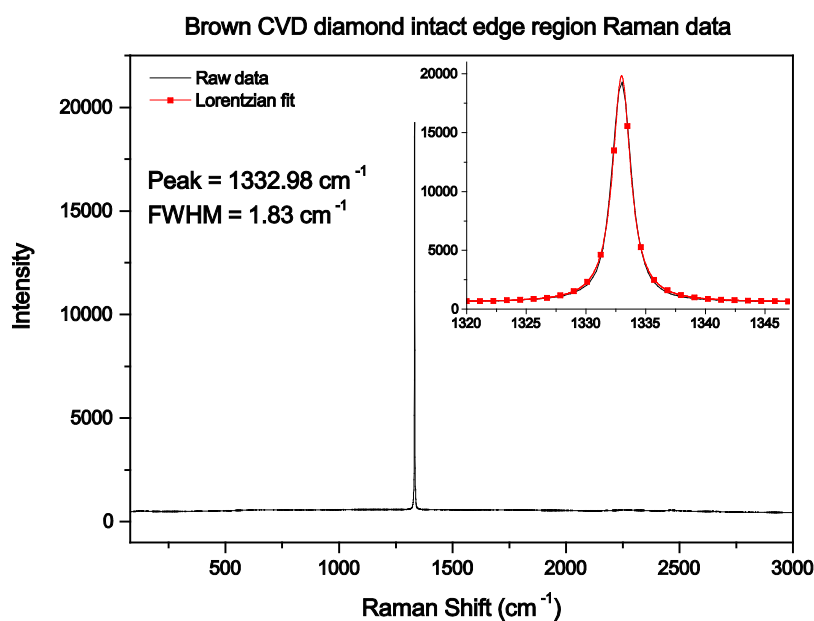


Figure 5-56 Brown CVD diamond spectra acquired at intact sample edge.

The Raman spectrum acquired at the darker brown, chipped edge of the sample shows a more complex set of features than the previous two, shown in figure x below. The dominant feature is, as expected, the first order Raman line for diamond, with the presence of a high PL background and strong, broad peak centred at 2257 cm<sup>-1</sup> as seen in the other regions. In addition there are a number of peaks present in this region. The first order line can be fitted with a Lorentzian to give a peak position of 1332.92 cm<sup>-1</sup>, consistent with high sp<sup>3</sup> content, however the FWHM of 2.98 cm<sup>-1</sup> shows a clear signal of disorder in the lattice.



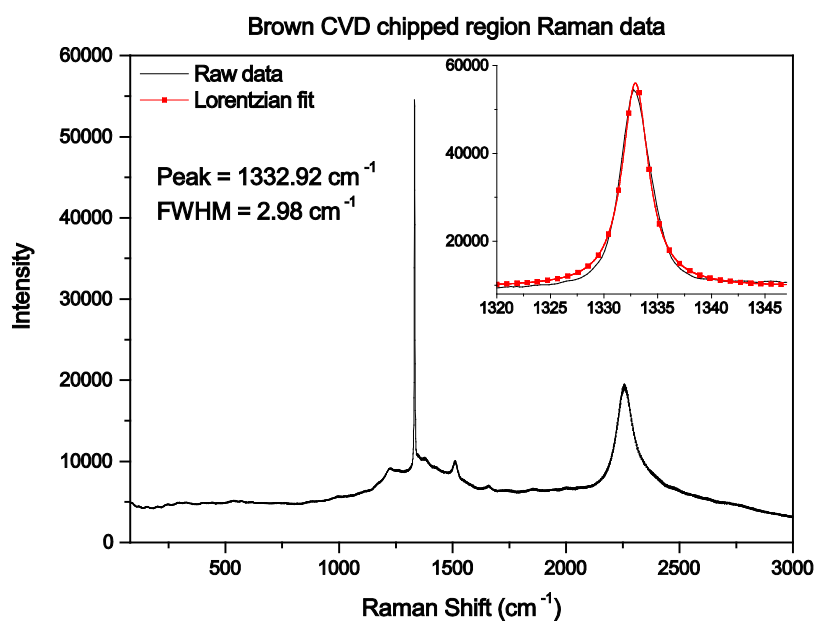


Figure 5-57 Brown CVD diamond chipped region Raman spectra.

Figure 5-58, below, shows a magnified region of the spectrum in Figure 5-58 with the first (red), second (blue), and third (green) order regions illustrated. Table 5-17 summarises the additional features present in this region.

## 5.2 Diamond samples

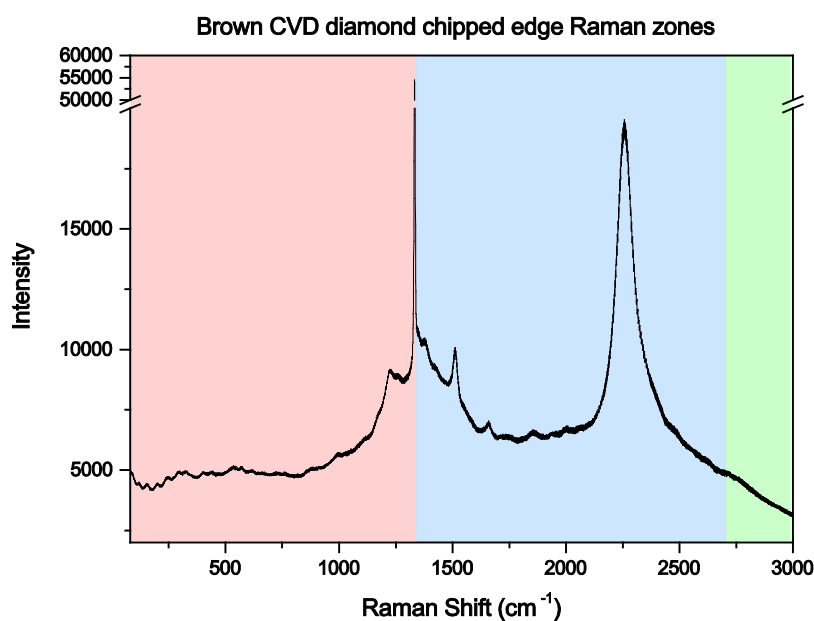


Figure 5-58 Raman spectrum of the chipped region of the brown CVD diamond, the coloured areas correspond to the spectral order; first order (red), second (blue), and third (green).

| Wavenumber<br>(cm <sup>-1</sup> ) | Comments   |
|-----------------------------------|--|
| 1223                              | Non-Diamond disordered carbon phase  |
| 1264                              | Band associated with indentation stress by diamond. Attributed to hexagonal and rhombohedral diamond polytypes   |
| 1333                              | First order diamond Raman line   |
| 1340-1380                         | D-band region (disorder peak). Seen in CVD diamonds which have undergone stress. Attributed to non-diamond carbon phases. Related in grain boundary defects. |
| 1420                              | Band originating in micro-twin regions of CVD diamond, related to the D-band   |
| 1510                              | Band observed in low temperature grown VD diamond, attributed to the 'diamite' or 'bridged graphite' structure   |
| 2257                              | Twinning dislocations  |

Table 5-16 Raman spectral features identified in brown CVD diamond

The three regions are plotted together in Figure 5-59 to illustrate the similarities between the centre and intact edge and the differences between those and the darker region. To examine the second order region further in the same window the three spectra have been normalised to the Raman peak and plotted together in Figure 5-60.

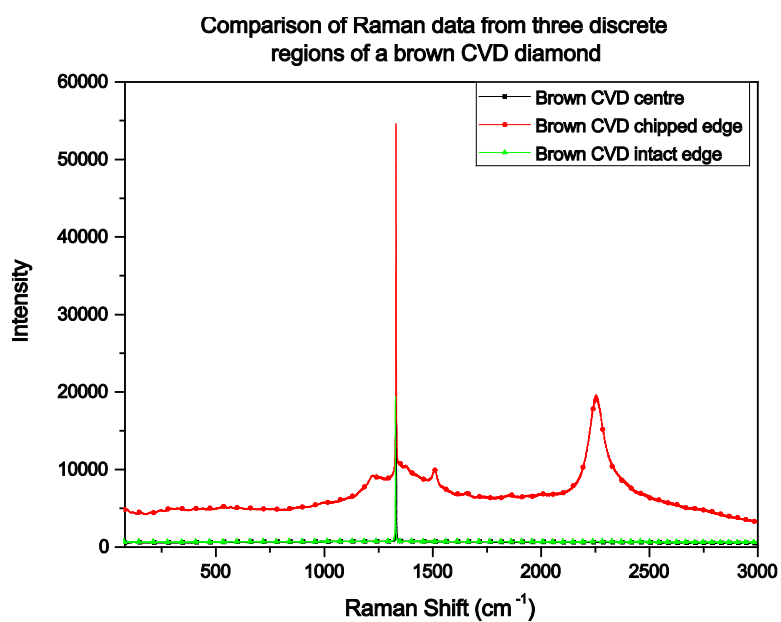


Figure 5-59 Raman spectra from three regions of the brown CVD sample.

## 5.2 Diamond samples

---

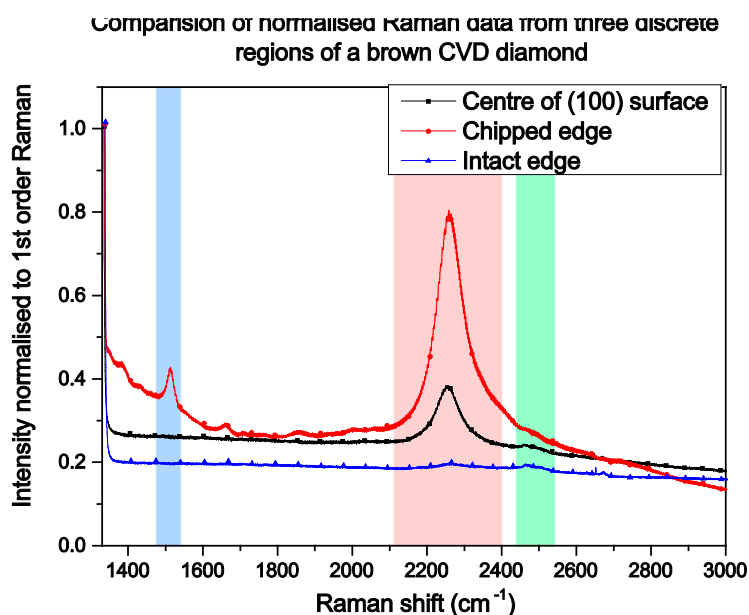


Figure 5-60 Raman spectra of the three regions of interest, normalised to the first order line

The strain is concentrated in an area where there appeared to be a small chip defect. To investigate the sample's inherent strain, Raman mapping spectroscopy was applied to several areas. The chipped edge of the sample shows far more features.

A MathCAD script was written to read in the multiple spectra acquired during mapping locate the Raman peak and fit it with a Lorentzian shape. Maps were produced to illustrate the sample's non-uniformities. Figure 5-61 shows those data presented as maps of Raman line peak height, Raman line FWHM, background and the shift from stain-free diamond (taken to be  $1332.5 \text{ cm}^{-1}$ ).

The centre of the sample shows little change, this is in agreement with the cross-polarisation microscopy.

The corner of the sample, where the colour does not visually seem uniform and strong strain patterns are observed under cross-polarisation, has significant spatial changes to the diamond line's FWHM and peak position shift.

A calculation of the inherent stress has been made and plotted as a map shown in Figure 5-62. When considering the sample as a whole, the strain varies from the chipped region to the centre from 29.9 MPa to 260.7 MPa.

It is well discussed and agreed in literature that plastic deformation plays a role in the brown colouration of natural diamonds. Here it can be shown the strain in the sample correlated to the colour, where the darker chipped region shows more intense strain. Undoped CVD diamond typically has a much higher concentration of vacancies than those doped. Boron doping has been shown to reduce this level; comparing the two CVD specimens studied shows evidence of this<sup>249</sup>.

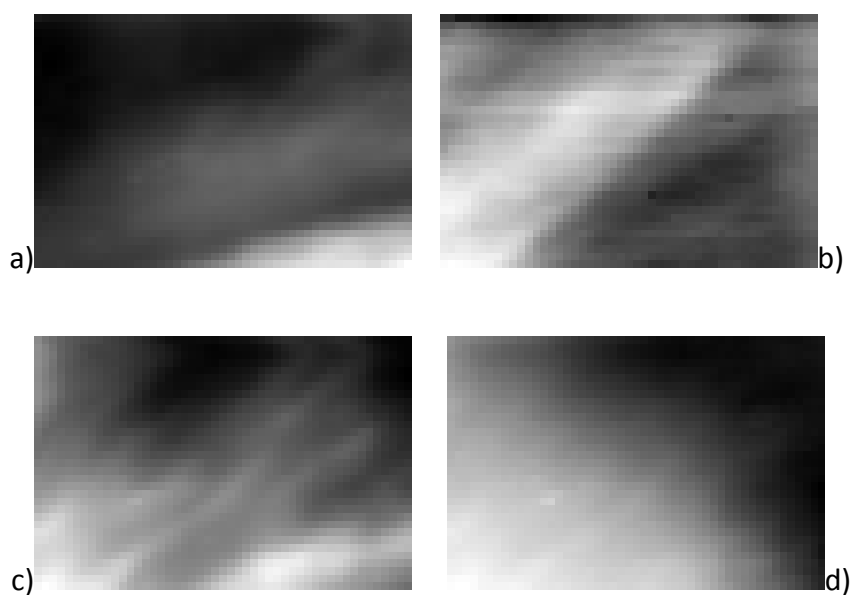


Figure 5-61 Brown CVD diamond maps of the first order Raman peak; a) background, b) peak position, c) FWHM, and d) peak intensity.

## 5.2 Diamond samples

---

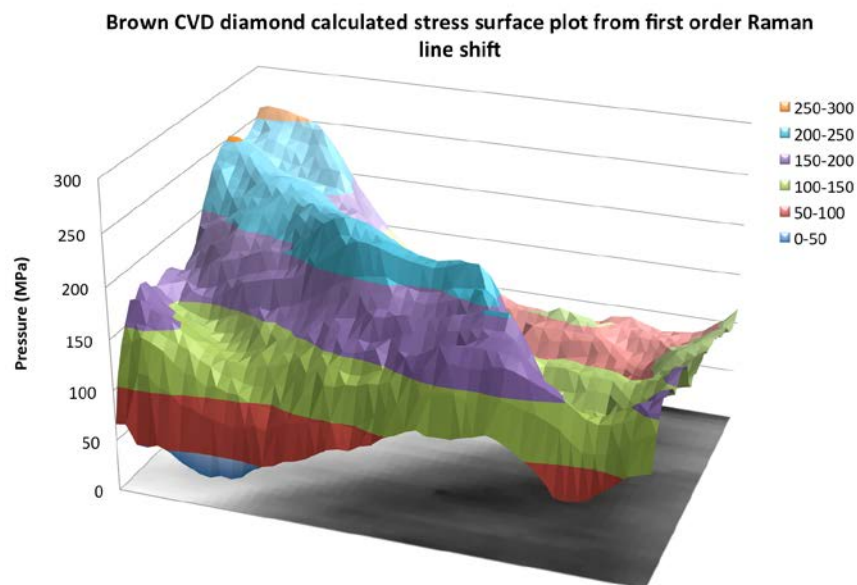


Figure 5-62 Brown CVD damaged region stress map generated from the shift in the first order Raman peak.

The stress was calculated to range from a minimum of 29.9 MPa to a maximum of 260.7 MPa.

The size of the mapped region comprised of 1617 points sampled (spectra acquired) over area of  $80.127\ \mu\text{m} \times 120.307\ \mu\text{m}$  at  $2.5\ \mu\text{m}$  intervals. The brighter regions, showing an increase in shift from the ideal  $1332\ \text{cm}^{-1}$ , indicate higher values in image b), and show the broadening of the FWHM in image c).

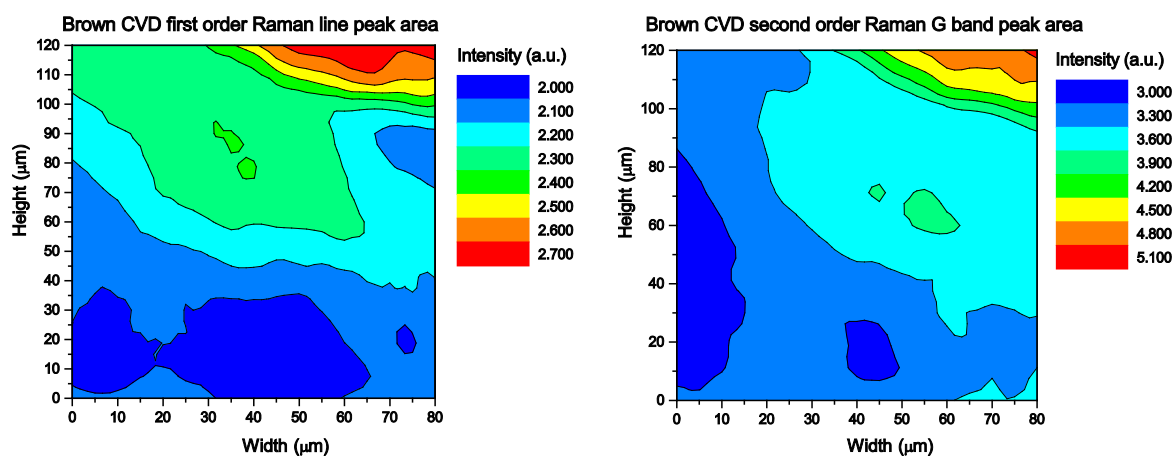


Figure 5-63 2D plot of the first order Raman line peak area (left), and of the  $1510\text{ cm}^{-1}$  peak area (right). The area of higher intensity (red) corresponds to the chipped region of the sample. This higher intensity of the first order line (left) corresponds to a broadening of the peak indicative of increased disorder. The intensity of the graphitic like feature at  $1510\text{ cm}^{-1}$  (right) is indicative of increased  $\text{sp}^2$  bonding.

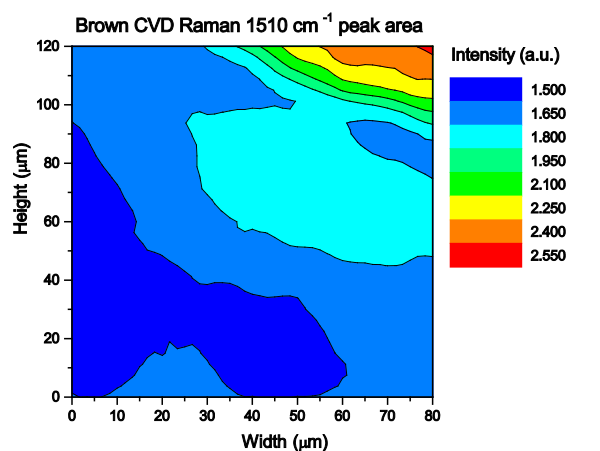


Figure 5-64 2D plot of the peak area intensity of the Raman G-Band. As in Figure 5-63, there is an increased  $\text{sp}^2$  component located at the site of the chipped region of the sample.

## 5.2 Diamond samples

---

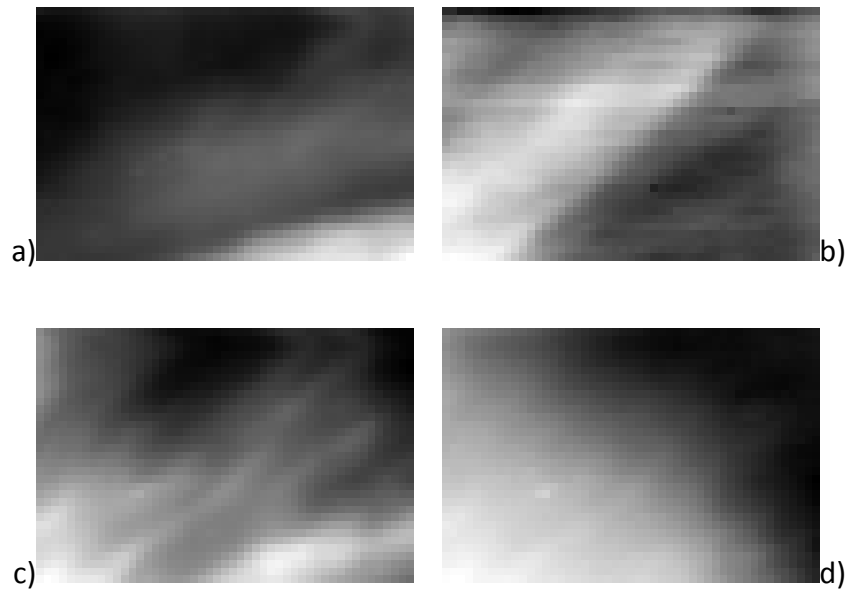


Figure 5-65 Maps of the first order Raman line of a brown CVD diamond; a) background, b) peak position, c) FWHM, and d) peak intensity of the darker chipped region.

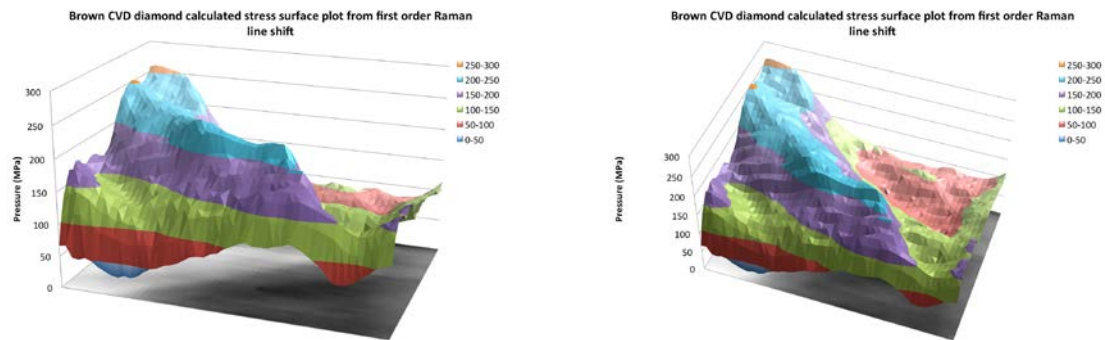


Figure 5-66 Brown CVD damaged region stress map from different angles of the calculated stress in the darker chipped region. The higher intensity region (orange) is located at the site of the chipped region.



### 5.2.2.3 Polycrystalline CVD Diamond

Polycrystalline diamonds are tougher than single crystal diamonds <sup>250</sup> , and are most frequently used for cutting and polishing other hard materials. They can be produced in nature and artificially by CVD and HPHT. For consistency with the single crystal samples the samples studied in this work have been produced by CVD.



Figure 5-67 Small grain PcCVD diamond under white light at 4x magnification. Image width is 4mm.

Polycrystalline diamond has promising potential applications, however the properties are often affected by chemical impurities (most often hydrogen incorporated during CVD growth), structural defects and the inclusion of other carbon allotropes such as amorphous and graphitic-like carbon. Such defects and inclusions have been shown to affect the material's properties, influencing hardness, optical transparency and electrical properties. For this reason it is imperative to develop a reliable method of characterisation for the examination of these defects. HeLIOS spatially resolved photoluminescence and Raman mapping have been used to investigate the spatial distribution of light emission and stress within a CVD polycrystalline sample. Two samples were available for investigation, one with

## 5.2 Diamond samples

---

larger grain sizes than the other. The smaller grain sized sample was selected as the larger grain exhibited a high surface roughness under AFM, reducing the accuracy of the Raman mapping due to focus shifting during data acquisition. This sample, and a larger grain sample, are of interest to the group as a potential substrates for localised graphene growth by iron mediation <sup>8</sup>.

PcCVD diamond consists of a mixture of  $sp^3$  and  $sp^2$  phased carbon <sup>251</sup>. Raman of undoped diamond had a line at  $1332\text{ cm}^{-1}$ , due to phonons of  $F_{2g}$  symmetry. The  $sp^2$  graphitic components of the spectra are identified at  $\sim 1360\text{ cm}^{-1}$  and  $\sim 1500\text{ cm}^{-1}$ , the D (disorder) and G (graphite) peaks respectively.

Polycrystalline materials are generally found to contain a wide variety of extended defects. Grain boundary defects are characteristic of polycrystalline material <sup>252</sup>.

Broad luminescence bands in PcCVD diamond films have been observed<sup>252</sup>, making links between grain boundaries and broadband luminescence. Extensive grain clusters are formed during CVD growth, composed of individual grains. Broadband PL at 1.698 eV. Polycrystalline materials are known to contain a wide variety of extended defects.

Micro-Raman spectroscopy has been used to study the residual stress in polycrystalline diamond cutting tools by monitoring the peak frequency and width of the first order diamond line<sup>253</sup>, as has resonant Raman scattering to examine polycrystalline diamond films<sup>254</sup>. This showed the  $sp^3$  peak at  $1332\text{ cm}^{-1}$  and a broader feature at  $1550\text{ cm}^{-1}$  which they attribute scattering by  $sp^2$  bonded carbon. This feature is seen to change in position and size with increasing incident photon energy. They rule out microcrystalline graphite (Raman peak  $1580\text{--}1600\text{ cm}^{-1}$ ).

Undoped CVD polycrystalline films commonly contain vacancies of different flavours such as; monovacancies, divacancies and vacancy clusters. Vacancies are often found coupled with other defects such as impurities and grain boundaries, making resolving them difficult<sup>249</sup>.

#### 5.2.2.4 Cross-polarisation spectroscopy

Cross polarisation microscopy has been used to examine birefringence in the PcCVD sample.

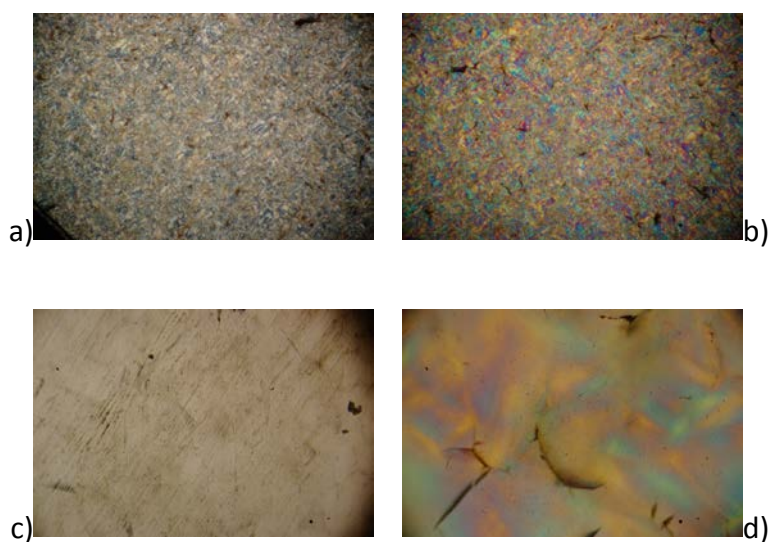


Figure 5-68 Small grain PcCVD diamond cross-polarisation images; a) and c) sample imaged between cross-polarisers at 4x magnification, image width 4 mm; b) and d) sample imaged with the addition of a  $\frac{1}{4}\lambda$  filter at 10x magnification, image width 1.5 mm.

### 5.2.2.4.1 HeLIOS spatially resolved PL

From the ROI data a similar spectral profile as that obtain in the brown banded region of the natural Ia diamond sample can be seen. This forms a link between the brown colouration and stress, from the Raman mapping presented next, the sample is seen to be highly stressed. The radiometrically corrected HeLIOS images in the figures below show the contrast in the luminescence across the sample which agree with its colouration and birefringence patterns from the cross-polarisation studies.

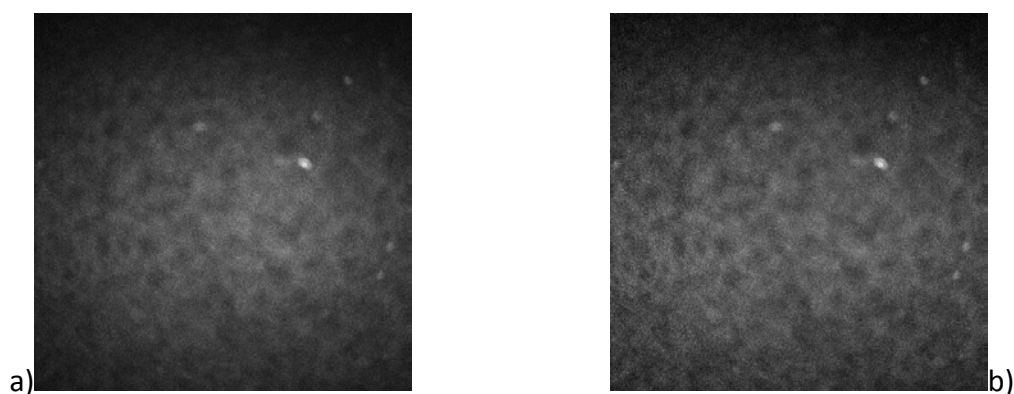


Figure 5-69 HeLIOS images of the PccVD sample under 365 nm excitation at 2x magnification; a) raw 520 nm image, and b) corrected image.

In figure 5-69 the effect of the flat field calibration can be seen correcting the vignetteing observed in the raw image (a).

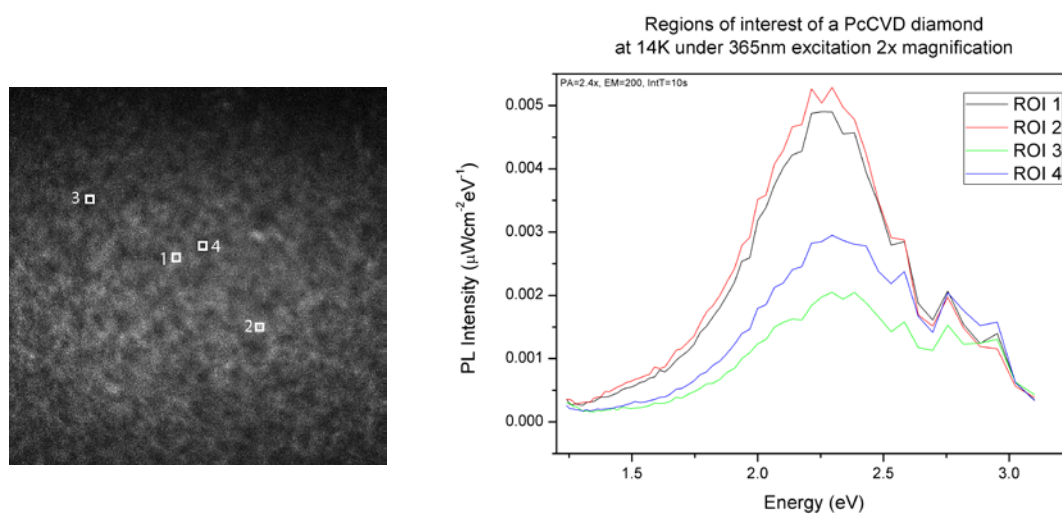


Figure 5-70 PcCVD diamond spatially resolved PL ROIs of 10 x 10 pixels. ROIs 1 and 2 correspond to brighter areas, shown with the higher intensity compared to 3 and 4 from darker regions when selected from the 500 nm image. A small peak shift can be observed between the light and dark ROIs in the 2.0 – 2.5 eV region.

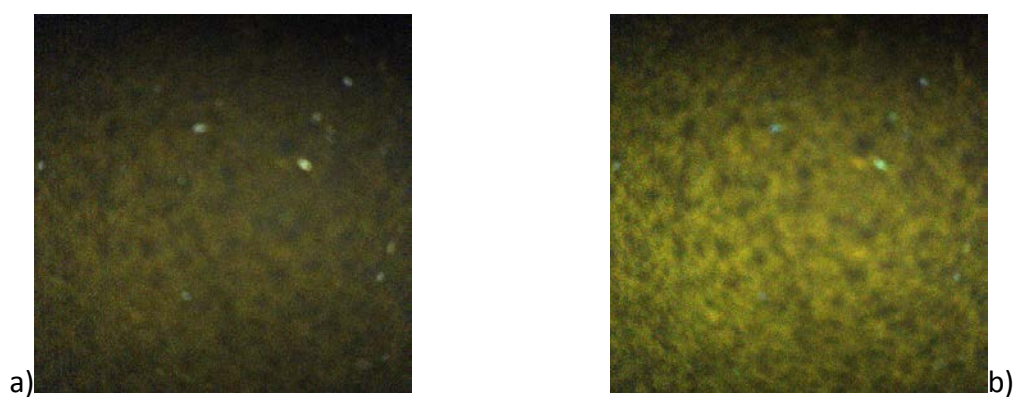


Figure 5-71 HeLIOS RGB composite images of the PcCVD sample under 365 nm excitation at 2x magnification; a) R=510, G=500, B=450 nm, and b) R=620, G=540, B=450 nm.

## 5.2 Diamond samples

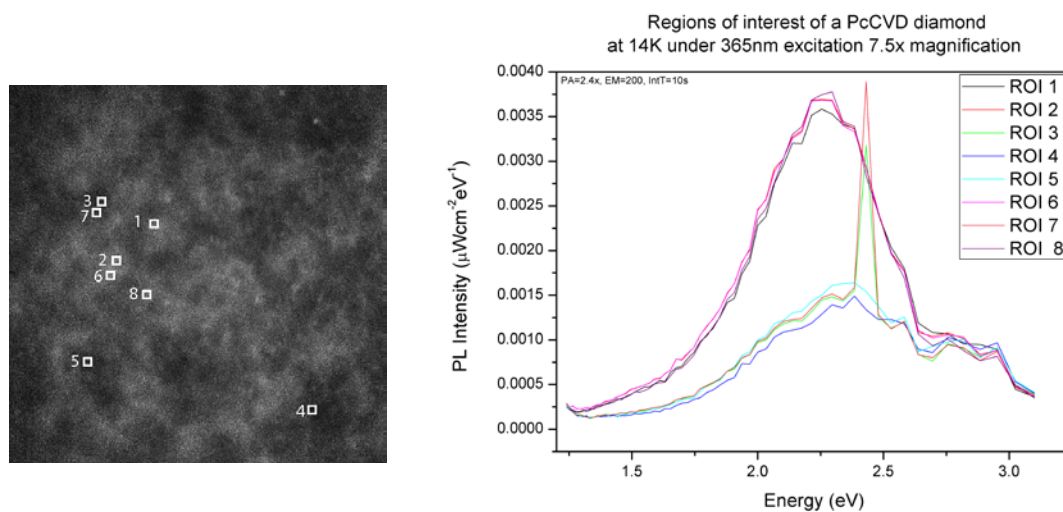


Figure 5-72 PcCVD spatially resolved PL ROIs of 10 x 10 pixels. Two ROIs (2 and 3) display sharp peaks at x eV. A slight shift can again be observed between the light and dark regions.

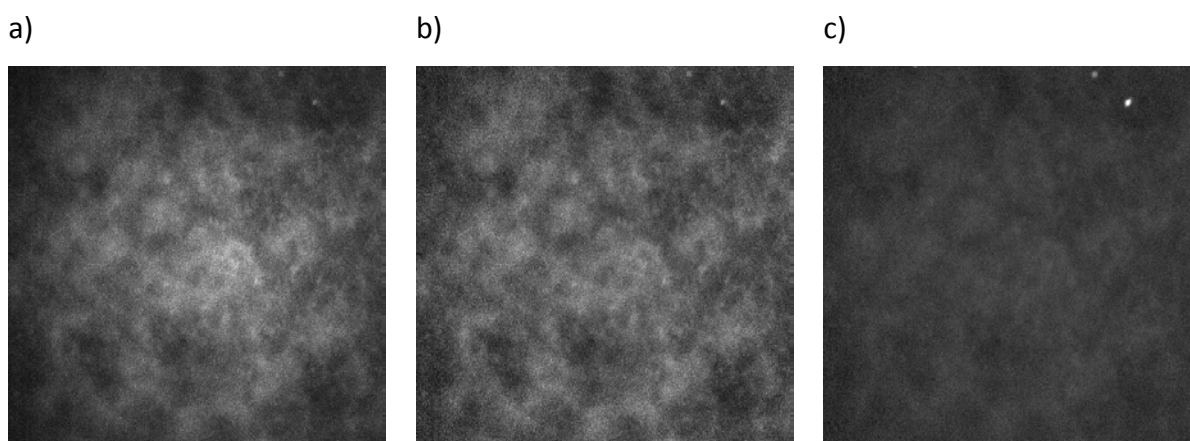


Figure 5-73 HeLIOS images of the PcCVD sample under 365 nm excitation and 7.5x magnification; a) raw image at 700 nm, b) corrected image at 600 nm, c) corrected image with enhances contrast at 500 nm.

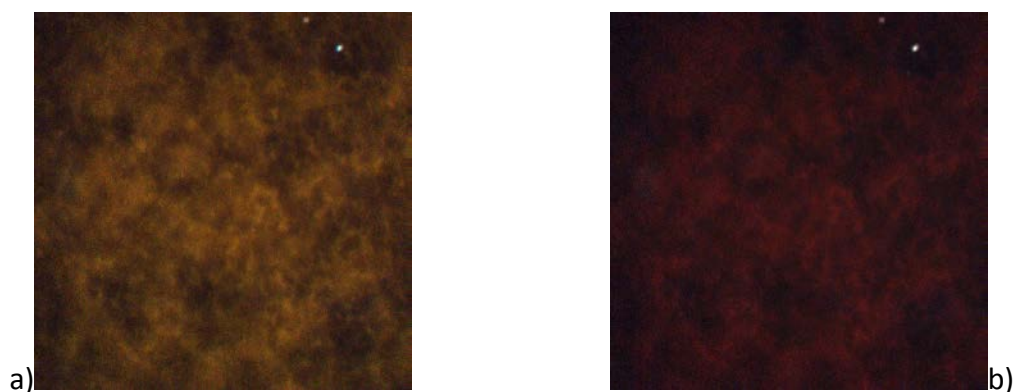


Figure 5-74 HeLIOS RGB composite images of the PcCVD sample under 365 nm excitation and 7.5x magnification; a) R=620, G=540, B=450 nm, and b) R=540, G=480, B=450 nm.

#### 5.2.2.4.2 Raman Spectroscopy

Raman spectroscopy has been used to investigate the stress in the material. The local stress fluctuations in a PcCVD sample have been illustrated in this work using Raman mapping.

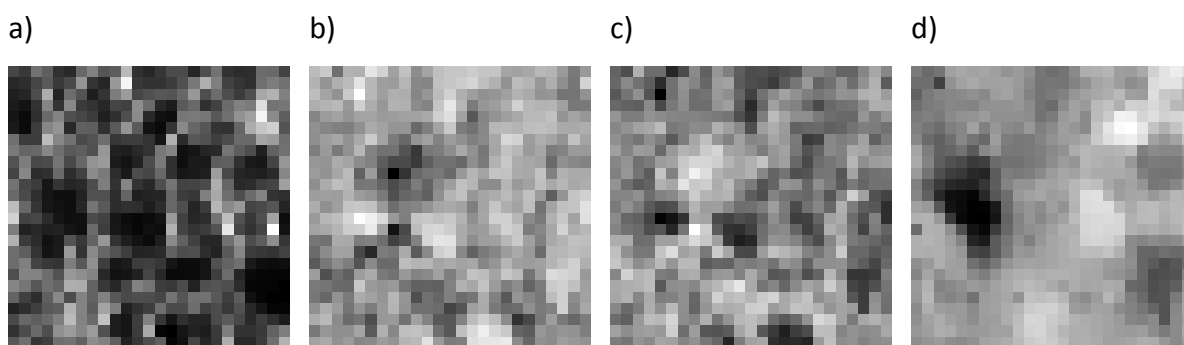


Figure 5-75 PcCVD maps of the Raman first order diamond line; a) background, b) peak position, c) FWHM, and d) peak intensity of a 100x100  $\mu\text{m}$  area.

## 5.2 Diamond samples

---

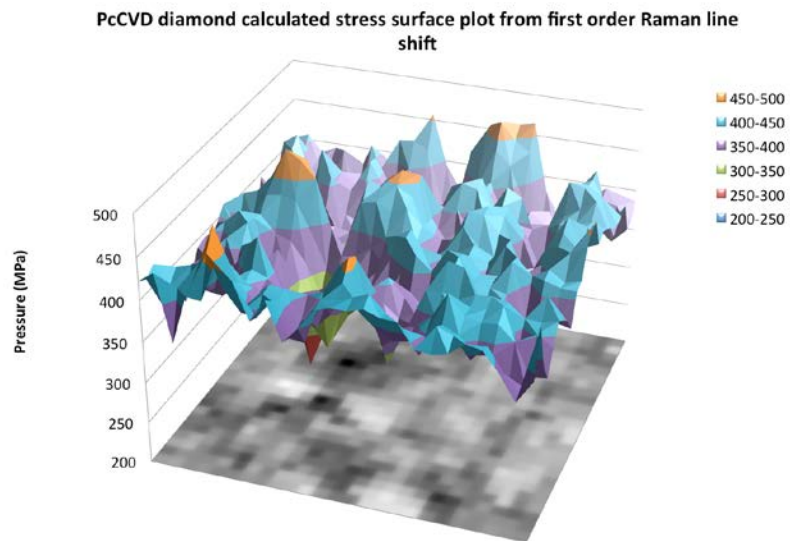


Figure 5-76 PCCVD stress map, stress is shown to be compressive ranging from 256.5 MPa to 483.2 MPa.

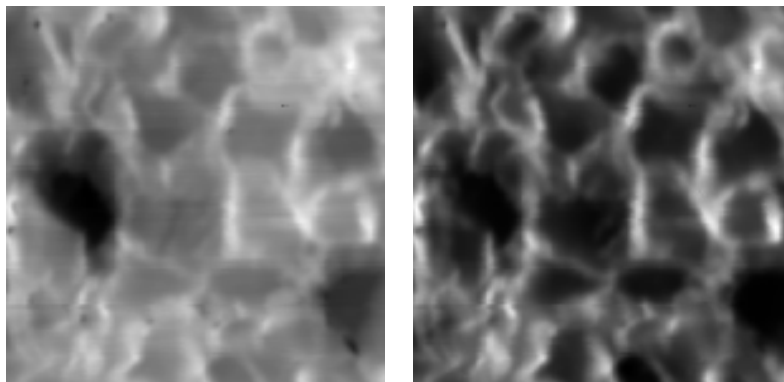


Figure 5-77 (left) The area of the first order peak, (right) the area of the G Band peak. The individual grains of diamond are clearly visible using this contrast.



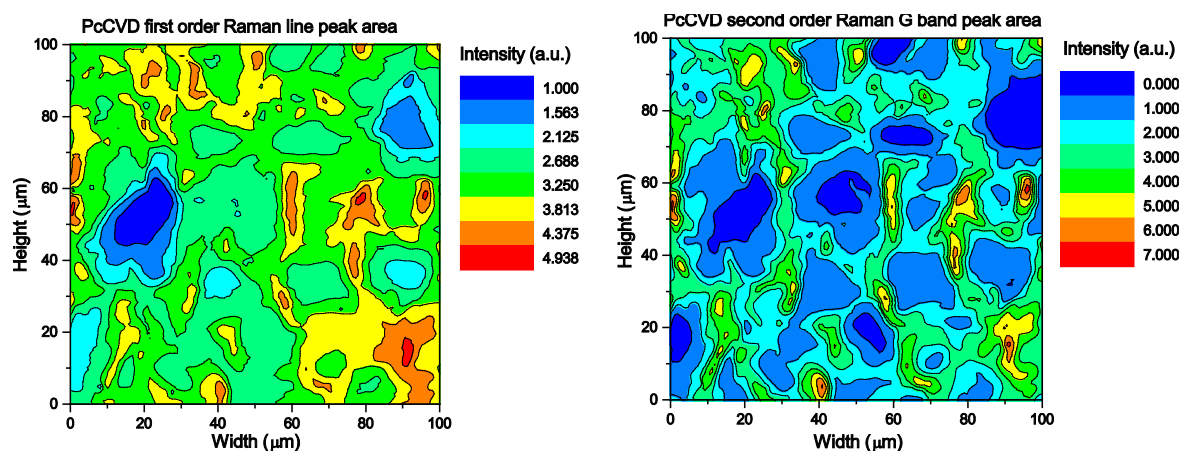


Figure 5-78 (left) Intensity of the area under the first order Raman peak, (right) The area under the Raman G Band.

The low intensity areas of the peak correspond to a smaller FWHM, where the diamond is more 'ideal' the first order Raman peak is sharper.

Figure 5-79 shows that in the most intense graphitic like region there is a distinct peak at  $1510\text{ cm}^{-1}$ , which is not present in the more diamond like regions. This peak is associated with CVD diamond grown at low temperatures.

## 5.2 Diamond samples

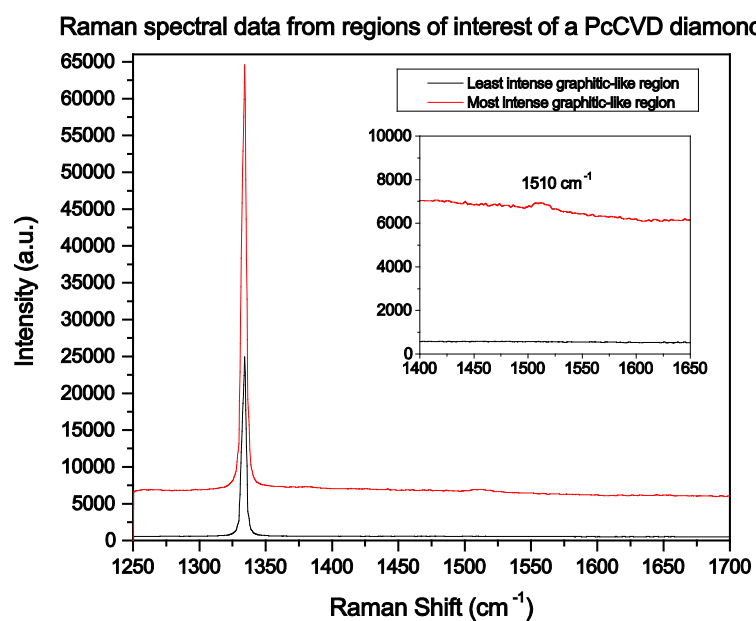


Figure 5-79 Two spectra extracted from the map in the regions of least and most intense graphitic-like diamond.

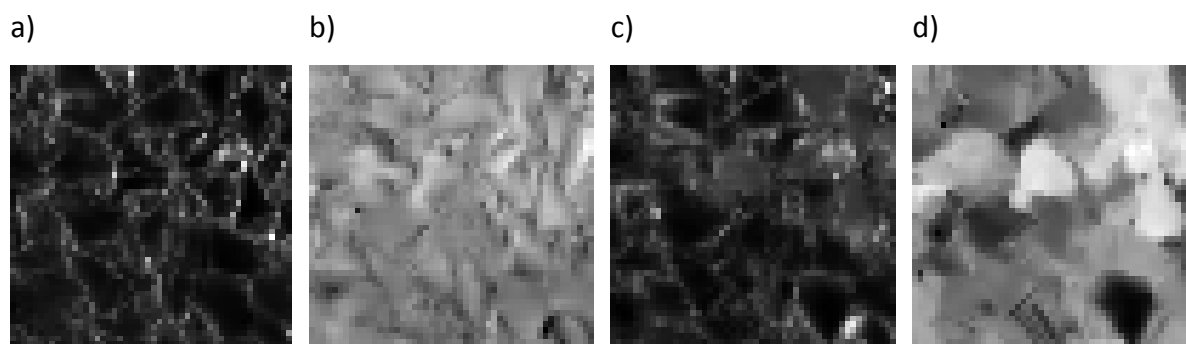


Figure 5-80 PcCVD diamond maps of the Raman first order line; a) background, b) peak position, c) FWHM, and d) peak intensity of a region  $300 \times 300 \mu\text{m}$ .

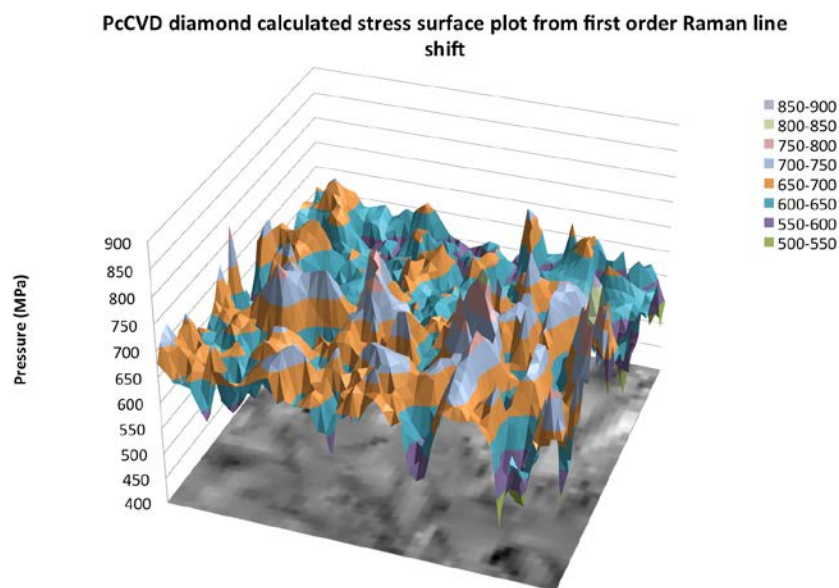


Figure 5-81 PcCVD stress map of the region shown in Figure 5-80. The compressive stress ranges from 392.5 MPa to 868.1 MPa.

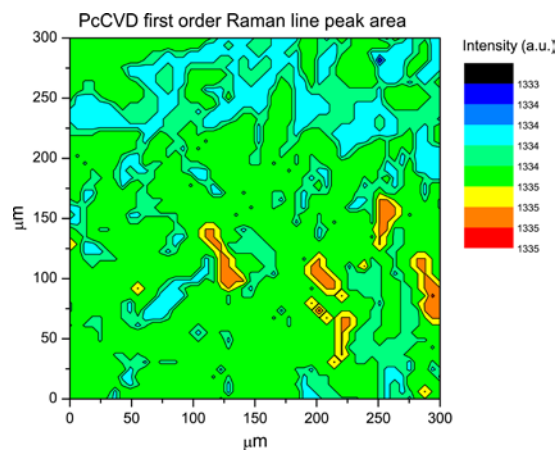


Figure 5-82 Intensity map of the area under the first order Raman peak of the mapped area.

## 5.2 Diamond samples

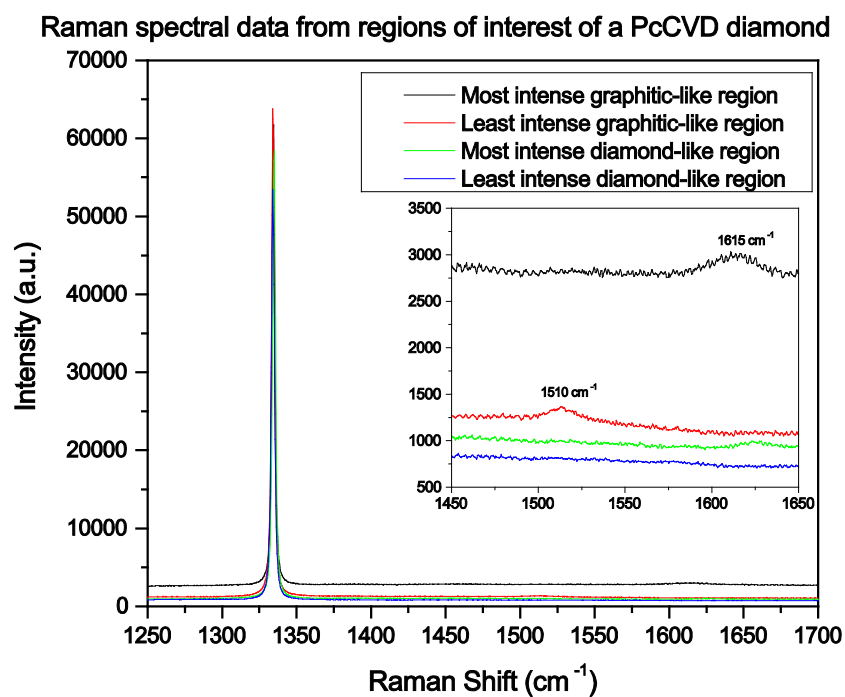


Figure 5-83 Spectra extracted from the map dataset at locations of low and high  $sp^2$  and  $sp^3$  bonded carbon.

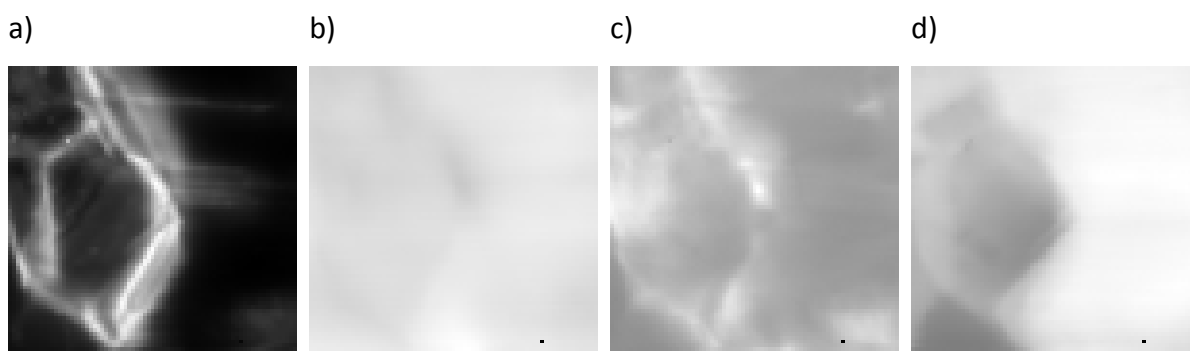


Figure 5-84 PcCVD diamond maps of the first order diamond Raman line; a) background, b) peak position, c) FWHM, and d) peak intensity of a 55x55  $\mu\text{m}$  area.

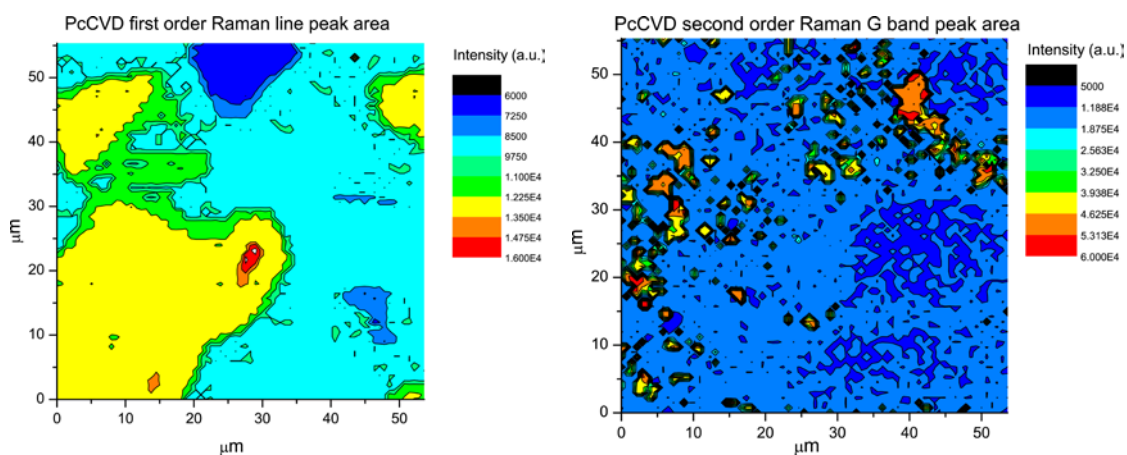


Figure 5-85 (left) 2D map of first order peak area intensity, (right) 2D map of G Band area.

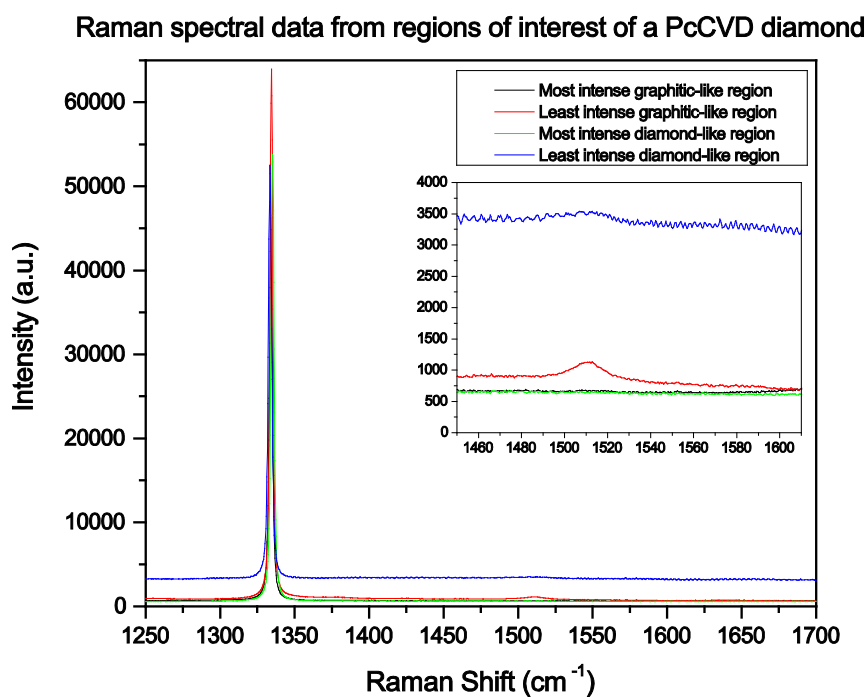


Figure 5-86 Spectra extracted from the map data set at locations of high and low  $\text{sp}^2$  and  $\text{sp}^3$ .

## 5.2 Diamond samples

---

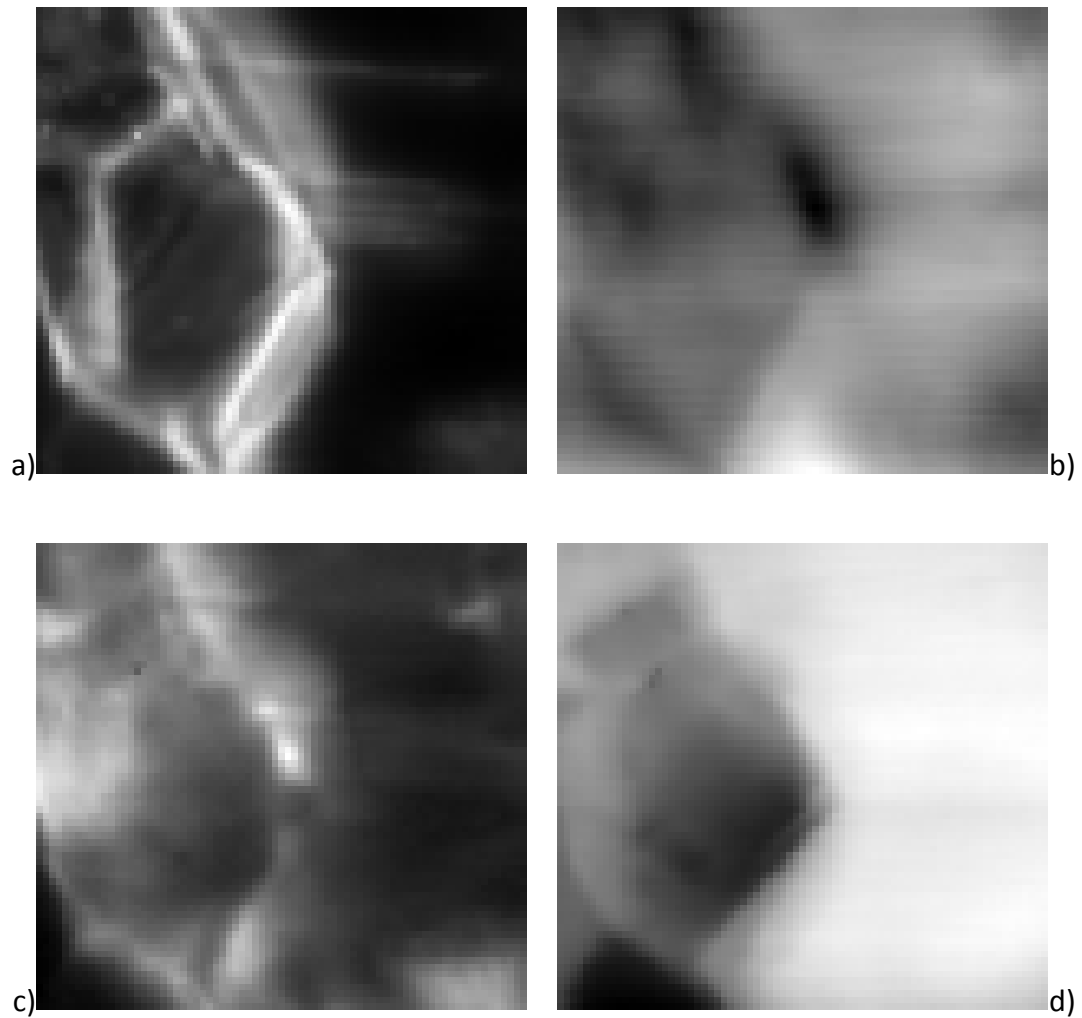


Figure 5-87 PcCVD diamond maps of the first order diamond Raman line; a) background, b) peak position, c) FWHM, and d) peak intensity of 55x55  $\mu\text{m}$  area.

Figure 5-88 below illustrates the calculated stress of the region mapped in Figure 5-87. This stress is seen to range from 593.1 to a maximum of 2023 MPa.

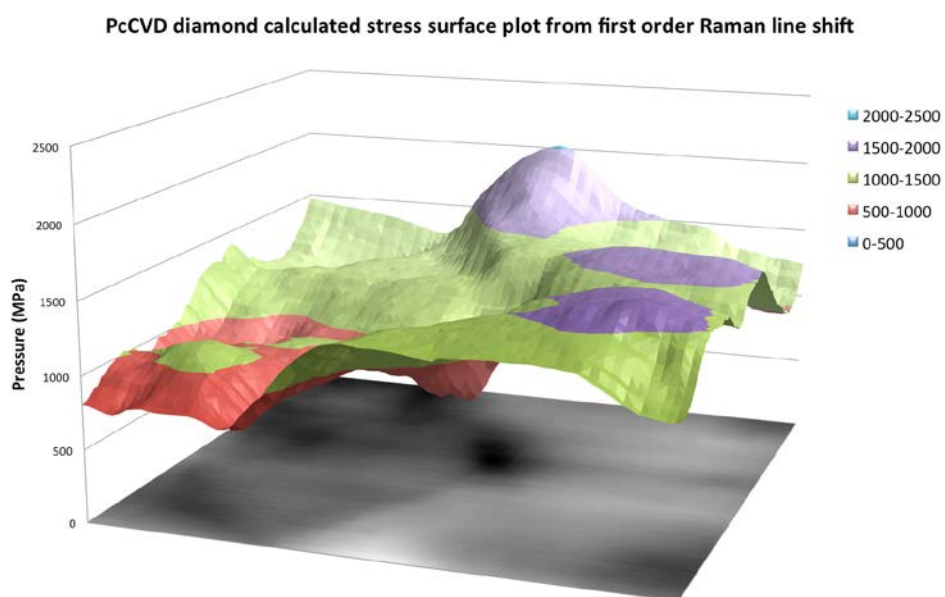


Figure 5-88 3D PcCVD stress map illustrating the magnitude of stress around the grain boundary.

## 5.2 Diamond samples

### 5.2.3 Non-diamond mineral samples

In addition to the diamond samples studied as part of this work a number of additional samples were studied to provide an assessment of the capabilities of HeLIOS. These have been selected to tie in with other research streams the author is involved in. Samples have been selected in order to demonstrate HeLIOS' applications to fields additional to materials physics such as Earth Science and Astrobiology.

The samples are summarised in Table 5-17.

| Sample             | ZnO   | Troll Springs CaCO <sub>3</sub>                                     | Glowed Bithynia Tentaculata Operculum                        |
|--------------------|---|---|--|
| Origin             | Hydrothermally grown                          | Natural   | Natural  |
| Dimensions         |   |   |  |
| Appearance         | Uniform, high quality clear (faint blue tint) | Striated sample with areas emitting VIS PL at different wavelengths | Spatially interesting sample showing concentric growth rings |
| Techniques applied | HeLIOS and ApREES PL                          | HeLIOS PL   | HeLIOS PL  |

Table 5-17 Non-diamond mineral samples

#### 5.2.3.1 ZnO

During the course of this work access was given to very high quality hydrothermally grown ZnO of different faces (m and c axis), kindly provided by Prof Allen of Canterbury University, New Zealand. This material has been included for study using HeLIOS as due to the exceptional quality and high brightness under UV excitation.

ZnO is a naturally n-type wide direct band-gap ( $E_g=3.37$  eV) semiconductor with a high room temperature exciton binding energy of 60 meV<sup>255</sup> of Wurtzite structure with numerous



applications, including piezoelectric transducers, varistors and phosphors due to this wide band-gap<sup>256,257</sup>. The higher exciton binding energy enhances the luminescence efficiency of light emission. It is transparent to visible light, operating in the UV to blue wavelength region. The high exciton binding energy is thought to potentially lead to room temperature lasing action based on exciton recombination<sup>258</sup>; it is considered to be a future alternative to GaN for high efficiency laser applications<sup>259</sup>. It has been observed to exhibit near-band-gap (NBG) emissions at 380nm as well as broad defect bands in the visible spectrum. The luminescence in the visible spectral range due to intrinsic defects<sup>255</sup>, including green at ~2.3 eV, yellow at ~2.1 eV and red at ~1.8 eV. The broad red luminescence has been related to surface defects and the green emission is speculated to arise from core defects. The origin of the green emission however is controversial<sup>28,33,258,260</sup>. Low temperature PL can be used to confirm the quality of a sample via the bands observed. The strongest features are observed in the NBE (Near Band Edge) spectrum; three sharp lines between 3.36 and 3.37eV are from excitons bound to donors. A second order line at 3.365 eV can be further resolved into three more lines. A weak spectral response centred at 3.374 eV is the A-band free exciton. Due the instrumental configuration these were not detectable. The green band at 2.4 eV is very weak compared to the NBE, but still readily detectable and can be observed by eye.

As stated the green band, a broad defect related peak extending from 1.9 to 2.8 eV is a common optical feature in ZnO. Gaspar *et al*<sup>261</sup> investigated the green (2.19eV) and yellow (2.00eV) luminescence bands commonly present in ZnO samples using above band gap excitation. They tentatively assign the green region to the Cu related excitonic band. Reshchikov *et al*<sup>262</sup> provided a description of the main PL characteristics observed in ZnO, these are summarised in Table 5-18 below.

## 5.2 Diamond samples

| PL band | Peak Position (eV) at 10K | Description  |
|---------|---------------------------|--|
| RL1     | 1.75                      | Red band, samples grown and annealed in air  |
| RL2     | 1.8                       |  |
| OL      | 1.95                      | Orange band, samples grown and annealed in air and those grown by hydrothermal method. Assigned to transitions from shallow donors to a deep acceptor with an energy level about 0.5-0.6 eV above the valence band |
| YL1     | 2.15                      | Yellow band, observed at low temperatures once the dominance of the red band is reduced. Assigned to transitions from shallow donors to an unidentified deep acceptor  |
| YL2     | 2.19                      | Postulated to be caused by transitions from shallow donors to a deep acceptor  |
| YL3     | 2.25                      | This band is seen to increase with UV exposure and is quenched at temperature above 200K   |
| GL1     |                           | Not observed at low temperature, seen at ~ 2.3 at RT   |
| GL2     | 2.38                      | Unresolved   |
| GL3     | 2.42                      | Unresolved   |
| GL4     | 2.47                      | Unresolved   |
| GL5     | 2.6                       | Unresolved   |

Table 5-18 Characteristic ZnO PL features adapted from Reshchikov *et al*<sup>262</sup>

### 5.2.3.1.1 HeLIOS high-resolution spectroscopy

HeLIOS high-resolution PL spectroscopy was performed on the c-axis face of the sample. An example can be seen in Figure 5-84. The spectrum shows the characteristic UV excited PL shape for high quality ZnO at low temperatures. Here the orange and yellow bands dominate the spectrum. A small contribution from the green band's ZPL at 2.86 eV is just visible. Inset to Figure 5-89 illustrates the flat, broad top of the peak.

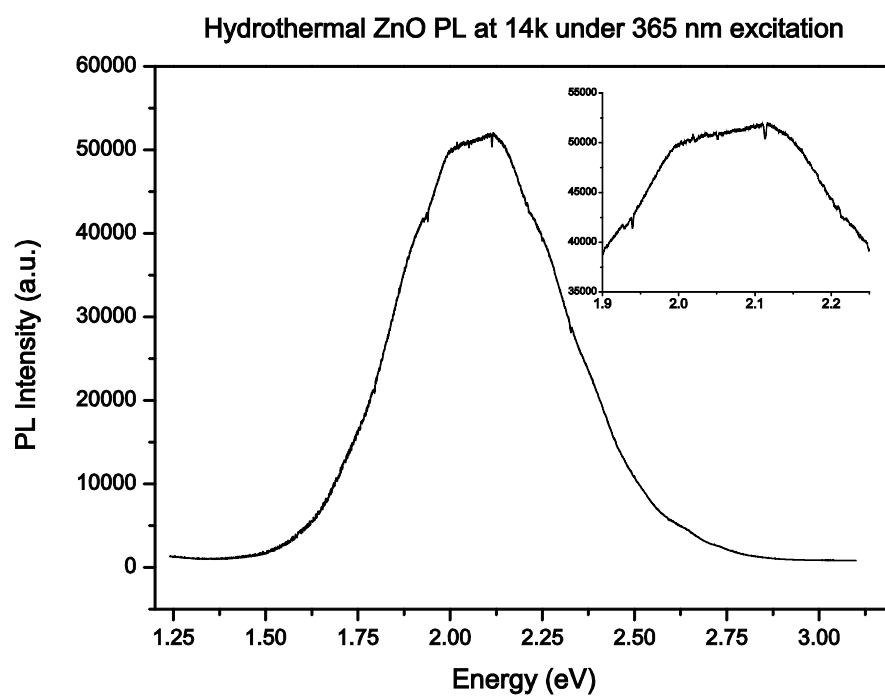


Figure 5-89 ZnO high resolution PL at 14K under 365 nm excitation.

### 5.2.3.1.2 HeLIOS spatially resolved PL

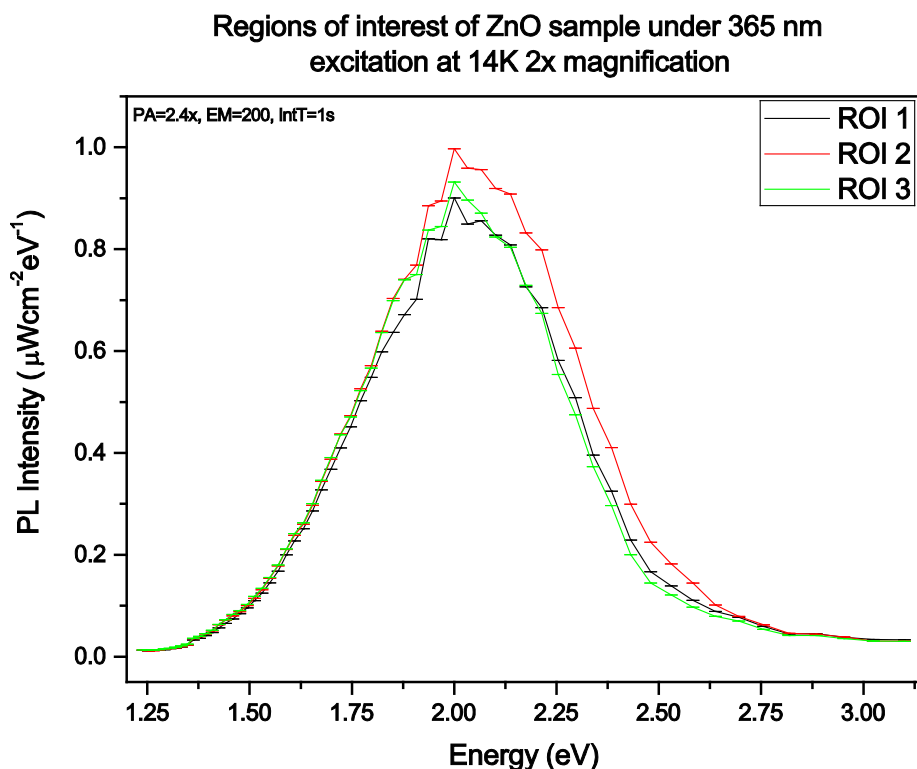


Figure 5-90 ZnO spatially resolved PL and ROI location.

Peaks are in agreement at 1.95 eV (orange band) and 2.19 eV (second yellow band) with those of Reshchikov<sup>262</sup>. Additional green band peaks can be identified through fitting of the data.

Comparison between the high resolution and spatially resolved data is shown in Figure 5-91 below by normalising both datasets. A broadening of the peak can be seen in the spatially resolved data, the cause of this is most likely the comparatively wide wavelength range (10 nm) of acquisition.

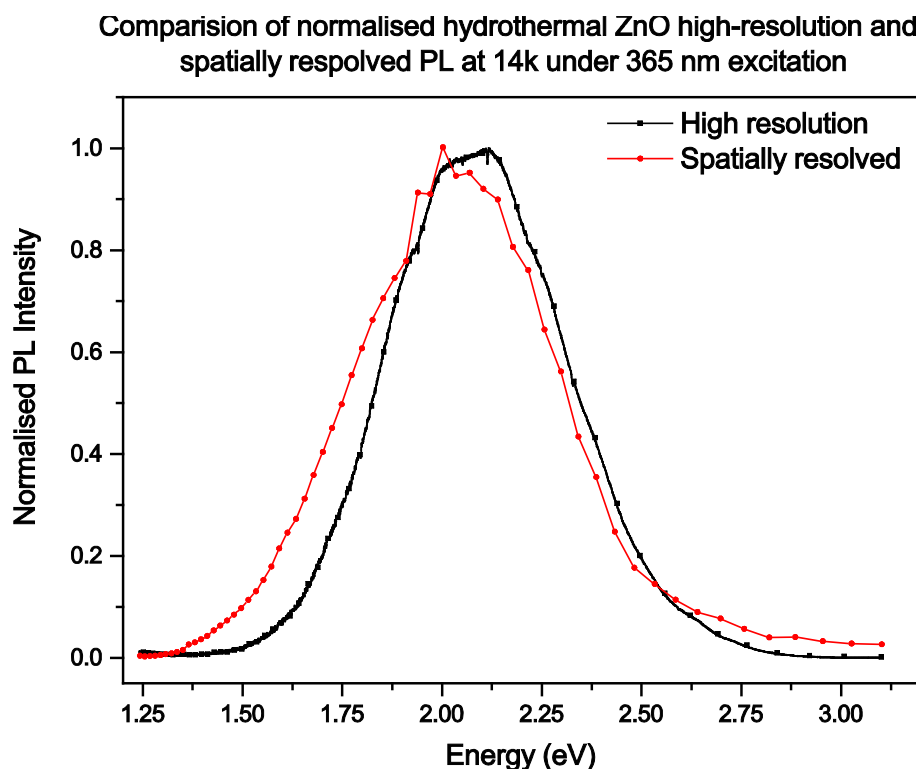


Figure 5-91 Comparison of normalised high resolution and spatially resolved ZnO PL under 365 nm excitation.

### 5.2.3.2 Calcium Carbonate

The  $\text{CaCO}_3$  sample studied in this work was kindly provided by Dr Claire Cousins. It was collected from a large carbonate terrace surrounding the warm Troll Spring in the Bockfjord complex of Svalbard. The sample was chosen to provide a geologically representative, spatially interesting example of an analogue Mars surface in order to provide a meaningful test for HeLIOS. The data taken during the preliminary studies into its luminescence have been fed into a number of proposals submitted during the course of this thesis<sup>89</sup>. Earlier work by Cousins<sup>263</sup> showed the importance of testing for hydrated minerals to identify regions which may have bio-signatures. The forthcoming ExoMars 2018 mission<sup>59,75,264,265</sup> has a distinctly

## 5.2 Diamond samples

---

astrobiological focus. Carbonates on Mars are high priority science targets for this and future missions, such as NASA's 2020 due to their association with neutral-alkaline aqueous environments<sup>263</sup>. They offer high preservation potential for signs of life past or present.

CaCo<sub>3</sub> is a wide band gap insulator<sup>266</sup> with a rhombohedral unit cell. The band gap has been calculated by theory to be  $4.4 \pm 0.35\text{eV}$ , however Reflection Electron Energy Loss Spectroscopy (REELS) measurements put it at  $6.0 \pm 0.35\text{ eV}$ <sup>267</sup>. CaCo<sub>3</sub> can exist in three crystalline polymorphs; Calcite, Aragonite and Vaterite<sup>268</sup>. Some of the most important and widely studied luminescent centres in CaCo<sub>3</sub> are Mn<sup>2+</sup> (green-red emission), Ni<sup>2+</sup> (green-red-IR), and Cu<sup>2+</sup> (blue) substitutes for Ca<sup>2+</sup> in many calcium minerals<sup>268</sup>. Most luminescence in CaCo<sub>3</sub> is attributed to Mn<sup>2+</sup><sup>268</sup>. Visible PL of CaCo<sub>3</sub> displays a broad peak and as such the detection of individual centres require time resolved luminescence for their discrimination, which is a technique hoped to be applied using HeLIOS in the future.

#### 5.2.3.2.1 HeLIOS high-resolution PL

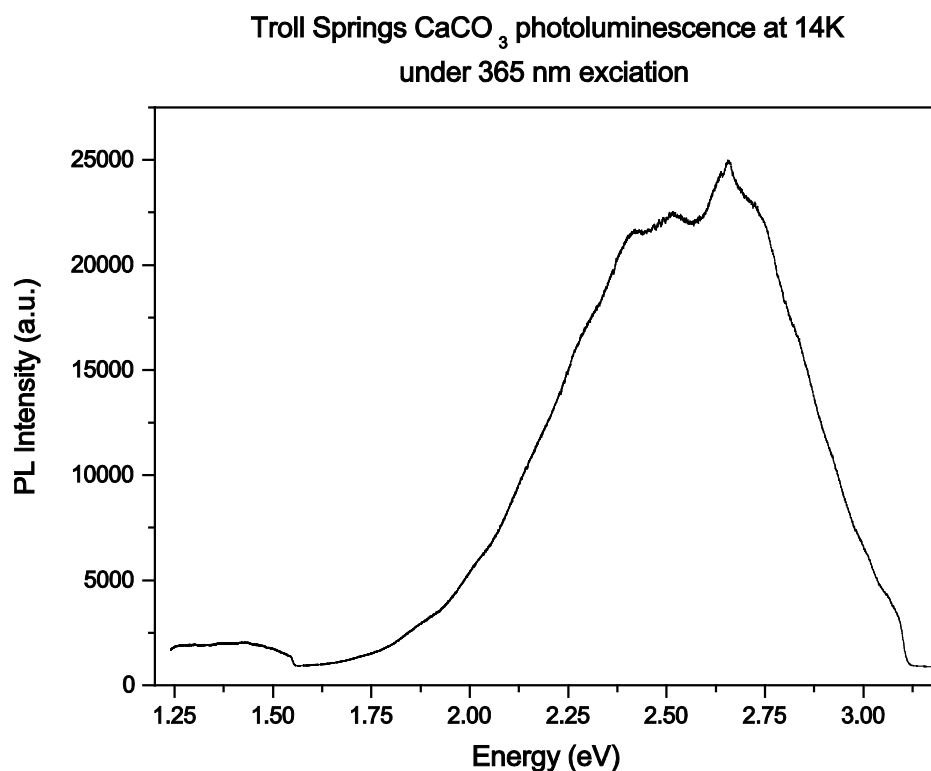


Figure 5-92 High resolution Troll Springs  $\text{CaCO}_3$  PL under 365 nm excitation at 14K.

#### 5.2.3.2.2 HeLIOS spatially resolved PL

Hyperspectral PL data have been acquired of the sample, focusing on the bright veined region; the sample is seen in Figure 5-93. These data have been processed using the calibration protocols discussed in Chapter 4 to provide radiometrically corrected, spatially resolved PL data from regions of interest (ROIs) of different sizes. Figure 5-94 provides an example of three images extracted from the hypercube, showing the contrast when the sample is imaged

## 5.2 Diamond samples

---

at different wavelengths. RGB composite images of three wavelengths have been produced to highlight the differences in composition for two representative datasets.



Figure 5-93 Troll Springs  $\text{CaCO}_3$  sample, mounted on a backplate for stability; left under white light and right under UV excitation photographed with a DSLR camera (no filter).



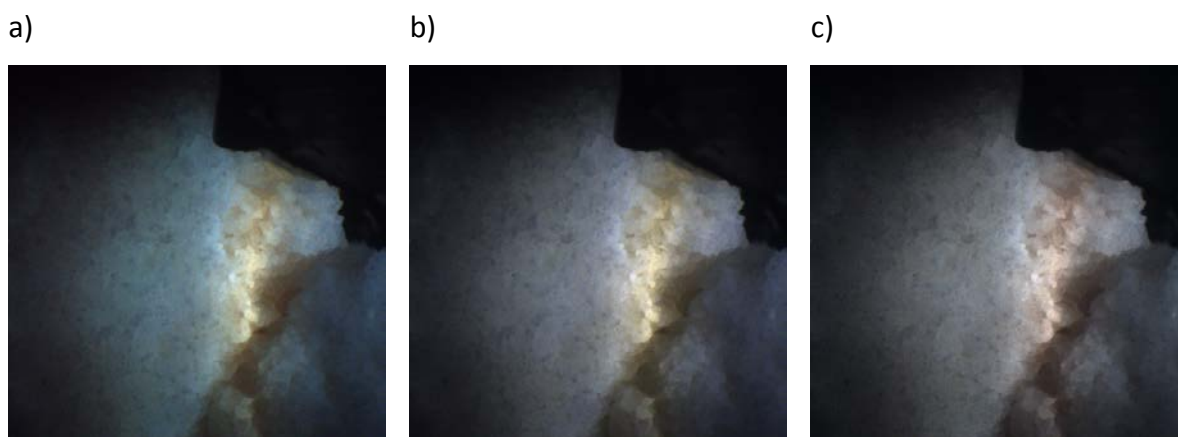


Figure 5-94 Troll Springs  $\text{CaCO}_3$  composite RGB images under 365 nm excitation, at 14K 2x magnification; a) R=700, G=520, and B=450 nm, b) R=560, G=520, and B=450 nm, and c) R=520, G=480, and B=450 nm. Here the bright banding within the sample can be clearer seen.

The RGB composite images in Figure 5-94 clearly show the different composition of the sample, with a complex PL signal from the veined region and a more characteristic blue emission from the bulk. From Figure 5-96 it can be seen that there is a degree of blurring in the image. This is thought to due to a combination of vibration of the cryostat, sample degassing in the vacuum environment and depth of focus shifting with changing wavelength.

## 5.2 Diamond samples

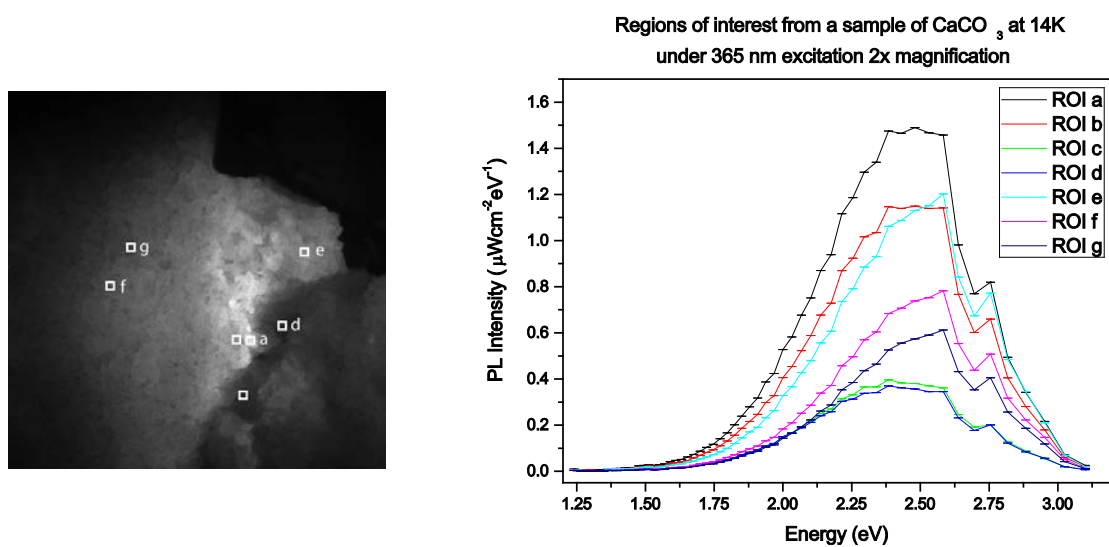


Figure 5-95 Regions of interest of Troll Springs  $\text{CaCO}_3$  under 365 nm excitation, at 14K 2x magnification. ROIs identified on a 500 nm image.



Figure 5-96 Troll Springs  $\text{CaCO}_3$  composite RGB image under 365 nm excitation, at 14K 7.5x magnification; R=700, G=520, and B=450 nm.

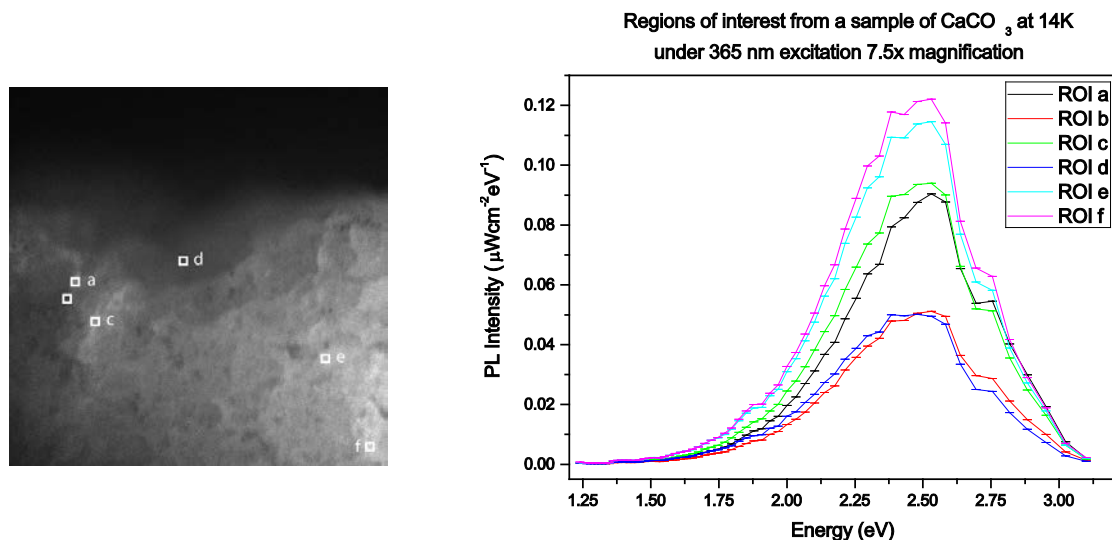


Figure 5-97 Regions of interest of Troll Springs  $\text{CaCO}_3$  under 365 nm excitation, at 14K 7.5x magnification.  
ROIs identified on a 520 nm image.

The spatially resolved data confirm that the sample emits a bright luminescence under UV excitation compared to the diamond samples. Comparing the area average PL and the spatially resolved the spitting of the broad peak is observed. The spatially resolved data, particularly ROI f of Figure 5-97, show the characteristic violet emission of the radiation induced  $(\text{CO}_3)_3^-$  centre, the orange band at approximately 2.066 eV with shoulder at 1.984 eV

### 5.2.3.3 Glowed Bithynia Tentaculata Operculum

An operculum from the species *Bithynia tentaculata* was measured using HeLIOS to investigate the spatial distribution of luminescence. The samples were kindly provided by Prof Geoff Duller. Thermoluminescence results presented by Duller *et al*<sup>269</sup> from *Bithynia* opercula show potential for providing chronological information. It is proposed to complement these studies with spatially resolved luminescence data to reveal the mineral formation in the distinct rings visible in the shells under UV excitation. Luminescence dating applications are largely reliant on non-spatially resolved detectors such as photomultipliers (PMTs), diodes and conventional spectroscopy. The luminescence from the sample originates from calcite within the sample, through further spatially resolved photoluminescence, and in the future thermoluminescence, it is hoped to relate the intensity and composition to form a dose record of material uptake in the samples. Calcite is calcium carbonate,  $\text{CaCO}_3$ , with a rhombohedral cell<sup>270</sup> as discussed in the previous sample.

#### 5.2.3.3.1 HeLIOS high-resolution PL

A comparative area averaged high-resolution PL spectrum was acquired using HeLIOS' 7.5x objective, in order to fill the sampled region with only the signal from the opercula, this can be seen in Figure 5-98. The peak situated at 2.632 eV corresponds to the violet emission band of calcite at sub 77K temperatures<sup>270</sup>. The dominant broad peak situated around 2.087 eV is the characteristic orange emission band<sup>270</sup>.

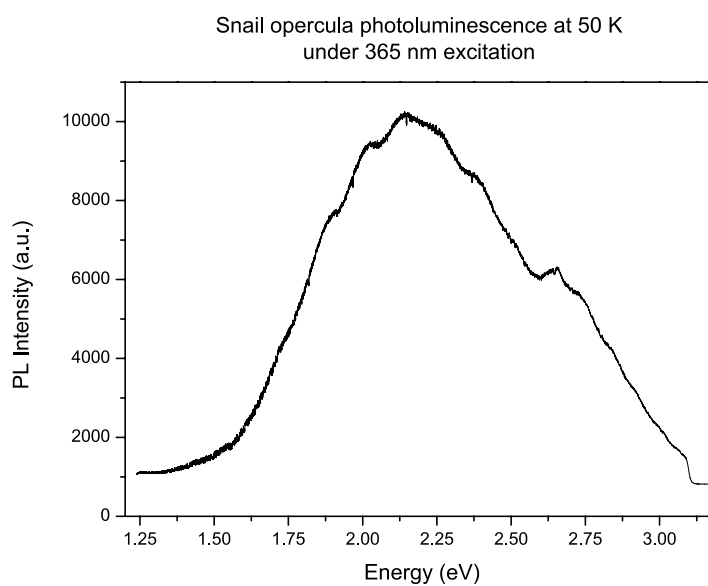


Figure 5-98 Snail operculum high-resolution PL at 50K under 365 nm excitation 7.5x magnification.

#### 5.2.3.3.2 HeLIOS spatially resolved PL

Hyperspectral PL data has been acquired of the whole sample at 2x magnification and a region showing high contrast on the outer rim at 7.5x magnification. These data have been processed using the calibration routines discussed in Chapter 4.

## 5.2 Diamond samples

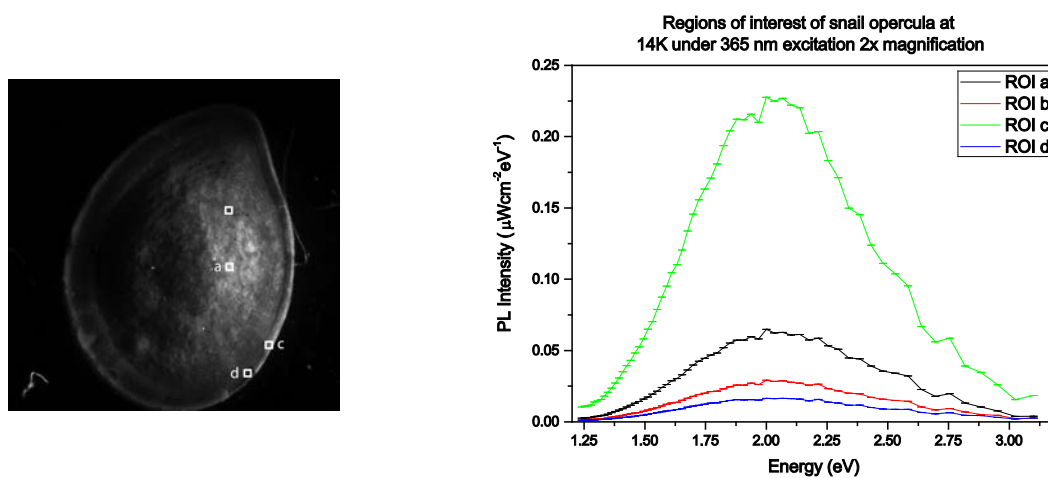


Figure 5-99 Regions of interest of a snail operculum under 365 nm excitation, at 14K 2x magnification. ROIs identified on a 630 nm image (left).

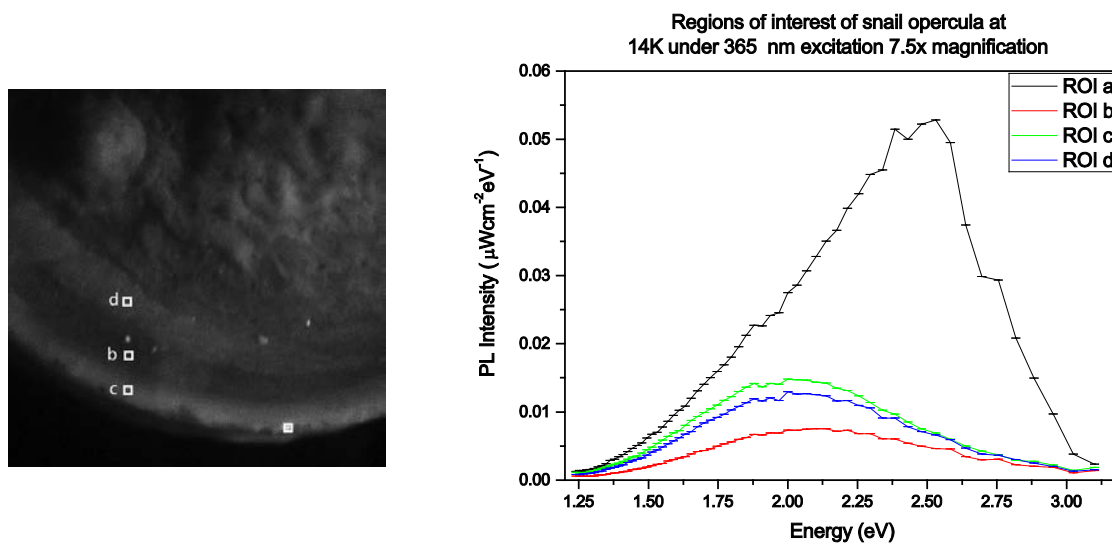


Figure 5-100 Regions of interest of snail opercula under 365 nm excitation, at 14K 7.5x magnification. ROIs identified on a 600 nm image.

### 5.3 Summary

In this chapter results from a range of diamonds samples (natural, CVD and PcCVD) have been presented together with an introduction to each sample. The diamond samples have been examined using birefringence, high-resolution photoluminescence and radiometrically calibrated spatially resolved photoluminescence. These data have been briefly compared to identify spectral differences due to the measurement technique. These results are further discussed in Chapter 6. Raman spectroscopy has been applied in single point and mapping modes to investigate the contribution of  $sp^2$  and  $sp^3$  bonded carbon to the colouration of the samples and the role of different bonding on the stress present within each sample. These Raman data have been converted to strain values and maps generated to identify the pattern of strain in the diamonds. In addition to the diamond samples studied, three additional interesting samples have been included (ZnO,  $CaCO_3$ , and snail operculum). These samples have been investigated using HeLIOS to compare high-resolution area average PL spectroscopy with spatial resolved data. These results are further discussed in Chapter 6.

## Chapter 6 Discussion and Conclusions

### 6.1 Introduction

This chapter collates the results from the samples studied in this work and the instrumentation developed for their study. The use of the ApREES instrument for in-situ monitoring is discussed with an example of the use of Raman as a temperature probe. Here the use of HeLIOS for spatially resolved PL as a spectro-radiometrically calibrated instrument and for area-averaged high resolution PL data is discussed. Through use of complimentary Raman spectroscopy and mapping, the correlation between strain and colouration in brown diamonds is discussed.

### 6.2 ApREES in-situ monitoring

Monitoring a sample during in-situ processing using a non-contact method is very desirable. This is especially true when samples need to remain in position, under vacuum for example. As discussed in Chapter 2, Raman spectroscopy can be used as a non-contact method of temperature determination in vacuum. Two methods are possible for the use of Raman as a temperature probe. The ratios of the Stokes and anti-Stokes peaks can be evaluated as described by Cui *et al* <sup>48</sup>, however this is only valid to temperatures up to 750 K. The alternative method, applied here, is to deduce the temperature change from the peak shift of the first order Raman line as these changes arise from within the lattice. By using this method, as described by Liu *et al* <sup>271</sup>, an evaluation of the suitability of the ApREES for such



measurements can be evaluated. Using the Super-Head optics described in Chapter 2 to deliver 632.81 nm excitation from a HeNe laser Raman spectra were acquired of a natural (111) diamond over a range of temperatures during a heating cycle using the designed filament heater. The ApREES Raman data are shown in Figure 6-1. The data have been magnified to show only the first order Raman line, which can be observed to increase with increasing temperature.

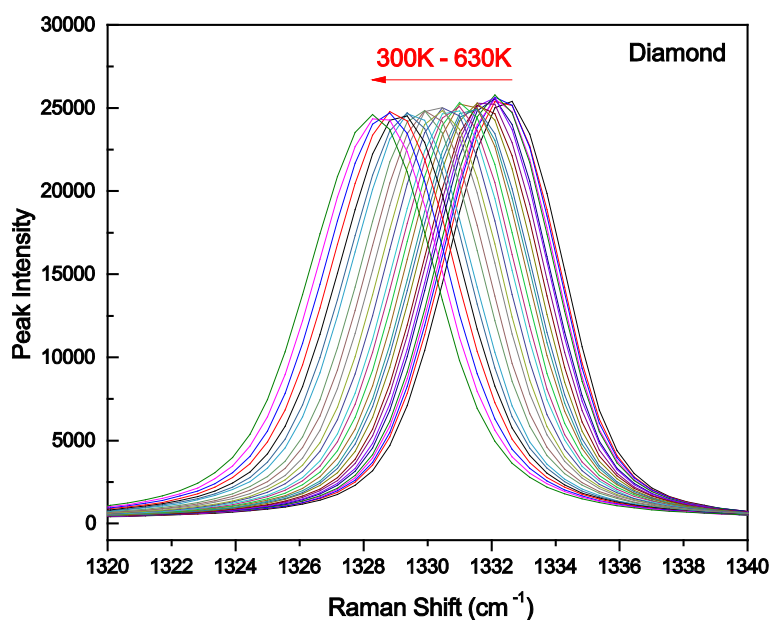


Figure 6-1 ApREES in-situ measurement of the first order Raman line of natural diamond (left). Comparison with theoretical model and measurements taken in the REES (right) showing the closer agreement of the ApREES data with the model.

These data were fitted and compared with literature and comparative data acquired by the REES system of the same sample during a heating cycle via a boron electric heater, Figure 6-2.

## 6.2 ApREES in-situ monitoring

---

From these data, it can be seen that although the temperature range is far wider in the REES data, the ApREES data fits the theoretical model far better.

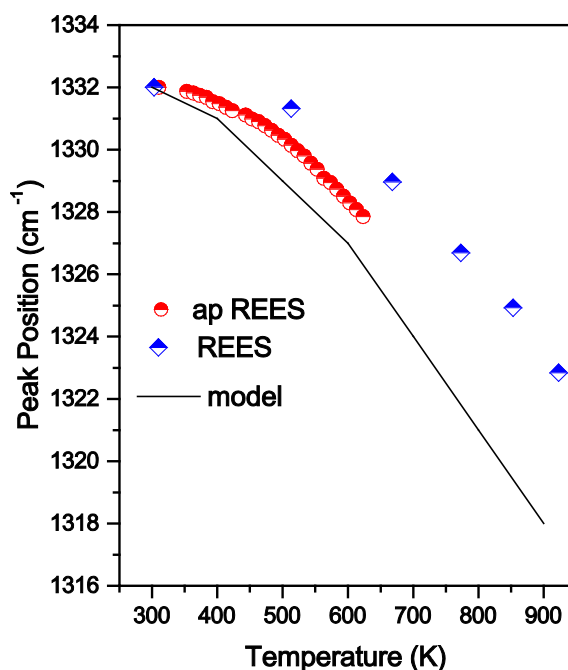


Figure 6-2 Comparison of data acquired using ApREES and REES with a theoretical model. The ApREES data can be seen to provide a closer fit to the model.

It is proposed this is due to a combination of finely controlled heating using the ApREES heater, designed as part of this work, which places the sample not in direct contact, as opposed to the REES' BN heater. The ApREES heater also benefits from a thermocouple spot welded very close to the sample, resulting in temperature measurements more representative of the mounted sample. These data provide confidence in the use of the ApREES system for in-situ Raman studies. It is proposed to use these data acquired from the ApREES to calibrate the REES temperature readings.

## 6.3 HeLIOS

HeLIOS, presented in Chapter 4, provides a significant enhancement in operation and data products compared to the previous instrumentation of CLASSIX and MoLES used in the group <sup>118,272–274</sup>. Both systems employ the same EMCCD camera for imaging, however in this work the detector has been characterised, and once integrated as part of the HeLIOS radiometrically calibrated. HeLIOS employs the same microscope objectives as CLASSIX, however in this work all data acquired have been flat field corrected to remove artefacts from the detector and the optical path. Improvements in light collection have also been made with fine focus provided by stepper motor control. CLASSIX employed a custom-built filter monochromator (filter wheel) to disperse the emission in the 200-1000nm range, at a spectral range up to a minimum 10nm bandpass. This filter wheel comprised of individual filters ranging from 10 -70 nm bandpass. HeLIOS employs a LCFT to disperse the emission in the 400-1000nm range and a series of manual filters to disperse in the 200-400nm range.

With respect to sample handling, HeLIOS has superior thermal transfer and so reaches, and maintains, lower temperatures when the closed loop cryostat is in operation. Temperatures as low as 14K have been recorded at the sample compared to the 40K minimum of CLASSIX. Both the pumping system on HeLIOS and the cryostat have also been improved to reduce vibrations during imaging.

HeLIOS, like CLASSIX, is an all photon system, which can be used in many experimental environments unlike electron based techniques, such as XPS, which have more specific requirements on UHV and sample cleanliness. With a LCFT each pixel accumulates a spectrum over time as each wavelength is captured sequentially, one at a time. The acquisition times can be seconds to minutes for an image cube to be generated, depending on the signal strength, with longer integration times required for low light applications. In this work the

integration time has been set an upper limit of 10 seconds per image for radiometrically calibrated data.

### 6.4 Birefringence in diamond

As diamond is a cubic crystal it should exhibit isotropic optical properties<sup>275,276</sup>. Birefringence in diamond is an anomalous optical property that is a result of strain in the diamond lattice modifying its natural isotropic properties. There have been a number of studies of birefringence in diamond, including those reviewed by Howell<sup>276</sup>, who describes the two types of birefringence found in diamonds; normal birefringence, where there is constant optical anisotropy throughout the sample, where rotating the sample shows no change in the birefringence; and stress induced birefringence, which is an anisotropy only due to the stress field present and is not constant throughout the sample.

In the diamonds examined here a number of defined birefringence features have been observed which are readily related to features in literature. Three examples are shown in Figure 6-3.

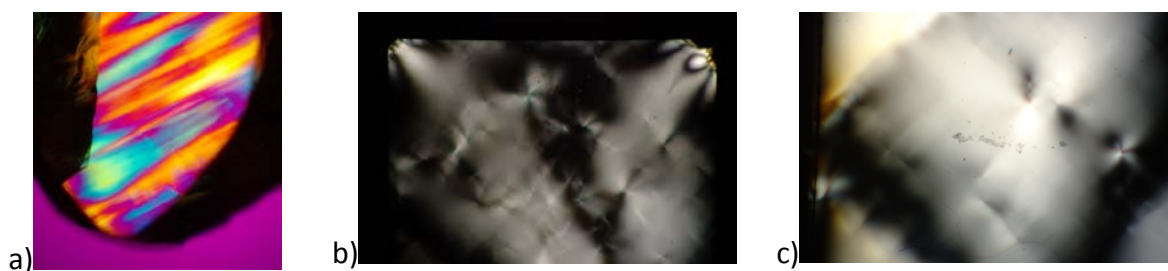


Figure 6-3 Cross-polarisation birefringence images of samples studied in this work.

The natural banded diamond a) in Figure 6-3 shows a classical Tatami pattern as observed in natural brown diamond by Collins *et al* and illustrated in Figure 6-3.

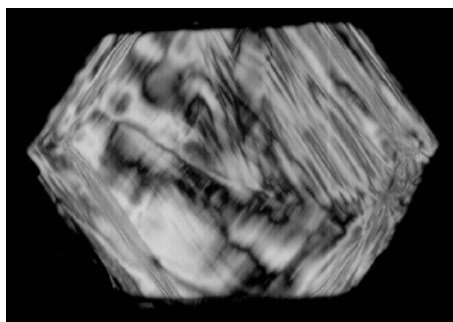


Figure 6-4 Tatami pattern observed in natural brown diamond, reproduced from Collins <sup>245</sup>.

The brown single crystal CVD diamond, b) in Figure 6-3, shows a number of features. In the body of the diamond petalled patterns radiate out from points throughout of different size and intensity. A small number of these features are observed in the blue boron doped single crystal diamond, c), however these are only readily observed at higher magnification. Such features were not observed at any location in the natural diamond. These features have been observed by others<sup>277,278</sup>, shown in Figure 6-4 below. Pure edge dislocations are petal shaped and can extend over a few hundred microns. Birefringence in single crystal CVD diamond is affected by the substrate the diamond is grown on, higher surface and subsurface damage leads to increased birefringence. Substrates with low densities of extended defects (dislocations and stacking faults) yield samples with lower birefringence. Post-growth strain can also be generated during cutting and polishing of the diamond. This is evident when imaging areas that have been chipped or cracked. Friel *et al* showed <sup>279</sup> anisotropy in the birefringence is characteristic of CVD diamond due to the preferred direction of propagation of the dislocations along the growth direction. Pure edge dislocations have been seen to

## 6.4 Birefringence in diamond

---

nucleate in isolated clusters at the substrate interface in CVD diamonds, which give rise to characteristic petal-shaped birefringence patterns.

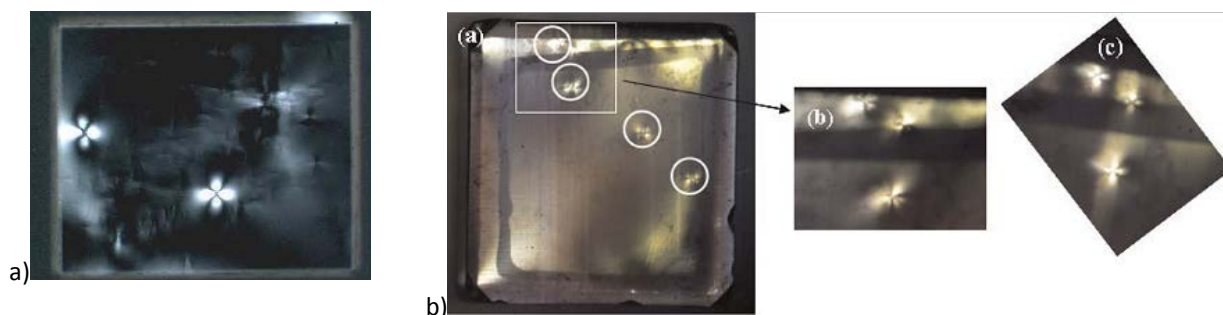


Figure 6-5 Birefringence patterns from literature showing petalled patterns; a) Birefringence seen in crossed-polarizers of two 4-petalled defects in CVD diamond observed by Pinto<sup>277</sup>. The plane of view is (001). The horizontal and vertical axes lie along  $\langle 100 \rangle$  and the polarizers lie along  $\langle 110 \rangle$ , and b) Birefringence images observed by Crisci<sup>278</sup>.

Dislocations act as non-radiative recombination centres also affect the photoluminescence and absorption spectra. Pinto and Jones<sup>277</sup> add that at the centre of a birefringence pattern the radial birefringence is due to growth dislocations. Where four petal patterns are observed (Figure 6-5) it is thought to be due to groups of edge dislocations emanating from a defect on or near the substrate surface. The patterns in the brown CVD sample agree with those observed by Pinto in the (100) face.

In a single crystal CVD diamond, bulk strain arises from lattice mismatches between the substrate and the epilayer. Orlov postulated in his 1977<sup>152</sup> paper that at the centre of a birefringence pattern the radial birefringence is due to growth dislocations. This agrees with the data collected in this work as the brown CVD diamond, b), shows a high density of nucleation points. In polycrystalline CVD diamond there are high strain regions between individual grain boundaries due to competitive growth which are clearly visible in the PcCVD

sample studied here. One of the causes of the highest levels of stress are extended defects such as planar defects (crystal twinning) and line defects (dislocations). These are most relevant in as grown CVD single crystal diamonds such as the ones studied here.

Many studies, summarised by Howell <sup>276</sup>, confirmed the refractive index of diamond decreases with hydrostatic stress. Raman is the most common method for investigating strain in diamonds however several authors have used the intensity of birefringence to quantify strain <sup>280,281</sup>.

Howell <sup>276</sup> examines diamonds which have undergone tip cracking, these pincushion/ petal type birefringence patterns are very similar to those revealed in the brown CVD diamond examined as part of this work.

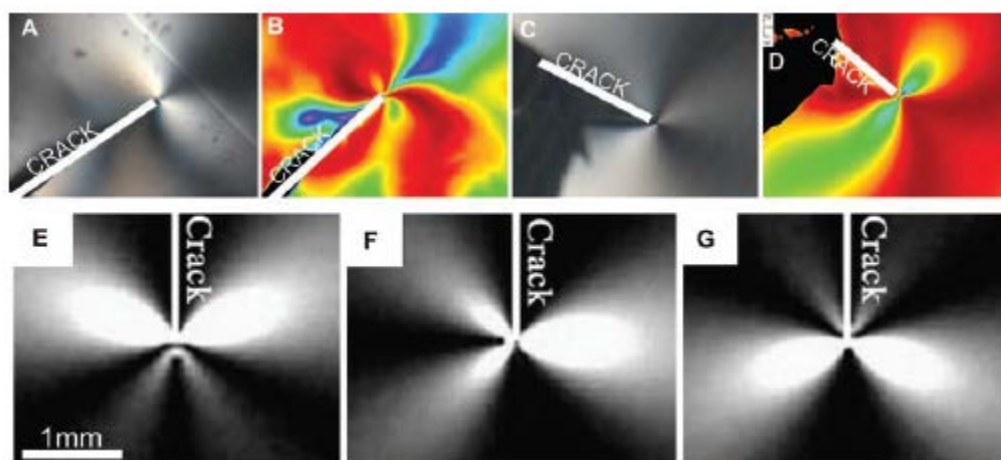


Figure 6-6 Images of fractures in diamond (a)–(d), (a) and (c) are taken between crossed polarizers, (b) and (d) are MetriPol  $|\sin \delta|$  images. These illustrate a classic ‘bow-tie’ pattern. Reproduced from Howell <sup>282</sup>.

### 6.5 Photoluminescence features in diamond

Photoluminescence spectroscopy has been the primary technique used in this work. As discussed in Chapter 2, a luminescence spectrum is obtained when the optical emission of a sample is monochromatically scanned. This has been achieved using the developed HeLIOS hyperspectral imaging system; with a CCD spectrometer and CCD hyperspectral imager with LCTF dispersion to collect high-resolution area averaged and hyperspectral data respectively.

As discussed throughout, the properties of wide band gap materials, such as diamond, are influenced greatly by the material's purity; defect concentrations of parts per billion and less can greatly change their properties and behaviour. Photoluminescence has been shown to be sensitive to such low concentrations <sup>283</sup> and so lends itself to the example given in this work; the investigation of the brown colouration in diamond. Measurements have been observed to deliver sensitivities to a single vacancy in specialised experiments <sup>284</sup>.

Defects in a diamond's crystal lattice can introduce new absorption features, which can be used as a fingerprint for that defect (both extrinsic and intrinsic) and transitions between defect-induced in-gap and bands (conduction or valence) appear as broad, mostly featureless continuums. In addition to the general classification scheme for diamonds reported in Chapter 5, classification is also possible with optical spectroscopy. Table 6-1 below, reproduced from Dischler <sup>60</sup>, shows how diamonds can be classified by their dominant optical features.



| Defect or property  | Type        |             |             |                             |                             |
|---|-------------|-------------|-------------|-----------------------------|-----------------------------|
|   | IaA         | IaB         | Ib          | IIa                         | IIb                         |
| <b>A-centre = <math>N_2^0</math></b>                          | Dominant    | Weak        | Weak        | Absent                      | Absent or weak              |
| <b>B-centre = <math>V_1N_4^0</math></b>                       | Weak        | Dominant    | Weak        | Absent                      | Absent or weak              |
| <b>C-centre = <math>N_1^0</math></b>                          | Weak        | Weak        | Dominant    | Absent                      | Absent or weak              |
| <b>Defining defect</b>  | A-centre    | B-centre    | C-centre    | Absent                      | Boron-acceptor              |
| <b>Boron content</b>  | Low         | Low         | Low         | Very low                    | Dominant                    |
| <b>Typical hydrogen content</b>                               | 500 ppm     | 200 ppm     | 70 ppm      | $< 10^{18} \text{ cm}^{-3}$ | $< 10^{16} \text{ cm}^{-3}$ |
| <b>Electrical resistance (<math>\Omega \text{ cm}</math>)</b> | $> 10^{15}$ | $> 10^{15}$ | $> 10^{15}$ | $> 10^{16}$                 | Semiconducting              |

Table 6-1 Alternative classification scheme for diamond type<sup>60</sup>

A and B band photoluminescence have been observed in the diamond samples studied here. These features are associated with dislocations within the lattice. The spectral position of the A-band in natural diamond may range between 2.0 eV and 3.0 eV<sup>46</sup>. It is a characteristic feature, visible in natural and synthetic diamonds<sup>46</sup>. In synthetics, it is shown to be particularly strong near macroscopic inclusions which distort the lattice<sup>285,286</sup>. Where the A-band is shifted down to 2.8 eV this has been explained in literature as being due to strain around dislocations. It is especially strong in low-nitrogen diamonds, low-nitrogen (sub 20 ppm) natural diamonds mostly contain a high amount of dislocations, suspected to be due to plastic deformation and subsequent annealing during growth<sup>287</sup>. Nitrogen acts as a quencher for the A-band luminescence.

The B-band can be observed in luminescence emission centred on 1.8 eV (690 nm) as a broad band in natural brown diamonds and type II diamonds.

The high number of optical centres observed in diamond is due to its extended optical transparency (from bandgap absorption edge in the UV to the microwave region) and extreme hardness. It is this hardness that causes defect migration of vacancies to the surface to require high activation energies. High temperature annealing is seen to cause mobility of defects and is the subject of intense research, particularly in the treatment of less desirable brown diamonds to become valuable colourless samples.

### 6.5.1 High-resolution and spatially resolved PL of diamond

In this section the photoluminescence of the diamond samples studies are reviewed, including a comparison of the high-resolution area averaged and spatially resolved data.

In this work spatially resolved PL has been used to show the spectral differences between brown banded and clear regions of a polished (110) natural type Ia diamond. Analysis and peak fitting of the complex PL spectrum of a natural type Ia diamond have been presented in the previous chapter. These data have shown the diamond to contain a high degree of incorporated nitrogen, observed most conclusively as the N3a centre and the H3a centre which correspond to centres comprised of an additional three and two nitrogen atoms respectively. As the sample was studied at very low temperature (14K) the resolution of many associated lines of the N3a centres were distinguishable. In addition to these nitrogen inclusions, which classify the sample as an Ia, further sub-classification is proposed to IaA due to the aggregated nitrogen centres observed. Natural diamonds displaying photoluminescence have been observed to be mechanically weaker than those showing no luminescence<sup>46,60</sup> as the defects present affecting the PL are disturbing the tetrahedrally bonded lattice from which diamond draws its strength. This would agree with the theory of defects located at points of weakness in the lattice causing the complex brown coloration.

Comparing regions of interest selected in the data processing protocol, described in Chapter 4, radiometrically calibrated spectra have been extracted for inspection and presented in Chapter 5. An example of the contrasting spectra resolved for two regions of interest, on and off the brown banded region is given in Figure 6-7 below.

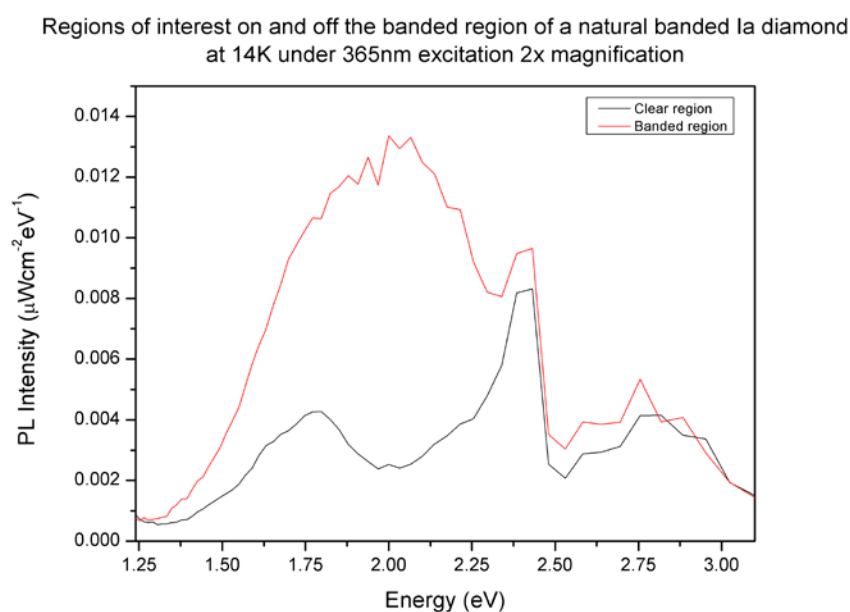


Figure 6-7 Spatially resolved PL spectra acquired from regions of interest on the clear and brown banded surface of a natural Ia banded diamond.

As these data have been radiometrically calibrated the PL response of regions of interest can be compared independent of selection size. In Figure 6-7 the spectra from the clear diamond region is observed to be consistent with that of the area average PL data used for type classification. Spectral data collected from the brown banded regions however display a strikingly different profile, with the introduction of a new band in the low-energy (long wavelength) region of the spectrum. The remainder of the spectrum towards the higher

energies shows a spectral shape consistent with the clear region and the area-averaged high resolution data implying the type IaA classification is valid across the entire sample, with additional components in this matrix affecting the brown coloured banding. The new broad band observed in the spatially resolved data has been fitted with a number of components in Chapter 5. Correlating these features to literature, a broad band in the 2 eV regions has a number of assignments associated with brown colouration. Orlov<sup>152</sup> and Gomon<sup>46</sup> associated this band to dislocations observed in smoky brown diamond. Later Ruoff<sup>46</sup> associated the band to pressure where it was observed that the band increased dramatically in type Ia diamonds which had been subject to pressure and assigned it as a stress induced luminescence centre. It can be seen from the data presented in Chapter 5 that the intensity of this band changes considerably over the areas samples. This is postulated to be linked to the tensile stress calculated from Raman mapping of the region as there is increased stress in the vicinity of the brown banding. The green band, a boron related feature, centred around 2.3 eV<sup>247</sup> is associated with grain boundary defects which are associated brown colouration in diamond.

In addition to the brown colouration in the natural diamond the distribution of colouration in a single crystal CVD diamond has also been investigated using high-resolution area averaged and spatially resolved PL spectroscopy, data presented in Chapter 5. The brown CVD diamond showed the strongest birefringence of the two single crystal diamonds, with particularly high intensity in the region of darker colouration and cracking. In the high resolution PL data the spectrum is dominated by an intense peak arising from the neutral nitrogen vacancy ( $NV^0$ ) at 2.156 eV (575 nm) caused by five non-bonded electrons. As discussed in Chapter 5, this feature can be caused by plastic deformation. The  $NV^0$  centre is preferentially located at grain boundaries in CVD, however this cannot be resolved in these bulk PL data. Where present, increasing concentrations of dislocations are seen to quench its PL. No such quenching has been observed in this sample therefore it can be assumed that there is a low concentration of

dislocations present in the sample. As with the natural diamond, spatially resolved PL data have been acquired using HeLIOS. The spectral resolution in these data appear lower than expected, even considering the very low PL emission of the sample, highlighting the need in further work to extend the radiometric calibration to a finer resolution.

From the plotted normalised data shown in Figure 6-8, the spectra can be compared. Here it can be seen that in the darker region of the sample, there is a broader feature present in the higher energy range (green line), which is different to that observed in the natural diamond's brown region which showed changes in the lower energy region. Only in this location is there a clear feature in the expected position of the  $NV^0$  centre. This could suggest that the area averaged PL is being dominated by the damaged region as considering the sampling position; these data were acquired on a particularly bright region near a crack (ROI 4 pictures in Figure 5-44). When these data are analysed, the peaks are associated with nickel impurity defects and the H3 centre which comprises of a vacancy and two nitrogen. Where the sample has been imaged at the highest magnification, although the PL is very weak for hyperspectral imaging, there is a distinct feature present on the darker edge of the diamond (black line). This is located at 2.38 eV; literature defines this feature as a nickel centre, also referred to as S2. This centre arises from a cluster structure of a nickel atom, two nitrogen atoms and 2 carbon atoms ( $1Ni+2N+2C$ ) making it a physically large centre. This identification is in agreement with the weaker nickel signatures identified in the data. Nickel can be readily incorporated in the diamond from the growth chamber during synthesis. The hyperspectral data averaged over the whole image (red line) is in agreement in the lower energy region, however the shape is notably different as the energy increases. A proposed reason for the differences in the data is the incorporation of nickel into the structure preferentially in this location. This should be further investigated with higher resolution hyperspectral data, however without knowledge of the growth and process of the sample a conclusive agreement may not be reached.

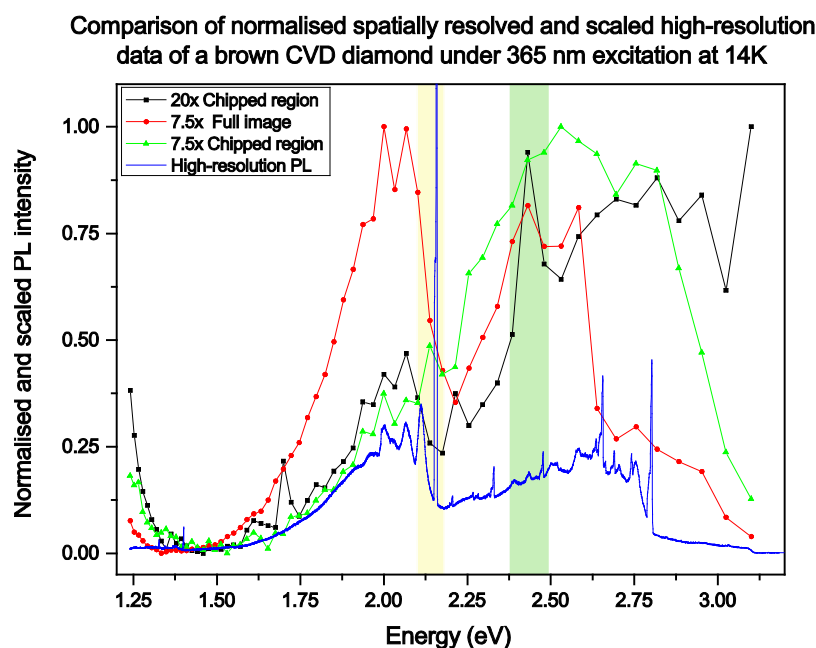


Figure 6-8 Normalised brown CVD diamond PL data.

An additional blue boron doped single crystal CVD diamond was investigated alongside the brown CVD diamond for direct comparison. As expected of a high quality boron doped pure sample the high resolution PL and the spatially resolved PL showed consistent spectra containing predominantly boron and nitrogen related features. These data can be examined in Chapter 5. From this it can be seen that the features observed in the brown diamond are specific to its composition rather than generic amongst CVD diamond.

The final diamond examined was selected primarily for Raman spectroscopy investigations due to its polycrystalline composition. Under microscope examination the sample showed an uneven fine brown graining and so has been examined using HeLIOS spatially resolved PL. This fine graining in a transparent matrix provided an interesting challenge for imaging. The data presented in Chapter 5 shows that at low magnification (2x) there is little difference between

the data extracted from dark and light ROIs due to the small grain size apart from a subtle shift in the main, broad peak from 2.25 eV to 2.29 eV. This peak, its shoulder at 2.58 eV, and an additional peak at 2.75 eV are attributed to the Green-band, a nickel defect associated with inclusions near seeding and interfaces, and another nickel related defect associated with the growth conditions respectively. Inspecting the same region under higher magnification (7.5x) produced images with improved resolution of the fine detail which enabled more accurate ROI selection for processing, an example can be inspected in Figure 5-72. In these data the shifting of the broad peak observed under low magnification is more noticeable. In addition to this broad feature two of the illustrated ROIs display an intense peak located at 2.43 eV. This peak can be confirmed as genuine and not an artefact of the measurement for two reasons. The two ROIs are from independent locations and had the feature been an artefact in one image, such as a cosmic ray causing the higher intensity, the feature would be present in all ROI data using that image which is not the case. Through referencing this peak is attributed to the S1 centre.

## **6.6 Raman spectroscopy of diamond**

Raman spectroscopy and mapping have been used to investigate the intrinsic stress present and the ratios of  $sp^2$  to  $sp^3$  carbon in diamond samples containing brown colouration. Spectra and maps obtained from both synthetic and natural diamonds have been presented in Chapter 5. The Raman maps have been produced using the peak position, FWHM and peak intensity of the first order Raman line. The stress properties are clearly illustrated at its extremities with a Raman map showing a polycrystalline CVD diamond. Areas of  $sp^2$  and  $sp^3$  can be clearly shown and the shift of the first order peak at the edges of each crystal boundary show the residual internal stress present.

## 6.6 Raman spectroscopy of diamond

Much of the work done to date on the monitoring of stress using Raman has considered thin, freestanding films. It has been shown that taking the assumption of uniform stress throughout a sample is only valid for thin films <sup>197</sup>. A film on a substrate is considered to be in a biaxial stress state, however the samples considered here are thick, bulk samples for which the constant has been taken to be uniaxial. The stress in the mapped regions has been evaluated using the relationship between the deviation from undisturbed diamond ( $1332.5\text{ cm}^{-1}$ ) and the uniaxial stress coefficient for diamond. From these data it has been shown that the natural diamond is under tensile stress and the CVD samples exhibit compressive stress. The range of stresses calculated are summarised in Table 6-2.

| Diamond Type                   | Stress (MPa) |         | Type        |
|--------------------------------|--------------|---------|-------------|
|                                | Minimum      | Maximum |             |
| Natural Ia (110)               | 5.87         | 104.2   | Tensile     |
| Single crystal brown CVD (100) | 29.9         | 260.7   | Compressive |
| Polycrystalline CVD            | 593.1        | 2023    | Compressive |

Table 6-2 Summary of calculated stress present in three diamond samples containing brown colouration.

One source of stress arises from the incorporation of non-diamond phases at grain boundaries. Differences in the domain size can be assessed by examination of the FWHM of the first order Raman line. Graphite ( $\alpha$ -C) is commonly found in diamond as lamellae and disordered graphite, shown by peak at  $1350\text{ cm}^{-1}$ , the D-band. Additionally a peak at  $1580\text{ cm}^{-1}$  G-band, indicates the presence of non-diamond carbon, stretching vibration of any pair of  $\text{sp}^2$  sites, such as  $\text{C}=\text{C}$  chains or in aromatic rings. Presence of graphitic-like carbon is preferentially detected compared to diamond-like as the scatter due to graphite is 75 stronger



than that due to diamond for a Ar laser and can be greater than 233 for a 514.5nm excitation<sup>46</sup>.

An estimation of the quality of a CVD diamond film can also be found by examining the ratio between the intensities of the G-band and the diamond band, or the G-band plus the D-band and the diamond Raman line. An estimation of the structural quality can be made by examining the FWHM of the main diamond Raman peak; the narrower the peak, the higher the quality. The intensity of the PL background is also used as an estimation of quality; the lower the better. A flat background with no obvious peak in the 1500-1550  $\text{cm}^{-1}$  range is indicative of a pure diamond sample with virtually no  $\text{sp}^2$  carbon components. When the incident wavelength is in the red/IR range this is an even stronger indication, as there is a pronounced enhancement in the Raman sensitivity to  $\text{sp}^2$ -bonded carbon at longer wavelengths. Features in the 1450 to 1480  $\text{cm}^{-1}$  range with FWHMs from 20 to 150  $\text{cm}^{-1}$  have been observed for samples that have received indentations with diamond tips<sup>46</sup>.

The Raman spectrum for single crystal diamond is dominated by the characteristic first-order Raman line at 1332  $\text{cm}^{-1}$  with a full width half maximum of 1.2  $\text{cm}^{-1}$ . This corresponds to the vibrations of the two interpenetrating cubic sub-lattices<sup>194</sup>. First-order Raman modes are triply degenerate TO(X) phonons. The FWHM of the Raman line is often given as a measure of the perfection of the diamond and the peak position is taken as an estimate of the residual stress. Micro-Raman mapping has been used to monitor the width, position and intensity of the 1<sup>st</sup> order Raman peak.

Growth is known to incorporate non-diamond phases and crystallographic defects and thermal effects in CVD's post growth cooling rates and control can introduce strain due to thermal mismatch between diamond and growth substrate. Intrinsic growth stress as a result of chemical and microstructural defects incorporated during CVD growth is seen to correlate to substrate temperatures and methane content in the gas phase.

A number of potential causes of strain were postulated by Long and reviewed more recently by Howell <sup>276</sup>. These are:

- Dislocations – extended or linear defects common in diamond, generated by growth and movements. These are intrinsic to plastic deformation.
- Inclusions – these cause strain-nodules that create in-grown dislocations. Lattice errors are caused by the inclusion of foreign bodies and act as nucleation points.
- Residual stress after growth can be due to differences in thermal expansion of the diamond and substrate, lattice mismatches, bonding at grain boundaries and bonding changes during growth <sup>45,288</sup>
- Intrinsic stress is due to bonding and grain boundaries, and bonding changes during the growth process. Intrinsic stress manifests itself around features such as twins, dislocations, amorphous carbon and voids <sup>289</sup>.

In the banded natural diamond the variation of  $sp^2$  and  $sp^3$  in the maps align with banded regions. In the brown CVD, which was previously thought to be homogenous in previous studies work by Jones <sup>239</sup> showed that Raman spectroscopy can be used to show  $sp^2$  distribution. After sampling several areas it was observed that the sample was not uniform, with a feature prominent towards the edge of the sample, decreasing to being completely absent in the centre of the sample. When viewed using a cross polarisation optical microscope there is strong evidence of plastic deformation at the edges, potentially caused during cut and polishing. This can be seen as inhomogeneous colour distribution in under white light illumination and by the strain pattern visible under cross polarisation.

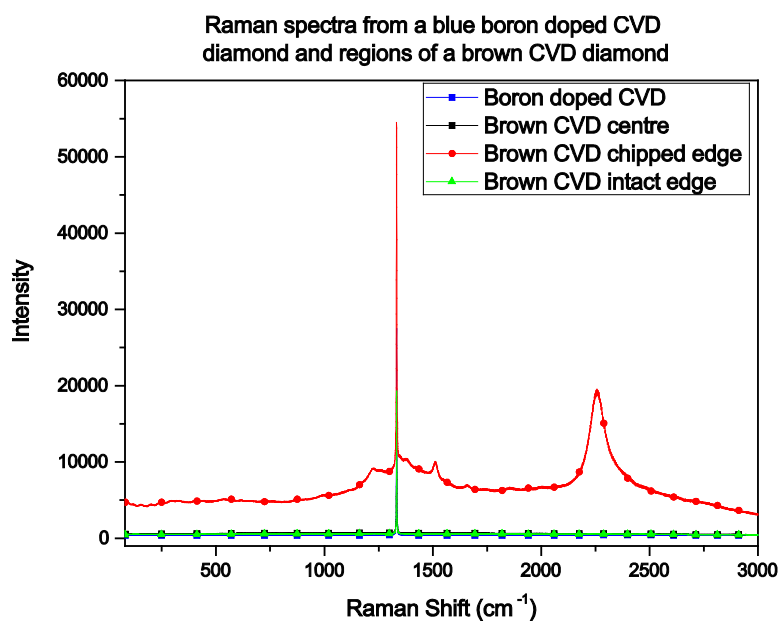


Figure 6-9 Comparison between two coloured CVD diamond.

Figure 6-9 illustrates a comparison between Raman spectra acquired under identical conditions of the two single crystal CVD samples studied in this work. From these data there is a very little difference between the blue boron doped sample and the majority of the brown sample. The spectra depart from each other when the darker brown damaged corner is examined. In this region there is a very high background with multiple first and second order structure.

## 6.6 Raman spectroscopy of diamond

---

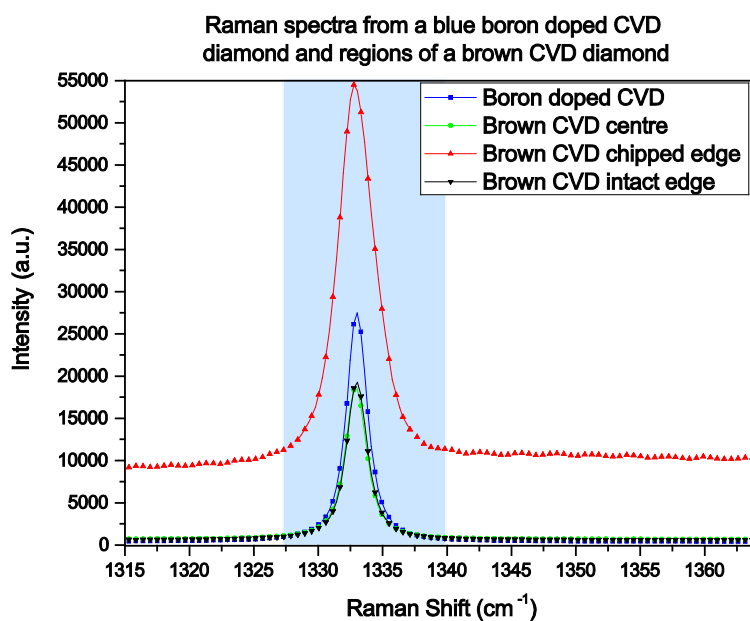


Figure 6-10 Comparison of two coloured CVD diamonds, magnified to show first order spectral detail; blue band highlights the differences in the first order Raman line.

Figure 6-10 provides a magnified view of the first order Raman line region. Here it can be observed that the first order peak of the brown diamond in two regions, the centre and on an undamaged edge, show the same position. This indicated the uniform nature of the bulk of the sample. Considering the darker region of the brown CVD sample, this has a higher background and much broader FWHM. The profile from the blue boron sample shows a more intense peak, with a similar FWHM to the undamaged region of the brown CVD sample.

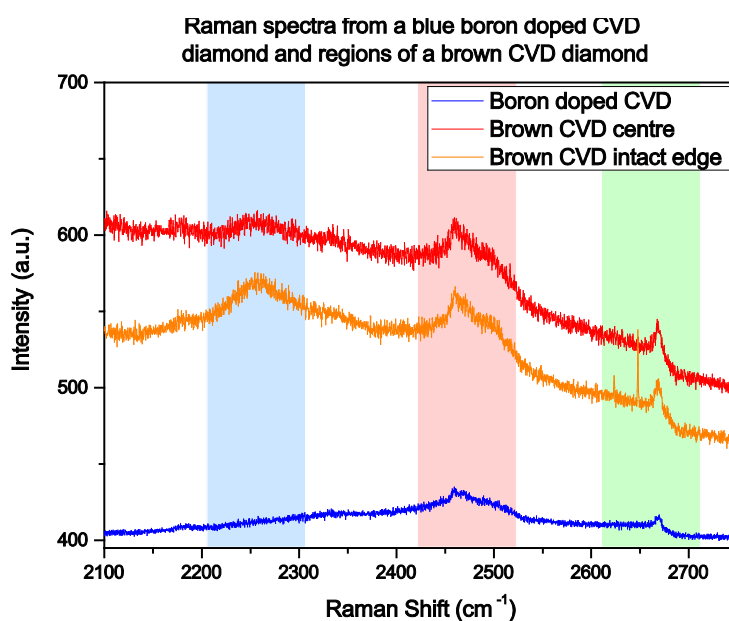


Figure 6-11 Comparison of two coloured CVD diamonds, magnified to show second order spectral detail; 2257 cm<sup>-1</sup>(blue band), 2460 cm<sup>-1</sup> (red band), and 2670 cm<sup>-1</sup> (green band).

Figure 6-11 provides a magnified view of the second order region of the two CVD single crystal samples. The brown CVD sample shows an additional peak centred at 2257 cm<sup>-1</sup>, illustrated in the blue band of the figure. Both samples display the characteristic band of high quality diamond centred around 2460 cm<sup>-1</sup>, identified in the figure by the red band. The region located at 2670 cm<sup>-1</sup>, highlighted with a green band in the figure is present in both CVD samples, more pronounced in the brown sample. This is associated with a strong characteristic band of pure graphite. Further examination of the feature at 2257 cm<sup>-1</sup> is given in Figure 5-60. This provides a magnified view of the feature present in the brown CVD diamond, which is absent in the blue boron doped sample. In order to compare the data from the three sampled regions on the same axis, the data have been normalised to the first order

## 6.6 Raman spectroscopy of diamond

---

Raman line. From these data the high intensity of the  $2257\text{ cm}^{-1}$  peak in the chipped region can be observed, highlighted in the red band. As presented in the previous chapter and Figure 6-9 above, the chipped region has a number of peaks located in the  $1510\text{ cm}^{-1}$  band compared to the undamaged regions.

There is very little literature published on the source of the peak located at  $2257\text{ cm}^{-1}$ . Breza *et al*<sup>290</sup> identified the feature in their study of diamond films on steel substrates. In their work, this strong band was observed in CVD films deposited on sapphire and tungsten carbide. They link the feature to diamond crystal twinning, which is strongly associated with cracking and fracture in CVD diamond. Pressure has been seen as responsible for deformation twinning, which creates faulted tetrahedral<sup>291</sup>. Twins are defined as two joined crystals sharing a common (111) direction about which one is rotated by  $180^\circ$  with respect to the other, as illustrated in Figure 6-12.

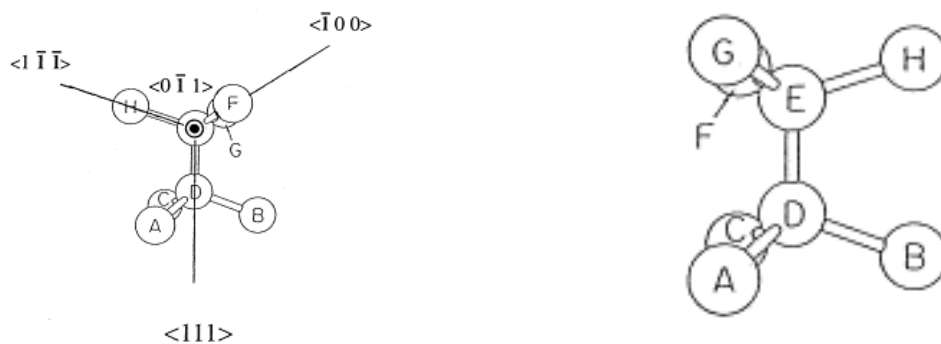


Figure 6-12 Atomic model for twinning in a diamond lattice; a) normal diamond, and b) twin produced by  $180^\circ$  rotation along the (111) direction. Reproduced from Yan *et al*<sup>292</sup>.

This is a promising cause of the  $2257\text{ cm}^{-1}$  Raman peak. Bright- and dark-field Transmission Electron Microscopy (TEM) would be beneficial in the future to confirming the presence of

twinning to help understand the cause of this peak and its link to brown colouration. It is encouraging that the intensity of this peak is considerably higher in the cracked region. This could be due to the edge of the sample being of (111) orientation, in which has been shown that open-ended tetrahedral faults are created <sup>291</sup>.

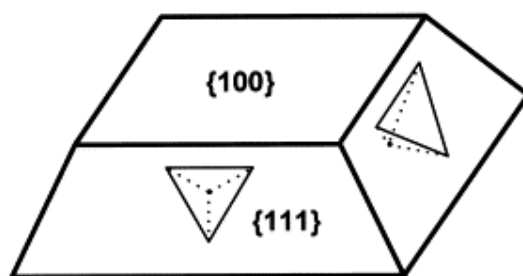


Figure 6-13 Schematic diagram showing CVD growth respective to the crystal faces, reproduced from Steeds *et al* <sup>189</sup>.

The incorporation of nitrogen-vacancy (N-V) and nitrogen di-vacancy (N-V<sub>2</sub>) defects in twins present in homoepitaxially grown CVD diamond have been previously identified, these can act as preferential sites for the incorporation of additional defects such as amorphous carbon <sup>293</sup>. Such twin formation leads to the incorporation of non-diamond carbon phases, reducing the quality <sup>292</sup>.

### 6.7 Colouration in diamonds

Colourless natural diamonds are considerably rare, the majority discovered to date are of mixed colourations due to imperfections in the crystal lattice, with by far the most common colouration being brown. Natural diamonds have been found to exist in a range of colours, where the colour has been linked to a particular composition or defect. For example the second most common colouration observed, yellow, is due to substitutional nitrogen <sup>294</sup>. A pink colouration observed in a small number of diamonds has been attributed to the presence of trace amounts of manganese <sup>152</sup>. The rarest in nature, blue diamonds, are as previously discussed in Chapter 5 coloured by the presence of boron.

Considering again that the majority of mined diamonds possess a degree of brown colouration, and as such are not of gem-trade interest due to their brown colouration, there is still a great deal of speculation regarding the origin of this colouration. Even though there has been much effort and resources spent on the determination of the origin of colour in diamonds <sup>294–302</sup>, much is still unknown <sup>60,303</sup>. Important review articles have been written over the years on spectral features in diamond <sup>46,60,303–305</sup>, and an examination of these papers show the rapid acceleration in the identification of features over the last ten years. From Walkers' review in 1976 to Dischler's in 2012 there has been an increase from thirty centres with 100 lines to over 300 centres with an excess of 2000 lines. However, there still remains much to be resolved. Dischler highlights that although many more features have been observed, they have yet to be assigned.

Positron measurements by Maki on natural type IIa diamonds show brown natural diamond contains a large concentration of clusters of 40-60 missing atoms and lifetime components corresponded to those of a monovacancy, postulated to be linked to dislocations. Maki proposes that visible wavelengths excite electrons to the vacancy clusters causing the brown colouration due to visible absorption leading to a suggestion that the defect(s) responsible



for the brown colouration introduce a continuum of states, which implies that it is unlikely that the cause is a single impurity related point defect. In natural brown diamonds the brown colouration is linked to dislocation formed during its movement through the Earth <sup>306</sup>. It was observed that the origin of brown colouration in a high-purity natural diamond was due to an absorption ramp starting at 2.0 eV, not due to impurities as the sample was observed to contain very few using TEM <sup>306</sup>.

Consulting the available literature on the brown colouration in diamonds three strong theories emerge:

- Absorption due to lattice dislocations,
- Absorption due to sp<sup>2</sup> carbon in the form of graphitic inclusions,
- Absorption due to sp<sup>2</sup> carbon in the form of amorphous carbon at micro domains.

Zaitsev <sup>46</sup> attributes brown colouration in natural diamonds to a broad absorption band in the blue spectral region, citing a very complex luminescence. Brown itself is a complex colour, composed of various other colours spectrally mixing to produce a particular hue. This complex colour clearly reflects its complex origins and the studies performed here on a natural diamond with brown banding agree with this.

This brown colour, common in natural and CVD diamond, has been shown to be affected by HPHT treatment, where the brown colouration has been observed to be lightened to yellow or removed to varying degrees <sup>294</sup>.

### **6.7.1 Absorption due to lattice dislocations**

It is thought all natural brown diamonds have undergone plastic deformation at some stage in their lives <sup>296</sup>. Plastic deformation is thought to be the main process that causes unevenness and the brown colour of diamonds<sup>297</sup>. However it should be noted that not all plastically

deformed diamonds show brown colouration. Brown colouration in diamonds is most frequently found concentrated in bands parallel to (111) planes and can be found in both Type I and Type II diamonds. Vacancy clusters are increasingly thought to play a significant part in brown colouration.

The cross-polarised images of the natural banded and brown CVD sample show the colour variations are clearly linked to the areas of highest strain in the samples. The HeLIOS spatially resolved PL data confirms there are different luminescent responses from the brown bands on the natural sample compared to the clear bulk.

During CVD growth Coe *et al* <sup>224</sup> state the brown colour can be due to the individual crystal grains becoming segregated at grain boundaries around dislocations. This could be the reason for the colouration in the polycrystalline samples which were examined by Raman spectroscopy and mapping. Studies show there is a link between  $sp^2$  bonding and dislocation cores in natural brown diamonds. Plastic deformation produced intense nitrogen related centres in diamond including:  $NV^0$ ,  $NV^-$ , and the H3 centre.

### **6.7.2 Absorption due to $sp^2$ carbon in the form of graphitic inclusions or amorphous carbon at micro domains**

As discussed internal stress (nonhomogeneous) in a diamond lattice can be evaluated from the FWHM and ZPLs when measured at low temperatures. Sussman <sup>46</sup> postulates the brown colouration of a number of CVD diamonds grown to a thick depth, rather than a film, is due to the colour of individual crystal grains, with finely dispersed non-diamond material collecting at grain boundaries. This agrees with the PL and Raman measurements taken here.

The lack of a strong Raman signature around  $1500\text{ cm}^{-1}$ , which is characteristic of  $\pi$ -bonded carbon <sup>199</sup>, suggests that this may not be the cause of colouration in brown CVD diamonds and further work is required.

The central region of the brown CVD sample, which exhibits the least strain through examining the Raman spectra, Raman maps and birefringence, does not display any features in the  $1500\text{ cm}^{-1}$  region. The chipped, darker region, which exhibits the greatest strain however has a strong band located at  $2257\text{ cm}^{-1}$ .

## **6.8 High-resolution and spatially resolved PL of additional samples**

The ZnO sample has been measured using high-resolution and spatially resolved photoluminescence. ZnO was selected to provide a high quality, uniform and bright source of PL to assess the detection capabilities of HeLIOS. These data show a good agreement, with ROIs selected across the sample showing only minor overall intensity changes due to the position of the incident light. This agreement is due to the high brightness of the emitted PL. As discussed in Chapter 3, the LCTF has a relatively low transmission, especially in the shorter wavelengths, therefore there is less light arriving at the EMCCD detector increasing the uncertainty in the radiometrically calibrated data. The data show a slight broadening of the spectrum, which in future work shall be improved by setting the imaging sampling interval to smaller increments. This proof of concept work used 10 nm due to the large volume of calibration data required to perform the radiometric calibration. Through the work conducted in Chapter 4, and feedback from the experimental data presented in Chapter 5, it can be seen there is much merit in acquiring further calibration data to reduce the sampling interval.

Two calcite based samples, calcium carbonate and a snail operculum have been investigated as they are spatially interesting and emit a strong PL under UV excitation. These samples have proved a challenging test for the resolving power of HeLIOS due to their texture casting shadows under the incident light confusing the spatially resolved data. All the data presented in this thesis have been time-average spectroscopy, and in these samples little spectral detail

was resolved, however the picture is far more complex showing the need for time-resolved studies. HeLIOS' EMCCD detector is capable of time resolved measurements and future work is proposed in this area to expand HeLIOS for more Mars analogue materials.

The glowed *Bithynia tentaculata* operculum sample elegantly illustrates the effect of spectral convolution in the high-resolution area averaged PL when compared with the spatially resolved data. Figure 6-14 compares the normalised spectra of two regions of interest located on the bright rim of the opercula with the high-resolution data. The different profiles show the violet and orange bands of calcite. The broader high-resolution spectra appear to be a convolution of a number of bands over the range of those from ROIs. These spatial variations in PL show hyperspectral imaging to be a promising technique to compliment the use of luminescence to provide chronological information.

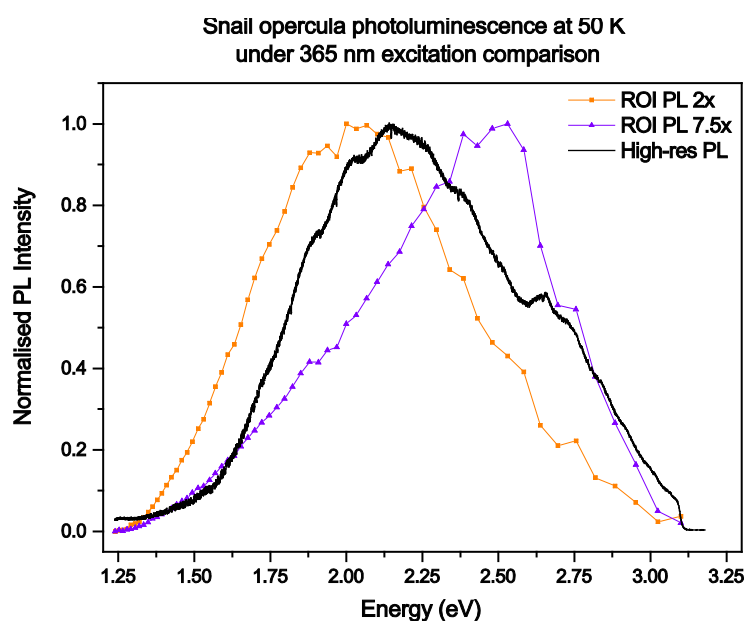


Figure 6-14 Comparison of high resolution PL data and of two regions of interest from the bright regions of the snail opercula; the orange and violet bands of calcite are shown as being dominant. These data are complicated further through the presence of biological material.

## 6.9 Summary

This thesis has presented a new instrument for spatially resolved photoluminescence studies of wide band gap materials in a controlled environment, which has been subject to rigorous characterisation and a full radiometric calibration.

The viability of hyperspectral photoluminescence spectroscopy to provide spatially resolved data has been demonstrated through the investigation of a number of diamond and mineral samples. The application of this technique, along with calibration protocol, has revealed a relationship between composition and brown colouration in diamond. To the knowledge of

## 6.9 Summary

---

the author this is the first time photoluminescence data has been presented and compared in absolute units of irradiance,  $\mu\text{Wcm}^{-2}\text{eV}^{-1}$ , traceable to international standards.

On investigation into the cause of brown colouration in diamonds, the stress present in the samples has been investigated using birefringence and Raman spectroscopy. A protocol for data processing of large Raman mapping datasets has been developed and implemented to investigate the correlation between colouration, stress and variations in the carbon bonding of the samples. These data have shown the natural diamond to be under tensile stress and the synthetic CVD samples compressive stress.

## Chapter 7 Further Work

The research conducted as part of this thesis has had a strong interdisciplinary nature, involving discussions in the fields of materials physics, chemistry, engineering, computer science, astrobiology and earth science. The nature of such discussions naturally posed more questions than answers in the course of this work. Through the work done in this thesis on the use of optical techniques for material characterisation, a number of potential developments to the HeLIOS and ApREES instrumentation and proposed future experiments are briefly discussed in this final chapter.

Instrumentation improvements have been identified for HeLIOS, a number of which are currently being performed. It was noted that at the higher magnifications and long integrations times, the vibration of the cryostat operation affected that sample imaging. The cryostat itself classed as low vibration, however modifications are in progress to vibrationally isolate the sample further using dampeners. For future studies it would be beneficial to have the ability to adjust the angle of the sample during excitation and imaging. Modifications of the sample mount on the cryostat to enable the sample geometry to be changed are planned, with rotation of the sample allowing angle resolved studies.

One of the most radical changes proposed to HeLIOS is a move away from the use of a LCTF, due to low transmission, to tuneable bandpass filters. This will be slower to select wavelengths across the whole range, however they are far more cost effective. What is lost in the speed of wavelength selection is more than made up in the higher transmissions, where integration times will be far shorter than those required with the LCTF. This is particularly

evident in the blue region. As a proof of concept one tuneable band pass filter was purchased and mounted onto a precision rotation drive and delivered promising results.

These proposed modifications are the result of building such a costly instrument from scratch; valuable lessons have been learned during the course of this work and should there be the opportunity to reproduce the instrument as part of a future beamline end station these modifications will provide an unrivalled system for optical characterisation of materials and surfaces. Should HeLIOS, in its current or improved form, be granted access to a synchrotron radiation source, the system can be used to further elucidate the origins of the colouration diamonds using X-ray Absorption Spectroscopy (XAS) and 2D XAFS-XEOL as in discussed by Ward *et al* <sup>28</sup>. In the soft X-ray regime of ~200-2000eV used as low excitation energy the quantum efficiency of XEOL is much higher than at high X-ray energy where XRF process dominates, also the X-ray attenuation length is sufficiently short to allow probing of surface, interfacial and bulk regions of a sample. In the interim experiments using the Aberystwyth Tuneable Light Source, described in Chapter 2, are planned to provide excitation-emission PL studies. A luminescence excitation-emission matrix, displayed as a 2D contour plot of PL intensities as a function of a range of excitation and emission wavelengths, could shed further light on the spectral differences between regions of interest.

As seen in the examination of the mineral samples (Troll Springs CaCO<sub>3</sub> and snail opercula) in chapter 5, the time average spectra of the high resolution and spatially resolved data yield a broad feature, shifted in energy depending on location. Laser-induced time-resolved spectroscopy (LITRS) allows discrimination between features in the same spectral range, but which occur at different decay times. This can be achieved using a shutter, such as that already in place on the X-ray source or iHR320 or using pulsed lasers<sup>307</sup>.

Raman spectroscopy has been proved as method of characterisation of diamonds. Although efforts were made to repeat measurements performed in HeLIOS and at the Raman



spectrometer on the same location, this was not exact. A simple addition of a flip mirror into the optical path between the microscope objective and fibre couple to the integrated iHR320 spectrometer is planned to allow Raman spectroscopy. Raman mapping can then be performed using the x,y,z movement of the cryostat stage.

Further characterisations of HeLIOS are planned, specifically the effects of EMCCD aging on the calibrations. It is planned to repeat the calibration routines and compare these data with those presented in this work to investigate if there are changes, which could be affecting the validity of the radiometrical calibrations. Ingley *et al*<sup>308</sup> performed an investigation into the gain characteristics of EMCCDs for space science deployment, showing there were some minor aging effects over the test period. Andor and e2v themselves have published a number of technical notes on EMCCD aging<sup>309,310</sup>.

Where investigating the link between optical characteristic and colouration in diamonds it would be most beneficial to work with a series of samples from growth through the stages of cutting, polishing and application of various treatments such as irradiation and heat. A systematic study on CVD and HPHT diamond is planned for future work. Knowledge of the growth mixes and conditions will vastly add to the interpretation of results derived from optical investigations of diamonds.

As touched on throughout this work, HeLIOS and the radiometric calibration protocols developed in this thesis have been incorporated into a number of funding proposals relating to the exploration of Mars. Those the author is currently involved in are listed below:

- UK Space Agency CREST 2 – Advanced Visible-Infrared Hyperspectral Camera. Development of a novel Vis-IR Hyperspectral camera for planetary exploration and remote sensing.
- UK Space Agency ExoMars2018 – Delivery of Panoramic Camera (PanCam) calibration target (PCT), fiducial markers (FidM), rear inspection mirror (RIM) and the

## 6.9 Summary

---

radiometrical calibration of PanCam. Application of the detector characterisation and radiometrical data processing protocols developed for HeLIOS

- Crown Estate – MINAR (Mine Analogue Research) programme. Field trials in Mars analogue environment of developed Hyperspectral imagers and application of UV luminescence spectroscopy to improve mining efficiency.

## References

1. Williams, G. T. Monitoring in-situ processing of solid surfaces with real-time x-ray photoelectron spectroscopy. (2011).
2. Roberts, O. The Application of Real-Time Photoelectron Spectroscopy to Carbon-Based Semiconductors. (2009).
3. Evans, D. A. *et al.* Direct observation of Schottky to Ohmic transition in Al-diamond contacts using real-time photoelectron spectroscopy. *Appl. Phys. Lett.* **91**, 132114 (2007).
4. Evans, D. & Roberts, O. Diamond–metal contacts: interface barriers and real-time characterization. *J. Phys. ...* (2009).
5. Heinhold, R., Williams, G. T., Cooil, S. P., Evans, D. A. & Allen, M. W. Influence of polarity and hydroxyl termination on the band bending at ZnO surfaces. *Phys. Rev. B* **88**, 235315 (2013).
6. Williams, G. T. *et al.* High temperature photoelectron emission and surface photovoltage in semiconducting diamond. *Appl. Phys. Lett.* **105**, 061602 (2014).
7. Langstaff, D. P., Bushell, A., Chase, T. & Evans, D. A. A fully integrated multi-channel detector for electron spectroscopy. *Nucl. Instruments Methods Phys. Res. Sect. B Beam Interact. with Mater. Atoms* **238**, 219–223 (2005).

## References

---

8. Cooil, S. P. Controlling the Epitaxial Growth of Graphene On Diamond Surfaces.
9. JosseJosset, J.-L. (2014). NASA Mars 2020 Hyperspectral CLoSe-UP Imager (HyperCLUPI).t, J.-L. *NASA Mars 2020 Hyperspectral CLoSe-UP Imager (HyperCLUPI)*. (2014).
10. Barnes, D. P. *The Search for Planetary Habitability - Theme 2: Detecting Habitability on Planetary Surfaces*. (2014).
11. Coates, A. & Barnes, D. P. *Technology development for PanCam-2020 : A VIS-IR Hyperspectral Panoramic Camera Instrument for Mars Exploration*. (2013).
12. Cousins, C. R. *Looking for life in the UV: autofluorescence as a future tool for planetary exploration*. (2013).
13. Edelman, G. J., Gaston, E., van Leeuwen, T. G., Cullen, P. J. & Aalders, M. C. G. *Hyperspectral imaging for non-contact analysis of forensic traces. Forensic science international* **223**, (2012).
14. Valeur, B. & Berberan-Santos, M. A brief history of fluorescence and phosphorescence before the emergence of quantum theory. *J. Chem. Educ.* 731–738 (2011).
15. Stokes, G. On the change of refrangibility of light. *Philos. Trans. R. Soc. ...* (1852).
16. Ronda, C. ., Jüstel, T. & Nikol, H. Rare earth phosphors: fundamentals and applications. *Journal of Alloys and Compounds* **275-277**, 669–676 (1998).
17. Nakamura, T., Takahashi, N., Poolton, N. R. J. & Malins, A. E. R. Optical and structural properties of CVD-grown single crystal SiO<sub>2</sub> using optically detected XAS. *Appl. Surf. Sci.* **244**, 318–321 (2005).

- 
18. Lakowicz, J. *Principles of fluorescence spectroscopy*. (2009).
  19. *Single-Photon Imaging*. **160**, (Springer Berlin Heidelberg, 2011).
  20. Gfroerer, T. Photoluminescence in analysis of surfaces and interfaces. *Encycl. Anal. Chem.* (2000).
  21. Fox, M. *Optical Properties of Solids*. (2007).
  22. Poolton, N., Bøtter-Jensen, L. & Duller, G. THERMAL QUENCHING OF LUMINESCENCE PROCESSES IN FELDSPARS. *Radiat. Meas.* **24**, (1995).
  23. Boscherini, F. *et al.* Optical measurements of nanoporous anodic alumina formed on Si using novel X-ray spectroscopy set up CLASSIX. *Nucl. Instruments Methods Phys. Res. Sect. B Beam Interact. with Mater. Atoms* **268**, 251–253 (2010).
  24. Mosselmans, J. F. W. *et al.* A time resolved microfocus XEOL facility at the Diamond Light Source. *J. Phys. Conf. Ser.* **425**, 182009 (2013).
  25. Soderholm, L., Liu, G. K., Antonio, M. R. & Lytle, F. W. X-ray excited optical luminescence (XEOL) detection of x-ray absorption fine structure (XAFS). *J. Chem. Phys.* **109**, 6745 (1998).
  26. Ivanov, S. N., Kolobanov, V. N. & Mikhailin, V. V. High-luminosity system for XEOL spectroscopy (abstract). *Rev. Sci. Instrum.* **63**, 1469 (1992).
  27. Taylor, R. P., Finch, A. A., Mosselmans, J. F. W. & Quinn, P. D. The development of a XEOL and TR XEOL detection system for the I18 microfocus beamline Diamond light source. *J. Lumin.* **134**, 49–58 (2013).

## References

---

28. Ward, M. J., Smith, J. G., Regier, T. Z. & Sham, T. K. 2D XAFS-XEOL Spectroscopy – Some recent developments. *J. Phys. Conf. Ser.* **425**, 132009 (2013).
29. Taylor, R. P. The development of X-ray Excited Optical Luminescence ( XEOL ) spectroscopic techniques for mineralogical and petrological applications. (2013).
30. Sham, T. K. K. *et al.* X-ray excited optical luminescence (XEOL): a potential tool for OELD studies. *Thin Solid Films* **363**, 318–321 (2000).
31. Soderholm, L., Liu, G. K., Antonio, M. R. & Lytle, F. W. X-ray excited optical luminescence (XEOL) detection of x-ray absorption fine structure (XAFS). *J. Chem. Phys.* **109**, 6745 (1998).
32. Hu, Y., Tan, K., Kim, P. & Zhang, P. Soft x-ray excited optical luminescence: Some recent applications. *Rev. Sci. ...* **73**, 1379 (2002).
33. Armelao, L. *et al.* The origin and dynamics of soft X-ray-excited optical luminescence of ZnO. *Chemphyschem* **11**, 3625–31 (2010).
34. Poolton, N. R. J., Towlson, B. M., Hamilton, B. & Evans, D. A. New instrumentation for micro-imaging X-ray absorption spectroscopy using optical detection methods. *Nucl. Instruments Methods Phys. Res. Sect. B Beam Interact. with Mater. Atoms* **246**, 445–451 (2006).
35. Poolton, N. R. J. *et al.* High-sensitivity instrumentation for spectrally-resolved optically detected X-ray absorption spectroscopy. *Nucl. Instruments Methods Phys. Res. Sect. B Beam Interact. with Mater. Atoms* **225**, 590–598 (2004).
36. Bauer, G. & Richter, W. Optical characterization of epitaxial semiconductor layers. 429 (1996).

- 
37. Das, R. S. & Agrawal, Y. K. Raman spectroscopy: Recent advancements, techniques and applications. *Vib. Spectrosc.* **57**, 163–176 (2011).
  38. Pérez, F. R. & Martinez-frias, J. Raman spectroscopy goes to Mars. *Spectrosc. Eur.* **18**, 18–21 (2006).
  39. Popp, J. & Schmitt, M. Raman spectroscopy breaking terrestrial barriers! *J. Raman Spectrosc.* **35**, 429–432 (2004).
  40. Bersani, D. & Lottici, P. P. Applications of Raman spectroscopy to gemology. *Anal. Bioanal. Chem.* **397**, 2631–46 (2010).
  41. Tu, Q. & Chang, C. Diagnostic applications of Raman spectroscopy. *Nanomedicine Nanotechnology, Biol. Med.* **8**, 545–558 (2012).
  42. Clark, R. J. H. Raman Spectroscopy in Archaeology and Art History. Edited by H. G. M. Edwards and J. M. Chalmers. Published by The Royal Society of Chemistry, Cambridge, UK, 2005, 508 + xxii pages, ISBN: 0 85404 522 8. *J. Raman Spectrosc.* **37**, 958–958 (2006).
  43. Brożek-Pluska, B., Szymczyk, I. & Abramczyk, H. Raman spectroscopy of phthalocyanines and their sulfonated derivatives. *J. Mol. Struct.* **744-747**, 481–485 (2005).
  44. Braun, R. *Introduction to instrumental analysis*. (Mcgraw-Hill Companies Inc.).
  45. Praver, S. & Nemanich, R. J. Raman spectroscopy of diamond and doped diamond. *Philos. Trans. A. Math. Phys. Eng. Sci.* **362**, 2537–65 (2004).
  46. Zaitsev, A. *Optical properties of diamond: a data handbook*. (2001).

## References

---

47. Tardieu, A., Cansell, F. & Petitet, J. P. Pressure and temperature dependence of the first-order Raman mode of diamond. *J. Appl. Phys.* **68**, 3243 (1990).
48. Cui, J. B., Amtmann, K., Ristein, J. & Ley, L. Noncontact temperature measurements of diamond by Raman scattering spectroscopy. *J. Appl. Phys.* **83**, 7929 (1998).
49. Pikov, V. & Siegel, P. Thermal monitoring: Raman spectrometer system for remote measurement of cellular temperature on a microscopic scale. ... *Med. Biol. Mag. IEEE* 63–71 (2010).
50. Yang, K.-H., Mai, F.-D., Yu, C.-C. & Liu, Y.-C. Room-temperature sensor based on surface-enhanced Raman spectroscopy. *Analyst* **139**, 5164–9 (2014).
51. Maher, R. C., Cohen, L. F., Lohsoontorn, P., Brett, D. J. L. & Brandon, N. P. Raman Spectroscopy as a Probe of Temperature and Oxidation State for Gadolinium-Doped Ceria Used in Solid Oxide Fuel Cells. *J. Phys. Chem. A* **112**, 1497–501 (2008).
52. Grimsditch, M., Anastassakis, E. & Cardona, M. Effect of uniaxial stress on the zone-center optical phonon of diamond. *Phys. Rev. B* **1**, (1978).
53. Hounscome, L. S., Jones, R., Shaw, M. J. & Briddon, P. R. Photoelastic constants in diamond and silicon. *Phys. Status Solidi* **203**, 3088–3093 (2006).
54. Zhu, H. & Blackborow, P. LDLS sheds light on analytical-sciences applications. *Laser Focus World* (2011).
55. Energetiq. *Model EQ-99 Laser-Driven Light Source Operation and Maintenance Manual*. (2011).
56. Horiba Jobin Yvon. *Triax series brochure*.



- 
57. Edmund Optics. Edmund Optics Catalogue. at <<http://www.edmundoptics.com>>
  58. Thorlabs. Thorlabs Catalogue. at <<http://www.thorlabs.co.uk/navigation.cfm>>
  59. Harris, J. K. *et al.* Remote detection of past habitability at Mars-analogue hydrothermal alteration terrains using an ExoMars Panoramic Camera Emulator. *Icarus* **252**, 284–300 (2015).
  60. Dischler, B. *Handbook of Spectral Lines in Diamond*. (2012).
  61. Bayer, B. E. Color imaging array. (1976).
  62. Holst, G. *CCD Arrays, Cameras, and Displays*. (1998).
  63. Li, Q. *et al.* Review of spectral imaging technology in biomedical engineering: achievements and challenges. *J. Biomed. Opt.* **18**, 100901 (2013).
  64. Goetz, A. F. H. Three decades of hyperspectral remote sensing of the Earth: A personal view. *Remote Sens. Environ.* **113**, S5–S16 (2009).
  65. Goetz, A., Vane, G., Solomon, J. & Rock, B. Imaging spectrometry for earth remote sensing. *Science* (80-. ). (1985).
  66. Li, Q., Wang, W., Ma, C. & Zhu, Z. Detection of physical defects in solar cells by hyperspectral imaging technology. *Opt. Laser Technol.* **42**, 1010–1013 (2010).
  67. Goltz, D., Attas, M., Young, G., Cloutis, E. & Bedynski, M. Assessing stains on historical documents using hyperspectral imaging. *J. Cult. Herit.* **11**, 19–26 (2010).
  68. Geladi, P., Burger, J. & Lestander, T. Hyperspectral imaging: calibration problems and solutions. *Chemom. Intell. Lab. Syst.* **72**, 209–217 (2004).

## References

---

69. Huebschman, M. L., Schultz, R. A. & Garner, H. R. Characteristics and capabilities of the hyperspectral imaging microscope. *IEEE Eng. Med. Biol. Mag.* **21**, 104–117 (2002).
70. Reed, G., Savage, K., Edwards, D. & Nic Daeid, N. Hyperspectral imaging of gel pen inks: An emerging tool in document analysis. *Sci. Justice* (2013).
71. England, J. *et al.* Hyperspectral cathodoluminescence imaging of modern and fossil carbonate shells. *J. Geophys. Res. Atmos.* **111**, G03001 (2006).
72. Pilorget, C. & Bibring, J.-P. Automated algorithms to identify and locate grains of specific composition for NIR hyperspectral microscopes: Application to the MicrOmega instrument onboard ExoMars. *Planet. Space Sci.* **99**, 7–18 (2014).
73. Pio Rossi, D. A., Witasse, D. O., Leroi, V., Bibring, J.-P. & Berthe, M. Micromega/IR: Design and status of a near-infrared spectral microscope for in situ analysis of Mars samples. *Planet. Space Sci.* **57**, 1068–1075 (2009).
74. Bousquet, P. W. *et al.* French instruments for in-situ missions: Past, present and future. *Acta Astronaut.* **81**, 358–368 (2012).
75. Vago, J., Gardini, B. & Kminek, G. ExoMars-searching for life on the Red Planet. *ESA ...* (2006).
76. Debus, A., Bacher, M. & Ball, A. EXOMARS 2018 ROVER PASTEUR PAYLOAD SAMPLE ANALYSIS. *38th COSPAR ...* 2018 (2010).
77. Kramer, H. J. *Observation of the Earth and Its Environment: Survey of Missions and Sensors (Google eBook)*. (Springer, 2002).

- 
78. Sellar, R. G. & Boreman, G. D. Classification of imaging spectrometers for remote sensing applications. *Opt. Eng.* **44**, 013602 (2005).
  79. Najiminaini, M., Vasefi, F., Kaminska, B. & Carson, J. J. L. Nanohole-array-based device for 2D snapshot multispectral imaging. *Sci. Rep.* **3**, 2589 (2013).
  80. Shrestha, R. Spatial arrangement of color filter array for multispectral image acquisition. *IS&T/SPIE ...* 787503–787503–9 (2011). doi:10.1117/12.872253
  81. Sellar, R. & Boreman, G. Classification of imaging spectrometers for remote sensing applications. *Opt. Eng.* (2005).
  82. Markham, B. L. & Helder, D. L. Forty-year calibrated record of earth-reflected radiance from Landsat: A review. *Remote Sens. Environ.* **122**, 30–40 (2012).
  83. Hastings, D. A. & Emery, W. J. The advanced very high resolution radiometer (AVHRR) - A brief reference guide. *Photogramm. Eng. Remote Sensing* **58**, 1183–1188 (1992).
  84. Chrien, T. Accuracy of the spectral and radiometric laboratory calibration of the Airborne Visible/Infrared Imaging Spectrometer. *Imaging ...* 37–49 (1990). doi:10.1117/12.21334
  85. Kamruzzaman, M., ElMasry, G., Sun, D.-W. & Allen, P. Prediction of some quality attributes of lamb meat using near-infrared hyperspectral imaging and multivariate analysis. *Anal. Chim. Acta* **714**, 57–67 (2012).
  86. Stuffer, T. *et al.* Hyperspectral imaging—An advanced instrument concept for the EnMAP mission (Environmental Mapping and Analysis Programme). *Acta Astronaut.* **65**, 1107–1112 (2009).

## References

---

87. Abrams, M. The Advanced Spaceborne Thermal Emission and Reflection Radiometer (ASTER): Data products for the high spatial resolution imager on NASA's Terra platform. *Int. J. Remote Sens.* (2000).
88. Edmund Optics. *X Rite ColorChecker*®. (2014).
89. Barnes, D. *et al.* Developing a Hyperspectral Close UP Imager With UV Excitation (HyperCLUPI) for Mars Exploration. in *European Planetary Science Congress* **9**, (2014).
90. Khan, N., Dicker, D., Flaherty, K. T., Lerner, J. & El-Deiry, W. Hyperspectral imaging: A noninvasive in vivo method of imaging melanoma lesions in a patient being treated with a novel B-RAF inhibitor. *ASCO Meet. Abstr.* **28**, e19019 (2010).
91. Uhr, J. W. *et al.* Molecular profiling of individual tumor cells by hyperspectral microscopic imaging. *Transl. Res.* **159**, 366–75 (2012).
92. Stacy, B. M., Comfort, K. K., Comfort, D. A. & Hussain, S. M. In Vitro Identification of Gold Nanorods through Hyperspectral Imaging. *Plasmonics* **8**, 1235–1240 (2013).
93. Pilorget, C. & Bibring, J.-P. NIR reflectance hyperspectral microscopy for planetary science: Application to the MicrOmega instrument. *Planet. Space Sci.* **76**, 42–52 (2013).
94. Markstrom, L. J. & Mabbott, G. A. Obtaining absorption spectra from single textile fibers using a liquid crystal tunable filter microspectrophotometer. *Forensic Sci. Int.* **209**, 108–112 (2011).
95. Hirvonen, T., Penttinen, N., Hauta-Kasari, M., Sorjonen, M. & Peiponen, K.-E. A wide spectral range reflectance and luminescence imaging system. *Sensors (Basel)*. **13**, 14500–10 (2013).

- 
96. Nikon. <http://www.microscopyu.com>. (2014).
  97. PerkinElmer Inc. *VariSpec Effortlessly tune to any wavelength in the VIS or NIR range – without moving parts*. (2013).
  98. Meadowlark. *Response Time in Liquid-Crystal Variable Retarders*. (2005).
  99. Meadowlark. *Liquid Crystal Tunable Filter User Manual*. (2010).
  100. Ward, J., Pannell, C. N., Wachmann, E. S. & Seale, W. *Applications of acousto-optic devices for spectral imaging systems*. (2010).
  101. Schott. Schott optical filters 2013 catalogue. (2013).
  102. Lerner, J. M. Imaging spectrometer fundamentals for researchers in the biosciences--a tutorial. *Cytometry. A* **69**, 712–34 (2006).
  103. Horiba Jobin Yvon. *Imaging Spectrometers - iHR Series*. (2014).
  104. Amelio, G., Tompsett, M. & Smith, G. E. Experimental Verification of the Charge Coupled Device Concept. *Bell Syst. Tech. ...* (1970).
  105. Boyle, W. & Smith, G. Charge Coupled Semiconductor Devices. *Bell Syst. Tech. J.* (1970).
  106. Smith, G. E. The invention of the CCD. *Nucl. Instruments Methods Phys. Res. Sect. A Accel. Spectrometers, Detect. Assoc. Equip.* **471**, 1–5 (2001).
  107. Healey, G. & Kondepudy, R. Radiometric CCD camera calibration and noise estimation. *Pattern Anal. Mach. ...* **16**, (1994).

## References

---

108. Janesick, J. Charge-coupled-device charge-collection efficiency and the photon-transfer technique. *Opt. Eng.* **26**, 972–980 (1987).
109. Robbins, M. & Hadwen, B. The Noise Performance of Electron Multiplying Charge-Coupled Devices. *Electron Devices, IEEE Trans. ...* (2003).
110. Andor Technology Ltd. *iXon DV887 camera specs.* **887**, (2004).
111. Andor Technology Ltd. *iXon EM + Back-illuminated EMCCDs.* (2006).
112. Andor Technology Ltd. EMCCD. 1–7 (2003).
113. Poolton, N. R. J. *et al.* Non-resonant X-ray/laser interaction spectroscopy as a method for assessing charge competition, trapping and luminescence efficiency in wide band-gap materials. *J. Lumin.* **130**, 1404–1414 (2010).
114. Poolton, N. R. J. *et al.* Luminescence excitation characteristics of Ca-, Na- and K-aluminosilicates (feldspars), in the stimulation range 20 500 eV: optical detection of XAS. *J. Phys. D. Appl. Phys.* **36**, 1107–1114 (2003).
115. Nakamura, T., Takahashi, N., Poolton, N. R. J. & Malins, A. E. R. Optical and structural properties of CVD-grown single crystal SiO<sub>2</sub> using optically detected XAS. *Appl. Surf. Sci.* **244**, 318–321 (2005).
116. Chao, Y. *et al.* Optical luminescence from alkyl-passivated Si nanocrystals under vacuum ultraviolet excitation: Origin and temperature dependence of the blue and orange emissions. *Appl. Phys. Lett.* **88**, 2006–2008 (2006).

- 
117. Poolton, N. R. J., Hamilton, B. & Evans, D. A. Synchrotron – laser pump – probe luminescence spectroscopy : correlation of electronic defect states with x-ray absorption in wide-gap solids. *J. Phys. D. Appl. Phys.* **38**, 1478–1484 (2005).
118. Evans, D. A. *et al.* Determination of the optical band-gap energy of cubic and hexagonal boron nitride using luminescence excitation spectroscopy. *J. Phys. Condens. Matter* **20**, 075233 (2008).
119. Poolton, N. R. J., Towlson, B. M., Hamilton, B., Wallinga, J. & Lang, A. Micro-imaging synchrotron–laser interactions in wide band-gap luminescent materials. *J. Phys. D. Appl. Phys.* **40**, 3557–3562 (2007).
120. Advanced Research Systems. Advanced Research Systems. 2014 at <<http://www.arscryo.com>>
121. Lakeshore Cryotronics. Lakeshore Cryotronics. 2014 at <<http://www.lakeshore.com/Pages/Home.aspx>>
122. Beyer, H. Accurate Calibration of CCD-Cameras. *Comput. Vis. Pattern Recognition, 1992. Proc. CVPR '92., 1992 IEEE Comput. Soc. Conf.* (1992).
123. Chander, G., Markham, B. L. & Helder, D. L. Summary of current radiometric calibration coefficients for Landsat MSS, TM, ETM+, and EO-1 ALI sensors. *Remote Sens. Environ.* **113**, 893–903 (2009).
124. Jacquez, J. & Kuppenheim, H. Theory of the integrating sphere. *JOSA* **45**, 460 (1955).
125. Palmer, J. & Grant, B. *The art of radiometry.* (2010).
126. Labsphere Inc. *Technical Guide Reflectance Standards.* (2012).

## References

---

127. Labsphere Inc. Labsphere Genral Purpose Integrating Spheres. (2014). at <<http://www.labsphere.com/products/spheres-and-components/general-purpose-spheres/default.aspx>>
128. Gunn, M. D. Spectral imaging for Mars exploration. (Aberystwyth University, 2013).
129. Ocean Optics. *CC-3 Series Cosine-corrected Irradiance Probes*.
130. Ocean Optics. Ocean Optics. (2014). at <<http://oceanoptics.com/product/cosine-correctors/>>
131. Ocean Optics. USB 2000 Prodcut Sheet.
132. Dinguirard, M. & Slater, P. N. Calibration of Space-Multispectral Imaging Sensors. *Remote Sens. Environ.* **68**, 194–205 (1999).
133. Yilmaz, O., Turk, F. & Selimoglu, O. Radiometric calibration and SNR calculation of a SWIR imaging telescope. in *AIP Conference Proceedings, 2nd International Advances in Applied Physics and Materials Science Congress* **1476**, 365–369 (2012).
134. López-Álvarez, M. a., Hernández-Andrés, J., Romero, J., Campos, J. & Pons, A. Calibrating the Elements of a Multispectral Imaging System. *J. Imaging Sci. Technol.* **53**, 031102 (2009).
135. Seitz, P. & Theuwissen, A. *Single-Photon Imaging*. (2011).
136. Ortiz, A. & Oliver, G. Radiometric calibration of vision cameras and intensity uncertainty estimation. *Image Vis. Comput.* **24**, 1137–1145 (2006).
137. Janesick, J. *Photon Transfer*. (2007).



- 
138. Janesick, J., Gunawan, F., Dosluoglu, T., Tower, J. & McCaffrey, N. Scientific CMOS Pixels. *Exp. Astron.* **14**, 33–43 (2002).
139. Bell, J. & Joseph, J. In-flight calibration and performance of the Mars Exploration Rover Panoramic Camera (Pancam) instruments. *J. Geophys. Res.* **111**, (2006).
140. Landgrebe, D. Information Extraction Principles and Methods for Multispectral and Hyperspectral Image Data. *Inf. Process. Remote Sens.* (1999).
141. Bannon, D. Hyperspectral imaging: Cubes and slices. *Nat. Photonics* **3**, 627–629 (2009).
142. Haggerty, S. E. Superkimberlites: A geodynamic diamond window to the Earth's core. *Earth Planet. Sci. Lett.* **122**, 57–69 (1994).
143. Griffin, W. L. Major transformations reveal Earth's deep secrets. *Geology* **36**, 95 (2008).
144. Recent Advances in Understanding the Geology of Diamonds | Gems & Gemology. at <<http://www.gia.edu/gems-gemology/WN13-advances-diamond-geology-shirey>>
145. Teukolsky, S. A., Vetterling, W. T. & Flannery, B. P. *Numerical Recipes in C: The Art of Scientific Computing.* (1992).
146. Nebel, C. E. *et al.* Diamond and biology. *J. R. Soc. Interface* **4**, 439–461 (2007).
147. Wang, W., Polo, M. & Sanchez, G. Internal stress and strain in heavily boron-doped diamond films grown by microwave plasma and hot filament chemical vapor deposition. *J. Appl. ...* **80**, (1996).
148. Sque, S. J. Bulk and Transfer Doping of Diamond. (2005).

## References

---

149. Stachel, T. & Harris, J. W. Formation of diamond in the Earth's mantle. *J. Phys. Condens. Matter* **21**, 364206 (2009).
150. Smith, D. C., Godard, G. & Green, H. W. Diamond-Lonsdaleite-Graphite Relations Examined by Raman Mapping of Carbon Microinclusions inside Zircon at Kumdy Kol, Kokchetav, Kazakhstan: Evidence of the Metamictization of Diamond. *Ultrahigh Pressure Metamorphism* 43–75 (2011). doi:10.1016/B978-0-12-385144-4.00001-1
151. Borrachudo, D. do rio. Diamonds from Borrachudo River, São Francisco Basin (Tiros, MG): Morphologic and Dissolution Aspects. *SciELO Bras.* **67**, 159–165 (2014).
152. Orlov, I. *The mineralogy of the diamond*. (1977).
153. Gurney, J. *Diamonds in Nature: A Guide to Rough Diamonds. Economic Geology* (2011).
154. Smith, D. C. & Godard, G. A Raman spectroscopic study of diamond and disordered sp<sup>3</sup>-carbon in the coesite-bearing Straumen Eclogite Pod, Norway. *J. Metamorph. Geol.* **31**, 19–33 (2013).
155. Bonnot, A. M. Raman microspectroscopy of diamond crystals and thin films produced by hot-filament assisted chemical vapor deposition. *Phys. Rev. B* **41**, 6040–6049 (1990).
156. Balmer, R. & Brandon, J. Chemical vapour deposition synthetic diamond: materials, technology and applications. *J. Phys. ...* 1–51 (2009).
157. Bundy, F. P. *et al.* The pressure-temperature phase and transformation diagram for carbon; updated through 1994. *Carbon N. Y.* **34**, 141–153 (1996).
158. Bundy, F. P. The P, T Phase and Reaction Diagram for Elemental Carbon, 1979. *J. Geophys. Res.* **85**, 6930 (1980).

- 
159. Robertson, R., Fox, J. J. & Martin, A. E. Two Types of Diamond. *Philos. Trans. R. Soc. A Math. Phys. Eng. Sci.* **232**, 463–535 (1934).
160. Breeding, C. M. & Shigley, J. E. The ‘Type’ Classification System of Diamonds and Its Importance in Gemology. *Gems Gemol.* **45**, 96–111 (2009).
161. Kucsko, G. *et al.* Nanometre-scale thermometry in a living cell. *Nature* **500**, 54–8 (2013).
162. Weng, J., Zhang, Z., Sun, L. & Wang, J. A. High sensitive detection of cancer cell with a folic acid-based boron-doped diamond electrode using an AC impedimetric approach. *Biosens. Bioelectron.* **26**, 1847–52 (2011).
163. Vaitkuvienė, A. *et al.* Impact of diamond nanoparticles on neural cells. *Mol. Cell. Probes* **29**, 25–30 (2015).
164. Man, H. B., Zhang, K., Robinson, E., Chow, E. K. & Ho, D. *Ultananocrystalline Diamond*. *Ultananocrystalline Diamond* (Elsevier, 2012). doi:10.1016/B978-1-4377-3465-2.00015-3
165. Satoshi Koizumi, Christoph Nebel, M. N. *Physics and Applications of CVD Diamond*. (2008).
166. Manson, N. B. *et al.* Fabrication of single optical centres in diamond—a review. *J. Lumin.* **130**, 1646–1654 (2010).
167. Smith, J. M. *et al.* Optical properties of a single-colour centre in diamond with a green zero-phonon line. *New J. Phys.* **13**, 045005 (2011).

## References

---

168. Bernien, H. *et al.* Heralded entanglement between solid-state qubits separated by three metres. *Nature* **497**, 86–90 (2013).
169. Robledo, L. *et al.* High-fidelity projective read-out of a solid-state spin quantum register. *Nature* **477**, 574–578 (2011).
170. Tokuda, N. *et al.* Atomically flat diamond (111) surface formation by homoepitaxial lateral growth. *Diam. Relat. Mater.* **17**, 1051–1054 (2008).
171. Yatsui, T., Nomura, W., Naruse, M. & Ohtsu, M. Realization of an atomically flat surface of diamond using dressed photon–phonon etching. *J. Phys. D. Appl. Phys.* **45**, 475302 (2012).
172. Nesladek, M. Conventional n-type doping in diamond: state of the art and recent progress. *Semicond. Sci. Technol.* **20**, R19–R27 (2005).
173. Lim, H., Park, S., Cheong, H., Choi, H.-M. & Kim, Y. C. Discrimination between natural and HPHT-treated type IIa diamonds using photoluminescence spectroscopy. *Diam. Relat. Mater.* **19**, 1254–1258 (2010).
174. Lindblom, J., Hölsä, J., Papunen, H., Häkkänen, H. & Mutanen, J. Differentiation of natural and synthetic gem-quality diamonds by luminescence properties. *Opt. Mater. (Amst)*. **24**, 243–251 (2003).
175. Evans, D. A. & Roberts, O. Diamond–metal contacts: interface barriers and real-time characterization. *J. Phys. ...* **21**, 364223 (2009).
176. Jones, G. O. *et al.* Detecting sp<sup>2</sup>-bonded carbon in diamond using optically detected X-ray absorption spectroscopy. *Diam. Light Source Proc.* **1**, e131 (2011).

- 
177. Williams, G., Cool, S. & Roberts, O. High temperature photoelectron emission and surface photovoltage in semiconducting diamond. *Appl. Phys. ...* (2014).
178. Lübke, M., Evans, D. A., Kampen, T. U., Okano, K. & Zahn, D. R. T. Angular-resolved study of secondary-electron emission from NEA diamond surfaces. *Diam. Relat. Mater.* **8**, 1485–1489 (1999).
179. Solin, S. A. & Ramdas, A. K. Raman Spectrum of Diamond. *Phys. Rev. B* **1**, (1970).
180. Nemanich, R. & Solin, S. First- and second-order Raman scattering from finite-size crystals of graphite. *Phys. Rev. B* (1979).
181. Ferreira, N. ., Abramof, E., Corat, E. . & Trava-Airoldi, V. . Residual stresses and crystalline quality of heavily boron-doped diamond films analysed by micro-Raman spectroscopy and X-ray diffraction. *Carbon N. Y.* **41**, 1301–1308 (2003).
182. Leeds, S., Davis, T. & May, P. Use of different excitation wavelengths for the analysis of CVD diamond by laser Raman spectroscopy. *Diam. Relat. ...* (1998).
183. Lippold, G., Aderhold, D., Comes, F. J. & Grill, W. Raman and photoluminescence microscopy mapping of CVD micro-diamonds. *Diam. Relat. Mater.* **6**, 1587–1594 (1997).
184. Wieligor, M. & Zerda, T. W. Surface stress distribution in diamond crystals in diamond–silicon carbide composites. *Diam. Relat. Mater.* **17**, 84–89 (2008).
185. Mitra, S. & Brafman, O. Pressure-Induced Phonon Frequency Shifts Measured by Raman Scattering. *Phys. Rev.* **186**, 942–944 (1969).

## References

---

186. Dumpala, R. *et al.* Adhesion characteristics of nano- and micro-crystalline diamond coatings: Raman stress mapping of the scratch tracks. *Diam. Relat. Mater.* **44**, 71–77 (2014).
187. Brookes, E. J., Comins, J. D., Daniel, R. D. & Erasmus, R. M. A study of plastic deformation profiles of impressions in diamond. *Diam. Relat. Mater.* **9**, 1115–1119 (2000).
188. Chen, K. H. *et al.* Micro-Raman for diamond film stress analysis. *Diam. Relat. Mater.* **4**, 460–463 (1995).
189. Steeds, J. W., Gilmore, A., Wilson, J. A. & Butler, J. E. On the nature of extended defects in CVD diamond and the origin of compressive stresses. *Diam. Relat. Mater.* **7**, 1437–1450 (1998).
190. Burton, N. C., Steeds, J. W., Meaden, G. M., Shreter, Y. G. & Butler, J. E. Strain and microstructure variation in grains of CVD diamond film. *Diam. Relat. Mater.* **4**, 1222–1234 (1995).
191. Fan, Q. H., Grácio, J. & Pereira, E. Evaluation of residual stresses in chemical-vapor-deposited diamond films. *J. Appl. Phys.* **87**, 2880 (2000).
192. Windischmann, H. & Gray, K. J. Stress measurement of CVD diamond films. *Diam. Relat. Mater.* **4**, 837–842 (1995).
193. Mossbrucker, J. & Asmussen, J. 3-D determination of the location and absolute amount of sp<sup>2</sup> and sp<sup>3</sup> bound carbon and stress components in CVD diamond films using multi-color polarized Raman spectroscopy. *Diam. Relat. Mater.* **8**, 663–667 (1999).

- 
194. Praver, S. & Nemanich, R. J. Raman spectroscopy of diamond and doped diamond. *Philos. Trans. R. Soc. London. Ser. A Mathematical, Phys. Eng. Sci.* **362** , 2537–2565 (2004).
  195. Mohammed, K., Davies, G. & Collins, A. T. Uniaxial stress splitting of photoluminescence transitions at optical centres in cubic crystals: theory and application to diamond. *Journal of Physics C: Solid State Physics* **15**, 2779–2788 (1982).
  196. Davies, G. & Hamer, M. F. Optical Studies of the 1.945 eV Vibronic Band in Diamond. *Proc. R. Soc. A Math. Phys. Eng. Sci.* **348**, 285–298 (1976).
  197. Windischmann, H. & Gray, K. Stress measurement of CVD diamond. *Diam. Relat. Mater.* **4**, 837–842 (1995).
  198. Bangert, U., Barnes, R., Gass, M. H., Bleloch, A. L. & Godfrey, I. S. Vacancy clusters, dislocations and brown colouration in diamond. *J. Phys. Condens. Matter* **21**, 364208 (2009).
  199. Jones, R. Dislocations, vacancies and the brown colour of CVD and natural diamond. *Diam. Relat. Mater.* **18**, 820–826 (2009).
  200. SØRENSEN, B. E. A revised Michel Levy interference colour chart based on first-principles calculations. *Eur. J. Mineral.* **25**, 5–10 (2012).
  201. Dean, P. J. & Male, J. C. Some properties of the visible luminescence excited in diamond by irradiation in the fundamental absorption edge. *J. Phys. Chem. Solids* **25**, 1369–1383 (1964).
  202. Dean, P. J. Bound excitons and donor-acceptor pairs in natural and synthetic diamond. *Phys. Rev.* **139**, (1965).

## References

---

203. Lawson, S. C., Kanda, H. & Sekita, M. New nickel-related optical absorption in high-pressure synthetic diamond. *Philos. Mag. Part B* **68**, 39–46 (1993).
204. Santos, L. & Pereira, E. Laser Emission from Natural Diamonds. *MRS Proceedings* **162**, 291 (1989).
205. Sandhu, G. S. *et al.* Regrowth of Damaged Layers in Diamond Produced by Ion Implantation. *MRS Proceedings* **162**, 189 (1989).
206. Collins, A. T. A spectroscopic survey of naturally-occurring vacancy-related colour centres in diamond. *J. Phys. D. Appl. Phys.* **15**, 1431–1438 (1982).
207. Sobolev, E. V & Yeliseev, A. P. Thermoluminescence and phosphorescence of natural diamonds at low temperatures. *J. Struct. Chem.* **17**, 933 (1976).
208. Buhaenko, D. *et al.* Advances in New Diamond Science and Technology (76th edn.) MYU, Tokyo (1994). in *Advances in New Diamond Science and Technology (76th edn.) MYU, Tokyo (1994)* 311 (1994).
209. Collins, A. T. The Physics of Diamond Course. 2730354 (1997).
210. Sobolev, E. V, Il'in, V. E. & Yureva, O. P. No Title. *Sov. Phys. Solid State* **11**, 938 (1969).
211. Bergman, L., Stoner, B. R., Turner, K. F., Glass, J. T. & Nemanich, R. J. Microphotoluminescence and Raman scattering study of defect formation in diamond films. *J. Appl. Phys.* **73**, 3951 (1993).
212. Bokii, G. B., Bezrakov, G. N., Kluev Ju, A., Naletov, A. M. & Nepsha, V. I. *Natural and Synthetic Diamonds (in Russian)*. (Nauka, 1986).



- 
213. Davies, G. *Properties and Growth of Diamond*. (INSPEC, the Institution of Electrical Engineers, 1994).
214. Nazaré, M. H., Woods, G. S. & Assunção, M. C. The 2.526 eV luminescence band in diamond. *Mater. Sci. Eng. B* **11**, 341–345 (1992).
215. Pereira, E. & Santos, L. Dynamical processes of the 2.818 eV centre in diamond. *Diam. Relat. Mater.* **4**, 26–32 (1994).
216. Reinitz, I. M., Fritsch, E. & Shigley, J. E. An oscillating visible light optical center in some natural green to yellow diamonds. *Diam. Relat. Mater.* **7**, 313–316 (1998).
217. Wight, D. R. & Dean, P. J. Extrinsic recombination radiation from natural diamond: Exciton luminescence associated with the N9 center. *Phys. Rev.* **154**, 689–696 (1967).
218. Walker, J. Optical absorption and luminescence in diamond. *Reports Prog. Phys.* **42**, 1605–1659 (1979).
219. Graham, R. J. & Buseck, P. R. Cathodoluminescence of brown diamonds as observed by transmission electron microscopy. *Philos. Mag. Part B* **70**, 1177–1185 (1994).
220. Pereira, E. & Santos, L. Brown diamonds: Long lived visible luminescing centres. *J. Lumin.* **40-41**, 139–140 (1988).
221. Iakoubovskii, K., Adriaenssens, G. ., Nesládek, M. & Stals, L. . Photoluminescence excitation and quenching spectra in CVD diamond films. *Diam. Relat. Mater.* **8**, 717–720 (1999).
222. Angus, J. C. Diamond Synthesis by Chemical Vapor Deposition: The Early Years. *Diam. Relat. Mater.* **49**, 77–86 (2014).

## References

---

- 223. Schwander, M. & Partes, K. A review of diamond synthesis by CVD processes. *Diam. Relat. Mater.* **20**, 1287–1301 (2011).
- 224. Coe, S. . & Sussmann, R. . Optical, thermal and mechanical properties of CVD diamond. *Diam. Relat. Mater.* **9**, 1726–1729 (2000).
- 225. Macpherson, J. V. A practical guide to using boron doped diamond in electrochemical research. *Phys. Chem. Chem. Phys.* **17**, 2935–49 (2015).
- 226. Ushizawa, K. *et al.* Boron concentration dependence of Raman spectra on {100} and {111} facets of B-doped CVD diamond. *Diam. Relat. Mater.* **7**, 1719–1722 (1998).
- 227. III, J. A. & Walukiewicz, W. Fano interference of the Raman phonon in heavily boron-doped diamond films grown by chemical vapor deposition. *Appl. Phys. ...* **66**, 616–618 (1995).
- 228. Deneuville, A., Papadopoulo, A. C., Gheeraert, E. & Gonon, P. No Title. *Le vide, les couches minces* 277 (1992).
- 229. Iakoubovskii, K. & Adriaenssens, G. J. Characterization of the broad green band luminescence in CVD and synthetic Ib diamond. *Diam. Relat. Mater.* **9**, 1017–1020 (2000).
- 230. Lawson, S. C., Kanda, H., Kiyota, H., Tsutsumi, T. & Kawarada, H. Cathodoluminescence from high-pressure synthetic and chemical-vapor-deposited diamond. *J. Appl. Phys.* **77**, 1729 (1995).
- 231. Collins, A. T. The characterisation of point defects in diamond by luminescence spectroscopy. *Diam. Relat. Mater.* **1**, 457–469 (1992).

- 
232. Collins, A. T., Kamo, M. & Sato, Y. Optical centres related to nitrogen, vacancies and interstitials in polycrystalline diamond films grown by plasma-assisted chemical vapour deposition. *J. Phys. D. Appl. Phys.* **22**, 1402–1405 (1989).
233. Sternschulte, H., Horseling, J., Albrecht, T., Thonke, K. & Sauer, R. Characterization of doped and undoped CVD-diamond films by cathodoluminescence. *Diam. Relat. Mater.* **5**, 585–588 (1996).
234. Freitas, J. a., Butler, J. E. & Strom, U. Photoluminescence studies of polycrystalline diamond films. *J. Mater. Res.* **5**, 2502–2506 (1990).
235. Freitas, J. A., Strom, U. & Collins, A. T. Photoluminescence and cathodoluminescence studies of semiconducting diamond. *Diam. Relat. Mater.* **2**, 87–91 (1993).
236. Ruan, J., Choyke, W. J. & Partlow, W. D. Cathodoluminescence and annealing study of plasma-deposited polycrystalline diamond films. *J. Appl. Phys.* **69**, 6632 (1991).
237. Ruan, J., Choyke, W. J. & Kobashi, K. Oxygen-related centers in chemical vapor deposition of diamond. *Appl. Phys. Lett.* **62**, 1379 (1993).
238. Dischler, B. *et al.* Diamond luminescence: resolved donor-acceptor pair recombination lines. *Diam. Relat. Mater.* **3**, 825–830 (1994).
239. Jones, G. Chemical State and Luminescence Imaging of Natural and Synthetic Diamond. (2011).
240. Brunet, F. *et al.* Microstructure evolution of boron doped homoepitaxial diamond films. *J. Appl. Phys.* **83**, 181 (1998).

## References

---

- 241. Nachal'naya, T. A., Andreyev, V. D. & Gabrusenok, E. V. Shift of the frequency and Stokes-anti-Stokes ratio of Raman spectra from diamond powders. *Diam. Relat. Mater.* **3**, 1325–1328 (1994).
- 242. Haq, S., Tunnicliffe, D. L. & Savage, J. A. Optical characterization of textured microwave CVD diamond. *Diam. Relat. Mater.* **3**, 593–597 (1994).
- 243. Janssen, G. *et al.* Rapid growth of single-crystal diamond on diamond substrates. *Surf. Coatings Technol.* **47**, 113–126 (1991).
- 244. Briddon, P. R. & Jones, R. Theory of impurities in diamond. *Phys. B Condens. Matter* **185**, 179–189 (1993).
- 245. Collins, A. T., Kanda, H. & Kitawaki, H. Colour changes produced in natural brown diamonds by high-pressure, high-temperature treatment. *Diam. Relat. Mater.* **9**, 113–122 (2000).
- 246. Cremades, A., Domínguez-Adame, F. & Piqueras, J. Study of defects in chemical vapor deposited diamond films by cross-sectional cathodoluminescence. *J. Appl. Phys.* **74**, 5726 (1993).
- 247. Iakoubovskii, K. & Adriaenssens, G. Luminescence excitation spectra in diamond. *Phys. Rev. B* (2000).
- 248. Khong, Y. L., Collins, A. T. & Allers, L. Luminescence decay time studies and time-resolved cathodoluminescence spectroscopy of CVD diamond. *Diam. Relat. Mater.* **3**, 1023–1027 (1994).
- 249. Dannefaer, S., Zhu, W., Bretagnon, T. & Kerr, D. Vacancies in polycrystalline diamond films. *Phys. Rev. B. Condens. Matter* **53**, 1979–1984 (1996).

- 
250. Irifune, T., Kurio, A., Sakamoto, S., Inoue, T. & Sumiya, H. Materials: Ultrahard polycrystalline diamond from graphite. *Nature* **421**, 99–101 (2003).
251. Krivchenko, V. a. *et al.* Study of polycrystalline boron-doped diamond films by Raman spectroscopy and optical absorption spectroscopy. *Tech. Phys.* **52**, 1471–1474 (2007).
252. Mora, a. ., Steeds, J. . & Butler, J. . Relationship between grain boundaries and broad luminescence peaks in CVD diamond films. *Diam. Relat. Mater.* **12**, 310–317 (2003).
253. Fish, M. L., Massler, O., Reid, J. A., MacGregor, R. & Comins, J. D. The application of photoluminescence and Raman spectroscopy of synthetic diamond. *Diam. Relat. Mater.* **8**, 1511–1514 (1999).
254. Wagner, J., Ramsteiner, M., Wild, C. & Koidl, P. Resonant Raman scattering of amorphous carbon and polycrystalline diamond films. *Phys. Rev. B* **40**, (1989).
255. Djurišić, a. B. *et al.* Green, yellow, and orange defect emission from ZnO nanostructures: Influence of excitation wavelength. *Appl. Phys. Lett.* **88**, 103107 (2006).
256. Look, D. C. Recent advances in ZnO materials and devices. *Mater. Sci. Eng. B* **80**, 383–387 (2001).
257. *Handbook of Zinc Oxide and Related Materials: Volume One, Materials.* (CRC Press, 2012).
258. Özgür, U. *et al.* A comprehensive review of ZnO materials and devices. *J. Appl. Phys.* **98**, 041301 (2005).

## References

---

259. Shishehchi, S., Garrett, G. & Rudin, S. Theoretical and Experimental Study of Time- and Temperature- Dependent Photoluminescence in ZnO. *J. Electron. ...* (2014).
260. Von Wenckstern, H. *et al.* Defects in hydrothermally grown bulk ZnO. *Appl. Phys. Lett.* **91**, 022913 (2007).
261. Gaspar, C., Costa, F. & Monteiro, T. Optical characterization of ZnO. *J. Mater. Sci.* **2**, 7–9 (2001).
262. Reshchikov, M. A. *et al.* Luminescence properties of defects in ZnO. *Phys. B Condens. Matter* **401-402**, 358–361 (2007).
263. Cousins, C. R. *et al.* Selecting the geology filter wavelengths for the ExoMars Panoramic Camera instrument. *Planet. Space Sci.* **71**, 80–100 (2012).
264. Griffiths, A. D. *et al.* Context for the ESA ExoMars rover: the Panoramic Camera (PanCam) instrument. *Int. J. Astrobiol.* **5**, 269 (2006).
265. Storrie-Lombardi, M. C., Muller, J.-P., Fisk, M. R., Griffiths, A. D. & Coates, A. J. Potential for non-destructive astrochemistry using the ExoMars PanCam. *Geophys. Res. Lett.* **35**, L12201 (2008).
266. Medeiros, S. K., Albuquerque, E. L., Maia, F. F., Caetano, E. W. S. & Freire, V. N. Electronic and optical properties of CaCO<sub>3</sub> calcite, and excitons in Si@CaCO<sub>3</sub> and CaCO<sub>3</sub>@SiO<sub>2</sub> core-shell quantum dots. *J. Phys. D: Appl. Phys.* **40**, 5747–5752 (2007).
267. Malins, A. & Poolton, N. Luminescence excitation characteristics of Ca, Na and K-aluminosilicates (feldspars) in the stimulation range 5–40 eV: determination of the band-gap energies. *J. Phys. D: Appl. Phys.* **37**, 1439–1450 (2004).

- 
268. Gaft, M., Reisfeld, R. & Panczer, G. *Modern luminescence spectroscopy of minerals and materials*. (Springer; 2005 edition, 2005).
269. Duller, G. A. T., Penkman, K. E. H. & Wintle, A. G. Assessing the potential for using biogenic calcites as dosimeters for luminescence dating. *Radiat. Meas.* **44**, 429–433 (2009).
270. Gaft, M., Nagli, L., Panczer, G., Waychunas, G. & Porat, N. The nature of unusual luminescence in natural calcite  $\text{CaCO}_3$ . *Am. Mineral.* **93**, 158–167 (2008).
271. Liu, M., Bursill, L., Prawer, S. & Beserman, R. Temperature dependence of the first-order Raman phonon line of diamond. *Phys. Rev. B* **61**, 3391–3395 (2000).
272. Poolton, N. & Towlson, B. Micro-imaging synchrotron–laser interactions in wide band-gap luminescent materials. *J. Phys. D ...* (2007).
273. Jones, G. O. *et al.* Detecting  $\text{sp}^2$ -bonded carbon in diamond using optically detected X-ray absorption spectroscopy. *Diam. Light Source Proc.* **1**, e131 (2011).
274. Poolton, N. R. J., Hamilton, B. & Evans, D. A. Synchrotron–laser pump–probe luminescence spectroscopy: correlation of electronic defect states with x-ray absorption in wide-gap solids. *J. Phys. D. Appl. Phys.* **38**, 1478–1484 (2005).
275. Mildren, R. & Rabeau, J. *Optical Engineering of Diamond*. (2013).
276. Howell, D. Strain-induced birefringence in natural diamond: a review. *Eur. J. Mineral.* **24**, 575–585 (2012).
277. Pinto, H. & Jones, R. Point and extended defects in chemical vapour deposited diamond. *J. Phys. ...* (2011).

## References

---

- 278. Crisci, A. *et al.* Residual strain around grown-in defects in CVD diamond single crystals: A 2D and 3D Raman imaging study. *Phys. Status Solidi* **208**, 2038–2044 (2011).
- 279. Friel, I. *et al.* Control of surface and bulk crystalline quality in single crystal diamond grown by chemical vapour deposition. *Diam. Relat. Mater.* **18**, 808–815 (2009).
- 280. Howell, D. *et al.* Quantifying strain birefringence halos around inclusions in diamond. *Contrib. to Mineral. Petrol.* **160**, 705–717 (2010).
- 281. Pinto, H. & Jones, R. Theory of the birefringence due to dislocations in single crystal CVD diamond. *J. Phys. Condens. Matter* (2009).
- 282. Howell, D. Strain-induced birefringence in natural diamond: a review. *Eur. J. Mineral.* **24**, 575–585 (2012).
- 283. Wotherspoon, A. *et al.* Photoluminescence studies of type IIa and nitrogen doped CVD diamond. *Diam. Relat. Mater.* **11**, 692–696 (2002).
- 284. McGuinness, L. P. *et al.* Quantum measurement and orientation tracking of fluorescent nanodiamonds inside living cells. *Nat. Nanotechnol.* **6**, 358–63 (2011).
- 285. Sobolev, E. V & Dubov, Y. I. Synthetic Dimonds. **2, 3**, (1979).
- 286. Cheljushkin, A. G., Laptev, V. A., I., R. B. & Al., E. No Title. in *Proc. IV All-Union Symp. on Luminescent Detectors of X-Rays* 121 (1982).
- 287. Sumida, N. & Lang, A. R. Cathodoluminescence evidence of dislocation interactions in diamond. *Philosophical Magazine A* **43**, 1277–1287 (1981).



- 
288. Occelli, F., Loubeyre, P. & LeToullec, R. Properties of diamond under hydrostatic pressures up to 140 GPa. *Nat. Mater.* **2**, 151–4 (2003).
289. Haouni, A., Mermoux, M., Marcus, B., Abello, L. & Lucazeau, G. Confocal Raman imaging for the analysis of CVD diamond films. *Diam. Relat. Mater.* **8**, 657–662 (1999).
290. Breza, J. *et al.* Diamond icosahedron on a TiN-coated steel substrate. *Microelectronics J.* **35**, 709–712 (2004).
291. Telling, R. H. & Field, J. E. Fracture in CVD diamond. *Int. J. Refract. Met. Hard Mater.* **16**, 269–276 (1998).
292. Yan, C.-S. & Vohra, Y. K. Multiple twinning and nitrogen defect center in chemical vapor deposited homoepitaxial diamond. *Diam. Relat. Mater.* **8**, 2022–2031 (1999).
293. Vohra, Y. K., Israel, A. & Catledge, S. A. Resonance Raman and photoluminescence investigations of micro-twins in homoepitaxially grown chemical vapor deposited diamond. *Appl. Phys. Lett.* **71**, 321 (1997).
294. Hounscome, L. *et al.* Origin of brown coloration in diamond. *Phys. Rev. B* **73**, 125203 (2006).
295. Godfrey, I. & Bangert, U. A Study of the relationship between brown colour and extended defects in diamond using core-loss electron energy loss spectroscopy. *J. Phys. Conf. Ser.* (2012).
296. Bangert, U., Barnes, R., Gass, M. H., Bleloch, a L. & Godfrey, I. S. Vacancy clusters, dislocations and brown colouration in diamond. *J. Phys. Condens. Matter* **21**, 364208 (2009).

## References

---

297. Fisher, D. Brown diamonds and high pressure high temperature treatment. *Lithos* **112**, 619–624 (2009).
298. Fisher, D. *et al.* The vacancy as a probe of the strain in type IIa diamonds. *Diam. Relat. Mater.* **15**, 1636–1642 (2006).
299. Eaton-Magana, S. & Post, J. FLUORESCENCE SPECTRA OF COLORED DIAMONDS USING A RAPID, MOBILE SPECTROMETER. *Gems ...* **43**, 332–351 (2007).
300. Hainschwang, T. Classification and color origin of brown diamonds. *Diplôme d'Université Gemmol. (DUG), ...* (2003).
301. Hainschwang, T., Notari, F., Fritsch, E. & Massi, L. Natural, untreated diamonds showing the A, B and C infrared absorptions ('ABC diamonds'), and the H<sub>2</sub> absorption. *Diam. Relat. Mater.* **15**, 1555–1564 (2006).
302. Hainschwang, T., Fritsch, E., Notari, F., Rondeau, B. & Katrusha, A. The origin of color in natural C center bearing diamonds. *Diam. Relat. Mater.* **39**, 27–40 (2013).
303. Collins, A. T. Things we still don't know about optical centres in diamond. *Diam. Relat. Mater.* **8**, 1455–1462 (1999).
304. Walker, J. Optical absorption and luminescence in diamond. *Reports Prog. Phys.* **42**, (1979).
305. Collins, A. T. The characterisation of point defects in diamond by luminescence spectroscopy. *Diam. Relat. Mater.* **1**, 457–469 (1992).

- 
306. Mäki, J.-M., Tuomisto, F., Kelly, C. J., Fisher, D. & Martineau, P. M. Properties of optically active vacancy clusters in type IIa diamond. *J. Phys. Condens. Matter* **21**, 364216 (2009).
307. Gaft, M., Nagli, L., Panczer, G., Waychunas, G. & Porat, N. The Nature of Unusual Luminescence in Natural Calcite CaCO<sub>3</sub>. *Am. Mineral.* **93**, (2008).
308. Ingley, R., Smith, D. R. & Holland, A. D. Life testing of EMCCD gain characteristics. *Nucl. Instruments Methods Phys. Res. Sect. A Accel. Spectrometers, Detect. Assoc. Equip.* **600**, 460–465 (2009).
309. e2v technologies limited. *Low Light Technical Note 5: An Overview of the Ageing Characteristics of L3Vision TM Sensors.* **44**, (2006).
310. Andor Technology Ltd. *EMCCD Gain and the Ageing Solution.* (2008).